

UNIVERSITY OF CALIFORNIA

Los Angeles

**The MOTion trap: a hybrid atom-ion trap
system for experiments in cold-chemistry and
the production of cold polar molecular ions**

A dissertation submitted in partial satisfaction

of the requirements for the degree

Doctor of Philosophy in Physics

by

Scott Trevor Sullivan

2013

© Copyright by
Scott Trevor Sullivan
2013

The dissertation of Scott Trevor Sullivan is approved.

Peter Felker

Hong-Wen Jiang

Troy Carter

Eric R. Hudson, Committee Chair

University of California, Los Angeles
2013

To my parents ...

TABLE OF CONTENTS

1	Introduction	1
1.1	Thesis Layout	1
1.2	What is the MOTion trap?	3
1.3	Why build the MOTion trap?	3
1.3.1	The prospects and progress using molecular structure	4
1.3.2	The trouble with molecular structure	6
1.3.3	The Born-Oppenheimer approximation	7
1.3.4	Cold molecular ion candidate - BaCl ⁺	12
1.4	The atom-ion interaction in the low collision energy regime	16
1.4.1	Short-range inelastic collision events	17
1.4.2	Atomic excited state inelastic shielding	18
2	Experimental Hardware and the Ion Trap	20
2.1	Introduction	20
2.2	Hardware	20
2.2.1	Vacuum system	20
2.2.2	Signal detection	23
2.2.3	Data acquisition and control	26
2.2.4	The lasers	26
2.3	The Ion Trap	32
2.3.1	The equations of motion for RF trapping	32

2.3.2	The low q limit - secular motion and micromotion	35
2.3.3	Cooling atomic ions	37
2.3.4	Sympathetic cooling and heating of RF trapped ions	41
2.3.5	Experimental trap realization	48
2.4	The atomic ions - Barium and Ytterbium	54
2.4.1	The Ytterbium ion	54
2.4.2	The Barium ion	55
3	Calcium Magneto-Optical Trap	58
3.1	MOT Basics	58
3.2	Properties of ^{40}Ca	60
3.2.1	The Calcium source	63
3.3	The Ca MOT Laser System	69
3.3.1	423 nm 4^1S_0 - 5^1P_1 Laser	69
3.3.2	The 672 nm repump	77
3.3.3	MOT laser polarization	78
3.4	The Magnetic Field Gradient	80
3.5	MOT Characterization and Control Techniques	85
3.5.1	Controlling the position of the MOT	85
3.5.2	Determining MOT density	85
3.5.3	Determining atom-ion co-location in 3D	87
3.5.4	Determining MOT temperature	90
4	Trapping molecular ions formed via photo-associative ionization	

of ultracold atoms	92
4.1 Summary	92
4.2 Introduction and Motivation	92
4.3 Experiment	95
4.4 Results	100
4.4.1 Physical interpretation of PAI pathway	104
4.5 Conclusion	106
5 Measurement of a large chemical reaction rate between ultracold closed-shell atoms and open-shell ions held in a hybrid atom-ion trap	110
5.1 Summary	110
5.2 Introduction and Motivation	110
5.3 Experiment	113
5.4 Conclusion	122
5.5 Appendix: reaction rates for even isotope number Yb^+	122
6 The role of electronic excitation in ground-state forbidden inelastic collisions between ultracold atoms and ions	124
6.1 Summary	124
6.2 Introduction and Motivation	125
6.3 Experiment	128
6.4 Conclusion	137
6.5 Appendix A: Time-variation of the atom-ion overlap factor	137

6.6 Appendix B: Calculation of Ba ⁺ fractional electronic state populations	139
6.7 Appendix C: ab initio calculation	142
7 Sympathetic vibrational cooling of translationally cold molecules	
144	
7.1 Introduction and Motivation	144
7.2 Method of Vibrational Level Thermometry	149
7.3 Experiment	152
7.4 Results and Conclusion	154
7.5 Methods	158
7.5.1 Photodissociative vibrational thermometry: caveats	161
8 Outlook and loose-ends: progress of a direct search for the low-energy ²²⁹Th nuclear isomeric transition in a thorium-doped solid with synchrotron radiation	
164	
8.1 Introduction	164
8.2 Experimental Design	166
8.3 Experimental Apparats	167
8.3.1 ²²⁹ Th:LiSrAlF ₆ crystal	167
8.3.2 Advanced Light Source	169
8.3.3 Fluorescence detection apparatus	169
8.4 Initial Experimental Results	174
8.5 Conclusion and Outlook	177

8.5.1	Monte Carlo exclusion region estimation	177
8.6	The future of the MOTion trap - version 2.0	180
8.6.1	Ion trap version 2.0	180
8.6.2	The radial ejection time-of-flight mass spectrometer	183
8.6.3	Outlook	184
References	186

LIST OF FIGURES

1.1	Schematic diagram illustrating typical molecular structure for a bound electronic potential. The molecular potential $E^{el}(R)$, indicated by a solid line, varies in energy with the internuclear separation. D_e indicates the electronic dissociation energy of the molecule on this potential. R_0 indicates the bond length i.e. the average internuclear separation for a well-bound vibrational level. Schematic vibrational spacing is marked by horizontal lines indicating the different oscillator levels. Each vibrational level supports a rotational spectrum, shown zoomed in.	8
1.2	Partition function for a rigid quantum rotor as a function of the ratio of the rotational splitting constant B to the thermal energy $k_B T$	12
1.3	Photodissociation measurement scheme and molecular potentials. Dissociation occurs by single photon excitation from the ground $X^1\Sigma^+$ (solid black) to the repulsive wall of the $A^1\Pi$ (solid red) potential.	14
1.4	BaCl^+ photodissociation cross-section. The data points fit well to the room temperature thermal average of the $v = 0\ldots 3$ vibrational contributions, calculated using the <i>ab initio</i> potentials shown in figure 1.3.	15

1.5 Schematic of charge transfer pathways. Charge transfer can occur directly with or without emission of a photon via radiative and non-radiative charge transfer, respectively (RCT, nRCT). Alternately, by emitting a photon, the atom-ion pair can form a molecular ion by radiative association (RA).	18
1.6 The left panel shows the relative shift, compared to the far separation limit, between the ground and excited electronic states of ^{40}Ca as a function of atom-ion separation. The horizontal line marks the natural linewidth of the transition, for scale. The double-headed arrow marks the typical distance a cold ^{40}Ca atom travels in the excited state lifetime. The right panel shows the fractional suppression of a laser's efficiency in driving the cooling transition as a function of atom-ion separation. The laser is detuned from the $r \rightarrow \infty$ transition wavelength by half a natural linewidth. The horizontal dashed line marks the laser's efficiency if the polarizabilities were equal.	19
2.1 A schematic of the experimental vacuum chamber. The experimental chamber is built around an 8" Kimball Physics extended spherical octagon (MCF800-ExtOct-G2C8A16). The system is supported by three v-block supports: one pair of supports, on each of the 2.75" CF tees to either side of the octagon and a third support at the reducer-tee near the ion pump.	21
2.2 A rendering of the support structure for the anti-Helmholtz coils. The coils are wound in phenolic spools, press fit between steel plates supported by a combination of 1" diameter and 0.5" steel rods.	24

2.3	Ion pump manufacturer specification for reading the chamber pressure as a function of current drawn. The vacuum system uses the 60 l/s model.	25
2.4	General schematic diagram and mechanically drawing of the ECDL design used for all the non-commercial lasers in this work. The particular mechanical drawing shown is for the 935 nm laser geometry.	29
2.5	Schematic of the ECDL transfer cavity feedback scheme. The 423 nm laser is first stabilized to an atomic absorption reference (described in 3.3.1), then co-coupled with light from the ECDL into a scanning cavity interferometer. A LabVIEW vi analyzes the cavity photodiode signal and performs stabilization feedback.	31
2.6	Inset (a) shows the first linear quadrupole stability region in terms of the dimensionless Mathieu parameters a and q . Part (b) shows the stability region scaled into units of voltage on the endcaps and two RF rods in the actual ion trap ($r_0 = 11.2\text{mm}$, $m = 173\text{amu}$). The stability region is within the dashed green line. The blue triangles are the experimental boundaries found when ablating a Yb target. The black dots are the experimental boundaries measured when ablating a pressed BaCl_2 target.	34
2.7	Mathieu cosine, from the expansion in equation 2.4, for $A = 1$, $B = 0$, $a = 0$ and $q = 0.25$. Note the bulk, lower frequency (secular) motion with a fractional modulation (micromotion). . .	36

- 2.8 A laser induced fluorescence profile on a trapped sample of atomic Yb⁺. The horizontal axis (laser frequency) has been re-scaled into units of the transition natural linewidth. The solid red line is not a fit, it is the Voigt fluorescence profile, equation 2.12, evaluated at the appropriate Doppler temperature limit, equation 2.11, for each laser detuning. The profile is truncated for frequencies above the resonance, because the ions are heated up quickly when the cooling laser passes the resonance due to Doppler heating. 40
- 2.9 Experimental measurement of the reduction in trap lifetime of trapped titanium-oxide (TiO⁺, $m \sim 64\text{amu}$) and titanium (Ti⁺, $m \sim 48\text{amu}$) ions due to introducing room temperature He ($m \sim 4\text{amu}$), Ar ($m \sim 40$ amu), and Xe ($m \sim 131.3$ amu) buffer gas. *SIMION* simulation results are shown as solid lines. 42
- 2.10 (a) The solid line shows the experimental measured laser induced fluorescence profile for a sample of ions near the Doppler temperature limit. The dashed line shows the profile if the ions were at $T = 90\text{K}$. The inset shows a typical ion cloud fluorescence image. (b) The result of a measurement of the ratio cold ion sample fluorescence at fixed laser detuning ($\delta = 30\text{MHz}$) to the fluorescence of the same sample after extinguishing the cooling beam for a variable heating time. A molecular dynamics simulation is shown as a solid line. (c) The dots in this panel represent the secular temperature inferred from the measured fluorescence ratio in panel b by the method schematically shown in panel a. The solid (dashed) line shows simulation results for the secular (total) temperature. . . 43

2.11 Measurement of the ion cloud density as a function of secular temperature, performed with a trapped of Yb^+ , shown in dots. The dashed line is equation 2.19.	47
2.12 The effect of the ^{40}Ca MOT on trapped Yb^+ fluorescence.	49
2.13 A rendering of actual ion trap used in this work. On the left, shown in perspective. Four sets of axial endcaps provide axial confinement for three possible trapping regions. A channel-electron multiplier (CEM) is mounted above for direct ion detection. Below are two mounts for pressed ablation targets for ion loading. To the right is an orthographic view down the trap axis, showing the pair of rods with the endcaps are used for DC offset voltages, to change a or shim micromotion, while the other pair of rods is driven with a RF potential.	50
2.14 Manufacturer's specification for the gain of the Burle 5901 Magnum channel electron multiplier. The detector was typically biased to -2000 V.	51
2.15 Measured gain as a function of PMT bias voltage for the Hamamatsu R3896.	53
2.16 Manufacturer's specification for the gain of the Burle 5901 Magnum channel electron multiplier. The detector was typically biased to -2000 V.	53

2.17 Energy level diagram for $^{174}\text{Yb}^+$. Solid lines show the optical transitions driven by the cooling (blue) and repumping (red) lasers. Dashed lines indicate spontaneous dipole decay channels. The wavelengths and decay rates are indicated with values from the NIST Atomic Spectra Database. Known meta-stable state lifetimes and decay branching ratios are indicated.	55
2.18 Energy level diagram for $^{138}\text{Ba}^+$. Solid lines show the optical transitions driven by the cooling (blue) and repumping (red) lasers. Dashed lines indicate spontaneous dipole decay channels. The wavelengths and decay rates are indicated with values from the NIST Atomic Spectra Database. Known metastable state lifetimes and decay branching ratios are indicated.	57
3.1 Magneto-optical trap schematic. This diagram shows the basic physical mechanisms behind the spatial trapping in a MOT. Pairs of counter-propagating, red-detuned beams generate an optical molasses via a velocity-dependent, dissipative force. The spring-like position-dependent, dissipative force is generated by the combination of a magnetic field gradient and red-detuned, circular-polarized light chosen to selectively drive atoms towards the magnetic field null. Note that the magnetic field defines the quantization axis for the atom, thus the correct polarization for all directions is σ^{-1} to selectively drive the high-field seeking sublevel. The handedness of the light, however, is different for the anti-Helmholtz axis and radial directions.	61

3.2 Relevent energy levels in ^{40}Ca . The solid lines are the transitions driven by the cooling and repumping lasers. The dashed lines spontaneous decay pathways. Approximate wavelengths and branching ratios are noted.	62
3.3 Ca MOT density as a function of decelerator beam power at trap beam detuning $\delta_T = -0.6 \Gamma$ and trap beam power $P_T = 24 \text{ mW}$	64
3.4 Ca MOT lifetime versus getter source current. The small decrease in lifetime is likely due to increased background collision with thermal Ca from the dispenser.	65
3.5 Photograph of the experiment chamber during decommission of version 1.5. Version 1.5 is identical to the original MOTion trap, except for a segmented ion trap rod. The calcium dispenser is mounted from a piece of Macor ceramic and shielded by a piece of stainless steel mesh. The BaCl_2 ablation target and channeltron are both also visible.	66
3.6 Capture velocity for a 1D MOT with 1 cm trapping region as a function of trap beam detuning and saturation intensity.	67
3.7 The estimated effect of the slowing beam under typical operating conditions. The calculation predicts an improvement in trap yield of over an order of magnitude compared to the getter source with no optical slowing, or over a factor of two better than a theoretical room temperature Ca background source.	68

3.8 Schematic of the optical system for the 423 nm laser system. A small fraction ($\sim 10\%$) of the light travels through the saturation absorption lock. After two frequency shifts via a double-passed AOM, the light saturates the transition inside the vapor cell. The overlapped probe beam signal ultimately servo locks the laser to the blue of the ^{40}Ca cooling transition resonance. The experimental arm employs three AOMs for fast switching and to shift to the appropriate frequencies for trapping, slowing, and absorption imaging.	71
3.9 CAD drawing of the vapor cell and brass cooling blocks.	73
3.10 Circuit diagram for the loop filter used in for the Ca laser systems frequency lock. This servo sufficed for all the work presented in this dissertation, but could be improved with a differential photodetector and a high-pass (or band-pass) before the photodetector signal goes into the mixer.	75
3.11 This figure shows examples of the error signal output, as fed back into the Toptica PZT servo. Panel (a) shows the error output as the laser frequency is swept over the lock point. Panel (b) shows a closed loop measurement of the error signal, with the PID parameters set to allow oscillation. Panel (c) is a measurement of the lock stability using the wavemeter, showing both the locked and unlocked laser stability since the laser comes unlocked roughly half way through the measurement.	76
3.12 Schematic diagram of the MOT coils with temperature interlock and bleeder shim circuit for axial control of the magnetic field zero.	82

3.13 MOT coil spool assembly. All dimensions are inches. Each spool was constructed from 3 pieces of machinable garolite (phenolic) epoxied together. The conducting tubes are wound in 10 layers of 10 windings, sealed with stycast adhesive at each layer.	83
3.14 Measurement of the magnetic field at the trap center with 25 A running through the anti-Helmholtz coils. In red circles, the field along the axis of the anti-Helmholtz configuration. In black squares, the field along the radial direction. With each measurement, a dashed line shows the best fit. The gradient along the axis is found to be $0.532(3)\frac{G}{cmA}$. And the gradient along the radial direction is found to be $0.267(1)\frac{G}{cmA}$	84
3.15 A measurement of the temperature of the ^{40}Ca MOT. A fit to equation 3.12 corresponding to $2.5(1)$ mK is shown in dashed red. Error bars are hidden by the plot markers.	91
4.1 MOTion trap: A ^{40}Ca magneto-optical trap is constructed inside a linear quadrupole ion trap. Below the trap are two ablation targets used to load calibration ions. The channel electron multiplier (CEM) is mounted above the trap.	94
4.2 Results of a excitation spectrum measurement performed at trapping parameters where the stability parameter (q) for $m = 80$ amu is 0.5, thus unstable for $m = 40$ amu. The observed loss near 70 kHz is within 10% of the predicted secular frequency for $m = 80$ amu. The split peak feature is likely due to trap imperfections (asymmetric endcap placement, machining, imperfect quadrupole ratio,etc).	96

4.3	Measurement of the ion number as a function of loading time is shown in panel (a). In panel (b), trap lifetime is measured by loading the trap to saturation and stopping production for a fixed amount of time before detection. Characteristic times are found by exponential fits (dashed lines)	98
4.4	Ion number measured as a function of the MOT density determined by absorption imaging. A quadratic trend (with a best fit shown to guide the eye) is observed until trap saturation occurs at higher densities (shown in the points with open circles)	99
4.5	Normalized production rate as a function of overall 423 nm laser power incident upon the MOT. Data is obtained both by attenuating the deceleration beam at fixed trapping power and by attenuating the trapping beams at fixed deceleration power. A quadratic fit is shown as the dashed line.	102
4.6	Molecular potentials of $^{40}\text{Ca}_2$ (black curves) and $^{40}\text{Ca}_2^+$ (red curve). Two vertical arrows indicate the energy carried in the 423 nm MOT photons. Note the ground state potential of the molecular ion is in the same energy region as the potentials dissociating to two ^1P ^{40}Ca atoms.	103
4.7	Ion number normalized by the square of the MOT density as a function of $^3\text{D}_2$ state density. Note the open circle points correspond to those in figure 4.4 at which trap capacity is reached. . .	108

5.1 MOTion trap schematic. Yb ⁺ ions and Ca atoms are laser cooled and trapped in the central region. Typical images of the ultra-cold clouds, shown in the upper left of the figure, are used for a 3D reconstruction that yields the degree of overlap. Ions are also detected with a voltage-gated CEM.	114
5.2 (a) Yb ⁺ ion trap lifetime in the presence of the MOT (solid curve) compared to the lifetime without a MOT (dashed curve). Dotted curves are single exponential decay fits. Inset: Images of the Yb ⁺ ion cloud in the presence of the MOT at various times. (b) Loss rate constant as a function of the Mathieu stability parameter q and the trap depth T _D	115
5.3 (a) Total experimental (points) and theoretical (black line) charge exchange rate constants as a function of ion kinetic energy. The horizontal location of the data point is the value of the secular kinetic energy as measured by the Doppler fluorescence technique. The horizontal “error bars” represent the contribution of the micromotion to the overall kinetic energy. Also shown are the calculated rate constants for the three charge exchange pathways. (b) The X ² Σ^+ and A ² Σ^+ potential energy curves and (c) the corresponding transition dipole moment of the CaYb ⁺ molecular ion as a function of the internuclear separation R. The dotted curves are the diabatized potentials constructed from these potentials. The dashed curve gives the coupling constant between the diabatic potentials.	117
5.4 Charge exchange rate constant measurement for Yb ⁺ ions for 170,172,174 and 176 isotopes.	123

6.1	a) Ba ⁺ and Ca relevant energies levels and laser cooling schemes. b) Fluorescence images of Ca MOT and Ba ⁺ ion cloud. c) and d) Molecular potentials of the $\Omega=\frac{1}{2}, \frac{3}{2}$ excited states of the CaBa ⁺ molecule, respectively, as a function of interatomic separation R . The bottom panels show higher detail for potentials near 20×10^3 cm^{-1} above the Ca ^{+(2S)} +Ba(¹ D) dissociation limit. Entrance and exit channels, as defined in the text, dissociate to green and red potentials, respectively.	127
6.2	Panel (a): experimentally determined excitation fraction in Ba ⁺ versus theoretical predictions of the quantum Liouville (●) and rate equation (red circles) treatment. Panel (b): experimentally determined excitation fraction in Ca versus predictions of a 4-level rate equation model. In both panels the solid line has a unit slope, representing ideal agreement.	130
6.3	Measured rate constant as a function of Ba ⁺ population fractions. Experimental result in black. Best fit ($\{k_{ps}, k_{sd}, k_{pd}, k_{dd}\} = \{4.2 \pm 1.9, \leq 3, \leq 20, \leq 7\} \times 10^{-10} \text{ cm}^3 \text{ s}^{-1}$) to the four entrance channel model shown as open red circles. For these measurements, Ca population fractions were fixed at $\rho_{ss}^{Ca} \sim 0.75$, $\rho_{pp}^{Ca} \sim 0.20$, $\rho_{dd}^{Ca} \sim$ 0.05.	132
6.4	Measured rate constant as a function of Ca population fractions. Experimental result in black. Best fit ($\{k_{ps}, k_{sd}, k_{pd}, k_{dd}\} = \{4.2 \pm 1.9, \leq 3, \leq 20, \leq 7\} \times 10^{-10} \text{ cm}^3 \text{ s}^{-1}$) to the four entrance channel model shown as open red circles. For these measurements, the Ba ⁺ population fractions were fixed at $\rho_{ss}^{Ba} \sim 0.4$, $\rho_{pp}^{Ba} \sim 0.1$, $\rho_{dd}^{Ba} \sim 0.5$. .	133

- 6.5 The dashed line shows the numerical calculation of the overlap factor as a function of charge exchange lifetimes expired in the case of perfect alignment of relative MOT to ion cloud position, with typical experimental waists and aspect ratio. The other three lines are randomly selected numerical calculations from actual experimental data to show how imperfect alignment changes the curve. 140
- 7.1 Photodissociation Thermometry of BaCl⁺. **a** Potential energy curves for the X ¹Σ⁺ and A ¹Π electronic states and a schematic indicating the photodissociation thermometry method described in the text. The different shapes of the v = 0 and v = 1 wavefunctions give rise to the different frequency responses of the two levels to the photodissociation laser. **b** The permanent dipole moment (PDM) of BaCl⁺ calculated as described in Methods. **c** Improved data (with standard error) obtained for the cross-section of the A ¹Π ← X ¹Σ⁺ of the photodissociation transition in BaCl⁺ using a separate ion trap and time-of-flight system. The dashed line is the thermally averaged cross-section at 300 K. Also shown are the improved calculations of the individual vibrational level contributions of the v = 0 and v = 1 levels. Although the model described in the methods section incorporates the lowest 4 vibrational levels, here only the v = 0 and v = 1 levels are shown for clarity. 148

7.2 Measurement of MOT-induced vibrational quenching of BaCl⁺ ions. **a** Example traces of the Ba⁺ ion fluorescence measured during the experimental sequence. Initially the trap is loaded with a pure BaCl⁺ sample (i). The photodissociation laser (PDL) is then turned on to create a mixed sample of BaCl⁺ and Ba⁺ ions (ii). Once the Ba⁺ ions have been laser cooled, the MOT is optionally turned on and the BaCl⁺ ions are collisionally cooled by the ultracold Ca atoms (iii). Following that, the BaCl⁺ ions are interrogated with the PDL to determine the amount of vibrational relaxation due to the MOT (iv). The ratio of Ba⁺ ion number created in each instance of photodissociation is then compared for the two cases when the MOT was on and off. The top and bottom panels are data for a PDL wavenumber of 41,500 cm⁻¹ and 44,675 cm⁻¹, respectively. **b** The average of all data points (with standard error) obtained, as described in the Methods, is plotted for various photodissociation wavenumbers. The blue points are cooling data and the grey points are a control analysis which should be consistent with unity (see Methods). The curves are the expected result from a rate equation model of the experimental sequence described in Methods and the agreement with the data shows the BaCl⁺ sample has been cooled to a ground state vibrational population of ∼90% in the average case. 151

7.3 Panel (a) shows the hybrid magneto-optical and ion trap (MOTion trap) system used in these experiments. The secular frequencies for the BaCl+ and Ba+ ions are 33 and 43 kHz, respectively. BaCl ⁺ ions are loaded by laser ablation of a solid BaCl ₂ target and are then photodissociated into Ba+ by a pulsed laser beam (\sim 1 mJ at a 10 Hz repetition rate) directed down the center axis of the ion trap. The Ba ⁺ ions are laser cooled, and thus translationally cool the remaining BaCl+ molecules, by a pair of axial cooling lasers. The intensities of the 493 nm and 650 nm lasers at the ion cloud are \sim 500 mW/cm ² and \sim 100 mW/cm ² , respectively. Spatial overlap between the trapped Ca and the ions is verified by two nearly-orthogonal EMCCD imaging systems. Panel (b) shows an overlaid set of experimentally obtained images of the Ca MOT and laser-cooled Ba ⁺ cloud. These images have been colorized (the Ca in purple, Ba ⁺ in green) for clarity. Also included, is a reconstruction of the expected position, taking into account the diminished trap depth due to higher mass, of the BaCl ⁺ molecular cloud (in red).	155
8.1 Results characterizing the UV radiation background in the thorium-229 doped sample. An emission peak is observed, in solid black, at 295 nm with best-fit, in dashed red, FWHM of 75 nm. In future measurements, VUV bandpass filters will be used to eliminate this background.	168

8.2 Results for the photon flux measurement at beamline 9.0.2 T1 at the Advanced Light Source using a NIST traceable photodiode. In dashed red, the measurement for the 1.5 GeV operation. In solid black, the result for normal operation at 1.9 GeV ring energy. The rate is normalized to the ring current. The drop off at higher energies seen in the black trace is due to the MgF window and Argon gas filter in the beamline. The apparent increase in flux near 14 eV during low energy operation is likely a harmonic leak through.	170
8.3 Transmission curves measured for the $f = 250\text{mm}$ LiF lens (blue, dashed), the $f = 75\text{mm}$ (red, solid), and the LiSAF crystal itself (black, dotted). The transmission is measured using the McPher- son 302 monochromator.	171
8.4 A schematic diagram of the optical mounting flange for the thorium experiment. Four $1/8''$ rods hold adjustable aluminum mounting rings that hold the LiF lenses in place. The 159 nm (190 nm) optimized configuration has A= 59.05 (64.44) mm and B = 225.65 (222.44) mm. Also shown in a drawing of the integration sphere used to measure the collection efficiency.	172

8.5 Overall light collection efficiency for the LiF lens collection system. The solid black line is a measurement of the collection efficiency performed by shining light from the deuterium lamp source, through the monochromator onto an integration sphere placed at the position the crystal occupies during the actual experiment. The dashed line is the result of a ray tracing model for a one-dimensional source of light at the crystal position. The red line is the result of a ray tracing model for a two-dimensional source of light at the crystal position, to better approximate behavior of the integration sphere.	173
8.6 Results for the R7639 PMT calibration measurement using the NIST-traceable photodiode. Plotted in dashed green is the manufacturer's specified typical quantum efficiency. In solid orange, the measured efficiency.	175
8.7 Typical measurement result from the first ALS run with the ^{229}Th -doped crystal. All the measurements had some short-lived fluorescence on a characteristic timescale of about 5 seconds. A portion of the measurement time is taken with the PMT shutter closed for a dark count rate.	176
8.8 Transmission of the Esource Optics broadband VUV bandpass filter is shown as measured with the deuterium lamp source and McPherson spectrometer.	178

8.9 Monte Carlo calculation of 95%-confidence exclusion region, in grey, for the ^{229}Th transition properties after planned detection improvements are made. The green region is where the transition is expected to be by indirect measurement in [BBB07]. The orange region is the region where the transition is expected to be after a recent indirect de-excitation measurement [ZEN12]	179
8.10 Schematic of MOTion trap v2.0. The time-of-flight ion optics are mounted in the former position of the Ca dispensers. New dispenser holders are mounted directly to the ion trap rod holders.	181
8.11 Picture of the second iteration ion trap and rendering of the segmented rod design.	182
8.12 Schematic of the time-of-flight device operation. Panel (a) shows the configuration of the high voltage pulsing circuit for the trap rods for two stage acceleration into the flight tube. Panel (b) shows some results of <i>SIMION</i> trajectory simulations used to optimizing the collimation and collection of ejected ions.	184

LIST OF TABLES

1.1 BaCl ⁺ molecular spectroscopic constants	13
2.1 Basic information about the different components in the home-built ECDL systems. *The power is measured after the optical isolator. **For the 672 nm laser, the current is supplied by a Vescent Photonics current controller, the piezo-electric transducer (PZT) stack is driven by home-built electronics, and the temperature is controlled by both a Vescent Photonics (diode-stage) and a Wavelength Electronics (PTC-10-K-CH) controller for the baseplate. The MOGLabs MOGbox laser controller has single-stage temperature control, a PZT driver, and current control all-in-one.	27
3.1 Atomic parameters for laser cooling and trapping ⁴⁰ Ca. The parameters for ⁸⁷ Rb are shown for comparison.	62
3.2 The mapping between the handedness of the circular-polarized light, as measured via thumb along the \vec{k} , and the $\sigma^{+,-}$ selection basis for a given relation between the magnetic field and light propagation direction.	80
3.3 Unit vectors in the lab-frame for the camera system imaging planes, for the camera configuration shown in schematic 2.1. The ion trap axis is along the laboratory frame z-axis. The ion pump is off in the negative x direction, which leaves the direction anti-parallel to gravity as the y direction in figure 2.1. The constants are $a = 0.38256$, $b = -0.92393$, $c = 0.2547$, $d = 0.96125$, $e = 0.1055$, $f = 0.888125$, $g = 0.27569$, $h = 0.36774$	89

5.1 Table of isotopic abundances for the even numbered isotops of Yb ⁺ detected via laser fluorescence in the trap system. Values for the laser wavenumbers are from [MNS11].	123
--	-----

ACKNOWLEDGMENTS

I consider myself extremely lucky to have found my way into the Hudson lab. My enrollment status upon arrival at UCLA was a graduate school equivalent of “undeclared”. Luck would have it that one of the seminars I enrolled in during my second year was an Atomic Physics course taught by a freshly hired Prof. Eric Hudson. Shortly after the start of the quarter, I’m touring a mostly empty lab (making a mixed first impression wearing my “Frank the Tank” t-shirt) and subsequently signing on to be Eric’s second graduate student.

The decision to work with Eric was the best decision I made in graduate school. Eric Hudson is a great scientist, leader, and friend. While it is obviously important for an advisor to be a good scientist, I think it is even more important that they are able to communicate, motivate, and understand the personal dynamics of leading a group of individuals. It has been fun to watch Eric steer the experiments, and the personalities running the experiments, towards success. Eric has a contagious joy for experimental science and I can’t imagine having as much fun or as much success during my PhD if it weren’t for him being him.

The solitary person sitting around in the mostly empty lab when I first toured it was none other than the legendary Dr. Wade Rellergerd. In a lab without yet any infrastructure, Wade was stuck with the task of handling two untrained graduate students: Kuang Chen (who I will be writing about next) and myself. Wade was perfect for the job because he was, and is, a getting-things-done machine. I’ve joked that the acknowledgement section in this dissertation would need to be subtitled “the legend of Wade Rellergerd” because I spent so much time working with and learning from Wade. I can only hope that his “minimize-nonsense” and get things done attitude has rubbed off on me. Wade is a pleasure to be around both inside the lab and out. I don’t remember who started the policy of “singing”

songs of the butchered lyric variety in the lab while we were working, but it is hilarious.

In the early days, Kuang and I were the only students in the lab. I remember hanging around with him, completing menial tasks around the lab. Kuang is much more gifted at the mathematically (or programmatically) rigorous aspects of the job, and he can always be counted on for advice. He's also got a knack for finding steep discounts on optics. Sometimes I feel a little bad for him though, since he's picked up a lot of his idiomatic expressions from hanging around with Wade, Steven Schowalter (who I will be writing about next) and me.

Steven Schowalter is about to become the senior member of the group when Kuang and I graduate. Steven's a perfect fit for the lab. He brings a great sense of brotherhood to the whole situation. I also think he was the original initiator of the "ghost mouse". In all seriousness though, Steven plays a big part in making the experience of working long hours on the experiment a pleasure. Bonus fact, he saved me from choking on a roast beef sandwich by successfully implementing the Heimlich maneuver and I'm pretty happy that worked out.

The newest graduate student, Justin Jeet, is taking up the reins of the Thorium experiment. It has been a lot of fun to have someone new on the experiment, particularly on the road trips to use the beam in Berkeley. I would also be remiss if I didn't acknowledge John Koulakis. When study crunch time came around for the comprehensive written exam, John and I studied together on a regular schedule (i.e. every day the weeks prior). Without the social pressure to consistently show up, I'd likely have hardly studied at all! Speaking of social pressure, it has been a lot of fun interrupting Andrew Jayich's workflow to go work out or discuss the finer points of light weight and other obsessive hobbies.

Finally, I want to acknowledge, of course, the support of my friends and family.

Jen has been, as always, incredibly supportive. I owe so much to my father who has always made me and my siblings his first priority. I can't single everybody out, but if you're bothering to read this, you know who you are. Thank you.

VITA

2005-2006	Undergraduate research under Prof. Michael Dennin. Soft Condensed Matter, Flow dynamics, SURP Fellowship UCI
2006-2007	Undergraduate research under Prof. Asantha Cooray, Cosmology, Dynamical Dark Energy analysis
2007	B.S., Physics, University of California, Irvine. Cum Laude
2007-2009	Teaching Assistant, Department of Physics and Astronomy, UCLA
2007	Fellowship, Graduate Assistance in Areas of National Need (GAANN)
2009	M.S., Physics, University of California, Los Angeles
2009-2013	Graduate Student Research, UCLA, Atomic, Molecular and Optical Physics with Prof. Eric R. Hudson

PUBLICATIONS

W.G. Rellergert, S.T. Sullivan, et. al., *Evidence for sympathetic vibrational cooling of translationally cold molecules*, Nature 495 7442 (2013)

S.J. Schowalter, et. al., *An integrated ion trap and time-of-flight mass spectrometer for chemical and photo-reaction dynamics studies*, Rev. Sci. Instr. 83

043103 (2012)

S.T. Sullivan, et. al., *Role of Electronic Excitations in Ground-State-Forbidden Inelastic Collisions Between Ultracold Atoms and Ions*, Phys. Rev. Lett. 109 223002 (2012)

K.Chen, et.al., *Molecular-ion trap-depletion spectroscopy of BaCl⁺*, Phys. Rev. A 83 223002

S.T.Sullivan, et. al., *Trapping molecular ions formed via photo-associative ionization of ultracold atoms*, Phys. Chem. Chem. Phys. 13 42 18859 (2011)

W.G. Rellergert, S.T. Sullivan, et. al., *Measurement of a Large Chemical Reaction Rate between Ultracold Closed-Shell ⁴⁰Ca and Open-Shell ¹⁷⁴Yb⁺ Ions Held in a Hybrid Atom-Ion Trap*, Phys. Rev. Lett. 107 243201 (2011)

M.P. Hehlen, et. al., *Optical spectroscopy of an atomic nucleus: Progress toward direct observation of the ²²⁹Th isomer transition*, Journal of Luminescence, Volume 133, Pg 91-95 (2013, available online 2011)

W.G. Rellergert, et. al., *Progress towards fabrication of ²²⁹Th-doped high energy band-gap crystals for use as a solid-state optical frequency reference*, IOP Conference Series: Materials Science and Engineering 15 012005 (2010)

D. Sarkar, S.T. Sullivan, et. al., *Beyond Two Dark Energy Parameters*, Phys. Rev. Lett. 100, 241302 (2008)

S.T. Sullivan, et. al., *Narrowing Constraints with Type Ia Supernovae: Converging on a Cosmological Constant*, JCAP0709:004 (2007)

C. Gilbreth, S.T. Sullivan, & M. Dennin, *Flow transitions in two-dimensional foams*, Phys. Rev. E 74, 051406 (2006)

ABSTRACT OF THE DISSERTATION

The MOTion trap: a hybrid atom-ion trap system for experiments in cold-chemistry and the production of cold polar molecular ions

by

Scott Trevor Sullivan

Doctor of Philosophy in Physics

University of California, Los Angeles, 2013

Professor Eric R. Hudson, Chair

This dissertation details of the construction of and experiments performed in a hybrid system consisting of a cold neutral atomic magneto-optical trap (MOT) contained within a linear radio-frequency quadrupole ion trap (LQT). The combination of these two workhorses of atomic physics facilitates a variety of developing science such as the controlled investigation of ion-neutral quantum chemistry and the production of ground-state molecular ions. While the primary focus of this work is the production of ultracold molecular ions via sympathetic cooling, there has been investigation of cold ($T \sim mK$) ion-neutral charge exchange processes in two different ion-neutral pair systems. In addition, a possible method of producing ultracold homonuclear molecular ions via a photo-associative ionization (PAI) pathway is studied in the MOT. The LQT traps ions in spatial overlap with a ^{40}Ca MOT constituting an ultracold buffer gas purposed to sympathetically cool molecular ions.

An effective, general method of producing ground-state molecular ions would open a field of physics allowing, for example, precise measurements of molec-

ular transitions which are uniquely sensitive to parity violation, or the possible variation of fundamental constants. Another promising application of cold molecular ions is an implementation of a quantum computing architecture by coupling micro-fabricated strip-line resonators to the microwave rotational transition found in many diatomic molecular ions. The molecular ion BaCl^+ is chosen to be used in proof-of-principle sympathetic cooling experiments. Ultimately, a vibrational internal state thermometry experiment shows that the Ca MOT performs very efficiently at quenching the vibrational motion of the BaCl^+ molecular ion.

As a product of overcoming experimental challenges, this thesis discusses several experiments to characterize trapping and reaction dynamics in the hybrid system. For example, charge transfer measurements are performed with two different laser-cooled atomic ion species, Yb^+ and Ba^+ , which are allowed and disallowed ground-state reaction, respectively. Controlled measurements of these inelastic processes test the cutting edge of quantum theory of ion-neutral interaction in both the ground-state and under optical excitation.

CHAPTER 1

Introduction

This dissertation details a experimental system consisting of magneto-optically trapped ^{40}Ca atoms, with a typical temperature of a few milliKelvin, co-trapped with ions of various species within a linear radio-frequency quadrupole trap. The primary design purpose of the hybrid trapping system, dubbed the MOTion trap, is to prepare diatomic molecular ions in the quantum ground state via collisions with the cold, trapped atoms. This work details the first complete experimental effort to sympathetically cool molecular ions using a MOT. Consistent with any first scientific endeavor, there were many challenges and discoveries along the way, detailed in the first six chapters. The climax of this dissertation (chapter 7) is a measurement demonstrating that the atoms are extremely efficient at freezing out the vibrational quantum state, using a novel vibrational thermometry technique.

This first chapter begins by outlining of the structure of the rest of the thesis with a very brief description of each chapter's purpose and contents. Next, this chapter motivates the construction of and experiments within the atom-ion apparatus. This requires an overview of physics and applications relevant to a hybrid atom-ion trap system as well as cold, diatomic molecular ions.

1.1 Thesis Layout

- Chapter 2 is an overview of the experimental hardware and the ion trap,

including a summary of the principles of ion trapping that covers important techniques and theoretical concepts in the context of a hybrid trap.

- Chapter 3 reviews the ^{40}Ca magneto-optical trap (MOT). This consists of an explanation of general MOT physics, experimental techniques, and details particular to the hybrid system and the Ca MOT.
- Chapters 4, 5, 6, 7 are based on experiments performed in the MOTion trap, each of which culminated in publication in a peer-reviewed research journal. These publications have been recast in the form of a chapter and a sort of director’s cut. Figures or sections that were removed to meet length requirements, for example, have been re-introduced.
- Chapter 4 is about an experiment conducted early in the lifecycle of the MOTion trap when it was discovered that the presence of the trapped neutrals was leading to the production of Ca_2^+ dimer molecular ions via photo-associative ionization.
- Chapter 5 details an experiment that came about while using $^{174}\text{Yb}^+$ as a laser-addressable proxy ion for BaCl^+ to look for indications of translational cooling via collisions with the MOT atoms. Yb^+ is energetically allowed to chemically react via charge exchange with Ca, and is found to be highly reactive.
- Chapter 6 is about a similar experiment to that in chapter 5, except the ion is Ba^+ . The Ba^+ ground electronic state is energetically forbidden from charge exchange reactions with Ca. In this experiment the chemical reaction rate is measured as a function of the quantum state of the reactants.
- Chapter 7 demonstrates experimentally that the vibrational motion of trapped

BaCl^+ molecules is quenched by collisions with ultracold calcium atoms at a rate comparable to the classical scattering, or Langevin, rate.

- Chapter 8 is an extra chapter for wrapping up loose-ends and discussing an unrelated project: a direct search for the low-energy ^{229}Th nuclear isomeric transition in a thorium-doped solid using synchrotron radiation. Finally, the outlook of the next generation of the MOTion trap system is detailed.

1.2 What is the MOTion trap?

The MOTion trap is a hybrid trap system consisting of a linear quadrupole radio-frequency Paul trap and a magneto-optical trap (MOT) in the same volume. In this dissertation, the principles of operation and implementation of the ion trap and the MOT are found in chapters 2 and 3 respectively. The original magneto-optical trap used the alkali metal sodium (Na) in 1987 [RPC87]. The conception of the quadrupole trap is credited to Wolfgang Paul in 1953 [PS53]. The hybrid system is the combination of these two Nobel prize winning technologies, with ion trapping technology winning in 1989 and the MOT winning in 1997. Two subsequent prizes, the award for Bose-Einstein condensation (BEC) in 2001 and the most recent 2012 prize for controlled quantum systems, are inarguably descendant products of the two techniques.

1.3 Why build the MOTion trap?

As a tool, the system is ideal for probing fundamental collision processes between ions and neutral atoms in a controlled, cold ($\sim\text{mK}$) environment. In recent years, the potential for using the strong atom-ion interaction has been noted to be a

promising avenue for studies of molecular ions [SML05]. The MOTion trap is the experimental implementation of a proposal to sympathetically cool trapped molecular ions into their quantum ground state [Hud09].

While there have been a few successful demonstrations involving other species-specific cooling techniques, producing molecular ions in the lowest few rotational states [SRD10, SjS10, TWW10], Hudson proposed to sympathetically cool BaCl⁺ using a generally applicable method of sympathetic collisions with trapped atoms in a MOT. The sympathetic cooling method is proposed to overcome the molecular quantum state preparation problem (section 1.3.2) in a species independent, laser-free manner. There are other species independent methods, like those involving cryogenic Helium buffer gas which have been found capable of quenching molecular internal states with a collisional efficiency of about 1 cooling event in 10^4 to 10^6 collisions [FDH85, TJT88]. Compared to cryogenic He, laser-cooled atoms offer a colder buffer gas temperature (μK - mK), since the cryogenic He is limited to temperatures of $\sim 4\text{K}$ ($\sim 300 \text{ mK}$ for ${}^3\text{He}$). In addition, laser-cooled atoms are generally much more ($\alpha_{\text{Ca}} \sim 10^2 \times \alpha_{\text{He}}$) polarizable. A higher polarizability yields stronger interaction ($\propto \alpha^2$ via Fermi's golden rule). The result, experimentally seen in chapter 7, is expected near unit collision internal state relaxation efficiency in a MOTion trap.

1.3.1 The prospects and progress using molecular structure

The proposed cooling method is among many efforts towards preparing samples of cold molecules or molecular ions as the next evolution beyond cold atoms in atomic, molecular, and optical (AMO) physics. Cold atom technology is ubiquitous in the field of atomic physics. Laser cooled atomic samples are the foundation of countless important measurements, discoveries and technologies, such as the

current [JSP02], and perhaps future [RHS08], definition of the second. The next most simple quantum system, compared to an atom, is a diatomic molecule. With the reduction in simplicity comes an increase in the richness physics. Molecules have additional internal degrees of freedom. They can rotate about their center of mass and they can vibrate. These extra degrees of freedom offer a huge space for future work such as exploring long range collective quantum effects (e.g. a dipolar BEC [GSL02, SSL03]), and tests of fundamental symmetries and variation of fundamental constants [HST02, HLS06, CFK09]. Many groups have made great progress producing cold samples of trapped molecules. Two particularly noteworthy projects have successfully begun applying the technique of laser cooling to diatomic molecules [SBD10, HYS13]. These feats using two uniquely appropriate molecules, strontium fluoride (SrF) and Yttrium Oxide (YO) respectively, are impressive as it was once thought that laser cooling molecules poses a nearly insurmountable technical challenge. The difficulties, discussed in section 1.3.2, lie in quantum preparation and control of the molecular state, chiefly due to the long-lived vibrational states. Two recent articles provide an overview of the prospects of extending laser cooling techniques to diatomic molecules [Ros04] and molecular ions [NVH11].

Spatially confining neutral molecules is very difficult. Fortunately, most types of molecule applications can be pursued with molecular ions as well, with the additional benefit of robust trapping techniques. The convenience of ion trapping technology comes at a price. Using ions likely costs the ability to investigate quantum degenerate dipolar gases, since ion-ion repulsion sets a limit to the density as ion crystallization occurs. However, there exist other applications that are bolstered by the net charge of the molecular ion. A possible future experiment particular to ground-state molecular ions is an extensible quantum computation scheme using strip-line microwave resonators coupled to surface-

trapped molecular ion qubits [ADD06]. For example of an experiment in progress, a project at JILA is leveraging a molecular state in trapped HfF⁺ to search for an electron electric dipole moment (eEDM) [LBL11].

1.3.2 The trouble with molecular structure

Atoms have an internal degree of freedom corresponding to different amounts of electronic excitation. The energy differential between states of different principal quantum number are typically some fraction of the kinetic energy of a Bohr orbit $E_e \sim \frac{\hbar^2}{2ma_0^2}$, where m is the electron mass and a_0 is the Bohr radius ($= 52.9$ pm). This energy scale is about a few eV. An electron volt, in temperature units, is $\frac{1\text{eV}}{k_B} \simeq 11610$ K. It is safe to say that at room temperature, it is not likely to naturally find an atom in an excited quantum state. For atoms and atomic ions, the principal internal degree of freedom is already “frozen” at room temperature. This is not true for molecules.

Molecules have additional rovibrational (rotational and vibrational) internal degrees of freedom, with smaller characteristic energy scales. The typical rotation splitting for a diatomic molecule is that of a rigid rotor with moment of inertia $I \sim \mu \langle R_0^2 \rangle$, where μ is the reduced nuclear mass $\frac{m_1 m_2}{m_1 + m_2}$ (typically ~ 10 amu) of the two bound atoms and R_0 is the bond length (typically a few Bohr radii). The rotational energy levels are spaced as $E_{rot} = BJ(J+1)$, a function of the rotational quantum number J . Typical spacing for this energy, $B \approx \frac{\hbar^2}{2I}$, is a few GHz. This energy scale is smaller than the electronic energy by about a factor of the electron to nuclear mass ratio i.e. $E_{rot} \sim \frac{m}{\mu} E_e$. (The electron to nuclear mass typically ranges between $\sim 10^3$ and 10^5 .) A GHz corresponds to roughly 48 mK of thermal energy, so many rotational levels are occupied at room temperature. A similar argument identifies the vibrational energy scale. The

nuclei of the molecule are bound to one another electronically, so the dissociation energy is of the order of a few eV. Vibration can be thought of a harmonic oscillation of this bond where $\frac{1}{2}\mu\omega^2a_0^2 \sim E_e \sim \frac{\hbar^2}{2ma_0^2}$. The vibrational quanta of energy is then $\hbar\omega \approx (m/\mu)^{1/2}E_e$. Thus, the typical vibration energy spacing corresponds to a thermal energy of a few hundred Kelvin, or more, depending on the molecule. A well-bound rovibrational manifold for a given electronic state looks roughly like a rigid rotor energy spectrum (GHz spacing) nested inside a simple harmonic oscillator spectrum (THz spacing) and will have a significant population spread at room temperature. Section 1.3.3.2 details the statistics of the internal state distribution. This thermal spread of internal quantum states is just the first part of the problem for quantum control of diatomic molecules. The Born-Oppenheimer approximation, a quantitative model of a diatomic system summarized in section 1.3.3, helps to understand the further complication of rovibrational structure: the lack of vibrational selection rules.

1.3.3 The Born-Oppenheimer approximation

The disparate energy, and thus time, scales $E_{rot} \sim (m/\mu)^{1/2}E_v \sim (m/\mu)E_e$ motivate the Born-Oppenheimer approximation (BOA). The BOA assumes that the problem is separable into three component wavefunctions: the center-of-mass, the electronic, and the nuclear. The center-of-mass component of the wavefunction is just the external, field-free, translation of the entire molecule. The approximation assumes that the latter two components of the wavefunction, the electronic and the nuclear, are decoupled since the fast, light electrons move much more quickly than the nuclei. That is,

$$\Psi = \psi(\vec{r}_{COM})\chi(\vec{R})\phi_e(R; r_1, r_2, \dots, r_N) \quad (1.1)$$

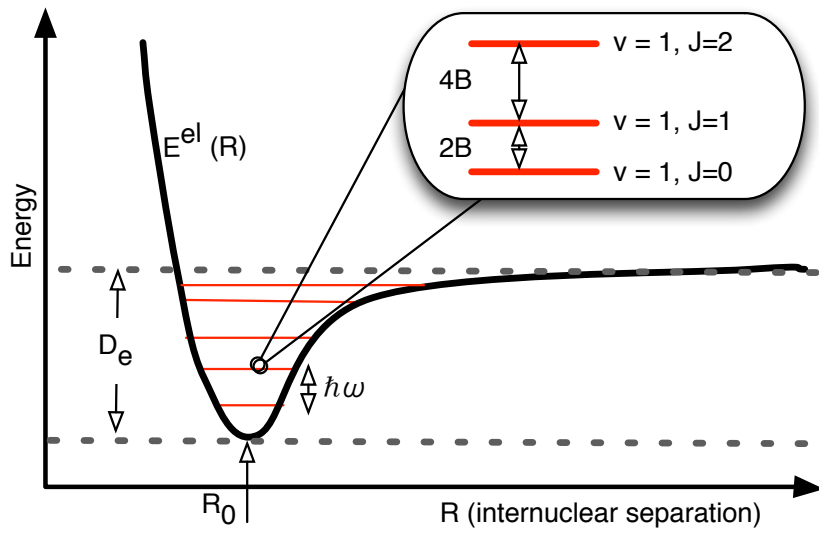


Figure 1.1: Schematic diagram illustrating typical molecular structure for a bound electronic potential. The molecular potential $E^{el}(R)$, indicated by a solid line, varies in energy with the internuclear separation. D_e indicates the electronic dissociation energy of the molecule on this potential. R_0 indicates the bond length i.e. the average internuclear separation for a well-bound vibrational level. Schematic vibrational spacing is marked by horizontal lines indicating the different oscillator levels. Each vibrational level supports a rotational spectrum, shown zoomed in.

where ϕ_e is the electronic component of the wavefunction which takes the internuclear spacing \vec{R} as a parameter and is a function of all of the electron coordinates r_i . χ is the nuclear part which only depends on \vec{R} . The full Schrödinger equation separates into two parts. First, for the electronic wavefunction the Schrödinger equation

$$\left[\sum_i \frac{\vec{p}_i}{2m} - \frac{1}{2M_{\text{total}}} \sum_{i,j} \vec{p}_i \cdot \vec{p}_j + \sum_{i < j} \frac{e^2}{4\pi\epsilon_0 |\vec{r}_i - \vec{r}_j|} + \sum_{i,\alpha} \frac{Z_\alpha e^2}{4\pi\epsilon_0 |\vec{r}_\alpha - \vec{r}_j|} \right] \phi_e = E^{el}(R) \phi_e \quad (1.2)$$

is solved in the center-of-mass (COM) frame for fixed nuclear positions \vec{r}_α where the indices i, j are summed over all the electrons in the molecule. Solving this equation requires state-of-the-art many-body computational techniques. The solution is a so-called internuclear molecular potential curve $E^{el}(R)$, which can be physically interpreted as the effective interaction potential between the two nuclei after the electron configuration has been taken into account. The molecular potential appears in the one-dimensional Schrödinger equation leftover, after separating the angular component, for the vibrational wavefunction $\chi(\vec{R}) = v(R)Y_N^{N_z}$,

$$\left[-\frac{\hbar^2}{2\mu} \left(\frac{1}{R^2} \frac{\partial}{\partial R} \left(R^2 \frac{\partial}{\partial R} \right) \right) + \frac{\hbar^2 \langle \vec{N}^2 \rangle}{2\mu R^2} + E^{el}(R) \right] v(R) = E v(R), \quad (1.3)$$

where \vec{N} is the nuclear rotation angular momentum, perpendicular to the internuclear axis. This equation, unlike equation 1.2, is tractable without advanced computational techniques and is useful to solve for different vibrational solutions to a given molecular potential. A typical molecular potential with bound solutions, and thus rovibrational structure, looks like figure 1.1. The rovibrational contribution to the molecular energy for low-lying bound states is given by

$$E_{v,J} = BJ(J+1) + \hbar\omega_v(v+1/2) - \hbar(\omega_v x_v)(v+1/2)^2 \quad (1.4)$$

where J (v) is the rotational (vibrational) quantum number. $\omega_v x_v$ is an anharmonic correction factor sometimes given in tables of spectroscopic data.

1.3.3.1 Molecular quantum numbers and selection rules

The Russell-Saunders term symbol $^{2S+1}L_J$ describes the angular momentum quantum numbers of an atomic state. Diatomic molecules have different “good” angular momentum quantum numbers, due to cylindrical symmetry replacing the spherical symmetry of an atom. The term symbol for a molecular state is $^{2\Sigma+1}\Lambda_\Omega$. Σ is the projection of the electronic spin \vec{S} onto the internuclear axis. Λ is the projection of the electronic orbital angular momentum \vec{L} onto the internuclear axis. In analogy to L in the Russell-Saunders term symbol, Λ takes Greek letter variants of S (Σ), P (Π), D (Δ) to denote $\Lambda = 0, 1, 2$ respectively. Ω is the projection of the total electronic angular momentum $|\Sigma + \Lambda|$ onto the internuclear axis.

The dipole (E1) electronic transition selection rules fall out by evaluating the expectation of the dipole operator, $\vec{d} = e\vec{r}$ with the Born Oppenheimer wavefunction of equation 1.1, $\langle\Psi|\vec{d}|\Psi\rangle$. Ultimately, this expression takes the form

$$\langle\vec{d}\rangle = \sqrt{S_{J'',J'}}\langle v_A(R)|d(R)|v_X(R)\rangle \quad (1.5)$$

for a transition with initial electronic state $X(v'', J'')$ into another potential labeled $A(v', J')$. $S_{J'',J'}$ is the Hönl-London factor, a molecular analog to the Clebsch-Gordon coefficient in atomic transitions. $d(R)$ is the radial dipole moment function and it is the result of a calculation involving the electronic portion of Ψ . Often, the variation of $d(R)$ with internuclear separation is small and neglected, allowing it to be factored out of the average over the vibration wavefunction as just an average electronic dipole moment \bar{d} . This leaves,

$$\langle\vec{d}\rangle = \bar{d}\sqrt{S_{J'',J'}}\langle v_A(R)|v_X(R)\rangle \quad (1.6)$$

where the latter term, the inner product between the initial and final vibrational wavefunctions, is the square root of the so-called Franck-Condon factor (FCF)

$\sqrt{F_v}$. Thus, the strength of an E1 transitions is proportional to $\langle \vec{d} \rangle^2 \sim \bar{d} S_{J'', J'} F_v$. The selection rules are determined by the rotational part only. The rotational selection rules for an E1 type transition are $\Delta J = 0$ ($J' \neq 0, \pm 1$), $\Delta \Omega = 0, \pm 1$, $\Delta \Lambda = 0, \pm 1$, and $\Delta \Sigma = 0$. The Franck-Condon factor can range from 0 to 1 for any variation of vibrational quantum number v . This is root cause of difficult in molecular laser cooling schemes. An excited electronic state can often decay into many different vibrational levels on the ground-state potential, ruining the laser cooling cycle.

1.3.3.2 Boltzmann (thermal) distribution of molecular degrees of freedom

Thermal population distribution in a particular state s is determined by the ratio of the Boltzmann factor $g_s e^{-E_s/(k_B T)}$ to the partition function Z . This factor includes the degeneracy g_s of the state s . The partition function is the sum of the Boltzmann factor over all states $Z = \sum_i g_i e^{-E_i/(k_B T)}$.

The population for a rigid quantum rotor state with quantum number J is given by

$$P_J = \frac{(2J+1)e^{-BJ(J+1)/(k_B T)}}{\sum_J (2J+1)e^{-BJ(J+1)/(k_B T)}} \quad (1.7)$$

where B is the rotational energy constant. The partition function does not have a simple analytic form. In certain temperature limits, however, it is possible to write down useful simple expression for partition function. In the high temperature limit ($B \ll k_B T$) the sum approaches the classical limit and can be integrated to yield $Z_{hot} \sim \frac{k_B T}{B}$. In the frozen limit ($B \gg k_B T$), only the first term of the sum contributes significantly to the partition function yielding $Z_{cold} \sim 1 + 3e^{-2B/(k_B T)}$. The exact partition is plotted in figure 1.2, along with the two limiting cases for comparison.

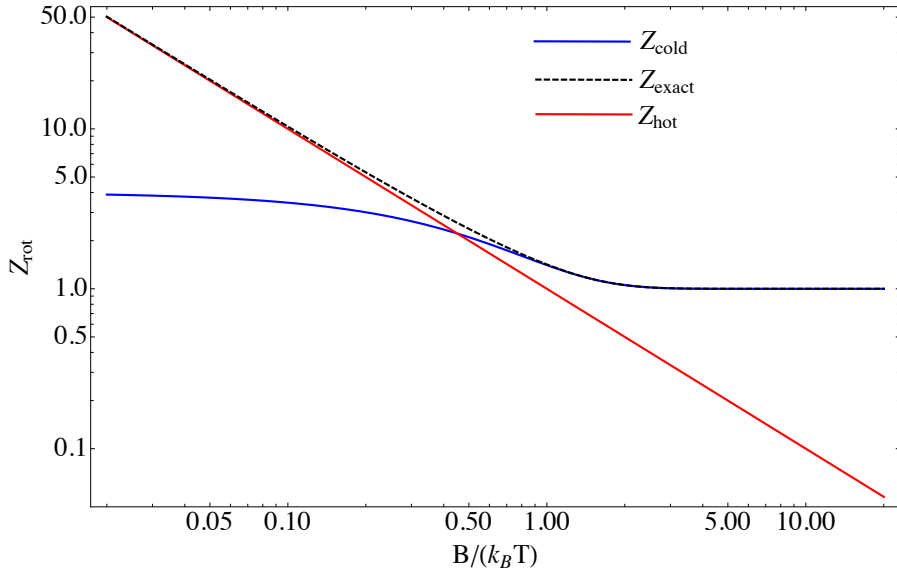


Figure 1.2: Partition function for a rigid quantum rotor as a function of the ratio of the rotational splitting constant B to the thermal energy $k_B T$.

The thermal distribution amongst the lowest lying vibrational levels is even simpler, since the partition function for a quantum oscillator can be evaluated as a geometric sum with a simple closed form result

$$P_v = \frac{e^{\hbar\omega_v v / (k_B T)}}{1 + e^{\hbar\omega_v v / (k_B T)}} \quad (1.8)$$

where v is the vibrational quantum number.

1.3.4 Cold molecular ion candidate - BaCl⁺

For the work detailed in this dissertation, BaCl⁺ is chosen to be cooled in demonstration of the general method of sympathetic cooling in the MOT. Compared to diatomic neutral molecules, there is very little spectroscopic information available for molecular ions. BaCl⁺ is chosen from a list of candidate molecules, listed in [Hud09], which have a higher electron affinity than the neutral atoms in the

State	R_0	D_e	ω_v	$\omega_v x_v$	B_{rot}
	[a_0]	[cm $^{-1}$]	[cm $^{-1}$]	[cm $^{-1}$]	[cm $^{-1}$]
X $^1\Sigma^+$	4.85	-39 055	328.3	-1.56	0.0918
A $^1\Pi$	6.42	-2 075	90.53	-1.26	0.0524

Table 1.1: BaCl $^+$ molecular spectroscopic constants

MOT (IP $_{Ca} = 6.1$ eV > IP $_{BaCl} = 5.0$ eV). This relation between ionization potentials energetically precludes the undesirable direct charge exchange reaction. Most other possible reaction pathways are also energetically forbidden, except the addition reaction Ca + BaCl $^+ \rightarrow$ CaBaCl $^+$. However, the addition reaction requires a third body in the collision for momentum conservations, and is a rare event at experimental densities.

Everything currently known about the molecular structure of BaCl $^+$ is a result of measurements done in the Hudson laboratory [CSK11], with theoretical support from Svetlana Kotochigova at Temple University. Spectroscopic constants for the ground molecular state and an excited repulsive potential are tabulated in table 1.1. The spectroscopic information is derived from *ab initio* calculations found to be consistent with a photo-dissociation measurement result. The scheme of the measurement, along with *ab initio* low-lying molecular potentials, is shown in figure 1.3.

The photo-dissociation cross-section measurement, shown in figure 1.4, is improved over the original measurement in [CSK11], by use of a time-of-flight apparatus to accurately measure the fragment ion production [SCR12]. The experiment is performed by measuring Ba $^+$ ion fragment production as a function of dissociation laser wavelength using the time-of-flight. The resulting cross-section agrees quite well with a theoretical calculation of the ground state vibrational

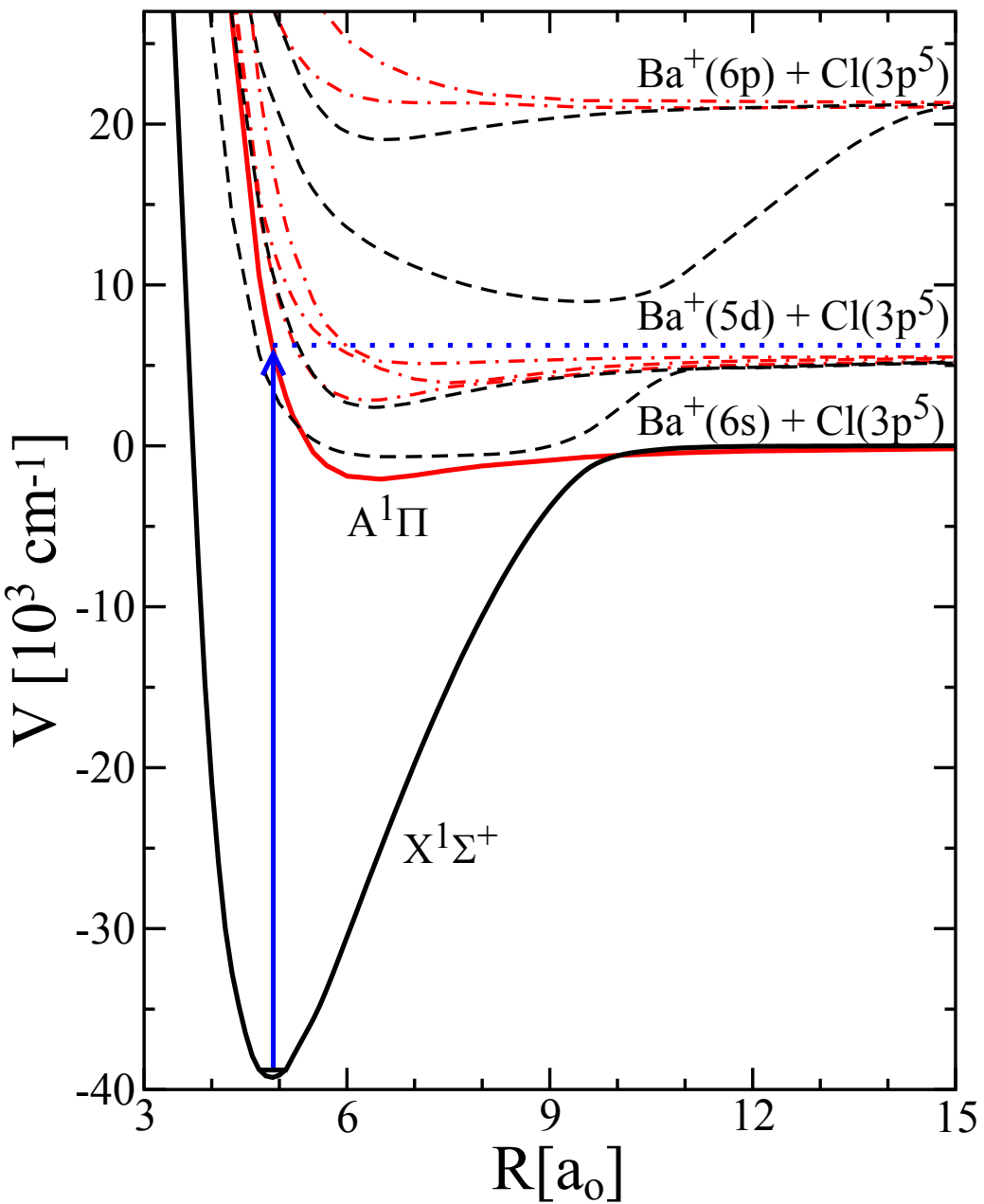


Figure 1.3: Photodissociation measurement scheme and molecular potentials. Dissociation occurs by single photon excitation from the ground $X^1\Sigma^+$ (solid black) to the repulsive wall of the $A^1\Pi$ (solid red) potential.

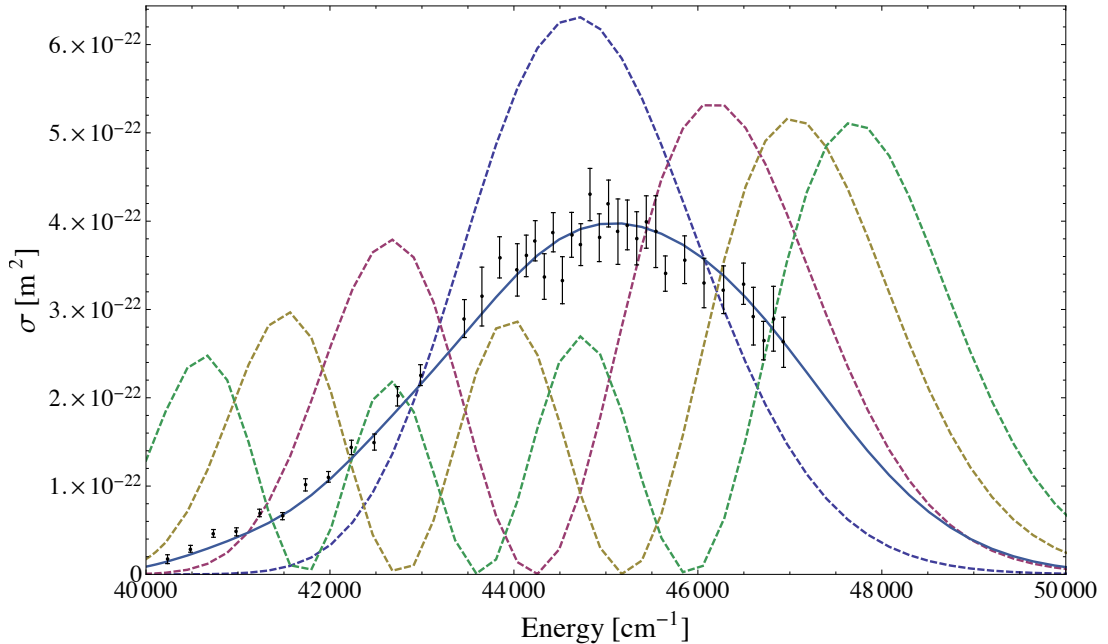


Figure 1.4: BaCl^+ photodissociation cross-section. The data points fit well to the room temperature thermal average of the $v = 0\dots 3$ vibrational contributions, calculated using the *ab initio* potentials shown in figure 1.3.

cross-sections thermalized to 300 K. There is no rotational state specific information in the bound-to-free dissociation process. However, there is a relatively weak dependence on the vibrational state occupancy which can be used to investigate the thermal distribution of the vibrational levels. This measurement is the basis of the vibrational thermometry technique employed to demonstrate internal state relaxation in chapter 7.

1.3.4.1 Laser cooling BaCl^+

Like most molecules, BaCl^+ is an example of a molecule with an internal structure not amenable to laser cooling. Laser cooling cannot be performed using the X and A molecular potentials in BaCl^+ due to a very poor Franck-Condon overlap

between the vibrational wavefunctions. The approximate Franck-Condon factor can easily be estimated from the parameters in table 1.1 by calculating the overlap between simple harmonic oscillator wavefunctions

$$\Psi_v = \left(\frac{\mu\omega_v}{\pi\hbar} \right)^{1/4} e^{-\frac{\mu\omega_i}{2\pi\hbar}(r-R_0)^2}, \quad (1.9)$$

where the parameters R_0 and ω_v are read off the table for each molecular configuration. These wavefunctions approximate the $X(v=0)$ and $A(v=0)$ vibrational wavefunctions, and have very small overlap ($\langle X(v=0) | A(v=0) \rangle \sim 10^{-8}$), so spontaneous decay from the bound excited state is very unlikely to arrive back in the required ground state configuration. A thorough discussion of conveniently calculating the Franck-Condon factor from spectroscopic parameters is available in [Nic81].

1.4 The atom-ion interaction in the low collision energy regime

At long range, an atom is polarized by the electric field of an ion, $\vec{p} = \alpha\vec{E}$, where α is the static polarizability of the atom. The induced dipole has its own electric field which exerts a force on the ion. The resulting interaction potential is often called the C_4 potential and is written in the form:

$$V(r) = -\frac{1}{2}\alpha|\vec{E}|^2 = -\frac{1}{2}\frac{\alpha e^2}{(4\pi\epsilon_0)^2 r^4} = -\frac{C_4}{r^4}. \quad (1.10)$$

When two particles collide with a center-of-mass collision energy E on a C_4 potential, there exists a critical impact parameter $b_0 = \left(\frac{4C_4}{E}\right)^{1/4}$ at which the classical distance of closest approach goes imaginary. Classical trajectories at or below this critical impact parameter spiral into very close range where inelastic events are much more likely to occur. The critical impact parameter b_0 defines

the so-called Langevin cross-section

$$\sigma_{\text{Langevin}} = \pi b_0^2 = 2\pi \sqrt{\frac{C_4}{E}} \quad (1.11)$$

and represents a good upper bound for any inelastic scattering cross-section in low energy atom-ion interaction. Since the Langevin cross-section goes like $E^{-1/2}$, the thermally averaged Langevin rate constant $\langle \sigma_{\text{Langevin}} v \rangle$ is temperature independent. In the low collision energy limit the full quantum mechanical partial wave treatment yields the same result for the collision rate constant [Gri04]. Therefore throughout the experiments detailed in this dissertation, the Langevin rate constant sets the scale at which an inelastic process can be considered efficient. For neutral ^{40}Ca collisions with heavier ions $m \sim 150\text{amu}$, the Langevin rate constant is $\simeq 5 \times 10^{-9} \text{ cm}^3 \text{ s}^{-1}$.

1.4.1 Short-range inelastic collision events

When a sufficiently slow ^{40}Ca atom collides with a trapped BaCl^+ molecular ion at short range, the only energetically allowed two-body inelastic outcome is the atom removing some energy from the diatomic molecule's internal degrees of freedom. This is the case because the collision entrance channel's energy is lower than any other outcome due to the difference in ionization potentials as mentioned in section 1.3.4. This is not always the case when an atom interacts with an ion. Oftentimes, the entrance channel $A + B^+$ is at a higher energy than states on a potential that dissociates to $A^+ + B$. When energetically allowed, there is a probability of charge transfer occurring during close range interaction. Charge transfer occurs via three mechanisms: non-radiative charge transfer (nRCT), $A^+ + B \rightarrow A + B^+$, radiative charge transfer (RCT), $A^+ + B \rightarrow A + B^+ + \gamma$, and radiative association (RA), $A^+ + B \rightarrow (AB)^+ + \gamma$. These three charge transfer mechanisms are shown schematically in figure 1.5. Chapters 5 and 6 detail the

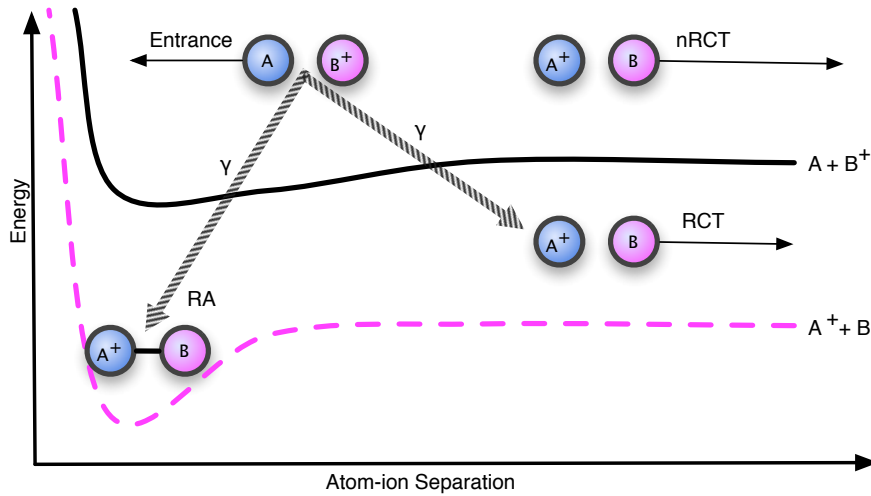


Figure 1.5: Schematic of charge transfer pathways. Charge transfer can occur directly with or without emission of a photon via radiative and nonradiative charge transfer, respectively (RCT, nRCT). Alternately, by emitting a photon, the atom-ion pair can form a molecular ion by radiative association (RA).

study of two such situations in which charge transfer can and does occur.

1.4.2 Atomic excited state inelastic shielding

Close-range inelastic collisions involving the excited state of the atom are suppressed. The suppression is due to the difference in polarizability of the atomic ground electronic state and excited electronic state. In the case of ⁴⁰Ca, the polarizabilities are different by roughly a factor of three. As the atom approaches the ion along a collision trajectory, the ion's Coulomb field induces different Stark energy shifts on each level. This pushes the atom off resonance with the MOT cooling laser (discussed in detail in section 3.1), early enough that close range interaction in the neutral atom's excited atomic state is rare, due to spontaneous decay. The magnitude of this suppression is shown in figure 1.6. This

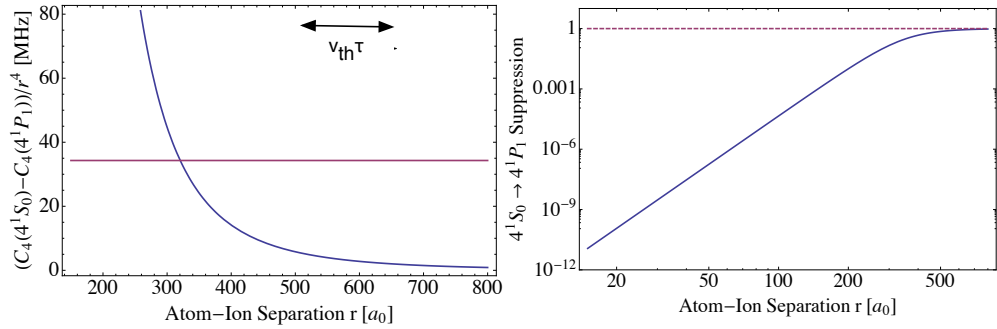


Figure 1.6: The left panel shows the relative shift, compared to the far separation limit, between the ground and excited electronic states of ^{40}Ca as a function of atom-ion separation. The horizontal line marks the natural linewidth of the transition, for scale. The double-headed arrow marks the typical distance a cold ^{40}Ca atom travels in the excited state lifetime. The right panel shows the fractional suppression of a laser’s efficiency in driving the cooling transition as a function of atom-ion separation. The laser is detuned from the $r \rightarrow \infty$ transition wavelength by half a natural linewidth. The horizontal dashed line marks the laser’s efficiency if the polarizabilities were equal.

atom-ion excited state shielding effect is an important issue in ultracold collision theory [BJ92]. The effect is particularly beneficial for applying the MOT as a cold buffer gas for molecular ions, since the extra energy from electronic excitation of the atom is often enough to energetically allow charge transfer.

CHAPTER 2

Experimental Hardware and the Ion Trap

2.1 Introduction

This chapter details the hardware involved in the construction and implementation of the hybrid atom-ion, or MOTion, trap system and the experiments performed therein. This includes specifics of the vacuum chamber 2.2.1, the different physical signal detectors 2.2.2, the data acquisition systems 2.2.3, the home-built external cavity laser systems 2.2.4, and the ion trap itself 2.3.5.2. In addition to the physical hardware of the ion trap, the principles of operating a linear quadrupole ion trap are discussed. In particular, ion trapping techniques and phenomena relevant to experiments probing atom-ion interaction are discussed, such as: determination of ion kinetic energy 2.3.3.2, limits to buffer gas sympathetic cooling 2.3.4, and methods of identifying products of potential chemical reactions 2.3.2.

2.2 Hardware

2.2.1 Vacuum system

This dissertation's experiments are performed in a ultra-high vacuum (UHV) system. A low background pressure, in these experiments $<\sim 10^{-8}$ mbar, keeps

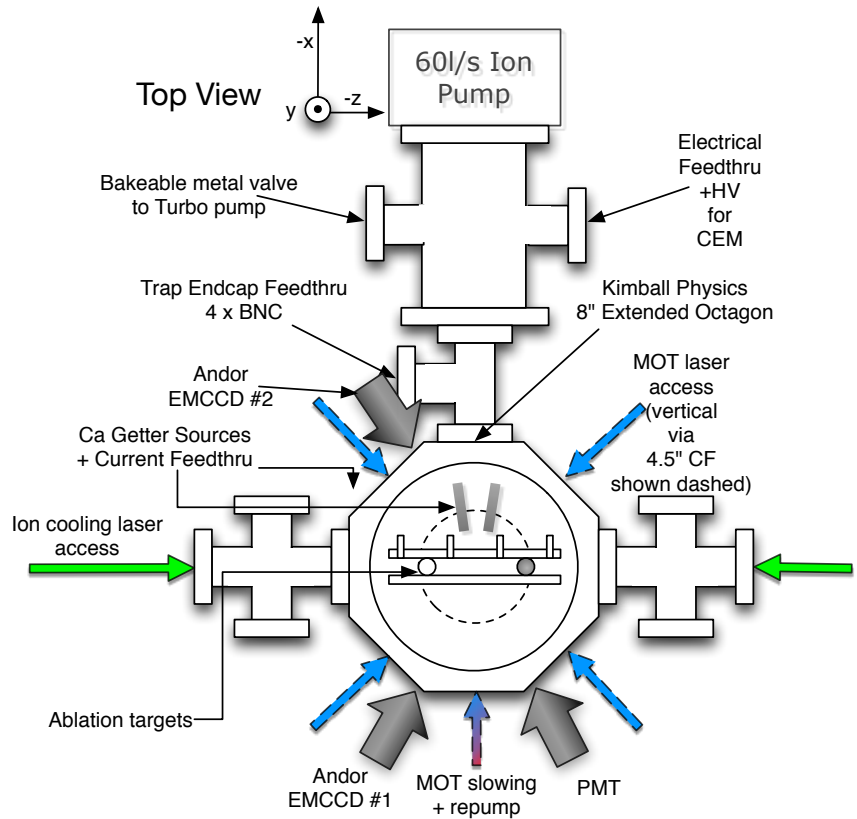


Figure 2.1: A schematic of the experimental vacuum chamber. The experimental chamber is built around an 8" Kimball Physics extended spherical octagon (MCF800-ExtOct-G2C8A16). The system is supported by three v-block supports: one pair of supports, on each of the 2.75" CF tees to either side of the octagon and a third support at the reducer-tee near the ion pump.

unwanted interactions and trap loss due to collisions with background gas to a minimum.

The hybrid trap in this work uses a relatively straightforward vacuum system design. There is only one science chamber, which has self-contained sources and means of loading both the ion trap and the cold atom magneto-optical trap. A schematic of the experimental chamber is shown in figure 2.1. The system is built around the main science chamber with an ion trap in the geometric center of an 8" Kimball Physics extended spherical octagon (MCF800-ExtOct-G2C8A16). The octagon has sixteen 1.33" (a.k.a mini-), eight 2.75", and two 8" CF ports. All of the 2.75" CF ports not explicitly shown occupied in figure 2.1 are fit with standard optical viewports. Five of the mini-CF flanges were fit with BNC feedthroughs, one connection for each rod the the quadrupole ion trap and one more for the signal out of the ion detecting channel electron multiplier (CEM). One mini-CF flange has a 4-pin power feedthrough for running current through either of the two calcium dispensers. The remainder of the 1.33 inch ports were covered with optical viewports, for access by two cameras, a photo-multiplier tube (PMT) and an absorption imaging beam. The two large flanges were set up with zero-length reducers to 4.5" CF, which were fit with optical viewports. The vertical facing viewports allow access for the vertical MOT trapping beams and the ablation laser used to load the ion trap. Four more electrical connections come into the chamber via a 4-pin BNC feedthrough on the 2.75" CF tee connecting the main chamber to the reducer tee (6 inch to 2.75" CF) connected to both the ion pump (Varian, VA-911-5034) and to the bake-able all-metal valve which is connected to a Varian turbo-molecular pump during the initial evacuation phase and during the activation of the Ca getter source.

The system is mounted above the optics table by three v-block supports: one

pair of supports holding the chamber on either side of the octagon at the 2.75" CF tees, and a third supporting the 6" CF reducer tee near the ion pump. The supports were designed to hold the geometric center of the chamber at a height of 9.5 inches from the surface of the optics table. The optics are arranged around the chamber on standard 3" long, 1" diameter steel optical posts, mounted to four 0.5" Thorlabs breadboards which in turn are mounted to the optics table by 5" steel posts. With this arrangement and standard kinematic mounts, all of the optics are vertically centered on the geometric center of the chamber. The anti-Helmholtz coils, described in more detail in chapter 3 are mounted independently from the experimental chamber by a steel cage structure, shown in figure 2.2. A final 0.5" Thorlabs breadboard is mounted upside-down from the coil support structure to allow the positioning of optics for the vertical trapping and ablation laser beams.

During typical operation, a 60 l/s ion pump maintains the vacuum level in the system. The background pressure, measured by the amount of current drawn through the ion pump and the manufacturer's specification (figure 2.3), varies between a few $\times 10^{-9}$ and 10^{-8} Torr, depending on the current running through the Ca dispenser.

2.2.2 Signal detection

For experimental science to proceed, there must be a signal. For the MOTion trap, the two sources of signal are photon detectors and direct (destructive) ion detectors.

For fluorescence detection, a Hamamatsu R3896 PMT is positioned pointing into one of the mini-CF viewports, as shown in figure 2.1. For fluorescence imaging and spatial location of both laser-cooled atomic ions and the ^{40}Ca MOT

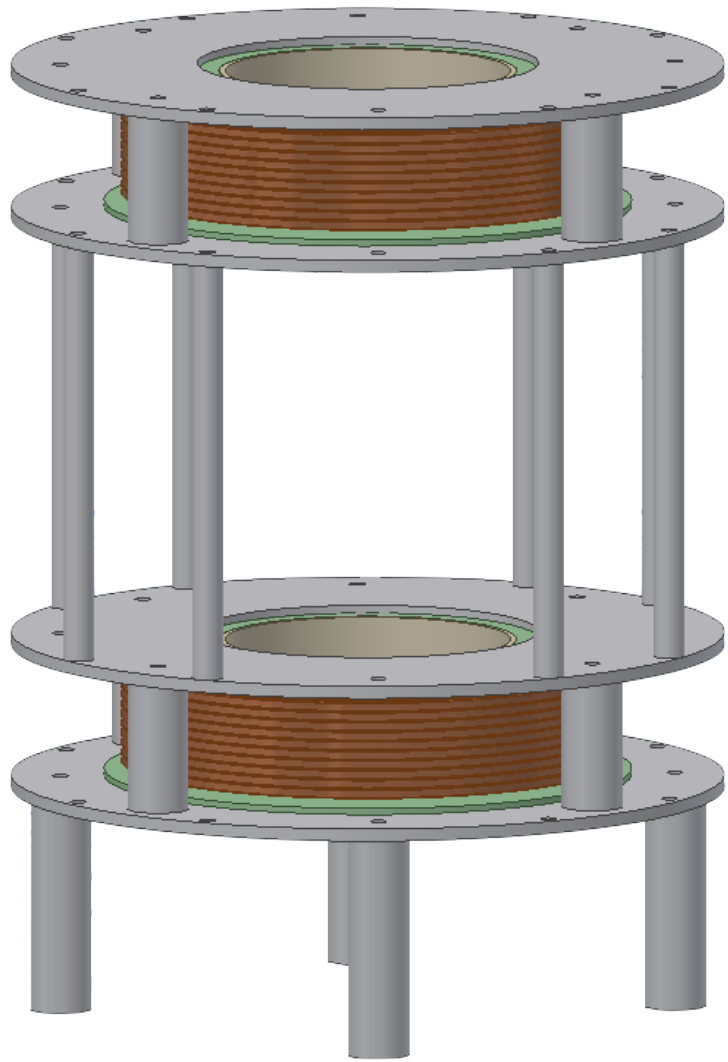


Figure 2.2: A rendering of the support structure for the anti-Helmholtz coils. The coils are wound in phenolic spools, press fit between steel plates supported by a combination of 1" diameter and 0.5" steel rods.

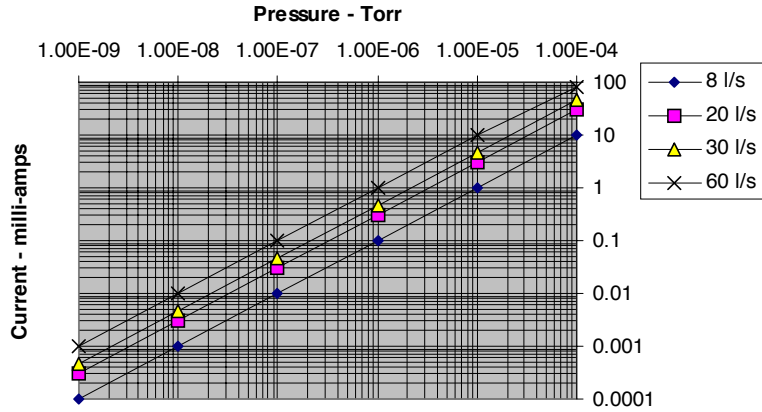


Figure 2.3: Ion pump manufacturer specification for reading the chamber pressure as a function of current drawn. The vacuum system uses the 60 l/s model.

cloud, two Andor Luca-R EMCCD cameras are mounted at mini-CF viewports, one on either side of the chamber approximately 116° apart. All three light collection systems use 75 mm Thorlabs broadband anti-reflection A-coated ($R < 2\%$ for 350-700nm) plano-convex lenses in the 2f-2f configuration. The MOT is bright enough to image without any optical filtering – typically with no gain and an exposure time of about 10 ms. To image either of the atomic ion species used in the system, a narrow bandpass (Chroma Technology) filter is used to filter out all but the fluorescence from the ion cooling transition, and typically requires the use of gain (~ 100) and a longer exposures of about 100 ms. Both the 369 nm and 493 nm narrow bandpass filters have transmission of $\sim 47 \pm 1\%$ at their respective laser wavelength. The PMT is powered by a Stanford Research Systems (SRS) PS325 high voltage (HV) power supply.

For direct ion detection, a channel electron multiplier (CEM) is mounted above the ion trap. As described in section 2.3.5.3, the CEM has an ion collection efficiency of $2 \pm 1\%$. The CEM model is the Burle (now Photonis) 5901, and, like

the PMT, is biased by a SRS PS325 HV power supply.

2.2.3 Data acquisition and control

National Instruments (NI) LabVIEW is used as the means of computer control in the experiment. The experiment computer has three data acquisition (DAQ) cards. First, there is a PCIe 6537 50 MHz digital I/O card which, in conjunction with a digital pulse generator (Quantum Composer 9518+), handles all the timing requirements of the experiment. Analog input and output capabilities are covered by a PCI 6236 and a PCI 6230, which handle current and voltage readings, respectively.

2.2.4 The lasers

With the exception of the 423 nm Toptica laser system, all of the continuous wave (CW) lasers in the laboratory are a homemade external cavity diode laser (ECDL). All five have the same general design, in the Littrow configuration [HWS01] using a holographic diffraction grating and a steering mirror, epoxied to a high stability LINOS Lee's optical mount. The design, shown in figure 2.4 with the geometry particular to 935 nm, is simple and robust. The primary variation in the geometry for different wavelengths is the position and angle at which to tap the holes for the laser diode collimation tube mounting piece. The piece must be positioned such that it nominally satisfies the Littrow feedback condition (i.e. that the first order diffraction off the grating is angled back into the laser diode). Furthermore, the laser diode is positioned at the first-order solution for geometric mode-hop suppression [Ye04], [LP93].

The laser mounting plate is a monolithic steel plate, with four holes in the body. The first two are clearance holes to affix the LINOS optical mount onto

Wavelength	Purpose	Diode	Controller(s)	Power*
672 nm	Ca repump	Alltronics 04L007	Mixed**	6 mW
650 nm	Ba ⁺ repump	Toptica LD-0650-040-AR-1	MOGbox	10 mW
493 nm	Ba ⁺ cooling	Nichia NDS4113	MOGbox	12 mW
935 nm	Yb ⁺ repump	Axcel 940-0100	MOGbox	14 mW
369 nm	Yb ⁺ cooling	Nichia NDU1113E	MOGbox	2 mW

Table 2.1: Basic information about the different components in the home-built ECDL systems. *The power is measured after the optical isolator. **For the 672 nm laser, the current is supplied by a Vescent Photonics current controller, the piezo-electric transducer (PZT) stack is driven by home-built electronics, and the temperature is controlled by both a Vescent Photonics (diode-stage) and a Wavelength Electronics (PTC-10-K-CH) controller for the baseplate. The MOGLabs MOGbox laser controller has single-stage temperature control, a PZT driver, and current control all-in-one.

which the grating and the steering mirror bracket are epoxied. The second two holes are tapped to fix the laser collimation tube holder on top of a thermo-electric Peltier cooler. A thermistor is fixed into a shallow hole bore into the collimation mount, to monitor the temperature of the laser diode holder for temperature stabilization. For all but one of the lasers, the baseplate is then set via “sticky blue stuff” vibrational isolation material (3M material 6309-0026) inside a contemporary-style corrosion-resistant washdown aluminum enclosure (McMaster-Carr). These aluminum enclosures have a neoprene seal, which helps isolate the laser from pressure and temperature variation in the environment. The exception to this is the 672 nm ECDL, which is set on another thermo-electric cooler for second-stage temperature control. Table 2.1 lists the laser diode part numbers with typical usable power output and laser controller type. Each laser employs a ~ 30 dB optical isolator from Optics For Research (OFR IO-5- λ -LP).

2.2.4.1 ECDL frequency control

Most of the experiments described in this dissertation require four of the CW laser systems to be frequency locked near a transition, in order to have both the cold neutral ^{40}Ca cloud and a sample of cold atomic ions. The MOT lasers (423 nm and 672 nm) are locked to vapor cell references as described in chapter 3. The atomic ion cooling (and repumping) laser systems are stabilized via transfer cavity (and wavelength meter) locking.

The 369 nm or 493 nm atomic ion cooling laser, for Yb^+ or Ba^+ respectively, is stabilized by a digital transfer cavity technique to the 423 nm MOT laser which, as described in 3.3.1.1, is stabilized directly to an atomic vapor cell. A transfer cavity technique uses the signal from a resonant cavity to transfer the stability of one laser to another. In principle, both atomic ion cooling lasers could

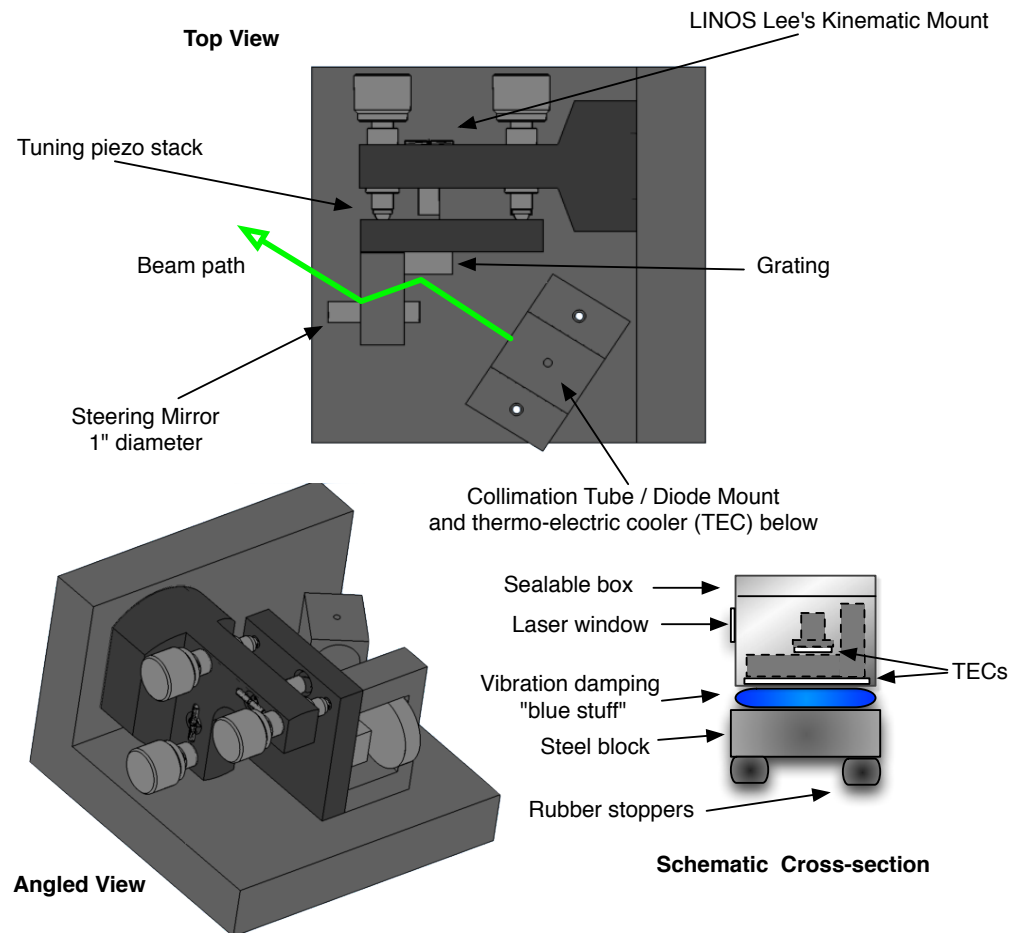


Figure 2.4: General schematic diagram and mechanically drawing of the ECDL design used for all the non-commercial lasers in this work. The particular mechanical drawing shown is for the 935 nm laser geometry.

be simultaneously stabilized by the transfer cavity technique but no experiment has yet required both species simultaneously. A small amount of light from the 423 nm and either the 493 nm or 369 nm lasers is coupled into a scanning cavity Fabry-Perot interferometer (Thorlabs SA-200-3B, 350-535 nm, 1.5 GHz free spectral range). As the cavity is scanned at 10 Hz, the photodiode signal from the interferometer is amplified by a SRS560 low-noise pre-amplifier and read into the DAQ computer. A LabVIEW virtual instrument (vi) determines relative positions of the two laser resonances, and feeds back on the atomic ion cooling laser via the piezo-stack modulation (PZT Mod) input on the MOGbox laser controller in order to keep the relative position stabilized. This stabilization is good to approximately $100 \mu\text{s}$ for a 10 Hz scan over the 1.5 GHz FSR cavity. This corresponds to relative stabilization at the order of ~ 1 MHz, which is consistent with concurrent wavemeter readings.

While the transfer cavity method transfers the stability of the absolute-referenced 423 nm MOT laser to the ion cooling laser by fixing the relative position of the two lasers in the scanning cavity, the absolute frequency, which manifests itself in this scheme as the actual time separation between the two resonant peaks as the cavity is scanned over a FSR, must be set in software. In practice, this is implemented by scanning the atomic ion cooling laser, while measuring the fluorescence off a sample of trapped ions to locate the position of the resonance and then using a known calibration between voltage applied to the piezo modulation input on the MOGbox to determine the initial desired tuning before engaging the lock. The PZT Mod voltage input to frequency calibration is known by scanning the laser over many FSR of the fixed length Fabry-Perot interferometer, with additional verification via a Bristol 621A-VIS wavelength meter.

The 935 nm or 650 nm atomic ion repump laser, for Yb^+ or Ba^+ respectively,

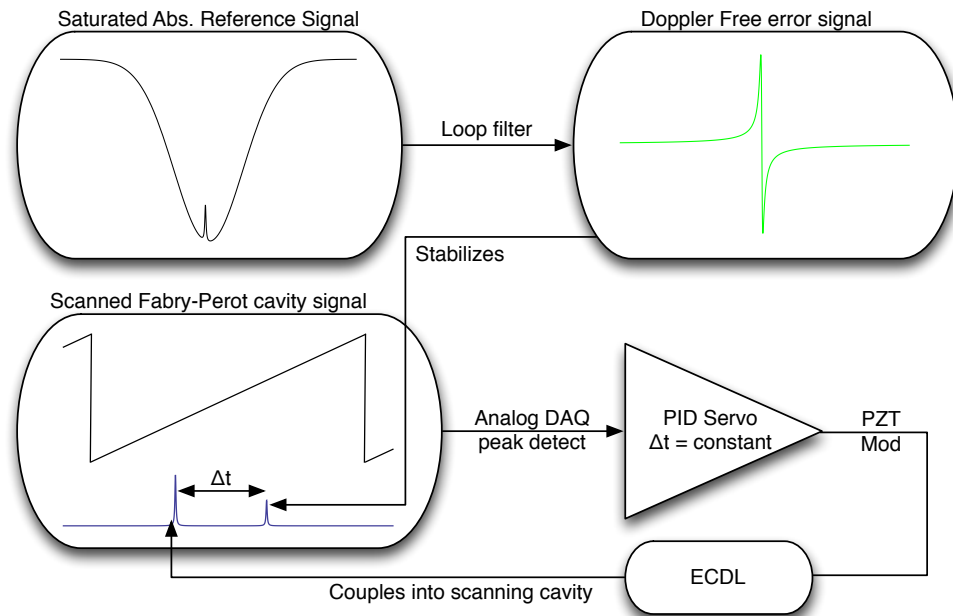


Figure 2.5: Schematic of the ECDL transfer cavity feedback scheme. The 423 nm laser is first stabilized to an atomic absorption reference (described in 3.3.1), then co-coupled with light from the ECDL into a scanning cavity interferometer. A LabVIEW vi analyzes the cavity photodiode signal and performs stabilization feedback.

is stabilized to the Bristol 621A-VIS wavelength meter. The LabVIEW vi feeds back to the MOGbox PZT Mod, and stabilizes the wavemeter reading to roughly ± 3 MHz i.e. to the last decimal place available from the meter. In principle, by using a fiber multiplexer, future experiments could use the wavemeter to simultaneously lock several lasers if needed.

2.3 The Ion Trap

2.3.1 The equations of motion for RF trapping

Due to one of the fundamental laws of electromagnetism, the Laplace Equation $\nabla^2\Phi = 0$, there cannot exist an electric potential minimum in all three spatial dimensions. However, in the quest to confine a charged particle, there are workarounds. For example, an electrostatic field set up by, in the ideal case, a quadrupole arrangement of hyperbolic electrodes, a.k.a a quadrupole potential $\Phi \propto r^2 - 2z^2$, has radial but not axial confinement. Adding a static magnetic field results in the so-called Penning trap, with axial confinement achieved via the Lorentz force. Due to the cyclotron nature of the confinement, the Penning trap is useful for confining charged particles with high charge-to-mass ratios, such as highly-charged ions or electrons. Another way to achieve full confinement is to use endcap DC electrodes combined with a two-dimensional quadrupole electrode configuration $\Phi \propto x^2 - y^2$ while varying the polarity of the quadrupole electrodes in time. For harmonic time variation, this results in the linear radio-frequency (RF) quadrupole Paul trap potential, formally:

$$\Phi = (U_{DC} + V_{RF} \cos(\Omega_{RFT})) \left(\frac{x^2 - y^2}{r_0^2} \right), \quad (2.1)$$

where r_0 , the so-called field radius, is the distance from the center of the potential and the electrode surface. The equations of motion derived by evaluating

Newton's second law, $F = ma = -Ze\vec{\nabla}\Phi$, on an ion with charge Ze and mass m are identical in x and y and of the form:

$$\frac{d^2x}{d\tau^2} + (a_x - 2q_x \cos(2\tau)x) = 0, \quad (2.2)$$

where the equation has been recast into units of $\tau = \frac{\Omega_{RF}t}{2}$ and in two other dimensionless parameters a and q . The unitless numbers a and q are related to the physical parameters as:

$$\begin{aligned} a_x = -a_y &= \frac{8ZeU_{DC}}{mr_0^2\Omega_{RF}^2} \\ q_x = -q_y &= \frac{4ZeV_{RF}}{mr_0^2\Omega_{RF}^2}. \end{aligned} \quad (2.3)$$

These equations of motion are known as the Mathieu equations and they are well-studied, especially due to the relevance to ion trapping and mass spectrometry [DFM05]. Most importantly for ion trapping, there exist stable solutions to the Mathieu equations. For example there is the first stability region, shown in the inset of figure 2.6, within which all the experimental work discussed in this dissertation is performed. It should be noted, that the edges of the stability region are hazy, and the theoretical plot shown here assumes trap-centered resting initial conditions. In practice the initial conditions are messy (e.g. loading by ablation). As shown in figure 2.6, the experimental realization of trap stability cuts out early on the low V_{RF} side and high U_{DC} , likely due to trap depth and loading efficiency issues.

It is important to note that the above equations are for a perfect, symmetric quadrupole potential (i.e. one that would be realized with four properly placed hyperbolic electrodes with alternating potentials). For practical reasons such as optical access, simplicity of machining, and convenient electronic design the

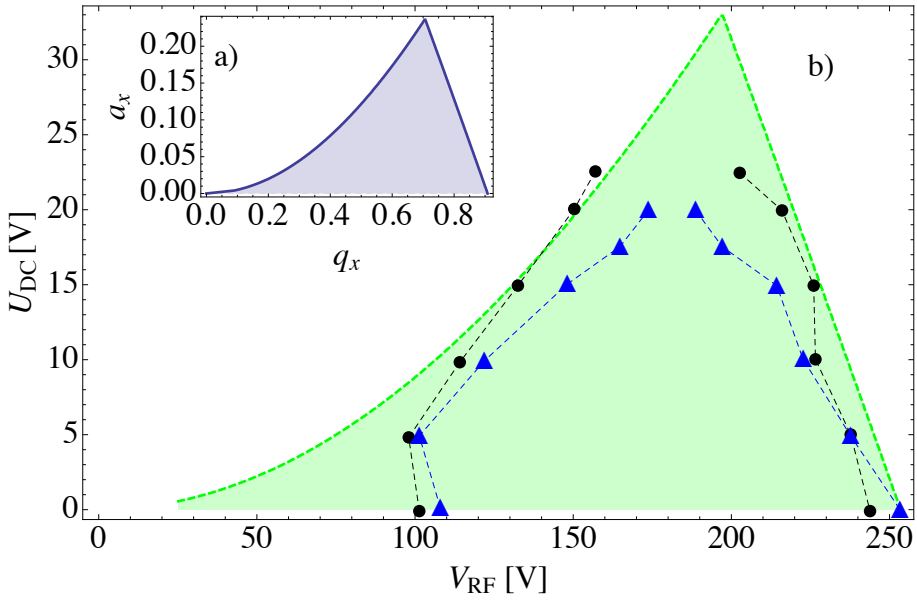


Figure 2.6: Inset (a) shows the first linear quadrupole stability region in terms of the dimensionless Mathieu parameters a and q . Part (b) shows the stability region scaled into units of voltage on the endcaps and two RF rods in the actual ion trap ($r_0 = 11.2\text{mm}$, $m = 173\text{amu}$). The stability region is within the dashed green line. The blue triangles are the experimental boundaries found when ablating a Yb target. The black dots are the experimental boundaries measured when ablating a pressed BaCl₂ target.

actual RF trap used in this work consists of four circular rods in a square configuration. Only two of the rods are driven with RF power as shown in figure 2.13. In the two RF rod experimental configuration only half the amplitude, for a given V_{RF} on the rods, is actually going into making oscillatory trapping fields, so the Mathieu parameters 2.3 must be reduced by a factor of two before any calculation.

2.3.2 The low q limit - secular motion and micromotion

The equations of motion 2.2 in the linear quadrupole trap have stable solutions with frequencies $\omega_n = (2n + \beta) \frac{\Omega_{RF}}{2}$ where n can be any integer, and β is a fairly complicated function of the Mathieu parameters a and q [Daw95]. More precisely, the trajectory of the trapped ion will be described by a Mathieu trajectory of the form:

$$x(t) = A \sum_{-\infty}^{\infty} c_n \cos(\omega_n t) + B \sum_{-\infty}^{\infty} c_n \sin(\omega_n t), \quad (2.4)$$

i.e. a linear combination of special functions of a and q sometimes referred to as the Mathieu cosine and Mathieu sine. A plot of the Mathieu cosine for $a = 0$ and $q = 0.25$ is shown in figure 2.7. To build intuition for what the different frequency components of the motion ω_n physically mean, it is illustrative to take the limit of low q . In this limit, and with $a = 0$, $\beta \simeq \frac{q}{\sqrt{2}}$, and the first few terms $n = 0, \pm 1$ in expansion sum are dominant. Taking initial conditions such that $B = 0$ and $c_0=1$, the trajectory becomes [MD68]:

$$x(t) = A \left(1 + \frac{q}{2} \cos(\Omega_{RF}t) \right) \cos\left(\frac{q}{2\sqrt{2}}\Omega_{RF}t\right). \quad (2.5)$$

In this limit, the physical interpretation of the $\omega_{n=0,\pm 1}$ contributions to the motion are apparent. The motion consists of a primary oscillation at the so-called secular frequency $\omega_0 = \beta \frac{\Omega_{RF}}{2}$ and the micromotion which is a higher frequency modulation at a fixed fraction of the secular amplitude. The secular frequency is unique to the particular charge to mass ratio of the trapped ion, and deliberate excitation of the secular mode to induce trap heating or loss is a useful tool for mass identification in trapped ion samples. The secular motion is what is usually identified as thermal, random motion, whereas the micromotion has a definite phase relation to the RF drive and is a coherent motion. A useful approximate

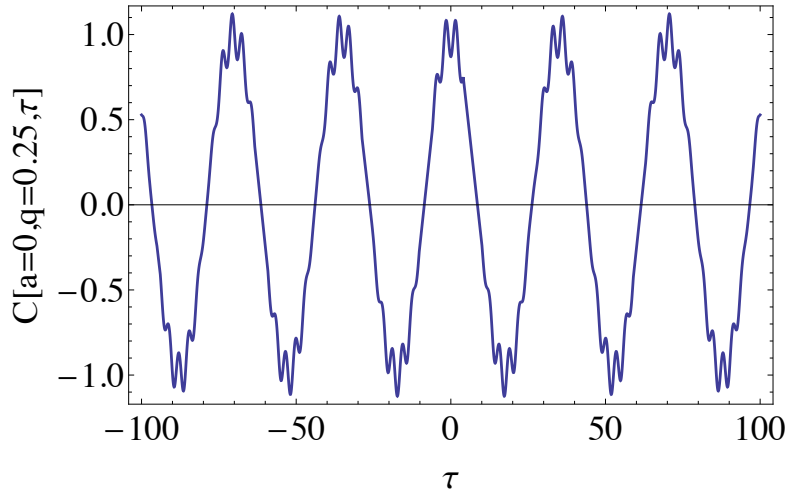


Figure 2.7: Mathieu cosine, from the expansion in equation 2.4, for $A = 1$, $B = 0$, $a = 0$ and $q = 0.25$. Note the bulk, lower frequency (secular) motion with a fractional modulation (micromotion).

formula for calculating β , and thus the secular frequency is given by [BTR06]:

$$\beta = \sqrt{a - \frac{q^2(a-1)}{2(a-1)^2 - q^2} - \frac{q^4(5a-7)}{32(a-1)^3(a-4)}}. \quad (2.6)$$

This approximation to β is sufficient, after some corrections due to trap imperfections as explained in section 2.3.5.2, for prediction of the secular frequency to better than the typical precision $\sim 1\text{kHz}$ of measurement by secular excitation induced trap loss. Trapped ion mass identification is made by applying an additional sinusoidal voltage to one of the trap electrodes, and measuring induced trap loss as a function of frequency. At a secular resonance, the excitation induces extra trap loss due to heating and reduces the number of ions detected by the channeltron when the trap is turned off.

The other term, the modulation at the trap frequency, is known as the RF micromotion, and it is important for several reasons. First, for systems with many trapped ions, the kinetic energy of the micromotion is often the limiting factor in

achieving low energy collisions [CGV12]. The ions may be cooled until the secular motion is frozen out, forming an ion crystal, but the micromotion can never be completely removed, except for at the exact trap potential minimum. Second, collisional interruption of micromotion by background gas or ion-ion interaction leads to phase disruption and work done by the ion trapping fields to bring the ion back into phase increases secular energy, leading to a natural trap heating rate further discussed in section 2.3.3.2. The contribution of the micromotion to the average kinetic energy for an ion in a finite cloud can be estimated by inspection of equation 2.5 and calculating the kinetic energy, $\frac{1}{2}m(a_{\mu m}\Omega_{RF})^2$, due to the extra micromotion amplitude (squared) averaged over an RF cycle, $a_{\mu m}^2 \approx \frac{Aq}{4}$. The resulting expression for the micromotion's energy contribution with A recast as r , the distance from the RF null [BMB98], is

$$E_{\mu m} = \frac{m(rq\Omega_{RF})^2}{32}. \quad (2.7)$$

This expression is useful for estimating the typical energy of the atom-ion interaction in the hybrid trap, by averaging over the ion cloud distribution. By using a single trapped ion and deliberating shimming the ion off the RF null towards $r > 0$, the interaction energy can be tuned using micromotion [ZPR10].

2.3.3 Cooling atomic ions

2.3.3.1 Laser cooling atomic ions

For ions with an appropriate electronic transition a red-detuned laser beam can be used to remove kinetic energy via Doppler cooling. This process is quite efficient and can easily outpace RF heating, cooling many ions down to very low secular temperatures. Some experiments, using more advanced techniques such as sideband cooling, even reach the the quantum limit by cooling a trapped ion

into a trap mode with $n < 1$ average phonon number [LMB03].

The standard technique of Doppler cooling relies on the scattering of red-detuned photons by trapped ions. The ions moving towards the red-detuned beam preferentially absorb the light due to the Doppler effect. The scattering rate of the photons,

$$S = \frac{\Gamma}{2} \frac{s}{1 + s + 4\frac{\delta^2}{\Gamma^2}}, \quad (2.8)$$

depends on the laser intensity saturation parameter $s = \frac{I}{I_0}$, detuning δ and the cooling transition's spontaneous decay rate Γ . I_0 is the saturation intensity which can be calculated by $I_0 = \frac{\pi h c A_{\text{total}}}{3\lambda^3}$, where A_{total} is the Einstein A coefficient for the excited state. The so-called Doppler cooling limit is reached when the cooling power of the scattering force is in equilibrium with the random heating induced by the absorption and emission of the photons from the cooling laser. These cooling rate can be written as:

$$\left(\frac{\partial E}{\partial t} \right)_{\text{cool}} = \bar{F}v = -\alpha v^2 = \hbar k \frac{\partial S}{\partial v} v^2. \quad (2.9)$$

The heating rate is determined by twice (once for emission, once for absorption) the total scattering rate times the kinetic energy imparted by the momentum carried in one photon:

$$\left(\frac{\partial E}{\partial t} \right)_{\text{heat}} = 2S \frac{(\hbar k)^2}{2m} \quad (2.10)$$

Taking the equilibrium of these two rates equation $\left(\frac{\partial E}{\partial t} \right)_{\text{heat}} + \left(\frac{\partial E}{\partial t} \right)_{\text{cool}} = 0$ and thermally averaging $\langle v^2 \rangle$ gives the expression 2.11 for the minimum temperature that can be reached as a function of the saturation parameter s and the detuning δ .

$$T_D(s, \delta) = \frac{\hbar\Gamma}{4k_b} \left(\frac{1 + s + 4(\delta/\Gamma)^2}{2\delta/\Gamma} \right) \quad (2.11)$$

The ultimate, so-called Doppler limit ($T_D \rightarrow \frac{\hbar\Gamma}{2k_b}$) is the low intensity $s \rightarrow 0$ limit evaluated at the optimal detuning $\delta \rightarrow \Gamma/2$. For both Yb^+ and Ba^+ laser cooled in the MOTion trap, temperatures near the Doppler limit have been observed. Techniques used in determining the atomic ion temperature are discussed in section 2.3.3.2.

2.3.3.2 Determining laser-cooled ion temperature

Two methods are commonly used to determine the temperature of trapped ions: comparison of images of ion clouds to molecular dynamics simulation results, and laser-induced fluorescence Doppler lineshape spectroscopy. In this work, all the explicitly measured ion temperatures are done with the latter method. To calculate the fluorescence rate when probing a thermal sample of trapped ions, equation 2.8 must be averaged over a thermal ensemble with $\delta \rightarrow \delta + kv$.

$$\Gamma_{\text{Voigt}}(\delta, T) = \sqrt{\frac{m}{2\pi k_B T}} \int dv \frac{\Gamma}{2} \frac{s e^{-\frac{mv^2}{2k_B T}}}{1 + s + 4 \left(\frac{\delta + kv}{\Gamma} \right)^2} \quad (2.12)$$

The resulting function of laser detuning, ensemble temperature and transition saturation parameter, equation 2.12, is known as the Voigt profile. This lineshape frequently appears in nature, since it is the convolution of a Gaussian (thermal) distribution with the Lorentzian lineshape. By scanning the ion cooling laser frequency from below the resonance frequency towards the resonance, the Voigt fluorescence profile is observed. For example, in figure 2.8, a sample of Yb^+ ions is cooled to their Doppler temperature limit by the 369 nm ECDL scanning slowly over the cooling transition in $^{174}\text{Yb}^+$. The profile is cut off for frequencies above the transition resonance due to Doppler heating quickly heating up the ions.

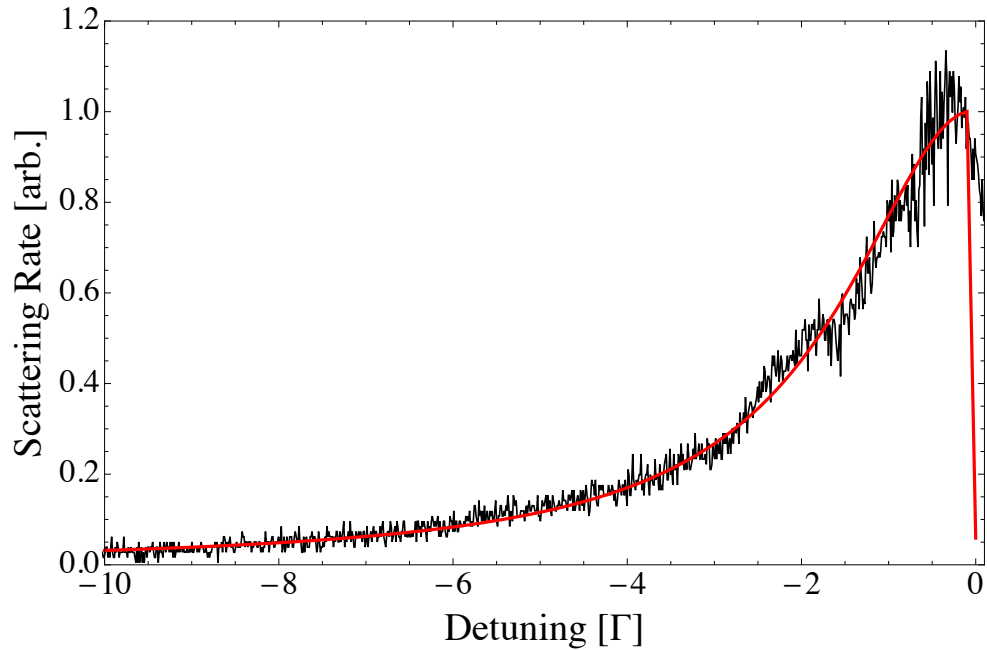


Figure 2.8: A laser induced fluorescence profile on a trapped sample of atomic Yb^+ . The horizontal axis (laser frequency) has been re-scaled into units of the transition natural linewidth. The solid red line is not a fit, it is the Voigt fluorescence profile, equation 2.12, evaluated at the appropriate Doppler temperature limit, equation 2.11, for each laser detuning. The profile is truncated for frequencies above the resonance, because the ions are heated up quickly when the cooling laser passes the resonance due to Doppler heating.

Nevertheless the temperature of the ions can be inferred [KCC06]. The below resonance half of the profile is fit to equation 2.12 to determine a temperature. A useful empirical formula relating the Voigt full-width at half-maximum (FWHM) to the Gaussian and Lorentzian contributions widths, Δ_G and Δ_L respectively, is

$$\Delta_G = \sqrt{(\Delta_V - 0.5346\Delta_L)^2 - 0.2166\Delta_L^2} \quad (2.13)$$

where Δ_V is the Voigt lineshape's FWHM [OL77]. The power-broadened Lorentzian contribution is calculated by $\Delta_L = \sqrt{1 + s \frac{\Gamma}{2\pi}}$.

In practice this measurement approach loses sensitivity as the temperature approaches ~ 100 mK, the temperature at which the FWHM Gaussian contribution $\Delta_G = \sqrt{\frac{8 \ln(2) k_B T}{m \lambda^2}}$ to the lineshape width is comparable/less than the power-broadened natural linewidth.

2.3.4 Sympathetic cooling and heating of RF trapped ions

It has been known since the early years of ion trapping [MD68] that, due to the non-equilibrium nature of the trap itself, sympathetic cooling by buffer gas in an ion trap is not as efficient as in static systems because the time-varying potential can do work on the ions. Over the years, many groups have studied the effect of trap dynamics on the statistical distribution [DeV09] and equilibration dynamics [BW02, MTM92], both for the ion-ion self interaction and for the ion-atom buffer gas interaction. Two particular aspects of many-body RF trapping dynamics are particularly important to understand and account for in the atom-ion experiments.

First, there is a buffer gas mass-dependent effect [MD68, DeV09] where, at a critical ratio of buffer gas to ion mass ($\frac{m_B}{m_i} \sim 1.55$), collisions with the buffer gas tend to increase the average ion temperature, regardless of the buffer gas

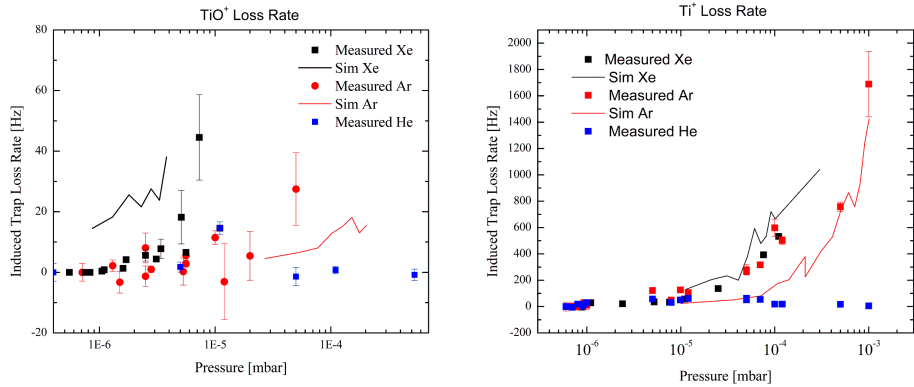


Figure 2.9: Experimental measurement of the reduction in trap lifetime of trapped titanium-oxide (TiO^+ , $m \sim 64\text{amu}$) and titanium (Ti^+ , $m \sim 48\text{amu}$) ions due to introducing room temperature He ($m \sim 4\text{amu}$), Ar ($m \sim 40\text{ amu}$), and Xe ($m \sim 131.3\text{ amu}$) buffer gas. *SIMION* simulation results are shown as solid lines.

temperature. This effect inspired an experiment, using the MOTion trap, on the effect of buffer gas mass on the lifetime of samples of trapped titanium-oxide and titanium ions (TiO^+ and Ti^+). The summary result of this investigation is shown in figure 2.9. The measurement is consistent with an expected increase in trap loss due to heavier buffer gas and qualitatively agrees with results a simple hard sphere collision simulation conducted using *SIMION 8.0*, an ion trajectory simulation software [SIM07]. The simulation results are shown in figure 2.9 as solid lines. No simulation is plotted for helium buffer gas because the helium induced no additional trap loss for all the buffer gas densities simulated.

The second important dynamic is the heating rate, inherent to the driven nature of the trap, due to micromotion interruption by ion-ion collisions. Ultimately, motivated by the need to truly understand the characteristic energy scale of the atom-ion interaction in the hybrid system, the self heating rate is measured

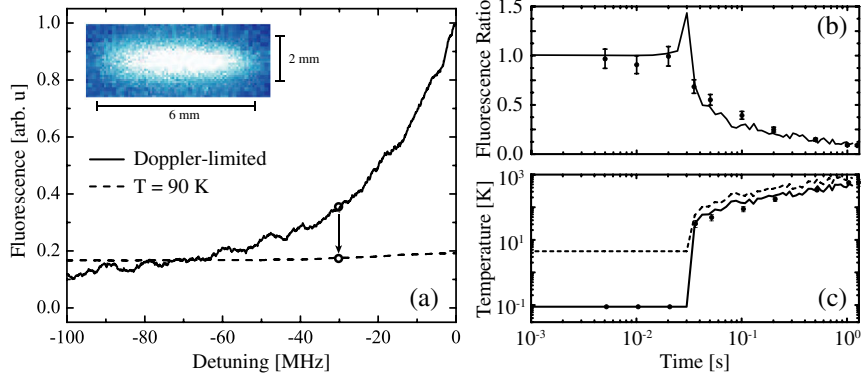


Figure 2.10: (a) The solid line shows the experimental measured laser induced fluorescence profile for a sample of ions near the Doppler temperature limit. The dashed line shows the profile if the ions were at $T = 90\text{K}$. The inset shows a typical ion cloud fluorescence image. (b) The result of a measurement of the ratio cold ion sample fluorescence at fixed laser detuning ($\delta = 30\text{MHz}$) to the fluorescence of the same sample after extinguishing the cooling beam for a variable heating time. A molecular dynamics simulation is shown as a solid line. (c) The dots in this panel represent the secular temperature inferred from the measured fluorescence ratio in panel b by the method schematically shown in panel a. The solid (dashed) line shows simulation results for the secular (total) temperature.

directly by laser induced fluorescence [CSR13]. This measurement, illustrated in figure 2.10, along with promising ongoing analytical and computational work by my labmate Kuang Chen, will be covered extensively in his dissertation. A brief summary of the important results is detailed here.

The heating rate measurement requires the ion Doppler cooling laser to be passed through an AOM for quick switching. Fluorescence from a sample of $^{174}\text{Yb}^+$ is used to measure the secular heating rate in the MOTion trap. First the ions are cooled to near the Doppler limit. After performing a series of frequency scans to measure the lineshape, and thus initial temperature T_i , the cooling laser

locks to a fixed detuning δ and is then switched off for a variable delay time Δt . The ratio of the fluorescence immediately after switching the laser back on ($f(\Delta t)$) to that measured immediately following the switching off ($f(0)$) is directly related to ion distribution secular temperature via equation 2.12 ($\frac{f(\Delta t)}{f(0)} = \frac{\Gamma_{\text{Voigt}}(\delta, T_f)}{\Gamma_{\text{Voigt}}(\delta, T_i)}$). The cumulative effect of the ion-ion heating rate is then determined by measuring the ratio as a function of light-free heating time. Figure 2.10 demonstrates the result of a heating rate measurement for one sample of trapped Yb^+ ions. The analysis of several measurements like the one shown in figure 2.10 results in a refined analytic model [CSR13].

An analytical expression for the heating rate of the secular temperature is

$$\dot{T}_{\text{sec}} = \frac{e^4 \rho(T_{\text{sec}}) \ln \Lambda}{2\pi \epsilon_0^2 \sqrt{m} (3k_B T_{\text{sec}})^{3/2}} \epsilon (T_{\text{sec}} + \eta T_{\mu m}), \quad (2.14)$$

where $T_{\mu m}$ is the “temperature” of the excess energy due to micromotion ($\frac{E_{\mu m}}{\frac{3}{2} N k_B}$, see equation 2.7). η is the ratio of the secular energy to the total energy ($\sim \frac{3}{5}$ for low q due to equipartition). $\ln \Lambda$ is the so-called Coulomb logarithm, and ϵ is the average fractional increase of ion energy per collision. Both of these last two terms require further discussion.

The latter term, ϵ , is a function of the Mathieu parameters a and q that arises when modeling elastic collisions in an RF trap [MTM92]. It characterizes the energy transfer from the trapping potential to the ions due to phase interruption during the collision process, and is found by averaging the change in kinetic energy due to a collision event over all the equally probable RF phases at the collision time then taking an ensemble average over all possible trajectories. The somewhat unwieldy exact expression for the fractional change in total kinetic energy for a 1D colliding pair is:

$$\epsilon = \frac{(c(\tau)\dot{c}(\tau) + s(\tau)\dot{s}(\tau))^2}{(c(\tau)\dot{s}(\tau) - s(\tau)\dot{c}(\tau))^2} \quad (2.15)$$

where the function of c and s , the Mathieu sine and cosine special functions shown in the trajectory expansion 2.4, is averaged over all phases τ . A more convenient analytical expression for ϵ in 3D collisions, accurate for low q and $a = 0$, is $\epsilon = \frac{2}{3}(1 + 2q^{2.24})$.

The Coulomb logarithm is a factor which naturally shows up when modeling scattering collisions between charged particles, due to the long range nature of the $\frac{1}{r}$ Coulomb interaction. The long range nature of this interaction brings about a divergence which is traditionally [Lan36] taken care of by introducing both a short and long-ranged cutoff to the interaction. In the simplest calculation, the long range cutoff is usually a screening length, such as the Debye screening ($\lambda_D = \sqrt{\epsilon_0 k_B T / \rho e^2}$). The short range cutoff is taken to be thermal distance of closest approach, a.k.a the Landau length ($R_C = \frac{e^2}{4\pi\epsilon_0 k_B T}$). Integrating over these length scales yields the term $\ln \Lambda = \ln(C\lambda_D/R_C)$, often written in terms of a constant multiplied by the inverse of the strong coupling parameter $g = R_C/\lambda_D$. In agreement with a series of measurements and simulations like that shown in 2.10, the Coulomb logarithm for strongly coupled ions in an RF trap is best fit by the following analytic form [CSR13]:

$$\ln \Lambda = \begin{cases} f_I(g) = \frac{\ln(1+0.7/g)}{1+125\sqrt{g}} & : g < 1 \\ f_{II}(g) = \frac{f_I(g=1)}{g^2} & : g \geq 1 \end{cases} \quad (2.16)$$

2.3.4.1 Ion cloud density and the Coulomb coupling parameter

When sufficiently confined, trapped ions exhibit phase transitions into spatially correlated structures, known as Wigner, or Coulomb, crystallization. The dynamics are parametrized by the Coulomb coupling parameter, a unitless parameter closely related to the strong coupling parameter g . The Coulomb coupling parameter, traditionally denoted Γ , is given the ratio of the average interparticle

Coulomb potential energy to the thermal kinetic energy,

$$\Gamma = \frac{e^2}{4\pi\epsilon_0 a} / (k_B T) \quad (2.17)$$

where a is the average ion nearest neighbor separation related to the density by

$$\frac{4\pi a^3}{3} \rho = 1. \quad (2.18)$$

Molecular dynamics simulations indicate that a liquid-solid phase transition occurs near $\Gamma \sim 170$, but observations in large ion crystals show the formation of correlated structure occurs at lower $\Gamma \sim 40$ [Dub90], [HDL08]. Ion structures are not observed in the first iteration of the MOTion trap system. Despite achieving Doppler-limited temperatures, Γ stays below the liquid-solid transition critical value due to the relatively large trap field radius and low trapping voltages. In addition, the 1:1 imaging system is not capable of resolving crystalline structure formation. The second generation MOTion trap, discussed in chapter 8, improves on these technical shortcomings.

In order to relate a heating measurement like that shown in figure 2.10 to the value of $\ln \Lambda$ in equation 2.14, the dependence of the ion cloud density on secular temperature needs to be understood. For higher secular temperature, where the strong coupling parameter is small, the ions are in a gaseous phase and the density scaling approaches that of an ideal non-interacting gas $\rho \sim T^{-3/2}$. Equation 2.14 appears to indicate never ending heating. In reality, an evaporative equilibrium occurs when the ions reach a high enough temperature that the fraction of the distribution escaping above the trap depth evaporatively “cools” the sample. A common rule of thumb says that this equilibrium temperature is approximately $T_{eq} = \frac{D}{10k_B}$, where $D \sim \frac{qeV_{RF}}{4}$ is the effective trap depth in the low q limit [DFM05]. Note that all these equations assume the electrode voltage configuration in which all four rods are driven with RF. If using an electrode

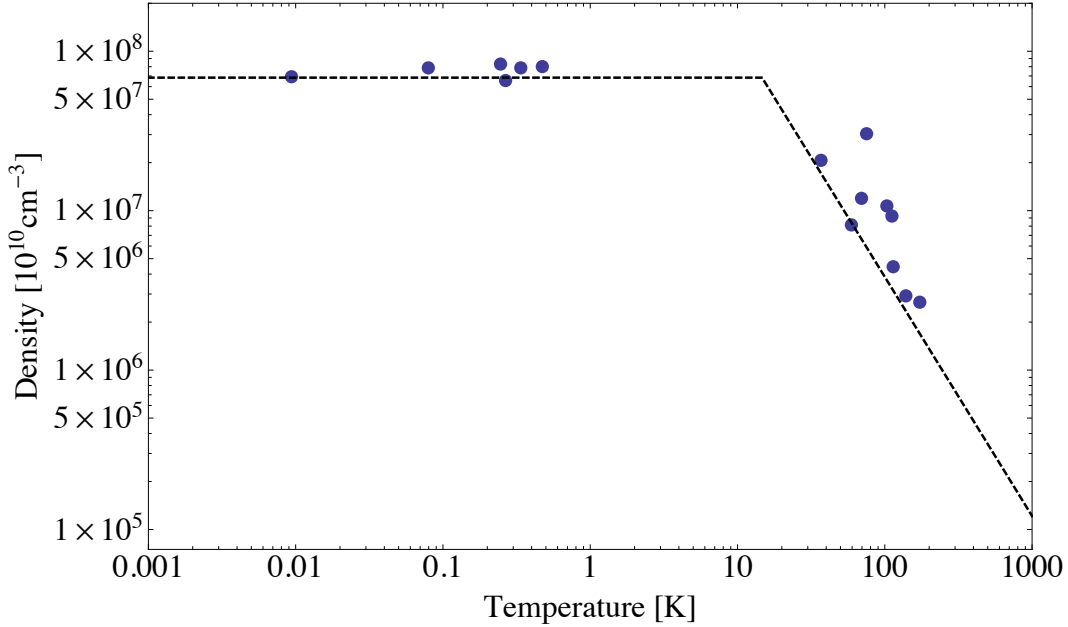


Figure 2.11: Measurement of the ion cloud density as a function of secular temperature, performed with a trapped of Yb^+ , shown in dots. The dashed line is equation 2.19.

configuration with only two RF rods, a factor of $\frac{1}{2}$ must be included wherever V_{RF} occurs. The density can be modeled with a piecewise expression that fits well to both regimes:

$$\rho(T_{sec}) = \begin{cases} \rho_{max} = \frac{\epsilon_0 V_{RF}^2}{mr_0^4 \Omega^2} & : T_{sec} \leq T_0 \\ \rho_{max} \left(\frac{T_0}{T_{sec}} \right)^{3/2} & : T_{sec} > T_0 \end{cases} \quad (2.19)$$

where $T_0 = \frac{m\bar{\omega}^2}{4k_B} \left(\frac{3Nm r_0^4 \Omega^2}{4\pi\epsilon_0 V_{RF}^2} \right)^{2/3}$ is the transition secular temperature between a constant density, strongly coupled regime and the a gaseous, thermal density regime.

2.3.5 Experimental trap realization

2.3.5.1 Experimental limitations due to RF heating

There are two important experimental design reactions to the ion-ion heating and buffer gas mass dependent heating effects for the hybrid system of this dissertation. First is the choice of ^{40}Ca for the MOT atom. Calcium is the compromise between low mass, high ionization potential, and convenient laser cooling wavelength. Second is the need to co-trap and laser cool an atomic ion with the molecular ion for translational cooling strong enough to overcome the ion-ion secular heating rate in large ion number samples because for achievable MOT densities the translational cooling rate alone is not sufficient. The MOT alone is found to cool a sample of trapped Yb^+ from $T = 775(25)$ K to the very modest temperature of $T = 515(20)$ K, as shown in figure 2.12. These temperatures are determined by a fast scanning of the laser from far red-detuned ($\delta < -50\Gamma/2\pi$). The quick scan rate minimizes the number of photons scattered, and thus minimizes any cooling that would lead to a systematic underestimate of the actual equilibrium temperature.

2.3.5.2 Constructing the ion trap

The physical implementation of the linear quadrupole trap in this system is shown in figure 2.13. It consists of four circular, $r_e = 9.02$ mm (0.355") stainless steel rods in a square configuration, with the field radius $r_0 = 11.2$ mm (0.441"). Two of the rods have four equally spaced notches to allow for attachment of the horseshoe-like axial endcap electrodes, with room for Kapton film isolation, creating three trapping regions. At least one of the two notched rods was typically grounded, with the other used as a field shim electrode to remove any stray DC

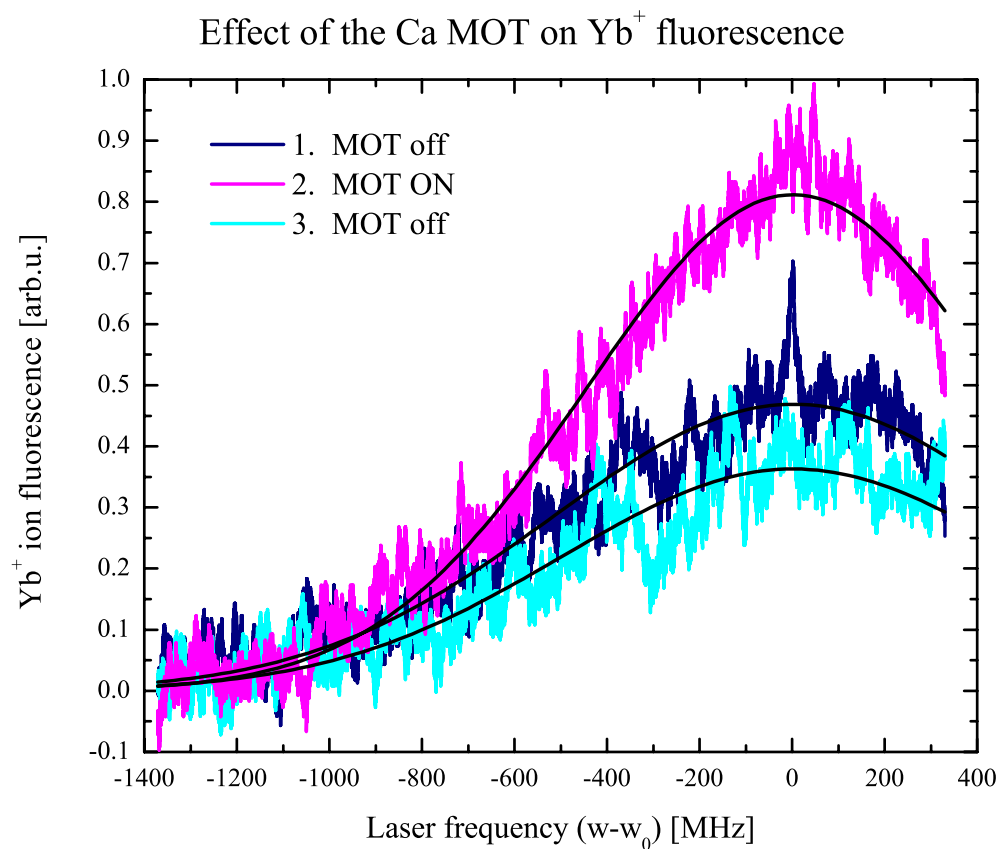


Figure 2.12: The effect of the ^{40}Ca MOT on trapped Yb^+ fluorescence.

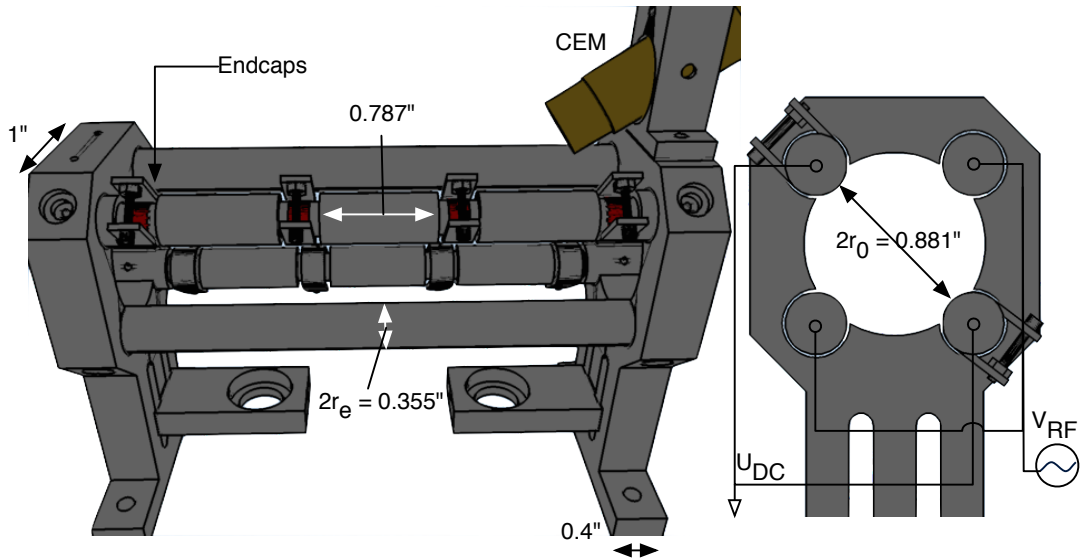


Figure 2.13: A rendering of actual ion trap used in this work. On the left, shown in perspective. Four sets of axial endcaps provide axial confinement for three possible trapping regions. A channel-electron multiplier (CEM) is mounted above for direct ion detection. Below are two mounts for pressed ablation targets for ion loading. To the right is an orthographic view down the trap axis, showing the pair of rods with the endcaps are used for DC offset voltages, to change a or shim micromotion, while the other pair of rods is driven with a RF potential.

field at the RF null. The two smooth rods are typically driven at approximately 300 kHz, via an amplified (HD Corp. HD17216 amplifier) function generator through a RF switch (ZASW-2-50DR+) into a simple LC circuit resonance, with the trap as the capacitor. The effective capacitance of the two rods, including a simple bias tee circuit in place for the option of DC offset voltages, was ~ 300 pF and the inductor(s) typically used to achieve a resonance of a few hundred kHz were ~ 1 mH. The endcaps are controlled either by an adjustable DC power supply, or by the Quantum Composer 9518+ if precise timing control is required.

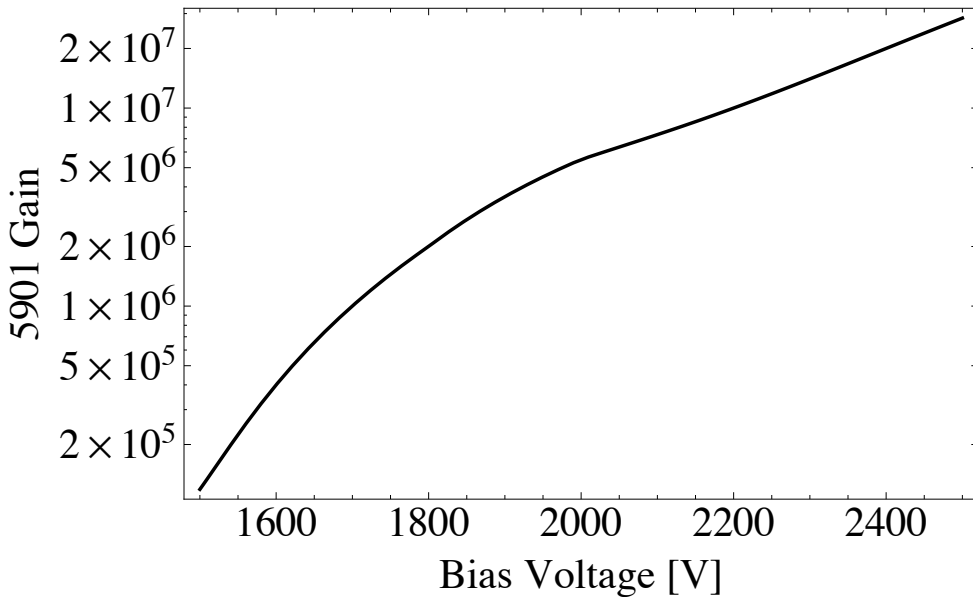


Figure 2.14: Manufacturer’s specification for the gain of the Burle 5901 Magnum channel electron multiplier. The detector was typically biased to -2000 V.

2.3.5.3 Loading and Detecting Ions

The ions are loaded into the trap by laser ablation of pressed targets mounted roughly an inch below the quadrupole trap. The ablation is performed by a 5 – 7 ns, focused pulse of light from a Continuum Minilite II Q-switch Nd:YAG laser at 1064 nm. The pulse power is tuned until a small plume of light is barely visible on the target. While the trap can be loaded with all the electrodes in operation, the trap yield improves by triggering the RF switch on with a delay of $\sim 15 - 50\mu s$ after the Q-switch. The ions are then detected upon shutting off the trap as the channeltron is pulsed on to negative high-voltage. A pulse of current, typically measured on an oscilloscope, indicates the number of ions hitting the detector’s effective area. The number of ions measured in the pulse

can be calculated as:

$$N_{\text{CEM}} = \int dt IRGe \quad (2.20)$$

where the actual signal is voltage ($= IR$) at a known oscilloscope termination voltage. G is the detector's gain, given by the manufacturer specification in figure 2.16 and e is the elementary charge. N_{CEM} is the number of ions which struck the sensitive part of the detector, not the number of ions that were in the trap immediately before removing the trapping potential. In order to determine the actual number of trapped ions, the detection efficiency is calibrated by laser-induced fluorescence. Similar to the temperature measurement described in section 2.3.3.2, the laser frequency is quickly scanned over the transition in ^{174}Yb while a sample at natural isotopic abundance was trapped. By measuring the fluorescence lineshape, both the ion number and temperature can be calculated because the voltage measured is related to the number of trapped ions by

$$V_{\text{PMT}} = \Gamma e \eta(\lambda) G N_{ion} R T \Omega, \quad (2.21)$$

where e is the elementary charge, $\eta(\lambda)$ is the wavelength dependent quantum efficiency of the photo-multiplier, G is the gain of the photo-multiplier, N_{ion} is the number of fluorescing ions, R is the terminating resistance, $T = 0.43(2)$ is the total optical transmission of the light collection elements, and $\Omega = 0.0012$ is the solid angle of the light collection. Γ is the average scattering rate of the laser, which is a function of the laser detuning, intensity, and the trapped sample's secular temperature, as described in section 2.3.3.2. The manufacturer only specifies the R3896 PMT gain at one bias voltage, so the gain curve shown in figure 2.15 is measured in the laboratory.

Based on a series of experiments with comparing the results of quick laser-induced fluorescence scans on a trapped sample of Yb^+ with the number of ions counted after trap release, the collection efficiency of the CEM is $2 \pm 1\%$.

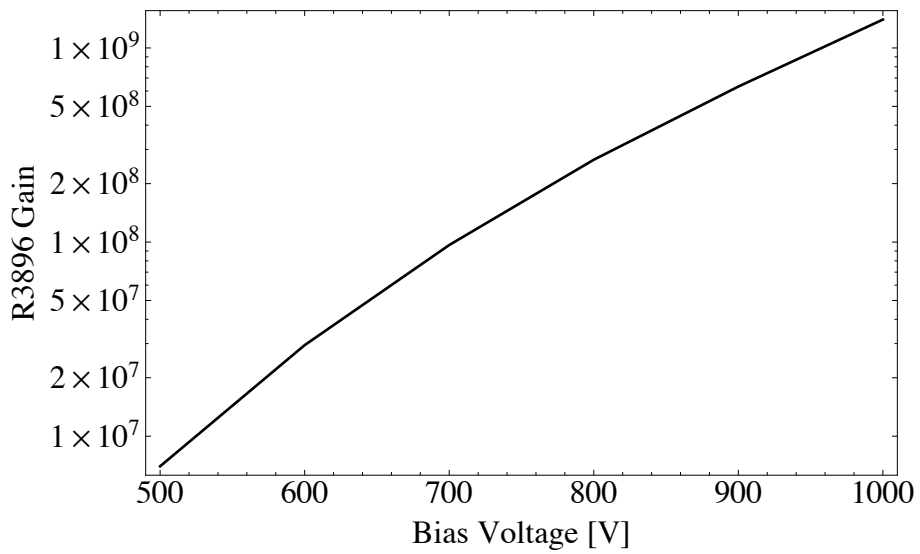


Figure 2.15: Measured gain as a function of PMT bias voltage for the Hamamatsu R3896.

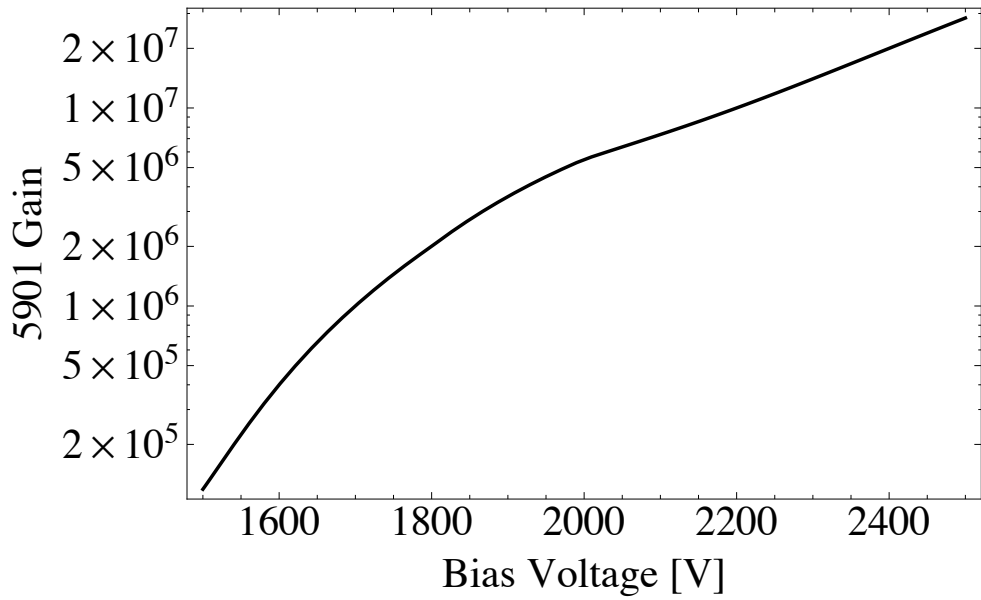


Figure 2.16: Manufacturer's specification for the gain of the Burle 5901 Magnum channel electron multiplier. The detector was typically biased to -2000 V.

2.4 The atomic ions - Barium and Ytterbium

2.4.1 The Ytterbium ion

The ytterbium ion is a popular ion for use in quantum computing experiments [OYM07] and optical frequency metrology [TRG97]. Yb^+ has a single valence electron and a relatively simple electronic structure, shown in figure 2.17. Laser cooling is possible with two lasers, one in the ultraviolet and one in the infrared. Both laser wavelengths are generated using semiconductor diodes in ECDL systems of section 2.2.4. In contrast to those used to cool barium ions, the wavelengths are less convenient because they are not visible. The 369 nm UV wavelength does not couple into fiber very efficiently.

The strong ($A = 2\pi 19.6 \text{ MHz}$) cooling transition is between a ${}^2\text{S}_{1/2}$ and a ${}^2\text{P}_{1/2}$ electronic state. Roughly one in every twenty cycles, the ${}^2\text{P}_{1/2}$ state spontaneously decays into a lower energy ${}^3\text{D}_{3/2}$ electronic state, emitting a 2438 nm photon [YM00]. This optical leak out of the cooling cycle can be removed by a repump laser at 935 nm [BGK91]. In contrast the the lambda structure in Ba^+ , the repump laser drives the ion back into the ground state by coupling the meta-stable D state into a higher-energy fourth electronic state which quickly decays back to the ground state by emission of a deeper UV photon. This difference is beneficial in several ways. First, since the two lasers are addressing different states there are no coherent effects. Thus, the laser induced fluorescence lineshape is simply the Voigt profile and the excited state populations can be described by a simple rate equation model. Second, the emission of a photon at a shorter wavelength than either of the lasers lends itself nicely to very low background measurement if needed.

During most experiments in the MOTion trap, ${}^{174}\text{Yb}^+$ is used as a proxy ion

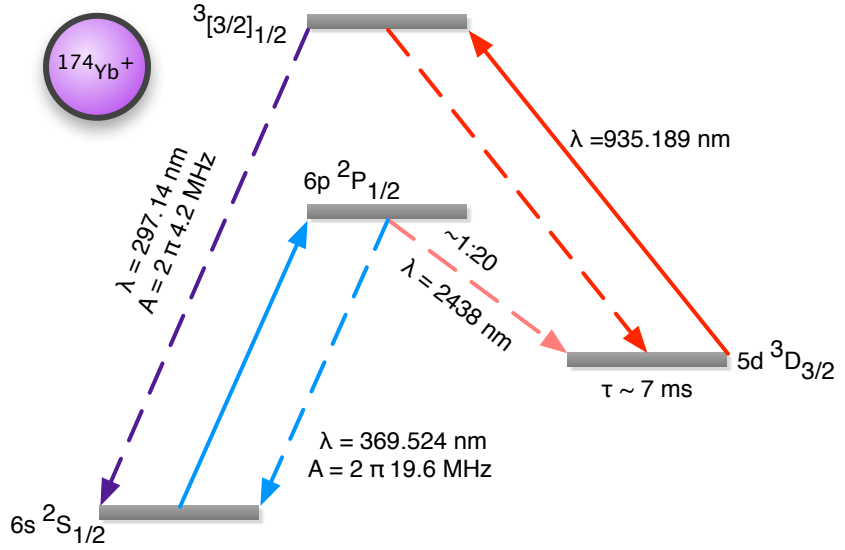


Figure 2.17: Energy level diagram for $^{174}\text{Yb}^+$. Solid lines show the optical transitions driven by the cooling (blue) and repumping (red) lasers. Dashed lines indicate spontaneous dipole decay channels. The wavelengths and decay rates are indicated with values from the NIST Atomic Spectra Database. Known meta-stable state lifetimes and decay branching ratios are indicated.

for measuring the trap dynamics of BaCl^+ because it has the highest natural abundance, no hyperfine structure, and close to the same mass of BaCl^+ . To check for isotopic variation in the charge exchange experiment, the other even isotopes are cooled as well (section 5.5).

2.4.2 The Barium ion

The barium ion is another attractive candidate for ion-based quantum computation [Die09]. In fact, barium was the first ion to be trapped in isolation [NHT80]. The barium ion has a single valence electron with a simple enough energy level structure, shown in figure 2.18, to allow laser cooling schemes with two visible

wavelength lasers (493 nm and 650 nm). Visible wavelengths are convenient for alignment and couple well into fiber optics. Both wavelengths for laser cooling the Ba⁺ ion can be generated with semiconductor laser diode technology, using ECDLs 2.2.4. The 493 nm laser light is also often produced using second-harmonic generation laser systems and can be stabilized to molecular tellurium absorption features [RBO98].

The energy level structure is a special type, known as a *lambda structure*. The lambda structure, in general, consists of three energy levels $|1\rangle, |2\rangle, |3\rangle$ where $E_1 < E_3 < E_2$ and $|2\rangle$ is dipole coupled to the other two levels. The resulting energy level diagram is shaped like the Greek letter λ . The lambda structure causes an interesting quantum effect, coherent population trapping (CPT), when addressed with two near resonance with both possible dipole transitions [GWS78]. Coherent population trapping when both lasers are detuned by the same frequency from the upper transition $|2\rangle$, driving the system into a superposition of the two lower energy states that is decoupled from the laser fields. This effect is useful for some applications such as frequency metrology [Van05] and magnetometry [NGN98]. In the context of the MOTion trap, CPT makes the laser induced fluorescence lineshape more complex, and the presence of the coherence null can make laser cooling less efficient. The coherent effects make measuring the temperature by lineshape spectroscopy difficult because they are a source of broadening. In contrast to Yb⁺, a full quantum rate equation treatment is necessary to calculate the average excited state population.

During experiments in the MOTion trap, ¹³⁸Ba⁺ is used as a translational sympathetic coolant for BaCl⁺ because it has the highest natural abundance, no hyperfine structure, and it can be produced by photodissociation of the BaCl⁺ molecular ion or by laser ablation of the BaCl₂ pressed target.

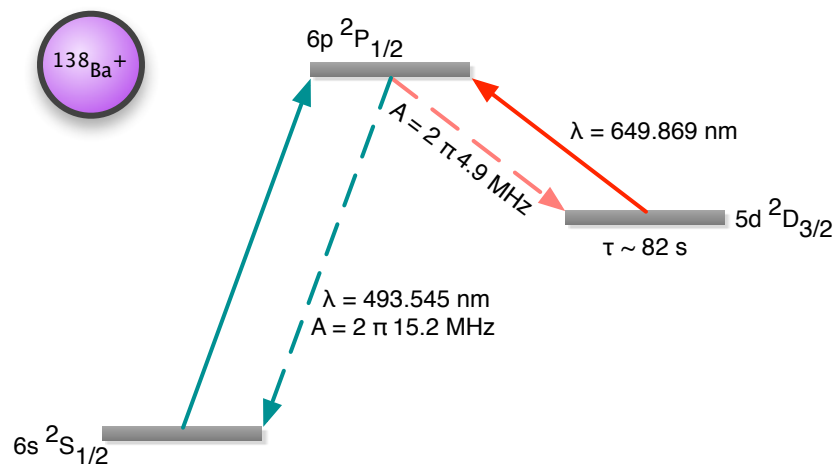


Figure 2.18: Energy level diagram for $^{138}\text{Ba}^+$. Solid lines show the optical transitions driven by the cooling (blue) and repumping (red) lasers. Dashed lines indicate spontaneous dipole decay channels. The wavelengths and decay rates are indicated with values from the NIST Atomic Spectra Database. Known metastable state lifetimes and decay branching ratios are indicated.

CHAPTER 3

Calcium Magneto-Optical Trap

The development of the magneto-optical trapping technique is the subject of a Nobel Prize in Physics [RPC87, Chu98] and the technique has become workhorse in the field, providing a source of cold atoms as a starting point for a wide range of experiments from matter-wave interferometry [AEK12], next-generation optical clocks [LZC08, LNP05, LLB09]. A calcium magneto-optical trap is the center of experiments in cold chemistry and the production of ground-state molecular ions detailed in this dissertation.

This chapter describes the design, construction, and characterization of the ^{40}Ca MOT. This includes a brief description of the basic physics and general diagnostic techniques of MOTs, as well as information specific to ^{40}Ca , and the MOTion system in particular, such as the required laser systems and atomic source. The description emphasizes features of the MOT relevant to operation as part of the hybrid trap system.

3.1 MOT Basics

A MOT has four ingredients:

- Atoms with an appropriate cycling transition, section 3.2
- Laser light, red-detuned from the cycling transition, section 3.3.1

- A magnetic field gradient 3.4
- An appropriately matched set of light polarization, section 3.3.3

When properly engineered, these ingredients form a magneto-optical trap, schematically shown in Fig. 3.1. Three pairs of counter-propagating, red-detuned beams generate an optical molasses via a velocity-dependent, dissipative force. By tuning the laser frequency below the cooling resonance, the radiation force is velocity selective because atoms moving in the direction opposite the incoming beam are Doppler shifted towards resonance. This velocity-dependent force is sufficient to cool the atoms, creating a so-called optical molasses as kinetic energy escapes the system via spontaneous emission. However, without the final two ingredients, there is no spatial restoring force. To realize the spatial trapping force, a position-dependent force is generated by the combination of a magnetic field gradient, see section 3.4, and the appropriate circular-polarized light chosen, see section 3.3.3, to selectively drive, via the Zeeman shift ($\Delta E = \mu_B g_J m_J B$), atoms back towards the magnetic field null. ^{40}Ca has a Landé g-factor $g_J = \frac{3}{2} + \frac{S(S+1)-L(L+1)}{2J(J+1)}$ of 1 and the Bohr magneton is $\sim 1.4\text{MHz/Gauss}$.

With all the ingredients in place, the scattering force for one beam of intensity I is a function of the laser's detuning δ as well as the position and velocity of the atom is

$$F(\delta, v, z) = \frac{\Gamma \hbar k}{2} \frac{\frac{I}{I_0}}{1 + \frac{I}{I_0} + \left(\frac{2(\delta - \vec{k} \cdot \vec{v} - \mu_B g_J m_J B(z))}{\Gamma} \right)^2}. \quad (3.1)$$

Γ is the decay rate of the transition, and I_0 is the saturation intensity which can be calculated by $I_0 = \frac{\pi h c A_{\text{total}}}{3\lambda^3}$, where $A_{\text{total}} = \frac{1}{\tau}$ is the total Einstein A coefficient for the transition. For the case of ^{40}Ca , relevant parameters can be found in table 3.1 of section 3.2. According to equation 3.1 a red-detuned laser ($\delta < 0$) maximizes the force when the velocity is anti-parallel to the beam

$(\vec{k} \cdot \vec{v} < 0)$. Given the correct circular polarization of the light field (discussed in section 3.3.3), the force also selectively drives into the high-field seeking Zeeman sublevel ($m_J < 0$), pushing the atoms towards the magnetic null $|\vec{B}| = 0$. Figure 3.1 demonstrates this trapping condition schematically.

3.2 Properties of ^{40}Ca

^{40}Ca is an alkaline-earth element, with two valence electrons. The recommended value for the static polarizability of Ca is $4\pi\epsilon_0 157a_0^3$ [PD06]. The relevant energy level structure states are depicted in figure 3.2. It has a relatively strong ($\Gamma_n = 2\pi 34.2$ MHz) cooling transition from its ground electronic configuration $^1\text{S}_0$ to the excited state $^1\text{P}_1$. The primary loss channel when cycling this transition is optical pumping into the meta-stable $^1\text{D}_2$ level. The branching into the meta-stable state is rare, about one in a hundred thousand cycles [BGM89], so the MOT can be operated with a maximum lifetime of approximately 20 ms without the use a laser to drive the atoms out of this D state. As described in section 3.3.2, this optical leak out of the cooling cycle can be patched with a 672 nm repump laser. The repump drives the atom into a higher-lying $^1\text{P}_1$ energy level, which couples back into the ground state. However, optical loss still occurs, since the meta-stable $^1\text{D}_2$ state has a lifetime of approximate 2 ms via spontaneous decay into two lower-lying triplet P states ($^3\text{P}_2$ and $^3\text{P}_1$). If an atom decays into the $^3\text{P}_1$ level, there is a chance of recapture due to a relatively short lifetime of ~ 0.5 ms via decay back to the ground state [DKW93]. Decay into the J=2 level leads to trap loss since it is dipole forbidden from decaying back into the ground state and has a lifetime of ~ 118 minutes [KS90].

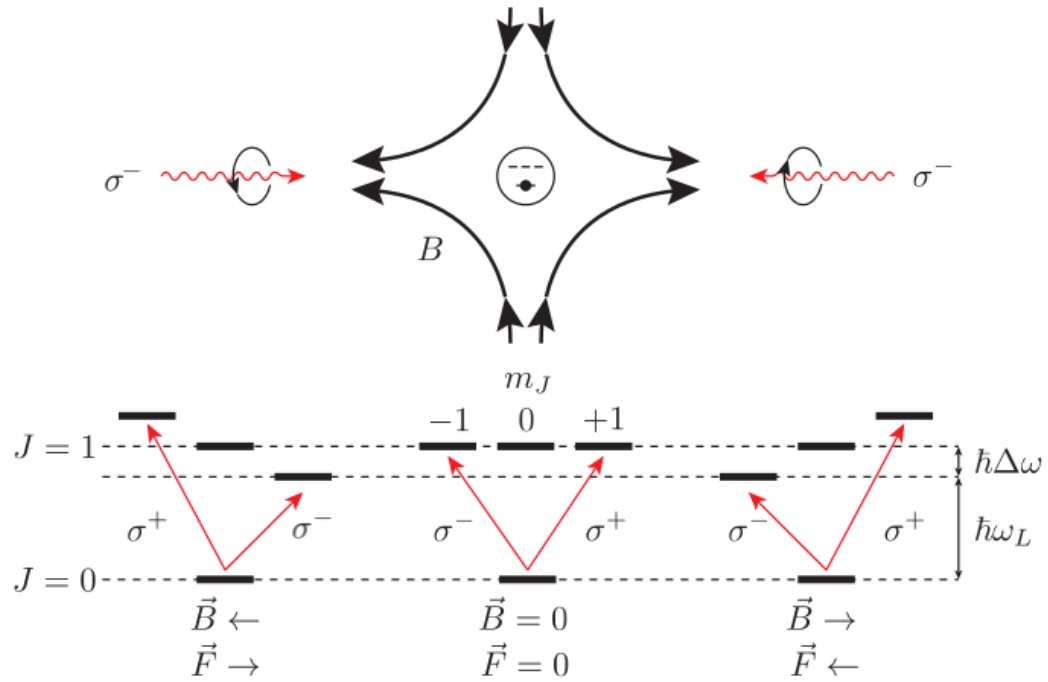


Figure 3.1: Magneto-optical trap schematic. This diagram shows the basic physical mechanisms behind the spatial trapping in a MOT. Pairs of counter-propagating, red-detuned beams generate an optical molasses via a velocity-dependent, dissipative force. The springlike position-dependent, dissipative force is generated by the combination of a magnetic field gradient and red-detuned, circular-polarized light chosen to selectively drive atoms towards the magnetic field null. Note that the magnetic field defines the quantization axis for the atom, thus the correct polarization for all directions is σ^{-1} to selectively drive the high-field seeking sublevel. The handedness of the light, however, is different for the anti-Helmholtz axis and radial directions.

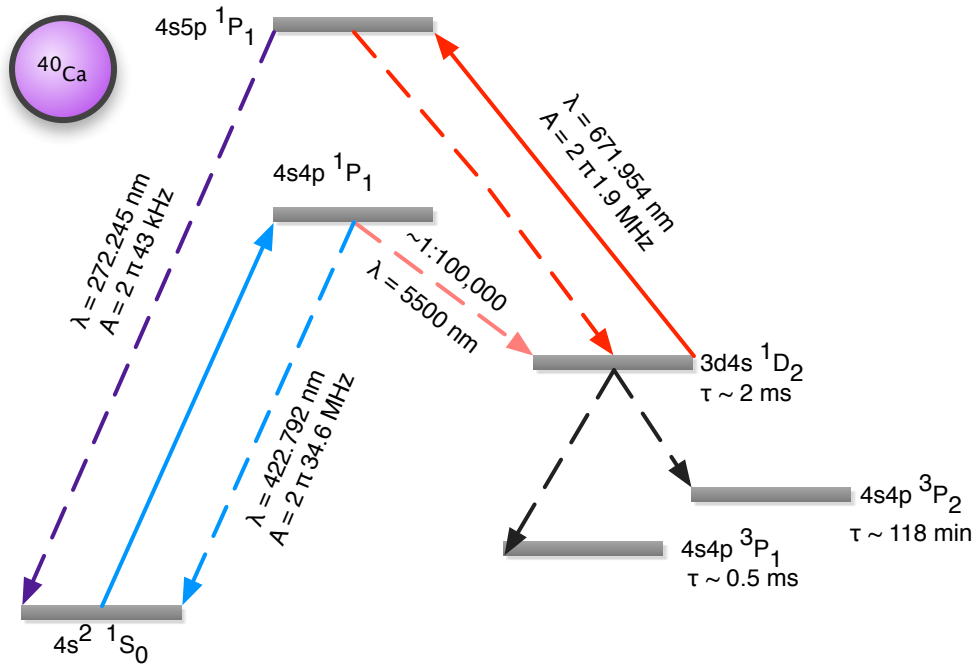


Figure 3.2: Relevant energy levels in ^{40}Ca . The solid lines are the transitions driven by the cooling and repumping lasers. The dashed lines spontaneous decay pathways. Approximate wavelengths and branching ratios are noted.

	^{40}Ca	^{87}Rb
Natural Abundance	97%	23%
Cooling transition	4^1S_0 - 4^1P_1	$5^2\text{S}_{1/2}$ - $5^2\text{P}_{3/2}$
A coefficient [s $^{-1}$]	2.18×10^8	3.81×10^7
λ [nm]	422.792	780.241
I_0 [$\frac{\text{mW}}{\text{cm}^2}$]	61	1.67

Table 3.1: Atomic parameters for laser cooling and trapping ^{40}Ca . The parameters for ^{87}Rb are shown for comparison.

3.2.1 The Calcium source

For nearly the last two decades alkali metal dispensers have been used as simple sources of alkali vapor for laser cooling and trapping experiments [WFG95]. These sources are typically composed of an alkali chromate compound, *e.g.* Rb_2CrO_4 , and a metallic alloy (typically 84%Zr and 16%Al) used as a reducing agent. When the dispenser is sufficiently heated, usually by running a current through a metal wire contained inside of the dispenser, the metal alloy reduces the alkali metal chromate producing alkali metal vapor. Since the reducing reaction usually only takes places at elevated temperatures (800 K - 1100 K), the velocity distribution of the alkali metal vapor emitted by the dispenser is usually not amenable to direct capture by a magneto-optical trap (MOT). For this reason alkali metal dispensers have only been employed for Na [MRM08], Rb [RWN01], and Cs [PCS04] where the vapor pressure is sufficient that the alkali vapor can thermalize with the chamber walls before capture by the MOT. (One notable exception is the work of [MPM05] where Rb atoms were likely captured without cooling by the chamber walls.) Likewise, because atoms with low room temperature vapor pressure, *e.g.* Li, alkaline earth metals, Yb, etc., are very unlikely to survive a collision with the vacuum chamber wall, metal dispensers have not been employed as sources for laser cooling and trapping experiments with these atoms.

Recently chromate free metal dispensers have become commercially available. Instead of chromate compounds, these dispensers use intermetallic compounds with non-toxic metals, like indium, gallium, tin or bismuth and can be made using both alkali and alkaline earth metals. By resistive heating, ultra-pure alkali or alkaline earth metal is released without the associated hydrogen, at temperatures comparable to the chromate compound sources but without their typical hydrogen, water and carbon dioxide contaminants. Although the low vapor pressure

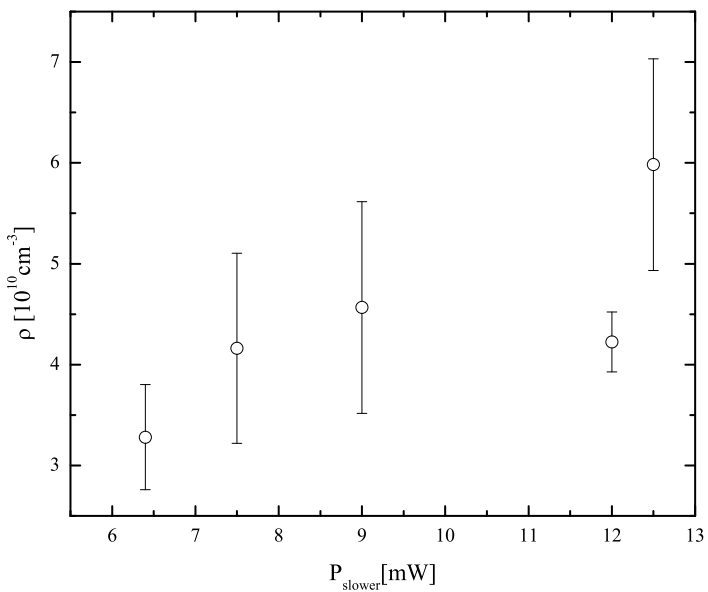


Figure 3.3: Ca MOT density as a function of decelerator beam power at trap beam detuning $\delta_T = -0.6 \Gamma$ and trap beam power $P_T = 24 \text{ mW}$.

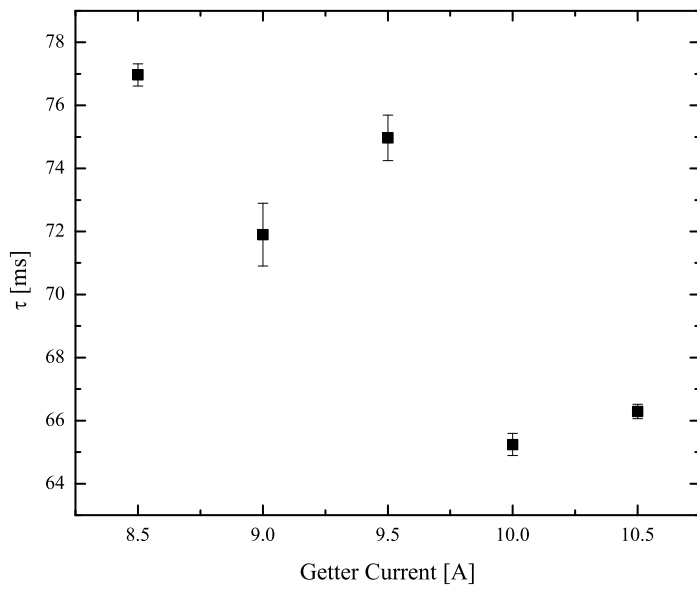


Figure 3.4: Ca MOT lifetime versus getter source current. The small decrease in lifetime is likely due to increased background collision with thermal Ca from the dispenser.

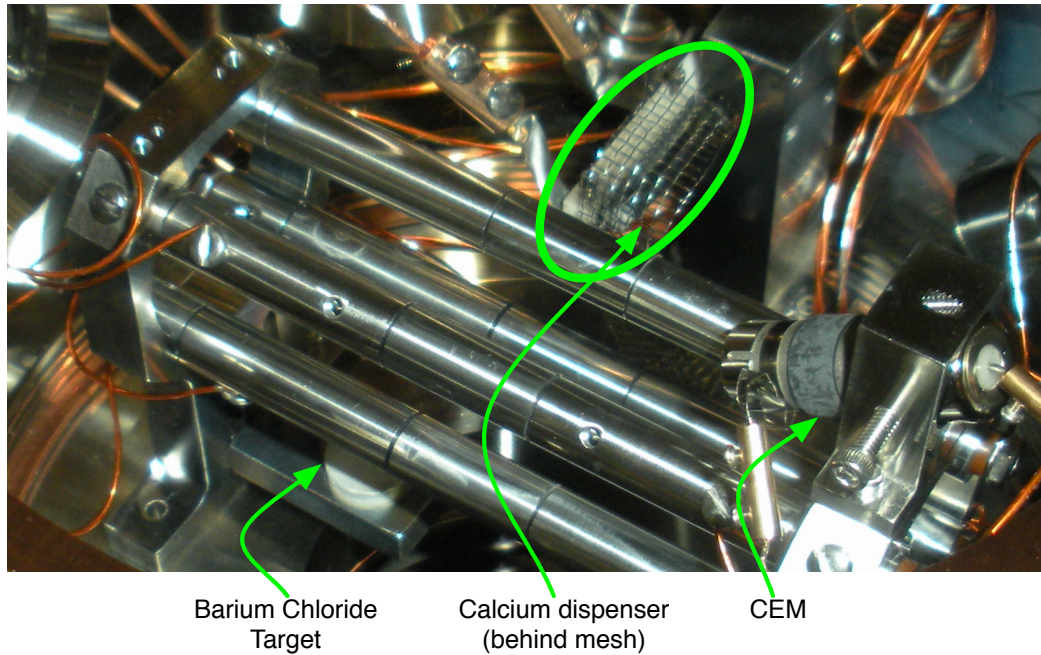


Figure 3.5: Photograph of the experiment chamber during decommission of version 1.5. Version 1.5 is identical to the original MOTion trap, except for a segmented ion trap rod. The calcium dispenser is mounted from a piece of Macor ceramic and shielded by a piece of stainless steel mesh. The BaCl₂ ablation target and channeltron are both also visible.

of the alkaline earth metals precludes the use of wall collisions as a mechanism of reducing the temperature of the emitted atoms, a single, red-detuned laser beam (overlapped with the deceleration beam as indicated in figure 3.3), provides sufficient deceleration to load from such a dispenser and trapped in a MOT with densities up to a few $\times 10^{10}$ cm⁻³. The dispenser (Alva-tec Alva-source tube getter, type C), is mounted 1.37 inch from the trap center as shown in figure 3.5.

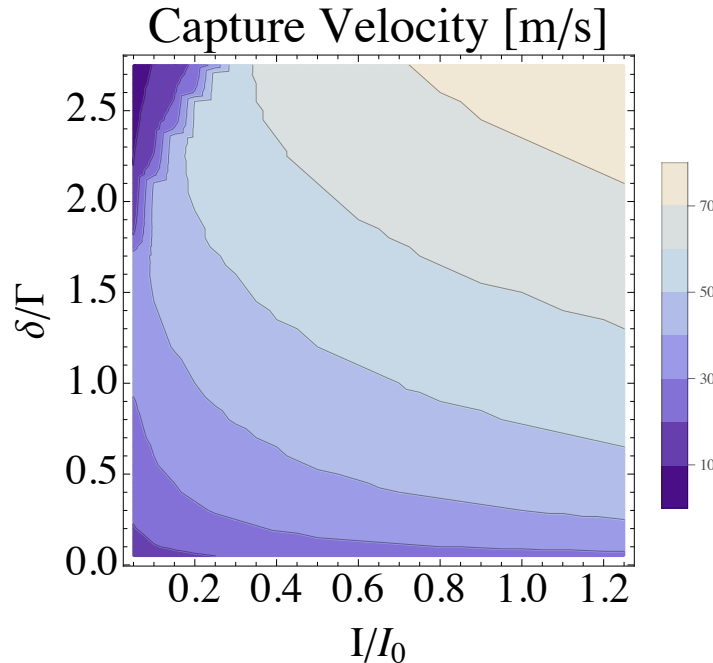


Figure 3.6: Capture velocity for a 1D MOT with 1 cm trapping region as a function of trap beam detuning and saturation intensity.

3.2.1.1 Loading dynamics

Due to having a relatively low vapor pressure calcium will not survive collisions with the vacuum chamber wall, and thus hot atoms flying out of the dispenser will not thermalize to room temperature. According to manufacturer measurements, the getter source temperature is roughly 600°C. To characterize the loading dynamics from the hot Ca source, the MOT's capture efficiency can be estimated by calculating the capture velocity using equation 3.1. For this calculation, the capture velocity is defined to be the maximum velocity that is brought to a stop before exiting the trapping region, taken to be 1 cm long in this 1D model. The maximum capture velocity as a function of relevant trapping parameters in the 1D model with two equally intense beams is shown in figure 3.6.

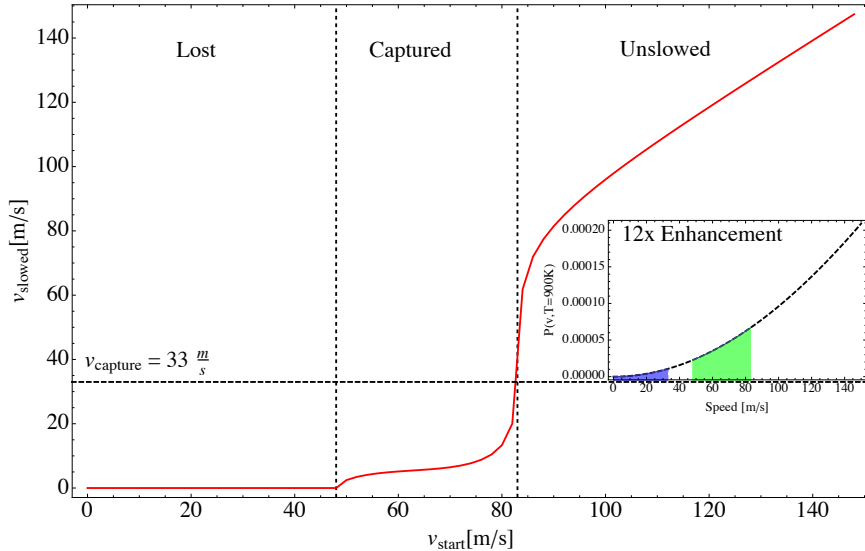


Figure 3.7: The estimated effect of the slowing beam under typical operating conditions. The calculation predicts an improvement in trap yield of over an order of magnitude compared to the getter source with no optical slowing, or over a factor of two better than a theoretical room temperature Ca background source.

For typical trapping parameters in this system ($\delta \approx \frac{2}{3}\Gamma$, $\frac{I}{I_0} \approx 0.1$ and 1 cm beams), an estimate for the capture velocity is found to be $\approx 33\text{m/s}$. An integration of equation 3.1 simulates the effect of slowing hot atoms coming towards the trap center under typical conditions ($\delta_{\text{slower}} \approx 2\Gamma$, $\frac{I}{I_0} \approx 0.2$). The simulations yields an estimate for the fraction of atoms reaching the trap volume traveling at or below the capture velocity which shows an improvement over the un-slaved distribution of more than an order of magnitude. In fact, the fraction of the velocity distribution that can be captured via the optically slowed 900 K source is over twice that of an un-slaved room temperature velocity distribution.

3.3 The Ca MOT Laser System

3.3.1 423 nm 4^1S_0 - 5^1P_1 Laser

The cooling laser for the MOT in this work is a Toptica TA-SHG-110 commercial laser system. This laser system consists of a master diode laser at 845 nm in the DL-Pro configuration which generates about 25 mW of light, which is then amplified in a tapered amplifier up to roughly 400 mW. The amplified light is then coupled into a bow-tie optical cavity, with a BBO (BaB_2O_4) crystal at the laser waist, for second harmonic generation of the desired 423 nm light. The Toptica system ultimately provides about 100 mW of light near the ^{40}Ca cooling transition wavelength. The frequency is directly locked near the transition as described in section 3.3.1.1.

3.3.1.1 Ca saturated absorption frequency reference

The saturated absorption Doppler free spectroscopy technique relies on the non-linear absorption by atoms in resonance with both the intense pump beam and the less intense probe beam. When the saturation occurs, the probe beam propagates through the medium with less attenuation, leading to a peak in the photodiode Doppler-broadened signal. In this experiment, the pump beam is detuned $\delta \sim 180$ MHz from the probe beam by two passes through an acousto-optic modulator (AOM) (Gooch and Housego R35085-3). The non-linear absorption occurs for a particular velocity class with the Doppler shift necessary to be in resonance

with both beams:

$$\begin{aligned}\omega_0 \mp kv &= \omega_L = \omega_{\text{probe}} \\ \omega_0 \pm kv &= \omega_L + \delta = \omega_{\text{pump}} \\ \omega_{\text{pump}} = \omega_{\text{probe}} &\Rightarrow \omega_L = \omega_0 - \frac{\delta}{2}\end{aligned}\tag{3.2}$$

where ω_0 is the ${}^{40}\text{Ca}$ 4^1S_0 - 5^1P_1 transition frequency, k is the wavenumber of the laser, kv is the Doppler shift, δ is the total frequency shift due to the double-pass AOM, and ω_L is the laser's output frequency. The solution of equation 3.2 for ω_L results in the laser output frequency when the saturation condition is met. As shown in the schematic layout of figure 3.8, the spectroscopy is performed with a weak probe beam that passes through a vapor cell while the saturation is produced by a pump beam that is detuned from the probe beam by a double-passed AOM in the cat's eye configuration. The laser power not used in the saturation locking arm is sent to the experiment via three AOMs (two custom modulators from Brimrose Corp. and another R35085-3) which can be switched via RF switches (Mini Circuits ZASW-2-50DR+). The modulators are driven by simple voltage controlled oscillators (VCOs) from Mini Circuits (POS-100+, POS-200+) and amplifiers (ZHL-1A, ZHL-03-5WF).

3.3.1.2 The Ca vapor cell

The design of the Ca vapor cell is based on earlier designs for Yb [Lof01]. The cell is sketched in figure 3.9. The design is a custom full nipple mini-conflat (mini-CF), 17" long, with a standard mini-CF cross at one end to allow the attachment of a valve (Lesker SL0037MCCF) and a pressure gauge (Varian 531). On both ends of the nipple are mini-CF quartz silica standard vacuum windows (Lesker VPZL-133PQ). The central region is heated by clamshell ceramic heaters (Mellen Co. 11C-1303-TC) set on firebrick ring spacers. The temperature is monitored by a

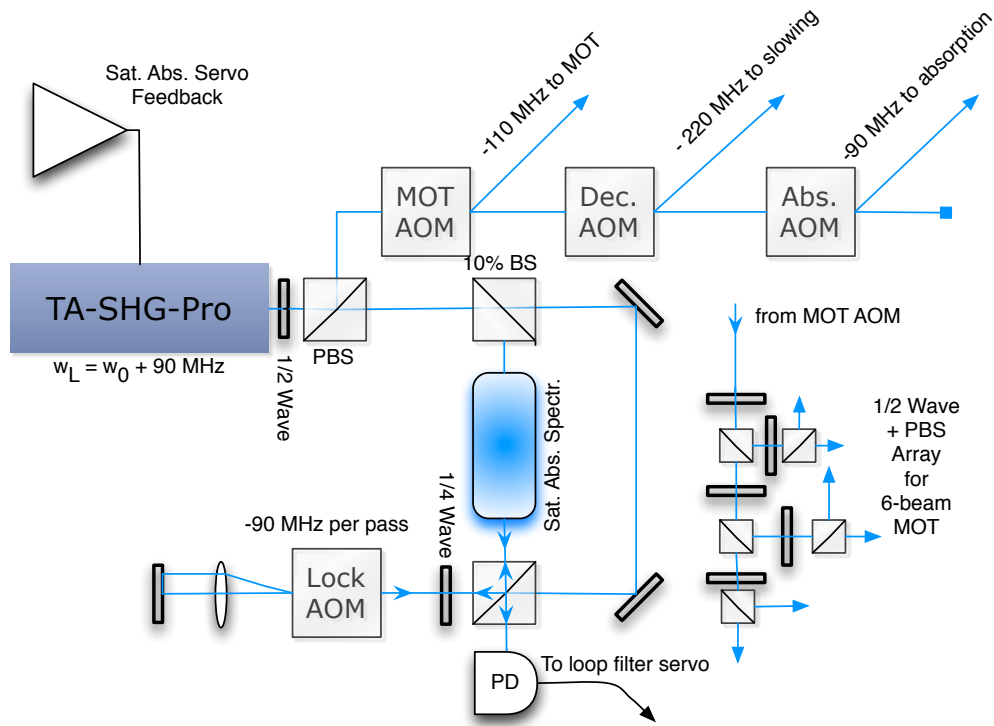


Figure 3.8: Schematic of the optical system for the 423 nm laser system. A small fraction ($\sim 10\%$) of the light travels through the saturation absorption lock. After two frequency shifts via a double-passed AOM, the light saturates the transition inside the vapor cell. The overlapped probe beam signal ultimately servo locks the laser to the blue of the ^{40}Ca cooling transition resonance. The experimental arm employs three AOMs for fast switching and to shift to the appropriate frequencies for trapping, slowing, and absorption imaging.

type K thermocouple (Omega XC-20-K-12) affixed by high temperature ceramic paste (Cotronics Durabond 954) to the center of the cell directly beneath the clamshell heater. The heater feedback current is controlled by a solid-state relay (SVDA-3V25) controlled by an Omega temperature controller (CN9600 series). The nipple areas near the windows are kept cold by water-cooled brass blocks attached to both ends of the nipple. The cold areas act as a capture region so hot Ca vapor is less likely to condense on the windows. After evacuation, an Argon leak sets the room temperature pressure to roughly 50 mTorr so the Ca is stopped from ballistically reaching the windows. The cell is fixed to the optics table by simple machined aluminum "v-blocks" designed to hold the optical axis 5" from the table. The temperature of the heated region was held at 300°C. The vapor pressure of Ca is modeled by

$$\log_{10} P = 5 + a + \frac{b}{T} + (c \log_{10} T) [\text{mPa}] \quad (3.3)$$

where the temperature is measured in Kelvin and $a = 10.127$, $b = -9517$, and $c = -1.403$ [Lid95].

3.3.1.3 The 423 nm laser lock error signal

The error signal to lock the laser frequency to the saturated absorption resonance is generated by a standard modulation spectroscopy loop filter. The filter circuit used in this work is shown in the schematic of figure 3.10. The AOM shifting the pump beam frequency is modulated at 100 kHz, and the photodetector signal from the probe beam is mixed with the modulation reference to ultimately produce an error signal. The output of the mixer is amplified and filtered through a low-pass filter to extract the DC error signal component, which is fed back to the laser via the Toptica's proportional-integral-derivative (PID) unit.

Standard literature on tweaking of a PID servo suggests an approach to op-

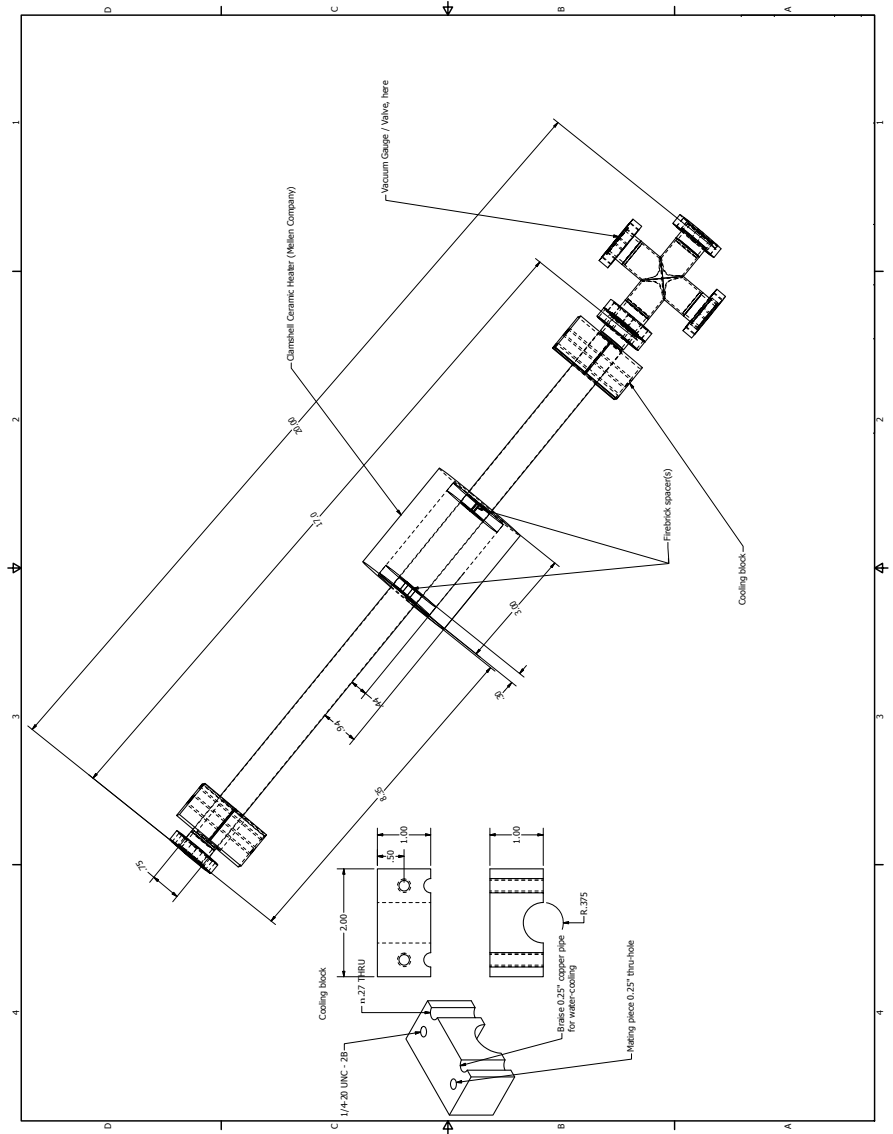


Figure 3.9: CAD drawing of the vapor cell and brass cooling blocks.

timizing the feedback. The suggestion is to start with minimal P,I, and D then slowly increase P until locking with oscillations are observed. Next, the suggestion is to increase I to reduce the oscillations. This standard suggestion does not work very well for the Toptica PID module, perhaps because the module is designed primarily for feeding back to the piezo on a doubling cavity. Instead, a protocol of first turning up the integral gain instead of the proportional gain works best. Another explanation could be that the particular module in the 423 nm laser has mislabeled trim pots.

A typical resulting error signal is shown in panel a of figure 3.11. Figure 3.11 also shows a wavemeter measurement of the laser frequency while the feedback is on, with a loss of the laser lock a few minutes into the trace as an example of the relative short term stability.

The expected size and shape of the servo signal can be calculated by determining the DC component of a hypothetical mixer output voltage V_{mix} , whose inputs are a reference modulation V_{ref} and a detuning modulated Lorentzian lineshape. The mixer output, assuming perfect efficiency,

$$V_{\text{mix}} = \frac{V_L V_{\text{ref}} \cos(\Omega t + \phi)}{1 + 4 \left(\frac{\delta + \Delta\omega \cos(\Omega t)}{\Gamma} \right)^2}, \quad (3.4)$$

is the product of the two input signals. Ω is the frequency of the detuning modulation and δ is the laser's detuning the line center. $\Delta\omega$ is the frequency modulation depth. V_L and V_{ref} are the sizes of the lineshape and modulation reference signals, respectively. Next, the output of the mixer is filtered with a perfect low-pass filter such that only the DC portion of the signal remains. This can be seen by assuming the deviation from the resonance and the frequency modulation depth is small compared to the linewidth and Taylor expanding equation 3.4 for small

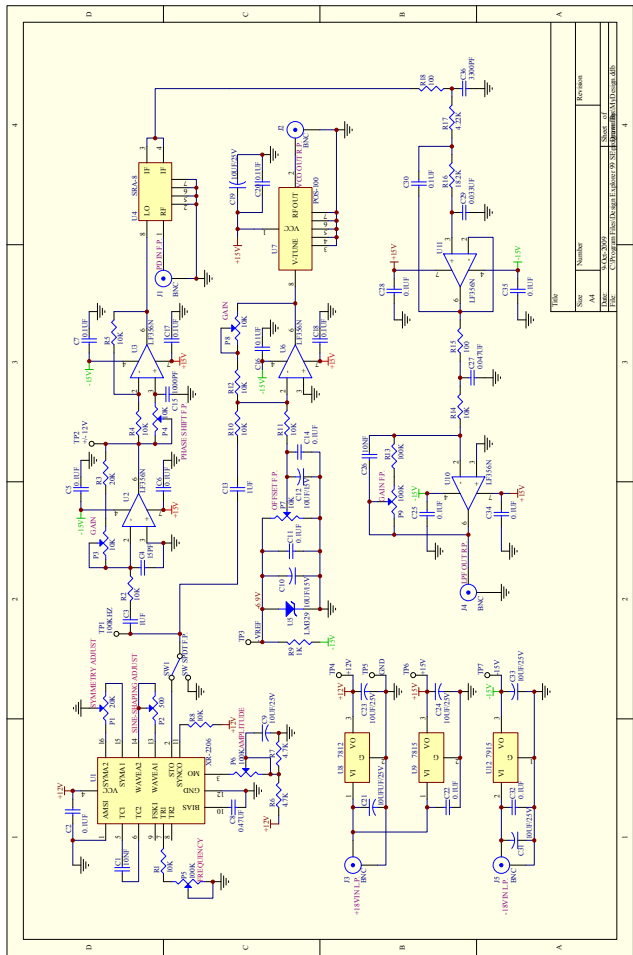


Figure 3.10: Circuit diagram for the loop filter used in for the Ca laser systems frequency lock. This servo sufficed for all the work presented in this dissertation, but could be improved with a differential photodetector and a high-pass (or band-pass) before the photodetector signal goes into the mixer.

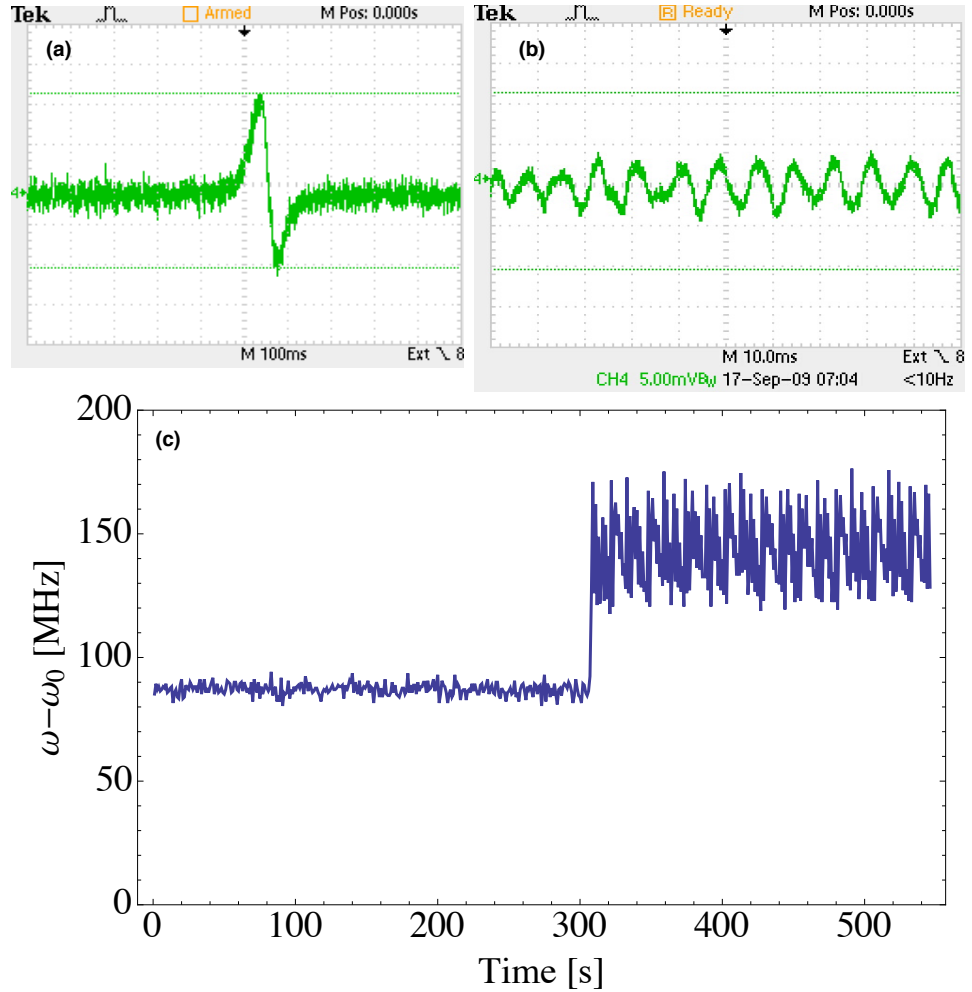


Figure 3.11: This figure shows examples of the error signal output, as fed back into the Toptica PZT servo. Panel (a) shows the error output as the laser frequency is swept over the lock point. Panel (b) shows a closed loop measurement of the error signal, with the PID parameters set to allow oscillation. Panel (c) is a measurement of the lock stability using the wavemeter, showing both the locked and unlocked laser stability since the laser comes unlocked roughly half way through the measurement.

deviations,

$$V(\delta)_{\text{DC}} \approx \frac{4V_L V_{\text{ref}} \Delta\omega \delta \cos(\phi)}{\Gamma^2 \left(1 + 4 \left(\frac{\delta}{\Gamma}\right)^2\right)^2}. \quad (3.5)$$

Equation 3.5 can be evaluated at its peak laser detuning value $\delta = \frac{\sqrt{3}}{6}\Gamma$ to find the expected value for an error signal generated with lossless electronics. This laser detuning value is also useful to estimate the width of the error signal feature compared to the linewidth of the saturated absorption feature Γ .

3.3.2 The 672 nm repump

The ${}^1\text{D}_2$ electronic state provides an additional pathway for the spontaneous decay from the ${}^1\text{P}_1$ state. The branching ratio for decay into the meta-stable ${}^1\text{D}_2$ has been measured to be approximately one in 10^5 [BGM89]. This sets a limit to the MOT lifetime without a repump laser of approximately 20 ms. This optical loss from the cooling cycle can be prevented, however, because there exists a higher excited state, the $5\text{p}{}^1\text{P}_1$ that is accessible with a 672 nm ECDL. The design of the ECDL is described in section 2.2.4. The laser is frequency stabilized to a transition in molecular iodine that is near the desired frequency.

The particular absorption line is the R69(2-5) transition in molecular iodine. A fraction of the beam is sent through a 10 cm iodine vapor cell (Triad Technology TT-I2-100-V-x) heated by fiber-glass resistive heating tape (Omega FGS-051-020). The bulk of the vapor cell is held at 200°C, while the cold finger is pressed against a water-cooled ($T \sim 17^\circ\text{C}$) heatsink. Under these conditions, there is sufficient population on the ($v''=5$, $J''=69$) energy level and a maximum absorption of about 50% is observed at $14881.989 \text{ cm}^{-1}$. The derivative of the absorption signal is obtained by adding a small dither (amplitude = 50 mV, frequency = 50 kHz) to the laser current and sending the photodiode signal through

a lock-in amplifier. By adjusting the DC offset of the error signal servo, the servo locks the laser near the repump transition. Similar to the results in other Ca MOT systems [MBG04] [OBF99], the lifetime of calcium atoms is increased by a factor of five as a result of the 672 nm laser.

The branching ratio out of the 5^1P_1 level favors return to the 1D_2 state, so the repump cycle needs roughly 100 cycles before the spontaneous decay back to the ground state occurs. During typical operation, shown in figure 2.1, the repump beam passes through the front chamber window overlapped with the deceleration beam. One might suspect there is efficiency to be won by overlapping the repump laser with all the trapping beams, but trying this configuration yields no measurable improvement over the much simpler typical arrangement.

3.3.3 MOT laser polarization

To make the MOT's position-dependent trapping force, the light polarization must be such that the red-detuned light selectively pushes the atoms back to the magnetic field zero. The low-field seeking Zeeman sublevel is resonant with the appropriate trap beam as the atom travels away from the trap center. For an atomic transition with a positive magnetic g-factor, like ^{40}Ca , this requires the $\Delta m = -1$ polarization selection, i.e. σ^- . For each axis of the trap, the beam polarization must correspond to a σ^- transition, e.g. the beam whose $\vec{k} \parallel \vec{z}$ must be correctly polarized, given the direction of the magnetic field $\vec{B}(z < 0)$, to selectively push atoms that have strayed towards $-\vec{z}$. However, in the laboratory, there is no $\sigma^{+,-}$ “switch” on the laser controller and light from external cavity diode lasers is typically linearly polarized.

In the laboratory, the knob that controls laser polarization is the orientation of a waveplate. The quarter waveplate allows the experimenter to choose the hand-

edness of the light, i.e. by correctly orienting the waveplate axis with respect to incoming linear-polarized light, one can choose either right-handed circular (RHC) or left-handed circular (LHC) polarization. In the context of this dissertation, since there exist contradictory conventions, the handedness of the light is determined with respect to the \vec{k} -vector. More concretely, right(left)-handed circular light's polarization is rotating in the direction of the right(left) hand's fingers when the thumb is pointed along \vec{k} . Traditionally, the slow-axis of a waveplate is marked and a convenient rule of thumb for linear-polarized light's response to passing through a waveplate is that the polarization will move towards the slow-axis. For example if a quarter waveplate whose slow-axis is initially parallel to the polarization axis of some incoming linear-polarized light is then rotated $-(+)$ 45° with respect to the incoming light's \vec{k} -vector (i.e. (counter-)clockwise if looking towards the direction of \vec{k}), the resulting light will be RHC(LHC). The only problem left is the translation from *handedness* to the $\sigma^{+,-}$ basis in the lab.

For an atom with a positive magnetic g-factor, there is a simple classical picture that is useful for translating handedness into the $\sigma^{+,-}$. The classical picture is that the rotating electric field vector induces a polarization ($\vec{p} \parallel \vec{E}$) in the atom due to movement of the electron only (imagine the nucleus is too heavy to respond). The translation of the light's handedness is then found by considering whether the magnetic moment formed by this induced classical current loop is aligned to the relevant magnetic field. For example, LHC light with $\vec{k} \parallel \vec{B}$ drives the σ^- transition. The other possible handedness-field combinations are tabulated in table 3.3.3.

Handedness	$\vec{k} \cdot \vec{B} > 0$	$\vec{k} \cdot \vec{B} < 0$
Left-handed Circular (LHC)	$\sigma^-, \Delta m = -1$	$\sigma^+, \Delta m = +1$
Right-handed Circular (RHC)	$\sigma^+, \Delta m = +1$	$\sigma^-, \Delta m = -1$

Table 3.2: The mapping between the handedness of the circular-polarized light, as measured via thumb along the \vec{k} , and the $\sigma^{+,-}$ selection basis for a given relation between the magnetic field and light propagation direction.

3.4 The Magnetic Field Gradient

Since the magnetic field gradient required for efficient trapping scales with the natural linewidth and magnetic moment of the cooling transition [LSW92], the design goal of the magnetic field coils was to deliver an axial field gradient of up to about $60 \frac{G}{cm}$. The anti-Helmholtz coils were designed by using the exact equations for the axial and radial components of the magnetic field due to a current loop of radius R at a distance L above the origin [BEM87],

$$B_\rho = \frac{I_c \mu_0}{2\pi\rho} \frac{z - L}{\sqrt{(z - L)^2 + (R + \rho)^2}} \times \\ \left(\frac{-(z - L)^2 + R^2 - \rho^2}{(z - L)^2 + (\rho - R)^2} E \left(\frac{4R\rho}{(z - L)^2 + (R + \rho)^2} \right) - K \left(\frac{4R\rho}{(z - L)^2 + (R + \rho)^2} \right) \right) \\ B_z = \frac{I_c \mu_0}{2\pi} \frac{\left(K \left(\frac{4R\rho}{(z - L)^2 + (R + \rho)^2} \right) + \frac{-(z - L)^2 + R^2 - \rho^2}{(z - L)^2 + (\rho - R)^2} E \left(\frac{4R\rho}{(z - L)^2 + (R + \rho)^2} \right) \right)}{\sqrt{(z - L)^2 + (\rho + R)^2}}, \quad (3.6)$$

which are in cylindrical coordinates and in terms of the elliptic integrals $E(m) = \int_0^{\pi/2} \sqrt{1 - m^2 \sin^2 \theta} d\theta$, and $K(m) = \int_0^{\pi/2} \frac{d\theta}{\sqrt{1 - m \sin^2 \theta}}$.

The experimental chamber for the ^{40}Ca MOT is relatively large to accommodate the ion trap so the field coil currents required to achieve the desired gradient are fairly high ($> 100\text{A}$). High current generates a significant resistive heat load. To handle the heat generated by the magnet, the magnet coils are made from

copper tubing that can be water cooled. The coils are wound with square copper tubing from Small Tube Products, Inc. with Kapton coating performed by S&W Wire Co. The square tubing is approximately 4.4 mm to a side, with a circular bore of \sim 1 mm radius, and each coil is wrapped 100 (10 by 10) times around a phenolic spool shown in drawing 3.13. The coils have an inner conductor radius of 6.1 cm and are positioned in the anti-Helmholtz configuration, with each coil (conductor) 8.6 cm from the vacuum chamber geometric center. According to equations 3.6 the design field gradient per unit current is $0.527 \frac{G}{cmA}$ along the anti-Helmholtz axis at the field zero, and $0.2635 \frac{G}{cmA}$ along the radial direction outward from the trap center. A measurement of the field directly with a hall probe agrees within better than 1% of the theoretical prediction for the coil geometry, shown in figure 3.14.

Chilled water ($T \sim 17^\circ C$) is pumped through the coils, in parallel, dropping from about 270 PSI to the house return pressure of about 40 PSI. At typical operation of about 12 V for 120 A through each coil, the temperature measured via thermocouple adhered to the outer portion of the coil equilibrates to roughly $60^\circ C$. To avoid runaway heating in the event of a cooling failure, the temperature reading on each coil is used to interlock the HP-6683A power supply via the alarm function on an Omega CN9600 temperature controller. If a temperature above the setpoint is detected, the alarm function shorts the interlock pins on the HP-6683A power supply, disabling it.

The setup for the MOT coils is shown schematically in figure 3.12. The power supply is run in constant current mode at 120 A for all the experiments described in this dissertation. The feedback servo shown in figure 3.12 is one of the ways to control the position of the MOT in the experimental chamber by siphoning off current from the bottom coil, thus changing slightly the position of

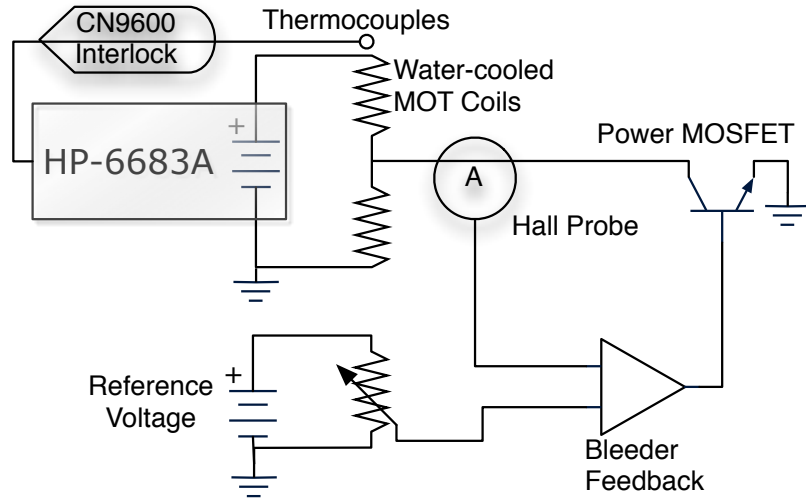


Figure 3.12: Schematic diagram of the MOT coils with temperature interlock and bleeder shim circuit for axial control of the magnetic field zero.

the magnetic field zero, via an alternate path to ground using a power MOSFET (STE180NE10). The bleeder feedback servo is a one-sided operational amplifier (MCP601), with the the voltage reading from a hall probe (Tamura S22P series) at the (-) terminal and a trimmed down voltage reading from a D cell battery at the (+). The feedback occurs over a $100\text{ k}\Omega$ resistor in series with a $0.1\text{ }\mu\text{F}$ capacitor, all in parallel $1\text{ }\mu\text{F}$ capacitor. The servo outputs to the gate of the MOSFET to hold the Hall probe current reading of the siphoned current to a chosen reference value. The power balance in the horizontal beam pairs controls the MOT position in the off-axis direction, as described in section 3.5.1.

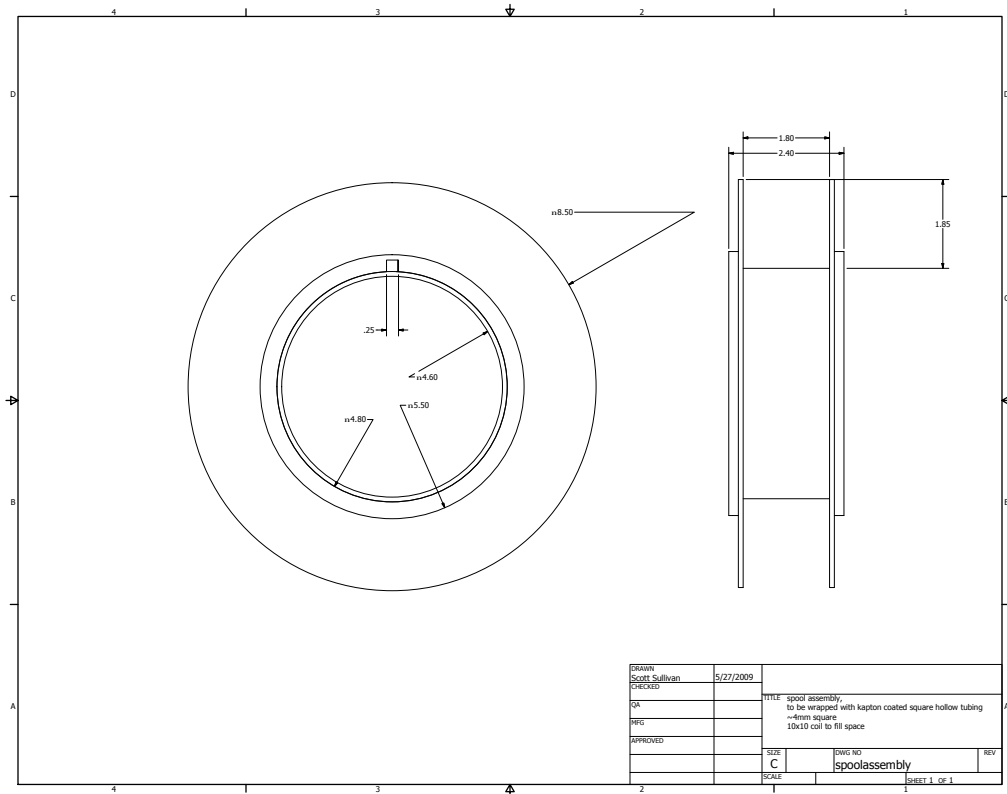


Figure 3.13: MOT coil spool assembly. All dimensions are inches. Each spool was constructed from 3 pieces of machinable garolite (phenolic) epoxied together. The conducting tubes are wound in 10 layers of 10 windings, sealed with stycast adhesive at each layer.

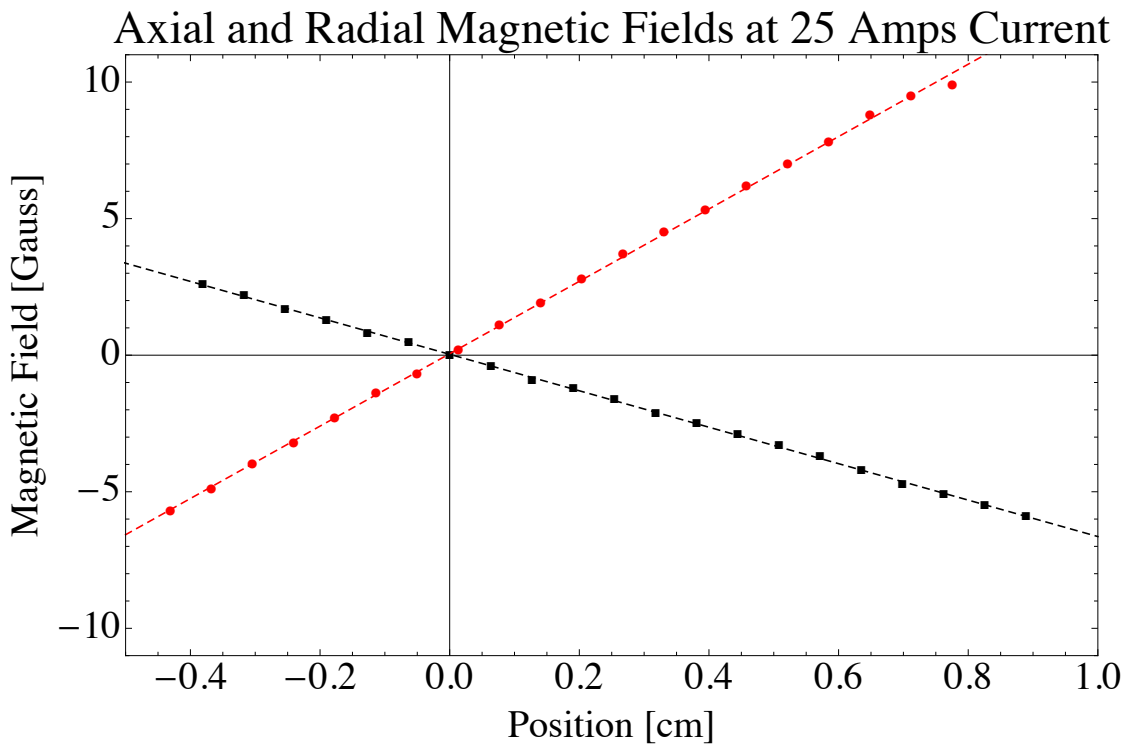


Figure 3.14: Measurement of the magnetic field at the trap center with 25 A running through the anti-Helmholtz coils. In red circles, the field along the axis of the anti-Helmholtz configuration. In black squares, the field along the radial direction. With each measurement, a dashed line shows the best fit. The gradient along the axis is found to be $0.532(3) \frac{G}{cmA}$. And the gradient along the radial direction is found to be $0.267(1) \frac{G}{cmA}$.

3.5 MOT Characterization and Control Techniques

3.5.1 Controlling the position of the MOT

For use in the MOTion trap, the Ca atoms must be spatially overlapped with the co-trapped ions. Thus, extra degrees of experimental control are implemented to control and verify the position of the trapped cloud of atoms. By using the series of half-waveplates and polarizing beam splitters shown in figure 3.8, the intensity in each of the six trapping beams are independently tunable. The equilibrium point of the trap scattering force for a given trap axis can be shifted slightly by deliberately tuning the relative intensity of a counter-propagating beam pair. According to equation 3.1, for typical trapping parameters in this system, a 20% variation in relative intensity results in a shift in the equilibrium position of approximately one e^{-1} cloud waist ($\approx 0.5\text{mm}$) for a radial trapping beam pair.

3.5.2 Determining MOT density

The density of the MOT is most reliably measured by absorption imaging. By measuring the fraction of light absorbed by a beam passing through the center of the atomic cloud and the size of the cloud, the density is computed using the Beer-Lambert law. For example, the fraction of light transmitted through the center axis of an atomic cloud with a Gaussian density distribution $\rho_0 e^{-\frac{z^2}{w^2}}$ is given in equation 3.7.

$$T = e^{-\rho_0 \sigma \sqrt{\pi} w} \quad (3.7)$$

For a symmetric atomic cloud, like the ^{40}Ca cloud which is well approximated by a spherical Gaussian, the result in equation 3.7 is accurate for measuring the

density via a single absorption image. The only parameters in equation 3.7 not directly measured by the absorption image are the peak density of the atomic cloud, ρ_0 , and the resonant absorption cross-section σ given by

$$\sigma = \frac{2J' + 1}{2J + 1} \frac{\lambda^2}{2\pi} \frac{\Gamma_n}{\Delta} \quad (3.8)$$

where the transition is $J' \leftarrow J$, with natural linewidth Γ_n and total linewidth Δ . Thus by acquiring an absorption image and numerically fitting for or calculating the RMS size and depth of the absorption feature, one can apply equation 3.7 to calculate the density, using the pixel size to set the length scale.

Absorption imaging can be implemented by shining an on-resonance ‘absorption’ laser beam through the cloud onto a CCD. In the MOTion trap experiments, an Andor Luca-R EMCCD camera, with a 75 mm lens in the $2f - 2f$ configuration, allows for simultaneous fluorescence imaging as well as 1-to-1 absorption imaging. A LabVIEW program controls the timing of the camera exposure and the firing of the absorption beam in sequence with release of the MOT trapping beams. For best results, the timing should be such that the absorption beam passes through the cloud within a few lifetimes of the cooling transition following the extinction of the trap beams. This timing allows the atoms time to decay into the ground state while avoiding unwanted fluorescence and ballistic expansion, two sources of systematic error in the density measurement. The intensity of the absorption beam should be set to be high enough to almost saturate the pixels of the camera in as brief a time as possible when no atoms are present. Short, intense pulses, with correspondingly short camera exposure, maximize the ratio of signal to noise for each shot. In addition, the shorter pulse sequence minimizes systematic errors due to ballistic expansion of the atomic cloud during an exposure.

3.5.2.1 Model independent fluorescence imaging for density

For most experiments in the MOTion trap, the MOT needs to stay on during the measurement. Absorption imaging requires turning the trap beams off, so it is convenient to be able to relate density to fluorescence without needing to turn off the MOT at the moment of measurement. In principle, an accurate model for the excited state fraction predicts the fluorescence to atom number or density. However, accurately modeling the excited state fraction in a Ca MOT is not a simple problem and it requires very good calibration of the imaging system photon sensitivity. A simple workaround involves measuring the density-to-fluorescence calibration before and after the measurement period, in a model independent way. Sequential fluorescence and absorption observations yield data to solve for the unknown constant in

$$\rho = C \frac{A}{w^3}, \quad (3.9)$$

where A is the measured brightness amplitude on the EMCCD image, and w is the measured geometric mean MOT waist. C is then a constant that accounts for the camera sensitivity and the atomic ensemble average excitation fraction. The latter quantity is a difficult to quantify function of laser intensities, overlap, and detuning. For a typical experiment's 10 ms exposure, with no bandpass filter, C is found to be roughly 10^{12} per digital number. Of course this number should be measured before and after any density dependent experiment.

3.5.3 Determining atom-ion co-location in 3D

3.5.3.1 Determining relative position

The pointing of each camera in the lab frame is known. Let the vectors \hat{z}_1, \hat{z}_2 represent these vectors pointing from the geometric center of the vacuum chamber

towards the face of each CCD. These vectors define the orientation of the image plane of both cameras. Two basis vectors, per camera, are then needed to describe the position of an image in the image plane. Let these vectors be \hat{x}_i and \hat{y}_i for $i = 1, 2$. While the choice of basis vectors in the image plane is arbitrary, \hat{y}_i is taken to be maximally oriented along the vertical direction as the angle of \hat{z}_i allows. Thus, after determining \hat{z}_i and \hat{y}_i , \hat{x}_i is determined as $\hat{x}_i = \hat{y}_i \times \hat{z}_i$.

Relative positions in the lab frame can then be determined by taking the center of a mutually observed object (in this case the ion cloud or MOT) to be the lab frame origin, and then taking information of the relative displacement from both cameras as follows:

$$\vec{r}' = \Delta x_1 \hat{x}_1 + \Delta y_1 \hat{y}_1 + ((\Delta x_2 \hat{x}_2 + \Delta y_2 \hat{y}_2) \cdot \hat{z}_1) \hat{z}_1, \quad (3.10)$$

where the information from the second camera $(\Delta x_2, \Delta y_2)$ is being used to get information missing along the first camera's pointing axis, by taking the projection of the displacements observed by the second camera along the \hat{z}_1 axis. For example, take the simple system where camera 1 points towards the lab frame negative x-axis and camera 2 points towards the lab frame negative z-axis. If this camera system images a pair of objects (one and two) located at lab coordinates $(0, 0, 0)$ and $(1, 2, 3)$, camera 1 will see object 2 at position $(\Delta x_1, \Delta y_1) = (3, 2)$ in its image plane. Camera 2 images the object to $(\Delta x_2, \Delta y_2) = (-1, 2)$. In this simple example, $\hat{z}_1 = \hat{x}$, $\hat{x}_1 = \hat{z}$, $\hat{y}_1 = \hat{y}_2 = \hat{y}$, $\hat{x}_2 = -\hat{x}$ and $\hat{z}_2 = \hat{z}$ so equation 3.10 yields $3\hat{z} + 2\hat{y} + ((-1(-\hat{x}) + 2\hat{y}) \cdot \hat{x})\hat{x}$ or $\vec{r}' = (1, 2, 3)$.

	\hat{x}	\hat{y}	\hat{z}
Camera #1	$\{a, 0, b\}$	$\{-c, d, -e\}$	$\{f, g, h\}$
Camera #2	$\{-a, 0, b\}$	$\{c, d, e\}$	$\{f, g, -h\}$

Table 3.3: Unit vectors in the lab-frame for the camera system imaging planes, for the camera configuration shown in schematic 2.1. The ion trap axis is along the laboratory frame z-axis. The ion pump is off in the negative x direction, which leaves the direction anti-parallel to gravity as the y direction in figure 2.1. The constants are $a = 0.38256$, $b = -0.92393$, $c = 0.2547$, $d = 0.96125$, $e = 0.1055$, $f = 0.888125$, $g = 0.27569$, $h = 0.36774$.

3.5.3.2 Determining effective overlap - the overlap factor

Experiments involving the hybrid atom-ion trap system require overlapping the atomic cloud with the ion cloud. In all, but one, of the experiments in this work it is important to be able to *quantify* the degree of interaction between the ions and the neutral atoms. The overlap factor quantifies the effective density of cold atoms experienced by a typical ion in the trap volume. The overlap quantity varies between zero, when the ion cloud is very far from the MOT center, and unity, when a single ion is tightly confined to the region of highest density of atoms. The overlap factor is calculated by a volume integral over the product of the ion density distribution with the MOT density distribution:

$$\phi = \int d^3\vec{r} \hat{\rho}_{\text{Ca}}(\vec{r}) \bar{\rho}_I(\vec{r}), \quad (3.11)$$

where $\hat{\rho}_{\text{Ca}}(\vec{r})$ is peak normalized (i.e. $\hat{\rho}_{\text{Ca}}(\vec{r}_{MOT}) = 1$) and $\bar{\rho}_I(\vec{r})$ is integral normalized ($\int d^3\vec{r} \bar{\rho}_I(\vec{r}) = 1$).

The Ca MOT has a roughly spherical gaussian density distribution, while the ion cloud has an ellipsoidal (cigar-shaped) density distribution due to the

anisotropic harmonic pseudo-potential. The trapping potential is anisotropic because during typical operation the DC confinement potential along the axis is shallower. A weaker axial trap depth minimizes micromotion by allowing ions to live closer to the RF zero. Due to the angle of the cameras and the departure from spherical symmetry in the case of the ion cloud spatial distribution, the apparent width of the ion cloud in the axial direction is reduced by a factor of 1.11 and this must be corrected for during the integration of equation 3.11. The calculation is thus the integral of a spherical gaussian with an ellipsoidal gaussian distribution and can be numerically evaluated by measuring the cloud widths and relative positions via dual camera fluorescence imaging. However, due to disparate levels of brightness, the MOT and the ions cannot be simultaneously imaged with the existing image filtering system. Therefore, the effective density is quantified from dataset to dataset by imaging only the MOT and relate it to images taken of ion clouds measured at the start of the data acquisition. The assumption is the ion cloud's center, aspect ratio (axial waist to radial waist, typically about 2.5), density, the overlap determining parameters, are constant over the course of a few hours. This assumption holds true according to images taken at various times throughout a day at fixed trapping parameters.

3.5.4 Determining MOT temperature

The MOT's temperature can be determined by measuring the cloud's rate of ballistic expansion upon extinction of the trapping beams. This is experimentally realized by taking a series of absorption images, as described in section 3.5.2, at different time delays after release of the trap. Due to the rate of ballistic expansion, the camera cannot image fast enough and the MOT must be remade between each shot of the time-series.

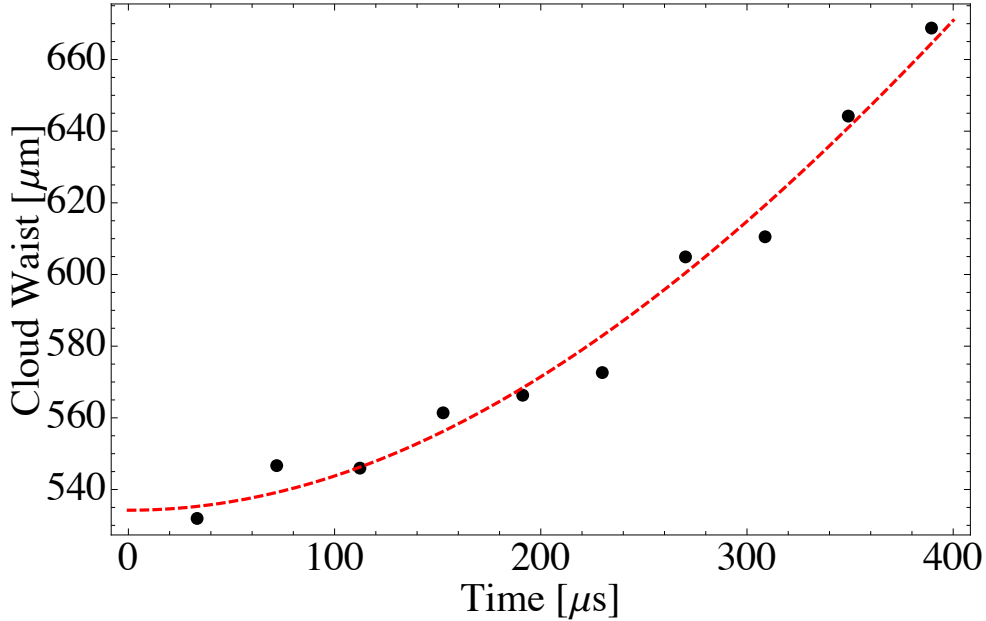


Figure 3.15: A measurement of the temperature of the ^{40}Ca MOT. A fit to equation 3.12 corresponding to $2.5(1)$ mK is shown in dashed red. Error bars are hidden by the plot markers.

The probability distribution $P(x)$ of finding an atom along a given dimension x after releasing the trap will evolve in time according to an average $\langle P(x \rightarrow x + vt) \rangle_v$ over the initial ballistic velocity distribution at temperature T , i.e.

$$\begin{aligned}
 P(x, t > 0) &\propto \int dv e^{-\left(\frac{x+vt}{w(t=0)}\right)^2} e^{-\frac{mv^2}{2k_b T}} \\
 P(x, t > 0) &\propto e^{-\left(\frac{x^2}{w(t=0)^2 + \frac{2k_b T t^2}{m}}\right)} \\
 \Rightarrow w(t > 0) &= \sqrt{w(t=0)^2 + \frac{2k_b T t^2}{m}}.
 \end{aligned} \tag{3.12}$$

The resulting expression for the cloud's e^{-1} , w , waist under free expansion can be used to with a time-series absorption measurement, like shown in figure 3.15, to measure the MOT temperature.

CHAPTER 4

Trapping molecular ions formed via photo-associative ionization of ultracold atoms

4.1 Summary

The formation of $^{40}\text{Ca}_2^+$ molecular ions is observed in a hybrid ^{40}Ca magneto-optical and ion trap system. The molecular ion formation process is determined to be photo-associative ionization of ultracold ^{40}Ca atoms. A lower bound for the two-body rate constant is found to be $\bar{\beta} \geq 2 \pm 1 \times 10^{-15} \text{ cm}^3 \text{ Hz}$. *Ab initio* molecular potential curves are calculated for the neutral Ca_2 and ionic Ca_2^+ molecules and used in a model that identifies the photo-associative ionization pathway. As this technique does not require a separate photo-association laser, it could find use as a simple, robust method for producing ultracold molecular ions.

4.2 Introduction and Motivation

The low-energy internal structure of a diatomic molecule, *e.g.* the electric dipole moment and vibrational, rotational, and Ω -doublet levels, presents a host of opportunities for advances in quantum simulation, precision measurement, cold chemistry, and quantum information [KSF09]. As such, the last decade has witnessed an enormous effort towards producing ultracold molecules in well-defined

rovibrational states. It appears that this goal is in now within reach, as several groups have reported production of ultracold molecular samples in the rovibrational ground state [NOM08, SRD10, DMH10]; in the case of the KRb work the sample is near quantum degeneracy [NOM08].

To date, most work has focused on neutral molecules, however, a sample of ultracold molecular ions presents interesting possibilities. While the Coulomb interaction overwhelms the electric dipole interaction between polar molecular ions in most cases, many of the goals of cold molecule physics can be accomplished with molecular ions, with the added benefit of a simple, reliable trapping. Indeed, a cold sample of molecular ions allows the study of cold chemistry [WB08], which not only has important implications for understanding the formation of interstellar clouds [Smi92], but for investigation, and possible control, of reactive collisions in the quantum regime [HTS06]; identification of carriers of the diffuse interstellar bands [RGM10]; precision measurement of molecular transitions, which can be used to sensitively measure parity violating effects [GQS04], as well as to constrain the possible variation of the fundamental constants [FK07]; and the implementation of a scalable quantum computation architecture [ADD06]. For these reasons, several groups have recently initiated work to produce samples of ultracold molecular ions [SRD10, SjS10, TWW10, Hud09]. In Refs. [SRD10, SjS10, TWW10], the molecular ion external degrees of freedom are sympathetically cooled with laser cooled atomic ions to ultracold temperatures. However, the long range ion-ion interaction does not couple to the molecular ion internal degrees of freedom and therefore the rovibrational temperature is unmodified by the sympathetic cooling process. To overcome this limitation, optical pumping schemes [SRD10, SjS10] and state selective photo-ionization of neutral molecules [TWW10] have been used to produce molecular ions in the lowest few rotational states. More generally, it should also be possible to use ultracold *neutral* atoms, in a magneto-optical trap

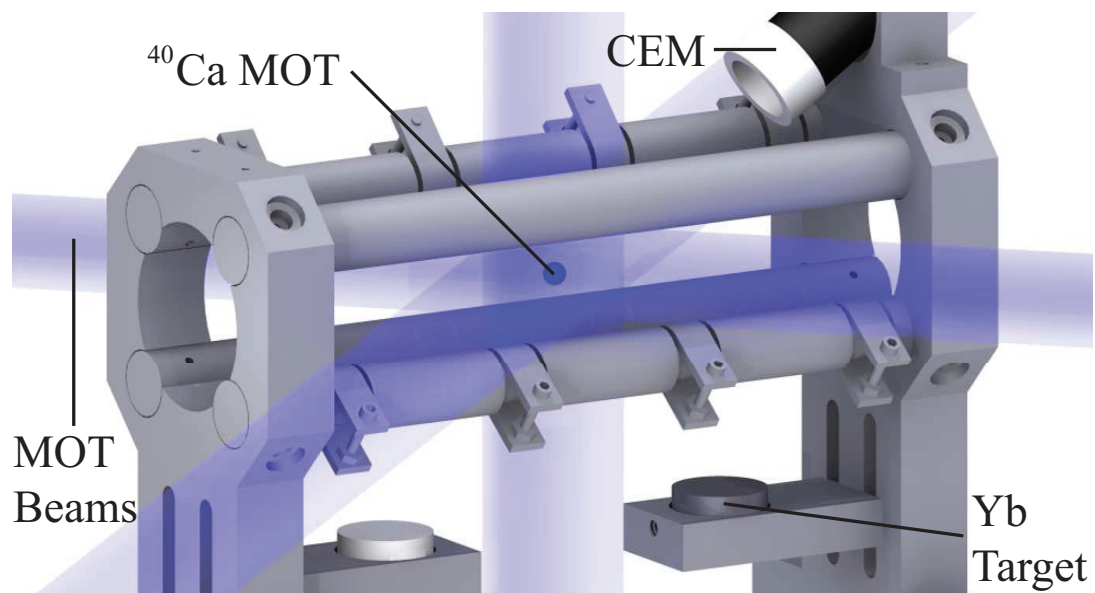


Figure 4.1: MOTion trap: A ^{40}Ca magneto-optical trap is constructed inside a linear quadrupole ion trap. Below the trap are two ablation targets used to load calibration ions. The channel electron multiplier (CEM) is mounted above the trap.

(MOT), to simultaneously sympathetically cool both the internal and external degrees of freedom of molecular ions [Hud09].

In addition to these methods, it is possible to create state-selected ultracold molecular ions directly from their atomic constituents through photo-associative ionization (PAI), a two-body process where colliding neutral atoms are photo-excited into either a bound molecular ion or auto-ionizing molecular potential. This chapter reports the formation of $^{40}\text{Ca}_2^+$ molecular ions via PAI in a hybrid system composed of a ^{40}Ca MOT constructed inside of a radio-frequency linear ion trap. The production of the dimer ion is quantified using standard ion trap mass spectrometry techniques [Maj09, DFM05] available for use in the MOTion trap system. The following section describes the apparatus used and present measurements characterizing the molecular ion production rate. Section 4.4.1 presents results from *ab initio* calculations of the $^{40}\text{Ca}_2^+$ molecular ion structure and a description of the most-likely mechanism of molecular ion production.

4.3 Experiment

The MOTion trap system used in this work is that proposed in Ref. [Hud09] and is shown in figure 4.1. As aforementioned, it is a hybrid system with a ^{40}Ca MOT constructed inside an linear quadrupole ion trap (LQT), designed to explore collisions between ultracold atoms and trapped molecular ions. Briefly, cold ^{40}Ca atoms are collected in a MOT by decelerating a beam of atoms produced by a Ca getter. The $\lambda = 422.6$ nm laser system , used to produce the MOT cooling and deceleration beams, is referenced to the $4^1\text{P}_1 \leftarrow 4^1\text{S}_0$ transition ($\Gamma = 2\pi \times 34.6$ MHz) using a saturated absorption signal from a Ca vapor cell. The trapping (deceleration) laser beams typically have detuning and total intensity of $-\Gamma$ (-3Γ) and 23 (31) mW/cm², respectively. The 671.7 nm $5^1\text{P}_1 \leftarrow 3^1\text{D}_2$

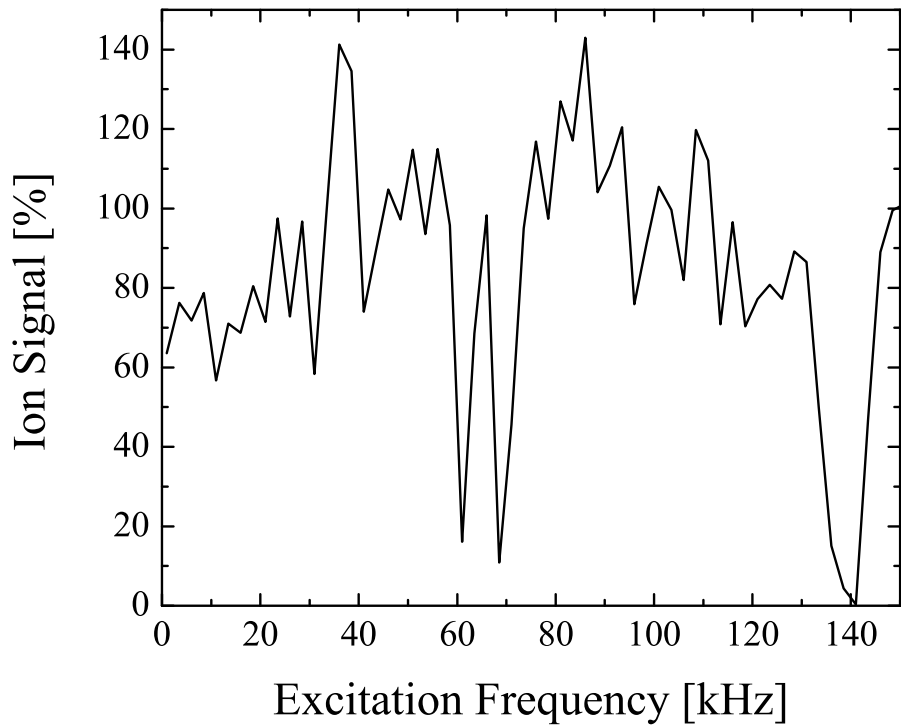


Figure 4.2: Results of a excitation spectrum measurement performed at trapping parameters where the stability parameter (q) for $m = 80$ amu is 0.5, thus unstable for $m = 40$ amu. The observed loss near 70 kHz is within 10% of the predicted secular frequency for $m = 80$ amu. The split peak feature is likely due to trap imperfections (asymmetric endcap placement, machining, imperfect quadrupole ratio,etc).

Ca repump transition is driven with a laser system referenced to the R69(2-5) molecular Iodine transition. The typical MOT atom number, density and temperature are measured by absorption and fluorescence imaging and found to be $N_{\text{Ca}} = 1.0 \pm 0.1 \times 10^7$ atoms, $\rho_{\text{Ca}} = 3.9 \pm 0.5 \times 10^{10} \text{ cm}^{-3}$, and $T_{\text{Ca}} = 4 \pm 1 \text{ mK}$, respectively. The LQT, which has a field radius of $r_o = 11.2 \text{ mm}$, is designed with three axial trapping regions to facilitate the shuttling of ions into and out of the center region for interaction with the MOT. The number of trapped ions is detected by grounding the trap electrodes, allowing the ions to escape and be detected by a channel electron multiplier (CEM) ion detector located near the trap center. The absolute ion number measured by the CEM is calibrated by comparing CEM detection to laser-induced fluorescence rates with $^{174}\text{Yb}^+$ ions loaded via laser ablation (see figure 4.1). Only the central trapping region is operated in this experiment since the MOT acts as the source of all ions observed in this work.

When the MOTion system is operated without deliberately loading ions into the LQT, an accumulation of ions is observed due to the presence of the MOT. Interestingly, though there exist several pathways to the formation of $^{40}\text{Ca}^+$ – *e.g.* photo-ionization of an atom in the 5^1P_1 state, populated via the repumping channel, by a 423 nm photon – an ion signal is still observed even when the LQT is operated such that the charge-to-mass ratio of $^{40}\text{Ca}^+$ is not trapped. The mass of this anomalous ion species is measured by the LQT stability parameters, a comparison of the relative CEM time-of-flight to that of ions with known mass (*e.g.* $^{40}\text{Ca}^+$) and, ultimately, by resonant excitation of the secular trap frequency as shown in figure 4.2. The excitation measurement is performed by applying a small (relative to the trapping potentials) oscillating voltage to one of the trap electrodes, inducing substantial heating that results in trap loss when the excitation is resonant with the mass-specific secular frequency of the ion motion.

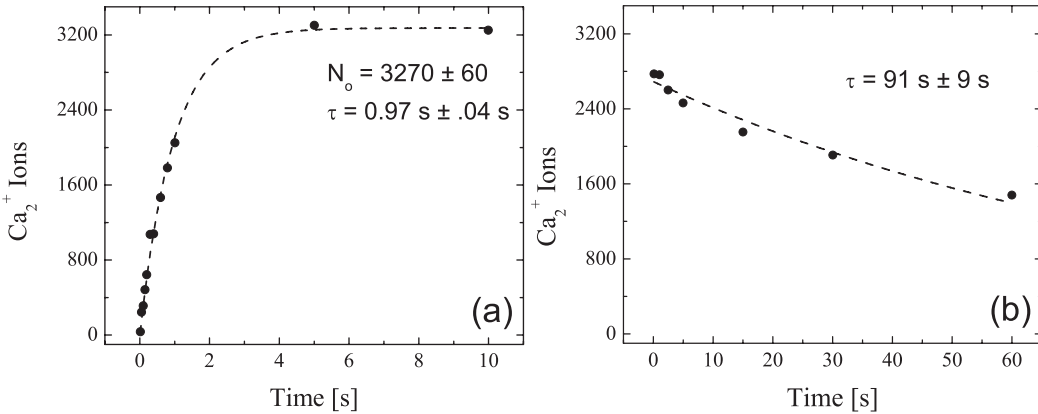


Figure 4.3: Measurement of the ion number as a function of loading time is shown in panel (a). In panel (b), trap lifetime is measured by loading the trap to saturation and stopping production for a fixed amount of time before detection. Characteristic times are found by exponential fits (dashed lines).

The excitation spectrum is taken by allowing the LQT to load with ions for 1.9 s at each excitation frequency before detection with the CEM. The ratio of detected ion number with excitation to detected ion number without excitation is plotted in figure 4.2. The trap loss resonance (and its second harmonic) is observed as the reduction in ion signal near $70 \pm 2 \text{ kHz}$ ($140 \pm 5 \text{ kHz}$), in good agreement with the predicted radial secular frequency of 76 kHz for 80 amu, confirming the production of $^{40}\text{Ca}_2^+$ molecular ions. The splitting of the fundamental peak is likely due to trap imperfections such as the asymmetric axial electrode placement, asymmetric voltages, and imperfect machining.

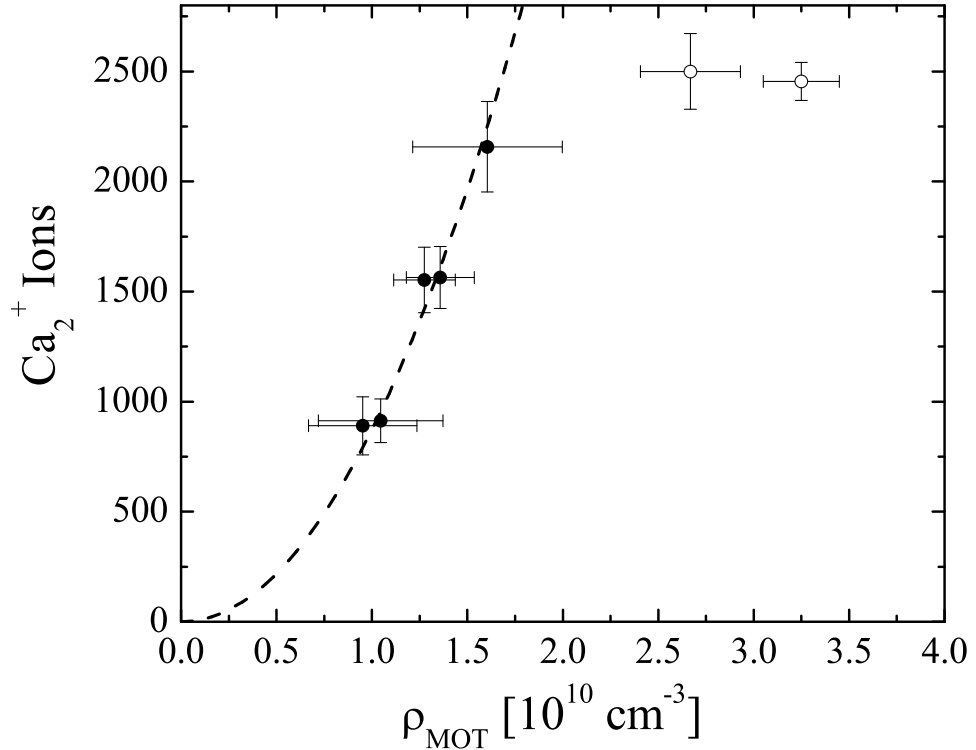


Figure 4.4: Ion number measured as a function of the MOT density determined by absorption imaging. A quadratic trend (with a best fit shown to guide the eye) is observed until trap saturation occurs at higher densities (shown in the points with open circles).

4.4 Results

The LQT loading dynamics of the dimer ion are shown in figure 4.3. For the data in figure 4.3(a), the LQT is first loaded with dimer ions from the MOT for a designated amount of time after which the ion number is measured by the CEM. As seen in this panel, the characteristic loading time is found to be ~ 1 s and typically leads to an equilibrium ion number of ~ 3000 ions. To measure the competing effects which lead to this equilibrium, a measurement of the trap lifetime is performed as shown in figure 4.3(b). For this measurement, the trap is loaded to saturation and then switch off the MOT at $t = 0$ s, stopping molecular ion production. After a designated time, the ion number is detected via the CEM. The molecular ion lifetime in the trap is ~ 90 s. Since inelastic processes between the ions and neutral atoms¹ do not change the number of dimer ions in the trap, the loading time is not affected by the presence of the MOT. Therefore, the large disparity between the molecular ion lifetime and its characteristic loading time shows that the equilibrium condition is not set by competition between the natural trap loss mechanisms and the dimer ion production rate. Instead, equilibrium is determined by a maximum ion density that sets a trap capacity at which the Coulomb repulsion between the ions already in the trap and the freshly formed ions is large enough to overwhelm the trapping potential [DFM05]. Further evidence to support this conclusion comes from measurements at different MOT parameters with different characteristic loading times which reach the same approximate equilibrium ion number, as well as measurements counting $^{40}\text{Ca}^+$ and $^{174}\text{Yb}^+$ loaded by photo-ionization and laser ablation, respectively.

To confirm that the dimer ion is produced by collisions within the MOT

¹An inelastic process leading to the production of heavier molecular ions, such as Ca_3^+ , could lead to dimer ion loss. However, a direct search for the appearance of heavier ions found no evidence for their production.

and not by other means, such as collisions of MOT atoms with hot Ca from the getter, the production of molecular ions is characterized as a function of MOT density, as shown in figure 4.4. For the data in this figure the dimer ions are detected number after 1.9 s of loading at various densities. The density is varied by controlling the intensity of the 672 nm repump laser; the density at each point is determined by absorption imaging. Quadratic dependence is found for sufficiently small densities, but trap saturation, due to the space charge effect, leads to constant ion number at higher densities. The dependence of the molecular ion production rate at smaller densities is indicative of a two-body process as would be expected for PAI between MOT atoms.

To determine the number of photons required for the PAI, a similar experiment as a function of overall 423 nm laser light power is performed. The results are shown in figure 4.5. Since the position and density of the MOT are sensitive to the exact power balance between the deceleration and trapping beams, there is higher systematic uncertainty in this measurement. However, a quadratic trend is observed, drawn as a dashed line to guide the eye in figure 4.5. This trend is observable by independently attenuating either the deceleration beam or the trapping beams, indicating that the PAI production pathway is sufficiently off-resonant that the beams contribute in the equally in the ionization process. This indicates that the $^{40}\text{Ca}_2^+$ molecular ions are most likely produced by a two-body, two-photon production mechanism as detailed in the following section. Because space charge effects dominate the LQT loading dynamics, the molecular ion production rate cannot simply be analyzed in terms of the competing rate equation model typically employed in trap loading dynamics. Therefore, in order to estimate this rate, an functional form for the number of Ca_2^+ molecular ions, N , in

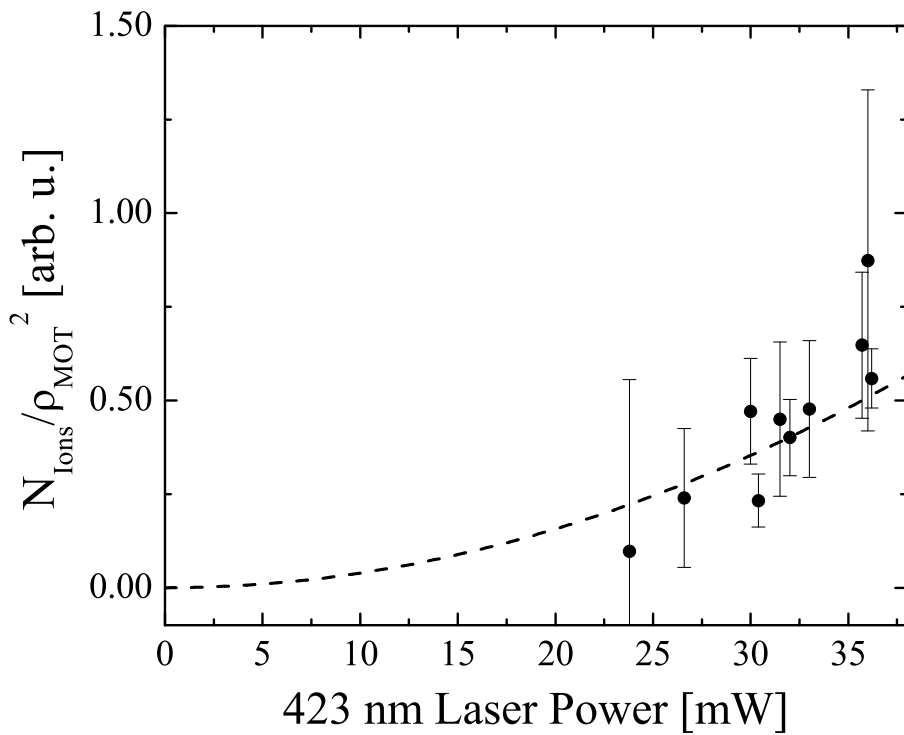


Figure 4.5: Normalized production rate as a function of overall 423 nm laser power incident upon the MOT. Data is obtained both by attenuating the deceleration beam at fixed trapping power and by attenuating the trapping beams at fixed deceleration power. A quadratic fit is shown as the dashed line.

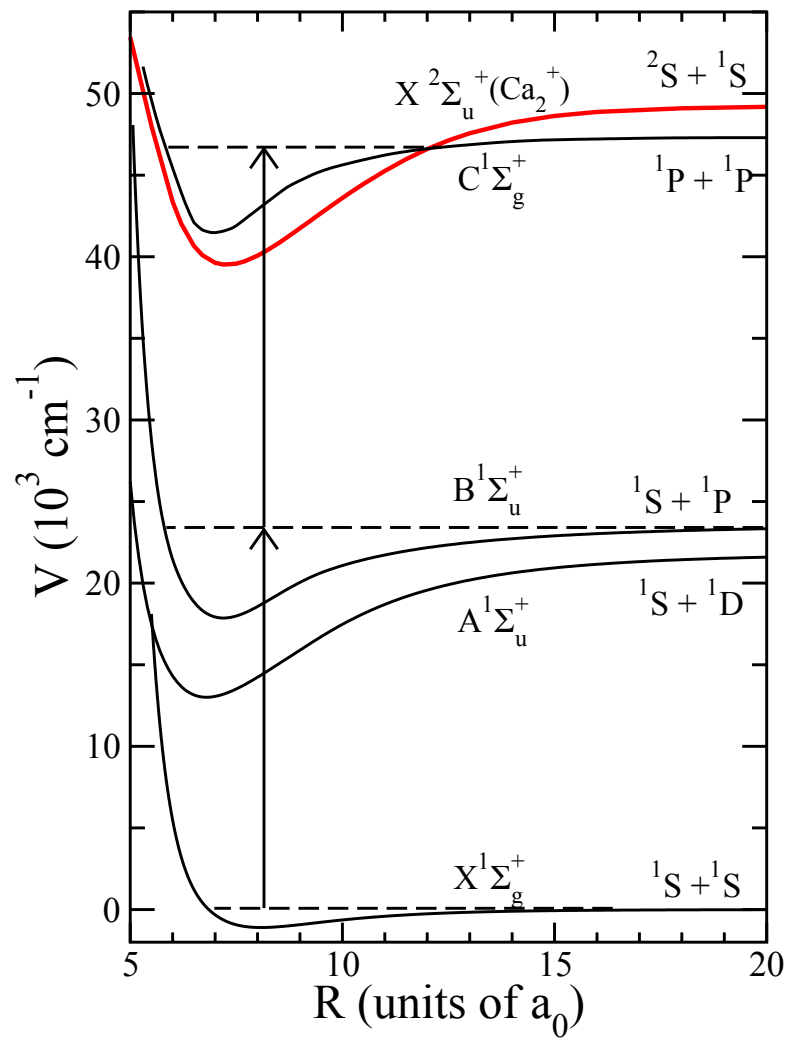


Figure 4.6: Molecular potentials of $^{40}\text{Ca}_2$ (black curves) and $^{40}\text{Ca}_2^+$ (red curve). Two vertical arrows indicate the energy carried in the 423 nm MOT photons. Note the ground state potential of the molecular ion is in the same energy region as the potentials dissociating to two ^1P ^{40}Ca atoms.

the ion trap as a function of time is used as:

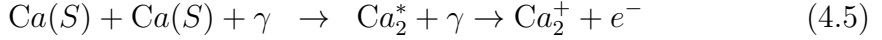
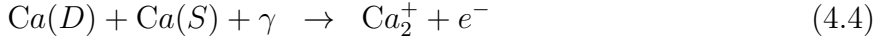
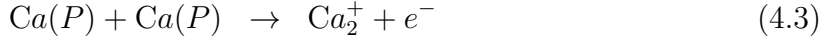
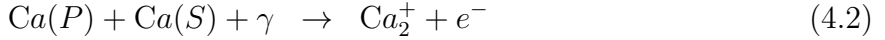
$$\begin{aligned}\frac{dN}{dt} &= \int \eta(\vec{r})\beta(\vec{r})\rho_{\text{Ca}}(\vec{r})^2 \left(1 - \frac{N}{N_o}\right) d^3\vec{r} \\ &= \bar{\eta}\bar{\beta}V\rho_{\text{Ca}}^2 \left(1 - \frac{N}{N_o}\right),\end{aligned}$$

where the average production rate is characterized by $\bar{\beta}$, the two-body intensity dependent rate coefficient; $\bar{\eta}$ is the average of a spatially varying capture efficiency which quantifies the probability of successfully trapping an ion formed at a particular location; ρ_{Ca}^2 and V are the average squared MOT density and volume, respectively. The last factor is an *ad hoc* model to take into account the trap saturation at the observed maximal ion number $N_o \sim 3000 \pm 300$. This model allows us to use full loading curve measurements to set a lower bound on the production rate in a way that is equivalent to performing a model independent linear fit to only the very early ($N \sim 0, t \sim 0$) portion of the loading curve, where space charge effects should be minimal. The rate coefficient from the fit, assuming perfect trap capture efficiency ($\bar{\eta} \rightarrow 1$), to the loading curve shown in figure 4.3 is found to be $\bar{\beta} = 2 \pm 1 \times 10^{-15} \text{ cm}^3 \text{ Hz}$. This rate coefficient should only be interpreted as a lower bound to the true rate constant since the capture efficiency is taken to be its maximal value. Interestingly, this rate coefficient is comparable to observations in alkali systems [BJ92, BMW93] when scaled to the relatively low intensities found in this experiment. This bound is independent of any assumptions about the specific mechanism leading to the PAI event.

4.4.1 Physical interpretation of PAI pathway

In order to determine the specific PAI pathway for molecular ion production, molecular potential curves for the neutral ${}^{40}\text{Ca}_2$ and ionic ${}^{40}\text{Ca}_2^+$ molecules are presented in figure 4.6. The potentials of the $X^1\Sigma_g^+$ and $B^1\Sigma_u^+$ states of ${}^{40}\text{Ca}_2$

are constructed from spectroscopic data in [ASP03, All04]. Other potentials are determined using non-relativistic configuration-interaction molecular-orbital restricted-active-space (MOL-RAS-CI) calculations. From these molecular potentials it is clear that there are several energetically allowed pathways for associative ionization that must be considered:



The first pathway (4.1) is the radiative association of the atomic ion with its neutral partner. To investigate this reaction, large numbers of $^{40}Ca^+$ are loaded into the trap by photo-ionization with a 369 nm laser and then the production of $^{40}Ca_2^+$ is monitored in the presence of the MOT. No evidence of this production mechanism is observed so radiative association cannot be the dominant pathway.

The next two pathways are *single step* processes in which one of the collision partners resides in an excited state before the collision reaches the Condon point, where a free-to-bound transition is possible. The excited collision pathways (4.2,4.3) are ruled out because the duration of the cold collision is longer than the excited 4^1P_1 state lifetime. As discussed in [BJ92], excited atoms are unlikely to be in close enough proximity to undergo association since the 423 nm laser driving the transition is far detuned due to the inter-atomic interaction even at distances large compared to the Condon length.

The other excited collision pathway (4.4) cannot be ruled out due to collision duration argument [BJ92] because the 3^1D_2 Ca state is relatively long

lived, with a radiative lifetime ~ 1 ms, and could survive for the duration of a collision event. To quantify this production mechanism, the dependence of the dimer ion production on the partial density of 3^1D_2 Ca in the MOT is measured. In steady state, the density of 3^1D_2 state Ca can be determined as $\rho_D = (\Gamma_{\text{PD}}\rho_{\text{Ca}}\rho_{ee}) / (\Gamma_{\text{rad}} + \Gamma_{\text{KE}})$ where $\rho_{\text{Ca}}\rho_{ee}$ is the density of atoms in the 4^1P_1 state, Γ_{PD} is the radiative decay rate for the $4^1\text{P}_1 \rightarrow 3^1\text{D}_2$ transition, Γ_{rad} is the total radiative loss rate from the 3^1D_2 state, and Γ_{KE} is the ballistic escape rate from the MOT volume. The ballistic escape rate is determined to be 1.4 ± 0.2 kHz by fitting to the cloud volume evolution measured during free expansion of the MOT atoms. The total radiative loss rate is determined by solving a rate equation model for the effect of the repump laser on the 3^1D_2 state population that includes the 5^1P_1 and 4^1S_0 states as well as the losses into the $3^3\text{P}_{2,1}$ states. Using this system of rate equations, the partial density of 3^1D_2 ^{40}Ca is determined for each data point in figure 4.4. The result, after dividing out the overall quadratic density dependence, is plotted in figure 4.7. Despite the fact the density of 3^1D_2 Ca varies by over factor of two, the rate constant is unchanged. The two points in open circles correspond to the points in figure 4.4 where the ion number is space charge limited, and should be ignored. Therefore it appears that the 3^1D_2 is unimportant for the observed PAI and thus pathway (4.2) is ruled out.

4.5 Conclusion

It is concluded that the two-step, two-photon PAI process (4.5) is responsible for the observed production of $^{40}\text{Ca}_2^+$ molecular ions. This formation proceeds by the excitation scheme sketched in figure 4.6, where colliding neutral atoms are photo-associated into an excited neutral molecule state, which is subsequently excited to the ground molecular ion state or a further excited, auto-ionizing

neutral molecule state. Sympathetic vibrational cooling of the excited neutral molecules by the MOT [Hud09] would introduce a multitude of strong pathways to molecular ion formation, however, given the short molecular excited state lifetime, there can be no significant vibrational relaxation. Thus, the first step in the molecular ion formation process is excitation to the last bound state, $v_i = 190$, of the $B^1\Sigma_u^+(Ca_2)$ state, which is detuned from the MOT laser beams by only $\sim 0.2 \text{ cm}^{-1}$. Molecular ion formation from this state via direct ionization on the $X^2\Sigma_u^+(Ca_2^+) \leftarrow B^1\Sigma_u^+(Ca_2)$ pathway appears unlikely as the nearest-resonant, excited vibrational state, $v_f = 80$, has a Frank-Condon factor (FCF) of $\sim 10^{-8}$ and is detuned from the MOT laser beams by $\sim 20 \text{ cm}^{-1}$. Molecular ion formation via an auto-ionization transition most likely occurs to the $v_f = 74$ vibrational state of the $C^1\Sigma_g^+$ potential, which has a FCF of $\sim 10^{-6}$ and is detuned from the MOT laser beams by only $\sim 0.4 \text{ cm}^{-1}$. Thus, while both processes can contribute to the molecular ion formation, the majority of the ions are formed via auto-ionization of an excited neutral molecule state. This step-wise pathway mechanism agrees well with the conclusions of Ref. [WBZ99].

In summary, this chapter details the observation of formation of $^{40}\text{Ca}_2^+$ molecular ions and sets a lower limit of its production rate constant at $\bar{\beta} \geq 2 \pm 1 \times 10^{-15} \text{ cm}^3 \text{ Hz}$. From the dependences of the production rate on MOT parameters and *ab initio* calculations, it is determined the production mechanism is a two-step, two-photon photo-associative ionization out of the ground state molecular potential that proceeds via an excited, auto-ionizing neutral molecule state. Under typical operational parameters, the MOTion trap produces roughly 3000 molecular ions, limited only by the space charge capacity of the ion trap. As this technique does not require a separate photo-association laser, it could find use as a simple, robust method for producing ultracold molecular ions. While molecular ions produced in this technique are likely found in specific highly excited

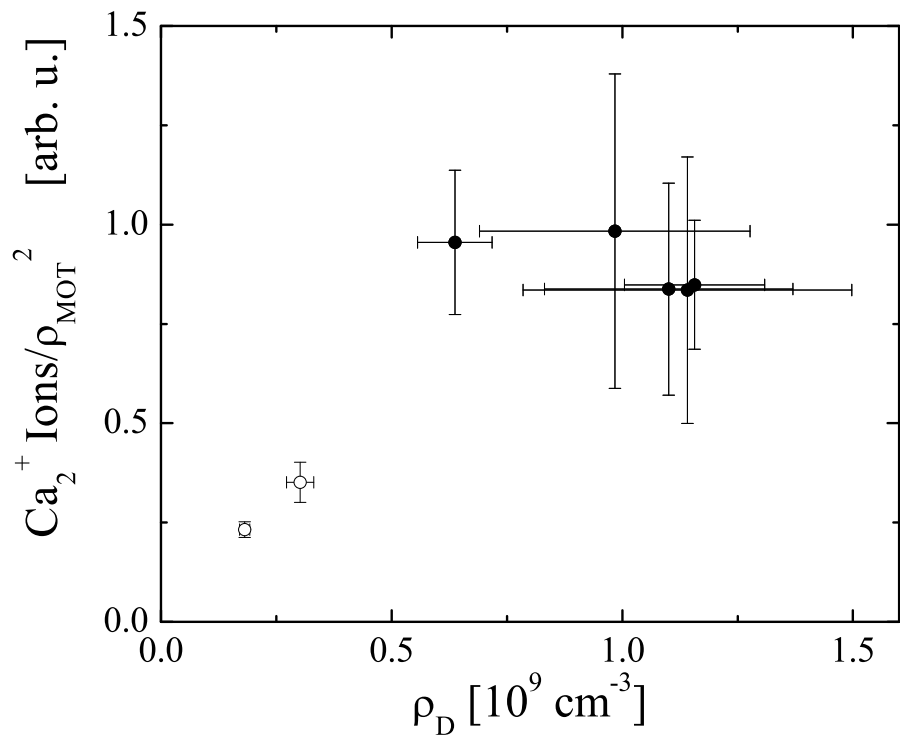


Figure 4.7: Ion number normalized by the square of the MOT density as a function of 3^1D_2 state density. Note the open circle points correspond to those in figure 4.4 at which trap capacity is reached.

ro-vibrational levels, further interaction with the MOT should lead to relaxation to the internal ground state.

CHAPTER 5

Measurement of a large chemical reaction rate between ultracold closed-shell atoms and open-shell ions held in a hybrid atom-ion trap

5.1 Summary

Ultracold $^{174}\text{Yb}^+$ ions and ^{40}Ca atoms are confined in a hybrid trap. The charge exchange chemical reaction rate constant between these two species is measured and found to be four orders of magnitude larger than recent measurements in other heteronuclear systems. The structure of the CaYb^+ molecule is determined and used in a calculation that explains the fast chemical reaction as a consequence of strong radiative charge transfer. A possible explanation is offered for the apparent contradiction between typical theoretical predictions and measurements of the radiative association process in this and other recent experiments.

5.2 Introduction and Motivation

Interactions between cold ions and atoms have been proposed for use in implementing quantum gates [ICZ07], probing quantum gases [KKG07], observing novel charge-transport dynamics [C00], and sympathetically cooling atomic and molecular systems which cannot be laser cooled [SML05, Hud09]. Fur-

thermore, the chemistry between cold ions and atoms is foundational to issues in modern astrophysics, including the formation of stars, planets, and interstellar clouds [Smi92], the diffuse interstellar bands [RGM10], and the post-recombination epoch of the early universe [SZ96]. However, as pointed out in Refs. [ICJ09] and [Woo07], both experimental data and a theoretical description of the ion-atom interaction at low temperatures, reached in these modern atomic physics experiments and the interstellar environment, are still largely missing.

Of particular interest in cold ion-atom physics are binary charge exchange reactions, which limit the performance of the aforementioned proposals and are important inputs to astrophysical models. Binary charge exchange reactions occur via three mechanisms: (i) non-radiative charge transfer (nRCT), $A^+ + B \rightarrow A + B^+$, (ii) radiative charge transfer (RCT), $A^+ + B \rightarrow A + B^+ + \gamma$, and (iii) radiative association (RA), $A^+ + B \rightarrow (AB)^+ + \gamma$. Due to the scarcity of reaction data and full quantum calculations, a number of approximation techniques for these processes have been developed, *e.g.* approximating all RA rate constants by $10^{-14} \text{ cm}^3\text{s}^{-1}$ [Kin95], Landau-Zener theory [BD80], the Demkov coupling method [Dem64], and the semi-classical optical potential method [ZD88]. These techniques, which have varying degrees of accuracy depending on the dominant charge exchange pathway, must be experimentally verified as demonstrated by a recent measurement where a factor of ~ 100 discrepancy was found with experiment [Woo07, LVG02].

Total charge exchange rate constants have recently been measured for two ultracold ion-atom species [GCO09b, ZPS10, ZPR10]. In the first system the charge exchange rate constant for the resonant, homonuclear case of $\text{Yb}^+ + \text{Yb}$ was measured by Grier *et al.* to be $\sim 6 \times 10^{-10} \text{ cm}^3\text{s}^{-1}$ [GCO09b], in good agreement with a subsequent theoretical calculation [ZDC09]. On the other hand, a measurement

of the rate constant for the non-resonant, heteronuclear case of $\text{Yb}^+ + \text{Rb}$ by Zipkes *et al.* yielded $\sim 3.5 \times 10^{-14} \text{ cm}^3\text{s}^{-1}$ [ZPS10]; an experiment on $\text{Ba}^+ + \text{Rb}$ appears to have yielded similar results [SHD10]. Finally, a calculation of the heteronuclear case $\text{Ca}^+ + \text{Na}$ yielded $2.3 \times 10^{-16} \text{ cm}^3\text{s}^{-1}$ [MCM03, SML05]. These values agree well with conventional wisdom for resonant versus non-resonant charge exchange. Interestingly, although the RA process is typically predicted to be the dominant mechanism for low-temperature, non-resonant charge exchange [ZDK89, LQZ09, ZS04], none of the experiments observed the formation of a molecular ion. Further, Zipkes *et al.* found the ratio of the rate of nRCT to RCT to be $K_{nRCT}/K_{RCT} \approx 2.3$, while most calculations predict $K_{nRCT}/K_{RCT} \leq 10^{-3}$ in the ultracold regime [ZDK89, LQZ09, ZS04].

This chapter reports the first measurement of the charge exchange chemical reaction rate constant, K , for the non-resonant, heteronuclear case of a closed shell atom, ${}^{40}\text{Ca}$, with an open shell ion, ${}^{174}\text{Yb}^+$, in a hybrid trap. Interestingly, though conventional wisdom says that closed-shell species are less reactive, a reaction rate of $K \approx 2 \times 10^{-10} \text{ cm}^3\text{s}^{-1}$ is found, four orders of magnitude larger than measured in open-shell systems. In addition, by monitoring the production of CaYb^+ molecular ions in the hybrid trap, an apparent upper bound is set on the branching ratio of the RA process, under the assumption that the produced molecular ions do not experience further chemical reaction. *Ab initio* potential curves for the CaYb^+ molecule describe the individual pathways for the reactions and explain this rate as a consequence of an avoided crossing and similar neutral atom polarizabilities, which yield a large transition dipole moment and large Franck-Condon factors. In the following section, the experimental setup, results, and theoretical model are described. The conclusion offers a possible explanation for the apparent contradiction between typical theoretical predictions and measurements of the RA process in this and other experiments [ZPS10].

5.3 Experiment

Figure 5.1 shows the hybrid magneto-optical and ion trap system used in these experiments [Hud09]. Yb^+ ions, created by laser ablation of a solid Yb target, are trapped in a radio-frequency linear quadrupole trap (LQT) [DFM05] ($250 \text{ kHz} \leq f_{\text{rf}} \leq 400 \text{ kHz}$, $V_{\text{RF}} \approx 300 \text{ V}$) and laser-cooled using laser beams ($\lambda = 369 \text{ nm}, 935 \text{ nm}$) aligned along the trap axis. A voltage-gated channel electron multiplier (CEM) provides a species non-specific method of ion detection. Ultracold Ca atoms are produced and held in a magneto-optical trap (MOT) constructed with laser beams ($\lambda = 422 \text{ nm}, 672 \text{ nm}$) that intersect at the LQT center. Fluorescence images of both the Ca MOT and the Yb^+ ion cloud from two nearly orthogonal camera angles allow a 3D reconstruction of the ion and atom clouds. An example of such images and the reconstruction is shown in the inset of figure 5.1.

The typical MOT atom number, density, and temperature are measured by absorption and fluorescence imaging and found to be $N_{\text{Ca}} = 3.7 \pm 0.5 \times 10^6$ atoms, $\rho_{\text{Ca}} = 7 \pm 1 \times 10^9 \text{ cm}^{-3}$, and $T_{\text{Ca}} = 4 \pm 1 \text{ mK}$, respectively. Ion number and temperature are determined by observing ion fluorescence while scanning the 369 nm laser ($\dot{f} = 500 \text{ MHz/s}$) and fitting the resultant truncated Voigt profile [KCC06]. When operating the LQT in a region where both Ca^+ and Yb^+ ions are stable, a large heat load on the laser cooled Yb^+ ions is observed due to the ionization of Ca atoms in the 4^1P state by the Yb^+ cooling laser. To eliminate this effect, the 422 nm and 369 nm lasers are intensity chopped out of phase with one another. Additionally, this effect is eliminated if the LQT is operated where Ca^+ ions are not trapped.

In absence of the Ca MOT, the trap lifetime of the laser-cooled Yb^+ ions, measured by monitoring the ion fluorescence, is $\sim 240 \text{ s}$. However, when an

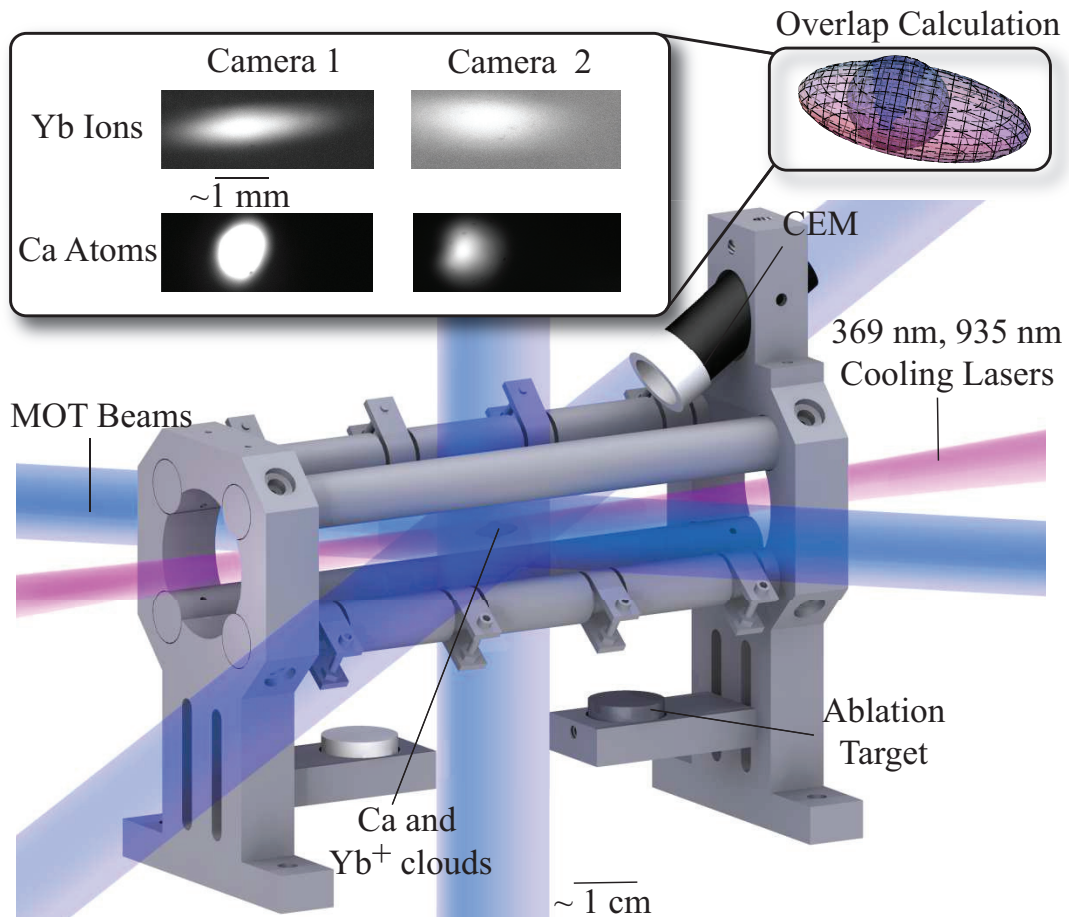


Figure 5.1: MOTion trap schematic. Yb^+ ions and Ca atoms are laser cooled and trapped in the central region. Typical images of the ultracold clouds, shown in the upper left of the figure, are used for a 3D reconstruction that yields the degree of overlap. Ions are also detected with a voltage-gated CEM.

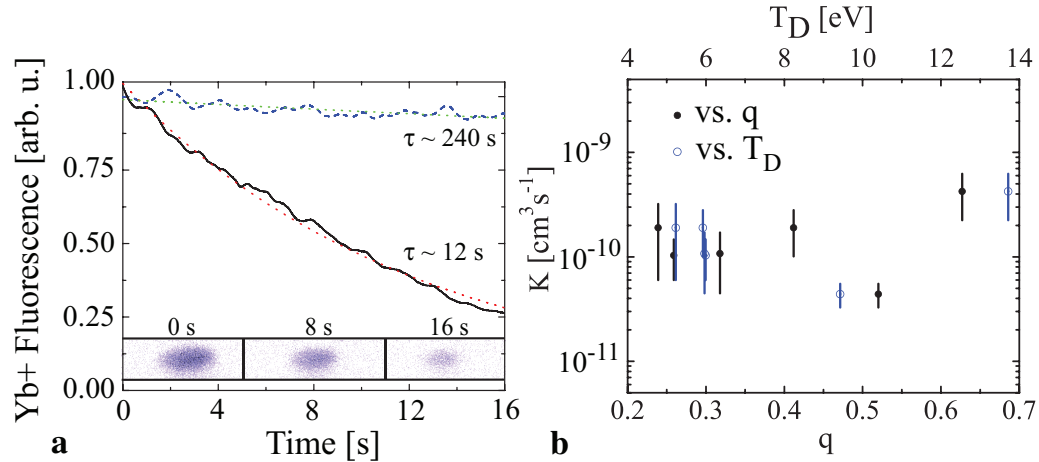


Figure 5.2: (a) Yb⁺ ion trap lifetime in the presence of the MOT (solid curve) compared to the lifetime without a MOT (dashed curve). Dotted curves are single exponential decay fits. Inset: Images of the Yb⁺ ion cloud in the presence of the MOT at various times. (b) Loss rate constant as a function of the Mathieu stability parameter q and the trap depth T_D .

overlapped MOT is introduced, the ion lifetime decreases to ~ 10 s, as shown in figure 5.2(a). This induced ion loss is also confirmed visually by imaging the ion cloud during the decay, as well as observing a decreased number of detected ions using the CEM. The inset in figure 5.2(a) suggests that the loss of ions is not due to ion heating, as such an effect would increase the ion cloud size. From data such as these, a loss rate constant is calculated using $K = \langle \sigma v \rangle = \frac{\Gamma}{\rho \Phi}$, where Γ is the measured fluorescence decay rate, ρ is the peak density of the MOT, and Φ a factor that quantifies the degree of overlap of the atom and ion clouds. The degree of overlap is quantified by $\Phi = \int \hat{\rho}_{Ca}(\vec{r}) \bar{\rho}_I(\vec{r}) d\vec{r}$, where $\hat{\rho}_{Ca}$ is the unit-peak normalized Ca atom density and $\bar{\rho}_I$ is the unit-integral normalized Yb⁺ density, thus $0 < \Phi < 1$.

To verify that kinematic effects were not responsible for the loss of Yb⁺ ions

from the trap, the loss rate constant is measured as a function of q , the Mathieu parameter, which determines the ions' stability and micromotion amplitude in the LQT [DFM05], as well as when only varying the trap depth, T_D (see figure 5.2(b)). As the rate constant appears independent of these fundamental trapping parameters, it is unlikely that the loss is due to kinematic effects in the LQT. In addition, BaCl^+ ions, produced by laser ablation of an additional target (see figure 5.1), are sympathetically cooled by co-trapped, laser cooled Yb^+ ions. Then after 20 s of interaction with the MOT, the number of ions remaining in the trap are compared. The Yb^+ ions decay away, the BaCl^+ ions remain. As BaCl^+ ions are energetically forbidden to charge exchange with Ca atoms [Hud09] and are very close in mass to Yb^+ , so it is concluded the loss of Yb^+ ions is due to a charge exchange reaction and not a trap kinetic effect.

After the systematic checks, the loss rate constant is measured as a function of kinetic energy, as shown in figure 5.3(a). For these measurements the MOT temperature was held at ~ 4 mK and the ion temperature was varied by changing the cooling laser detuning and intensity. The horizontal “error bars” of this figure represent the contribution of the coherent radial micromotion, not measured by the Doppler fluorescence technique, to the total ion kinetic energy [MD68]. The micromotion amplitude grows with radial position in the ion cloud and varies from zero on the axis of the trap to the value given by the rightmost tip of the “error bar” at the edge of ion cloud. The observed rate constant is roughly four orders of magnitude larger than typical non-resonant, heteronuclear charge exchange values and is constant within experimental error over all measured temperatures.

The measured reaction rate constant is the value for ground state atoms and ions. Reactions between excited state atoms and ions have been ruled out by measuring the rate constant while modulating the 422 nm and 369 nm cooling

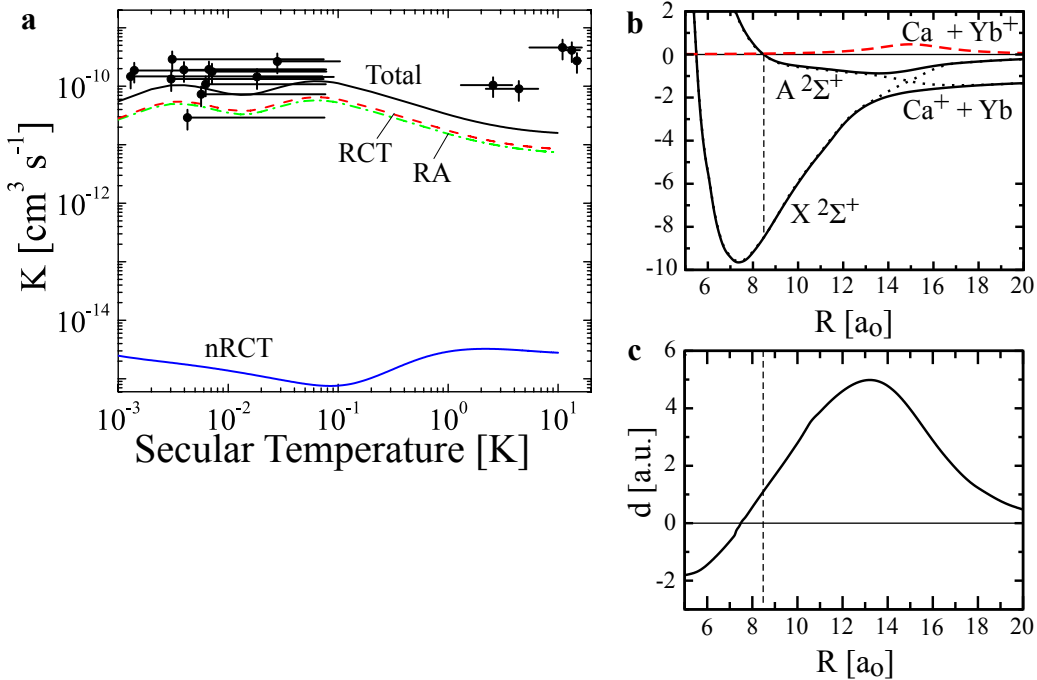


Figure 5.3: (a) Total experimental (points) and theoretical (black line) charge exchange rate constants as a function of ion kinetic energy. The horizontal location of the data point is the value of the secular kinetic energy as measured by the Doppler fluorescence technique. The horizontal “error bars” represent the contribution of the micromotion to the overall kinetic energy. Also shown are the calculated rate constants for the three charge exchange pathways. (b) The X $^2\Sigma^+$ and A $^2\Sigma^+$ potential energy curves and (c) the corresponding transition dipole moment of the CaYb⁺ molecular ion as a function of the internuclear separation R . The dotted curves are the diabatized potentials constructed from these potentials. The dashed curve gives the coupling constant between the diabatic potentials.

light out of phase. Additionally, measurements of the rate constant as a function of the excited state fraction of both the atoms and ions are measured by separately varying the intensity of their respective cooling lasers. In these measurements the rate constant is found to not vary within experimental error as a function of both atom and ion excitation fraction, indicating that the reported rate is the value for ground state reactions. It is possible that excited state atom collisions are suppressed by the long range atom-ion interaction, which shifts the cooling lasers out of resonance before the particles are close enough to react [BJ92, GCO09b], however, the possibly large micromotion velocity does weaken this argument. Finally, the results of Ref. [BJ92] do not apply to the case of an excited state ion since the ground and excited long range potentials are similar, thus the constancy of the rate indicates that excited and ground state ions react at a similar rate, though more investigation is needed.

The charge exchange reaction products can in principle be trapped, but due to the large mass ratio of Ca^+ ($m = 40$ amu) and Yb^+ ($m = 174$ amu) ions, Ca^+ ions are heated by the cold Yb^+ ions [MD68]. This effect is exacerbated by the fact that trap operation in a mutually stable region necessarily puts one or both ion species near a boundary of their LQT stability region. As a result, at the trap parameters used in this study, Ca^+ ions have a measured trap lifetime of only ~ 1 s. Given the comparatively low production rate from charge exchange reactions with Yb^+ ions, the equilibrium number of Ca^+ ions in the trap is ≤ 2 , which is below the system's detection sensitivity. Conversely, the mass of the CaYb^+ reaction product is much closer to that of Yb^+ and does not suffer from these effects. Therefore, neglecting further chemical reaction with the Ca MOT, CaYb^+ ions are expected to have a trap lifetime of at least that of uncooled BaCl^+ ions ($m \sim 17$ amu) which is measured to be ~ 30 s. Thus, by allowing the Yb^+ ion fluorescence to decay to background levels, measuring the number

of ions remaining in the trap using the CEM, and accounting for systematic effects such as trap loss and mass dependence of the ion detection efficiency, an apparent upper limit on the branching ratio for RA is found to be 0.02, under the assumption that all the signal ions are CaYb^+ .

Also shown in figure 5.3(a) are the results of the theoretical model for the charge exchange rate constant. Since the structure of CaYb^+ was previously unknown, the electronic potential surfaces are calculated for states that dissociate to the $\text{Ca}+\text{Yb}^+$ and Ca^++Yb limits, and their transition dipole moment [KLM03], as shown in figure 5.3(b) and (c) (solid curves), respectively. This approach worked well for the structure of the BaCl^+ molecular ion [CSK11]. The CaYb^+ $X\ ^2\Sigma^+$ and $A^2\Sigma^+$ states are asymptotically separated by an energy splitting of $1136\ \text{cm}^{-1}$ [KRR05] with an attractive long-range $-C_4/R^4$ behavior; C_4 is 71.5 a.u for the $X\ ^2\Sigma^+$ state and 78.5 a.u. for $A^2\Sigma^+$ state. Their values are determined by the static polarizability of the neutral Ca [PD06] and Yb [ZD07] atom. The two potentials have an avoided crossing near $R = 15a_0$ with a smallest separation of $946\ \text{cm}^{-1}$. Using these potentials, the rate constant for the charge exchange pathways is calculated via a quantum mechanical scattering calculation that assumed the particles collide on the $A^2\Sigma^+$ potential and charge exchange to bound or continuum states of the $X^2\Sigma^+$ potential.

Since the nRCT pathway occurs via a nonadiabatic transition near the avoided crossing, the rate constant is determined by a coupled-channels method with diabatized potentials – black dotted lines in figure 5.3(b). For the coupling between these potentials, a Lorentzian is assumed in R with a maximum value equal to half the minimum splitting of the adiabatic potentials. The width of the coupling matrix element is chosen such that diagonalization of the 2×2 potential matrix reproduces the original adiabatic potentials. Due to the strength of the atom-

ion interaction, up to several hundred partial waves are required for numerical convergence of the nRCT rate constants at the trap temperatures, which leads to a large number of shape resonances in the unthermalized rate constants as a function of collision energy. To characterize the nature of the coupling, the strength is varied between the diabatic potentials by 20%. Although the nRCT rate coefficient does increase with coupling strength, it does not exceed a few times $10^{-14} \text{ cm}^3\text{s}^{-1}$, indicating that the scattering is almost adiabatic.

For the calculation of the RCT and RA rate constants, Fermi's golden rule gives the rate for the spontaneous emission of a photon by the diatom. In principle, both the initial and final state wavefunctions are solutions of a two-channel calculation as for nRCT, however, since the scattering is nearly adiabatic, it is assumed that the initial state is a scattering solution of the $A^2\Sigma^+$ potential and the final state is either a bound or scattering state of the $X^2\Sigma^+$ potential. Thus, the total radiative rate coefficient for an initial $\text{Ca}+\text{Yb}^+$ energy-normalized state $|A, \epsilon\ell m\rangle$ with collision energy ϵ , relative angular momentum quantum number ℓ , and projection m is

$$K_{\epsilon\ell m} = \frac{2\pi^2}{\sqrt{2\mu\epsilon}} \sum_f \frac{4}{3} \alpha^3 \omega_{f,\ell}^3 |\langle X, f | d | A, \epsilon\ell m \rangle|^2 \quad (5.1)$$

where α is the fine-structure constant, μ is the reduced mass, and all quantities are expressed in atomic units. The sum is over final states f , which denote either a continuum wavefunction $|X, \epsilon'\ell'm'\rangle$ leading to RCT or a ro-vibrational state $|X, v\ell'm'\rangle$ of the $X^2\Sigma^+$ potential leading to RA. The quantity $\omega_{f,\ell}$ is the frequency difference between the initial and final states and the operator d is an abbreviation for $d(R)C_{1q}(\hat{R})$, where $d(R)$ is the R -dependent dipole moment between the X and A state, $C_{1q}(\hat{R})$ is a spherical harmonic, \hat{R} the orientation of the molecule in a space-fixed coordinate system, and $q = m - m'$ gives the polarization of the emitted photon. The selection rules of the dipole moment ensure that $|\ell - \ell'| \leq 1$

and $|m - m'| \leq 1$. Figure 5.3(a) shows the thermalized radiative rate constants due to both RCT and RA mechanisms versus temperature.

Figure 5.3(a) also shows the total rate constant which agrees well with the data. The calculations show that the enhanced rate constant is the result of the avoided crossing of the molecular potentials (figure 5.3(b)), which gives rise to a large transition dipole moment due to the mixing of the states (figure 5.3(c)). Additionally, there is good Franck-Condon overlap due to the similarity of the long range potentials. Similar systems with avoided crossings (e.g. Ba + Yb⁺, and Sr + Yb⁺) might show enhanced rate constants as well.

Although there is satisfactory agreement with the total calculated and measured rate constant, the predicted RA branching ratio of ~ 0.5 strongly disagrees with the measured value ≤ 0.02 . These ratios could be reconciled, however, if the CaYb⁺ further reacted with the Ca MOT atoms via subsequent RA reactions, *e.g.* $\text{CaYb}^+ + \text{Ca} \rightarrow \text{Ca}_2\text{Yb}^+ + \gamma$, to form heavier molecular ions, which, due to technical constraints, are unstable in the LQT. Given that RA will predominantly produce CaYb⁺ in high-lying vibrational states, which are typically very reactive, this explanation seems quite plausible. The RA process is observed in the CaRb⁺ system [HAB11]. Evidence for further chemical reaction of CaRb⁺ is observed, supporting the explanation for the apparent lack of RA products in the open-shell CaYb⁺ system. Further, if the same explanation is applied to the data of Ref. [ZPS10], the interpretation of trap loss as evidence of nRCT could be reinterpreted as evidence of RA, yielding a RA branching ratio that agrees well with typical theoretical predictions.

5.4 Conclusion

In conclusion, this chapter presents an experimental and theoretical investigation of the charge exchange reaction of the Ca + Yb⁺ system. The total measured and calculated rate constants are in good agreement and are surprisingly large for a non-resonant, heteronuclear charge exchange reaction. There is a plausible explanation for the apparent contradiction between typical theoretical predictions and measured rates of RA in this and other experiments. However, the discrepancy between theory and experiment clearly calls for future investigations into molecular ion formation. Given the importance of these types of reactions for determining astrophysical processes, this work highlights the need for fully quantum calculations on a case-by-case basis and a renewed effort in laboratory astrophysics. Finally, chemical reactions such as charge exchange could be a concern for the development of many of the applications of hybrid atom-ion trap systems, and thus, when designing future experiments, the choice of atomic and ionic species must be carefully considered.

5.5 Appendix: reaction rates for even isotope number

Yb⁺

After performing the charge exchange rate constant measurement for the most abundant isotope ¹⁷⁴Yb⁺, the measurement is repeated for the other even isotopes. There appears to be no measurable variation in the charge exchange rate constant as a function of isotope number. The measurements shown in figure 5.4 are taken together and analyzed separately from the main result shown for the most abundant isotope shown in figure 5.3.

Isotope	Abundance %	Cooling [cm ⁻¹]	Repump [cm ⁻¹]
170	3.04	27061.86809	10692.9284
172	21.83	27061.81609	10693.0444
174	31.83	27061.77288	10693.1313
176	12.76	27061.73187	10693.2141

Table 5.1: Table of isotopic abundances for the even numbered isotopes of Yb⁺ detected via laser fluorescence in the trap system. Values for the laser wavenumbers are from [MNS11].

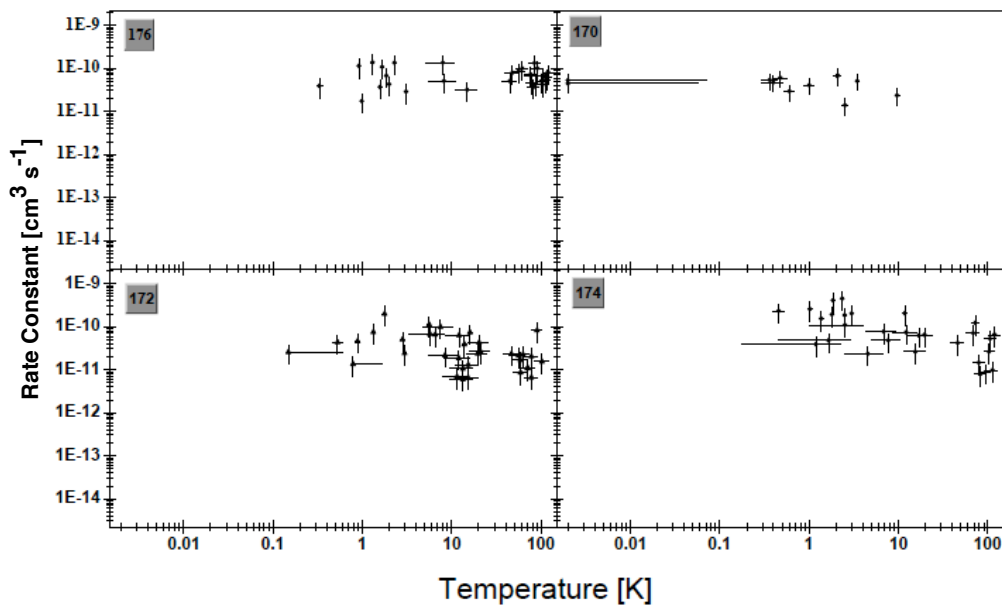


Figure 5.4: Charge exchange rate constant measurement for Yb⁺ ions for 170,172,174 and 176 isotopes.

CHAPTER 6

The role of electronic excitation in ground-state forbidden inelastic collisions between ultracold atoms and ions

6.1 Summary

The role of electronic excitation in inelastic collisions between ultracold Ca atoms and Ba⁺ ions, confined in a hybrid trap, is directly studied for the first time. Unlike previous investigations, this system is energetically precluded from undergoing inelastic collisions in its ground state, allowing a relatively simple experimental determination and interpretation of the influence of electronic excitation. It is found that while the electronic state of the ion can critically influence the inelastic collision rate, the polarizability mismatch of the neutral atom electronic states suppresses short-range collisions, and thus inelastic processes, involving electronically excited neutral atoms. As a result of these features, it is experimentally demonstrated that it is possible to mitigate inelastic collision loss mechanisms in these systems, marking an important step toward long-lived hybrid atom-ion devices.

6.2 Introduction and Motivation

Since the inception of laser-cooling, a chief focus of atomic physics has been the development of techniques for the production and study of ultracold matter – an endeavor that is centered on facilitating full control over matter at the quantum level. This work has been quite successful, enabling many long-sought-after goals, such as quantum degenerate gases [EMW95, JD99], quantum simulation [BN09], quantum information [LJL10], and precision measurement of fundamental physics [BW99, RHS08]. To gain this control, however, most ultracold matter production techniques rely on the scattering of a large number of photons from the system under study, potentially leading to a large degree of electronic excitation. Thus, the atom or molecule being cooled can be in a peculiar state: its external motion may be characterized by a temperature close to absolute zero, but its internal electronic degree of freedom may be characterized by a temperature approaching infinity. While this non-thermal distribution of electronic states has some notable important consequences for ultracold atoms [WMG89], most of its effects, such as photochemical reactions [GLJ88, RWG91, SRK11], are largely ignored as they occur at rates that have relatively little effect on the system. However, as the field now moves towards producing more complex systems at ultracold temperatures, *e.g.* molecules [SBD10] and hybrid systems [ZPR10, SHD10], the effect of these light-assisted processes must be reevaluated as their rates may be much larger due to, among other things, an increased density of accessible product states and longer range interactions. Thus, there is presently a need to better understand the role of electronic excitation in inelastic processes, such as chemical reactions, at ultracold temperatures to enable the next generation of experiments.

Interestingly, the rapidly emerging field of hybrid atom-ion systems offers

a unique opportunity to study ultracold collisions [GCO09b, ZPR10, RSK11, HAB11]. Like in all-neutral systems of traditional atomic physics, the co-trapped species can collide at short-enough range for reactions to proceed; but, unlike all-neutral systems it is possible to maintain a product of the reaction in the trap, since ion trap depths are large relative to the typical exothermic energy release. Already, such hybrid systems have been used to measure several important ion-neutral chemical reactions [RSK11, GCO09b, ZPR10, SHD10], culminating in the recent observation of molecular ion reaction products [HAB11].

The hybrid atom-ion MOTion trap system [RSK11, HAB11] is used to study chemical reactions between ultracold ^{40}Ca atoms and $^{138}\text{Ba}^+$ ions. Unlike all previous studies, inelastic collisions between ground-state atoms and ions are energetically forbidden in the $^{40}\text{Ca} + ^{138}\text{Ba}^+$ system and can thus only occur if at least one species is electronically excited. As a result, this system is relatively simple to interpret and allows a straightforward examination of the role of electronic excitation. The next section discusses how optical coherence and trap dynamics can critically affect the observed atom-ion chemical reaction rate when electronic excitation is involved, and presents experimental results detailing the observed chemical reaction pathways and the average radiative association branching ratio for formation of CaBa^+ molecular ions. In addition relativistic *ab initio* molecular structure calculations are calculated, which further illuminate the excited state entrance channels, as well as provide guidance for future experiments. This is the first detailed experimental investigation of the importance of neutral atom excitation. The results demonstrate that it is possible, with reasonable experimental parameters, to avoid the large chemical reaction rates seen in other hybrid atom-ion systems, marking a crucial step towards the next generation of hybrid atom-ion devices.

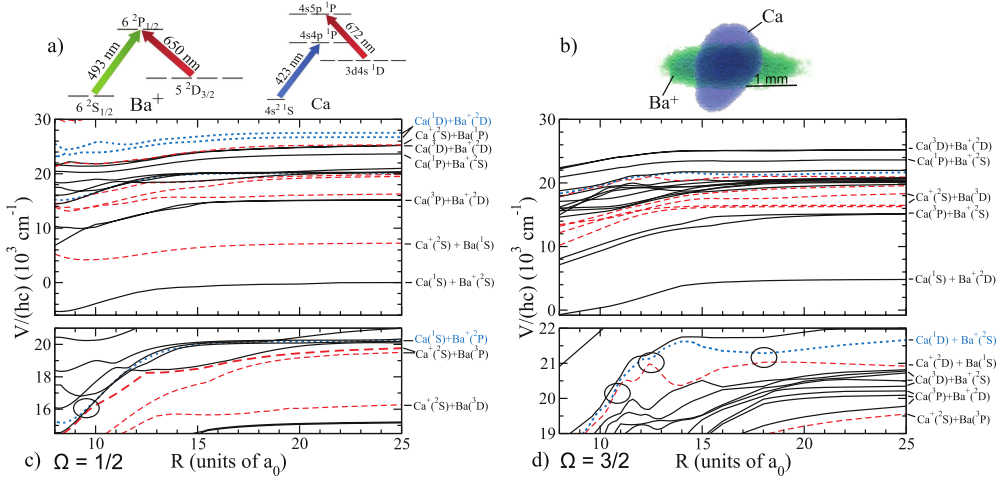


Figure 6.1: a) Ba⁺ and Ca relevant energies levels and laser cooling schemes. b) Fluorescence images of Ca MOT and Ba⁺ ion cloud. c) and d) Molecular potentials of the $\Omega = \frac{1}{2}, \frac{3}{2}$ excited states of the CaBa⁺ molecule, respectively, as a function of interatomic separation R . The bottom panels show higher detail for potentials near 20×10^3 cm⁻¹ above the Ca^{+(2S)}+Ba(^{1D}) dissociation limit. Entrance and exit channels, as defined in the text, dissociate to green and red potentials, respectively.

6.3 Experiment

The apparatus used in this work is similar to that described in Ref. [RSK11]. Briefly, $^{138}\text{Ba}^+$ ions ($N_{\text{ion}} \sim 1000$ ions) are loaded into a linear radio-frequency (rf) quadrupole trap via laser ablation of a BaCl_2 target [CSK11] and cooled with colinear laser beams. In the same region, ultracold Ca atoms ($N_{\text{MOT}} \sim 3 \times 10^6$ atoms, $\rho_{\text{MOT}} \sim 5 \times 10^9 \text{ cm}^{-3}$) are produced and trapped in a magneto-optical trap (MOT). (See figure 6.1(a) for the ion and atom electronic energy levels and cooling laser scheme, denoted by arrows.) Two nearly-orthogonal cameras allow for a 3-dimensional reconstruction of both the Ca MOT and the laser-cooled ion cloud, and are used to quantify the degree of overlap between the Ca atoms and $^{138}\text{Ba}^+$ ions, as shown in figure 6.1(b). Using the same approach as Ref. [RSK11], the laser-induced 493 nm fluorescence monitors the $^{138}\text{Ba}^+$ ion population, which is observed to decay in the presence of the Ca MOT due to charge exchange chemical reactions ($\text{Ca} + \text{Ba}^+ \rightarrow \text{Ca}^+ + \text{Ba}$, $\text{CaBa}^+ + \gamma$), allowing a direct measurement of the total inelastic collision (charge transfer) rate Γ . Special care must be taken to account for the time evolution of the degree of overlap, which requires a non-analytical numerical fitting technique to account for the deviation from simple exponential decay.

In this experiment, the atom-ion collision energies are primarily set by the coherent, driven motion of the ion due to the rf trapping potential (i.e. the micromotion) since the Ca MOT temperature ($T \simeq 4 \text{ mK}$) and the Doppler-cooling temperature limit of the Ba^+ ions ($T \simeq 0.5 \text{ mK}$) are both lower than the typical, position dependent, energy of micromotion in the ion cloud ($\frac{E_\mu}{k_B} \sim 10 \text{ mK-10 K}$). At these low collision energies, chemical reaction dynamics are primarily determined by the relative energies of the entrance and exit reaction channels, shown in black and red, respectively, in figure 6.1(c,d). Because the ionization

potential of Ca (6.1 eV) is significantly larger than that of Ba (5.2 eV), charge exchange reactions between the Ca 4^1S - and Ba $^+$ 6^2S - or 5^2D - electronic states are energetically precluded. As a result, inelastic collision between Ba $^+$ and Ca can only occur if the atom, the ion, or both are electronically excited. Of the ten energetically allowed entrance channels populated in this experiment, the six involving the short-lived Ca P-states do not contribute to the observed reaction rate. Because the Ca 4^1S -, 4^1P - and 5^1P -states have very different atomic polarizabilities [MTR01] (163.0 a.u., 55.3 a.u., and >1000 a.u., respectively), during the collision the strong monopole field of the ion alters the atomic transition frequency such that the Ca MOT lasers are shifted far from resonance for atom-ion separations of many hundred Bohr radii, a_o . Thus, though a collision leading to reaction may begin with a Ca atom in a P-state, by the time the atom and ion are close enough to react ($< 10 a_o$), the Ca atom has radiatively decayed from the P-state. Similar effects are discussed in Ref. [BJ92, WSD95, GCO09b], were observed in Ref. [RSK11], and are confirmed by the data presented here. This effect appears general and it is likely that short-lived excitations of ultracold atoms can be ignored in future experiments involving reactions of ultracold atoms and ions. (This effect is particularly beneficial to techniques for sympathetic cooling of molecular ions by ultracold atoms [Hud09], as it significantly relaxes the experimental constraints.) Interestingly, a similar argument cannot be made for short-lived, excited states of ions. Because excitation of the ion only changes the long-range dispersion coefficient, e.g. C₆, the ion cooling lasers are not shifted out of resonance until relatively small atom-ion separations. Thus, while these chemical reactions are suppressed, it is nonetheless possible for them to occur between atoms and excited state ions.

With these considerations, it is clear that the reactions proceed from the energetically allowed entrance channels involving 4^1S - or 3^1D -state Ca atoms and

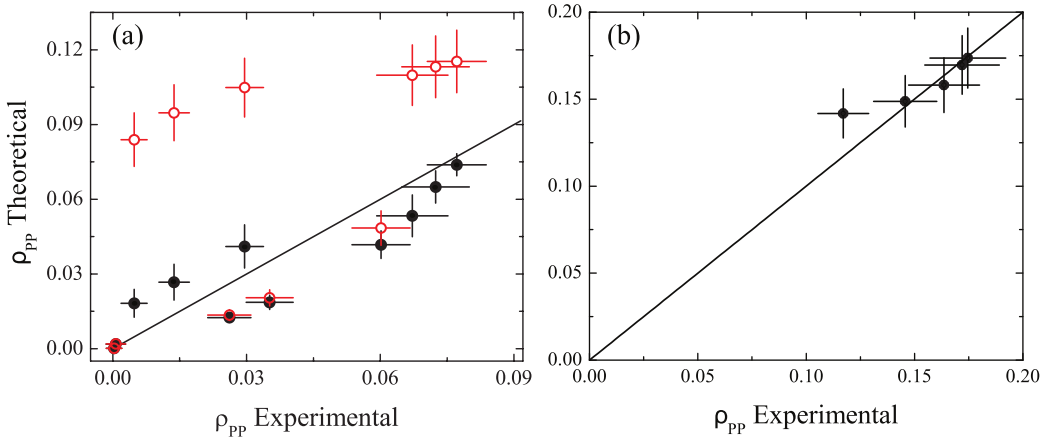


Figure 6.2: Panel (a): experimentally determined excitation fraction in Ba^+ versus theoretical predictions of the quantum Liouville (\bullet) and rate equation (red circles) treatment. Panel (b): experimentally determined excitation fraction in Ca versus predictions of a 4-level rate equation model. In both panels the solid line has a unit slope, representing ideal agreement.

6^2S -, 6^2P -, or 5^2D -state Ba^+ ions, highlighted in green in figure 6.1(c-d). While the charge exchange rate constant for each of the four distinct pathways depends sensitively on the details of the CaBa^+ molecular structure, they can nevertheless be probed by varying the excited state populations of the atoms and ions while recording the total reaction rate. Experimentally, this is accomplished by varying the intensities of the atom and ion cooling lasers. With known experimental parameters it is then possible to calculate the relative population of each atom and ion electronic state (the population fraction of the specie X in the electronic state i is denoted by the diagonal density matrix element ρ_{ii}^X), and extract the contribution of each reaction channel to the total measured reaction rate given by $\Gamma = \rho_{\text{MOT}} \langle \sigma v \rangle = \rho_{\text{MOT}} k_{\text{Total}} = \rho_{\text{MOT}} \sum_{i,j} \rho_{ii}^{Ba} \rho_{jj}^{Ca} k_{i,j}$, where $k_{i,j}$ is the rate constant for Ba^+ in electronic state i immersed in a pure sample of Ca in electronic state j.

The calculation of the Ba^+ electronic state populations is complicated by op-

tical coherence effects and the quadrupole magnetic field of the MOTION trap, whose direction and strength vary in a non-trivial way. The Ba^+ electronic state populations are determined by solving the steady-state quantum Liouville equation for an eight-level optical Bloch Hamiltonian [Ste05] and spatially averaging the result over the ion cloud. To confirm the accuracy of this calculation, a measurement the $\text{Ba}^+ 6^2\text{P}_{1/2}$ state fraction is performed via calibrated fluorescence and ion detection, as shown in figure 6.2(a) along with the prediction of a standard rate equation model for comparison. Similarly, a first principles calculation of the electronic state populations of atoms in a MOT environment is a well-known open problem and various phenomenological models have been proposed [SCT07, Jav93]. The Ca 4^1P -state excitation fraction is directly measured to determine the appropriate model for calculation of the Ca population fractions. As shown in figure 6.2(b), there is good agreement with a standard four-level rate equation model [SRK11], a likely consequence of the lack of hyperfine structure in ^{40}Ca .

The laser intensities are varied and the total inelastic rate constant is recorded as a function of the resulting excitation fractions. The resulting measurements, plotted as a function of ion and atom excitation fraction, are shown in Figs. 6.3 and 6.4, respectively.

As a function of Ba^+ excitation, the most obvious feature is a linear trend of increasing reactivity with increasing ρ_{pp}^{Ba} . In addition, the reaction rate constant diminishes at both extremes of the Ba^+ S-state, ρ_{ss}^{Ba} , and D-state, ρ_{dd}^{Ba} , population fraction. Taken together, these features indicate that the primary reaction channel involves the Ba^+ ion P-state, since a comparable S- or D-state contribution would result in measurable rate constants in the limit of unit occupation of the S- or D-state. Also shown in figure 6.3, as open triangles, are several measurements

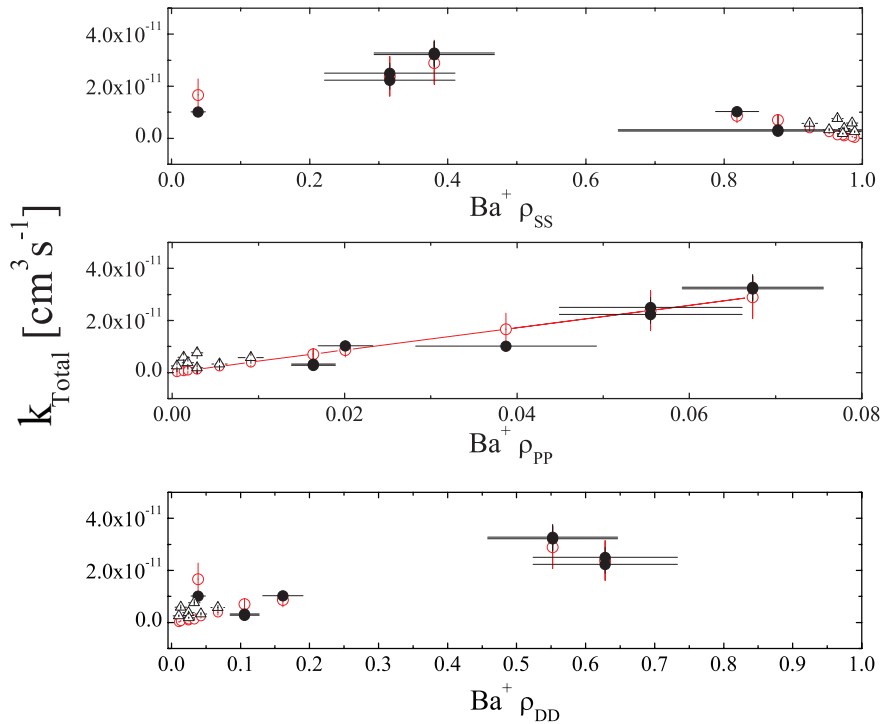


Figure 6.3: Measured rate constant as a function of Ba^+ population fractions. Experimental result in black. Best fit ($\{k_{ps}, k_{sd}, k_{pd}, k_{dd}\} = \{4.2 \pm 1.9, \leq 3, \leq 20, \leq 7\} \times 10^{-10} \text{ cm}^3 \text{ s}^{-1}\}$) to the four entrance channel model shown as open red circles. For these measurements, Ca population fractions were fixed at $\rho_{ss}^{Ca} \sim 0.75$, $\rho_{pp}^{Ca} \sim 0.20$, $\rho_{dd}^{Ca} \sim 0.05$.

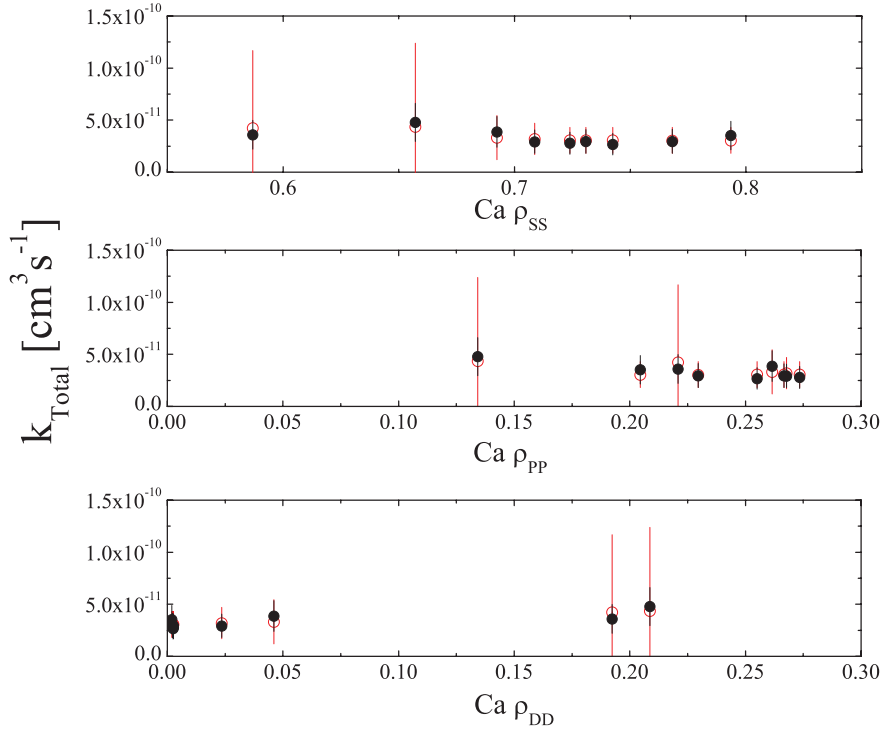


Figure 6.4: Measured rate constant as a function of Ca population fractions. Experimental result in black. Best fit ($\{k_{ps}, k_{sd}, k_{pd}, k_{dd}\} = \{4.2 \pm 1.9, \leq 3, \leq 20, \leq 7\} \times 10^{-10} \text{ cm}^3 \text{ s}^{-1}$) to the four entrance channel model shown as open red circles. For these measurements, the Ba^+ population fractions were fixed at $\rho_{ss}^{Ba} \sim 0.4$, $\rho_{pp}^{Ba} \sim 0.1$, $\rho_{dd}^{Ba} \sim 0.5$.

at low excitation fractions ($< 1\%$). While these points agree with the rest of the data, they are not included in the final analysis to avoid possible systematic inaccuracies due to higher secular energies.

As shown in figure 6.4, the rate constant exhibits no detectable variation over the experimentally accessible Ca excitation range. Neither the Ca 5^1P -state nor the 4^1P -state are expected to contribute to the rate constant shown here, the former due to a negligible population and the latter due the aforementioned radiative suppression effect. As a result only the Ca S- and D-states contribute to the observed reaction rate, thus it is concluded that the lack of a trend in figure 6.4 is an indication of similar reaction rates for the atomic S- and D-states with Ba^+ .

To extract channel-specific reaction rate constants from these data, the total reaction rate constant is quantified in terms of the excited state fractions of both Ba^+ and Ca as: $k_{\text{Total}} = \rho_{pp}^{Ba} \rho_{ss}^{*Ca} k_{ps} + \rho_{ss}^{Ba} \rho_{dd}^{Ca} k_{sd} + \rho_{dd}^{Ba} \rho_{dd}^{Ca} k_{dd} + \rho_{pp}^{Ba} \rho_{dd}^{Ca} k_{pd}$. By accounting for the conservation of probability ($\rho_{ss} = 1 - \rho_{pp} - \rho_{dd}$) and the fact that Ca atoms in the P-state radiatively decay to the S-state before the atom and ion are close enough to react ($\rho_{ss}^{*Ca} = \rho_{ss}^{Ca} + \rho_{pp}^{Ca}$), the totality of the data in figure 6.3 and figure 6.4 is subject to a multi-parameter fit along the manifold $\{\rho_{pp}^{Ba}, \rho_{dd}^{Ba}, \rho_{dd}^{Ca}\}$ to determine the contribution of each reaction pathway to the total rate constant. From this fit, the reaction rate constant of the primary entrance channel, $\text{Ba}^+(6^2P_{1/2}) + \text{Ca}(4^1S)$, is found to be $k_{ps} = 4.2(1.9) \times 10^{-10} \text{ cm}^3 \text{ s}^{-1}$, while the best fit for the rate constant of the only channel out of the Ba^+ ground state, $\text{Ba}^+(6^2S_{1/2}) + \text{Ca}(3^1D)$ is constrained to be $\leq 3 \times 10^{-10} \text{ cm}^3 \text{ s}^{-1}$. Because the remaining two entrance channels, $\text{Ba}^+(6^2P_{1/2}) + \text{Ca}(3^1D)$ and $\text{Ba}^+(5^2D_{3/2}) + \text{Ca}(2^1D)$, require simultaneous excitation of the atom and ion, the experiment is relatively insensitive to them and upper limits

are set on them of $k_{pd} \leq 2 \times 10^{-9}$ cm³ s⁻¹ and $k_{dd} \leq 7 \times 10^{-10}$ cm³ s⁻¹. To show the quality of agreement between the best fit and the results, a data point generated from the fit is plotted corresponding to each experimental condition (open circles) in Figs. 6.3 and 6.4. In addition to this fit, using the method described in Ref. [RSK11], the molecular ion product branching ratio is found to be ~ 0.1 . Future measurements, using time-of-flight detection as in Ref. [SCR12], are planned to further constrain the branching ratio.

To illuminate the charge exchange mechanisms responsible for the individual reaction pathways, *ab initio* calculations of the CaBa⁺ potentials are performed, with total body-fixed angular momentum of $\Omega = (\frac{1}{2}, \frac{3}{2})$, using a relativistic multi-reference restricted active space configuration-interaction method [KT05]. Spin-orbit effects are large in CaBa⁺ and a relativistic calculation is required. The resulting Born-Oppenheimer potentials for the ground and first-excited state of CaBa⁺ are shown in figure 6.1(c-d), and assigned by their atomic dissociation limit. The bottom panels of figure 6.1(c-d) show a higher resolution view of the closely spaced potentials above 20×10^3 cm⁻¹. Both panels reveal that there are strong interactions and avoided crossings between neighboring excited potentials. Potentials dissociating to energies $> 27 \times 10^3$ cm⁻¹ are not shown, as the exceedingly high level density makes it impossible to resolve the avoided crossings with this calculation.

In principle, a coupled-channels calculation that includes the mixings between these potentials due to radial non-adiabatic coupling and spontaneous emission, like that performed in Ref. [RSK11], can be used to calculate the non-radiative, radiative, and radiative association charge exchange reaction rate constants for each entrance channel; however, due to the high level density in the excited CaBa⁺ molecule, this calculation is extremely technically demanding and falls

outside the scope of this work. Nonetheless, the basic mechanisms of each charge exchange pathway can be qualitatively inferred from the calculated structure of its entrance channel molecular potential. For example, the experimentally dominant entrance channel, $\text{Ca}(4^1\text{S}) + \text{Ba}^+(6^2\text{P}_{1/2})$, exhibits strong interactions with several potentials as well as a narrowly-avoided crossing with a molecular potential dissociating to the $\text{Ca}^+(4^2\text{S}) + \text{Ba}(6^3\text{P})$ exit channel. The second most experimentally reactive entrance channel, $\text{Ca}(3^1\text{D}) + \text{Ba}^+(6^2\text{S}_{1/2})$, also shows several strong avoided crossings with the $\text{Ca}^+(3^2\text{D}) + \text{Ba}(6^1\text{S})$ exit channel. Strong, narrowly-avoided crossings facilitate non-adiabatic, non-radiative charge transfer, the likely mechanism for the aforementioned channels. By similar reasoning, it is expected that the $\text{Ca}(3^1\text{D}) + \text{Ba}^+(5^2\text{D})$ entrance channel would be relatively inefficient for charge exchange reactions since low energy scattering events do not experience an avoided crossing nor do they couple well to states accessible via spontaneous emission due to poor Franck-Condon overlap. The remaining $\text{Ca}(3^1\text{D}) + \text{Ba}^+(6^2\text{P}_{1/2})$ entrance channel resides in a host of densely packed levels, which prevents the *ab initio* calculation from providing reliable results and suggests that non-radiative and radiative chemical reactions could proceed very quickly from these states, a result that is consistent with the limit set for this channel by the measurement.

Finally, despite the fact that the rate constants measured here are large by atomic physics standards, roughly a third of the rate attained when assuming all collisions that cross the angular momentum barrier have a unit probability of being inelastic (i.e. the Langevin rate), with proper engineering of the atomic and ionic excited state populations, their effects can be mitigated. By using sufficient repumping laser powers to maintain a negligible Ca D-state fraction and using the minimum ion laser cooling power necessary to achieve Doppler-limited cooling, Ba^+ ion lifetimes in excess of several minutes are observed in the presence of the

MOT.

6.4 Conclusion

In summary, chemical reactions in a hybrid atom-ion system are studied in a system where only electronically excited states are energetically permitted to react. The observed reaction dynamics are qualitatively different than what is observed in systems where ground-state reactions are equally important [RSK11]. The measured reaction rate constant is found to be an appreciable fraction of the Langevin rate, similar to results found in other experiments involving excitation [GCO09a, HAB11, RZS12], and is most-likely due to non-radiative charge transfer occurring at narrowly-avoided crossings in at least two of the entrance channels. It has been demonstrated that, with a judicious choice of atomic species and degree of electronic excitation, it is possible to engineer experiments where the cold reactive species can co-exist for several minutes. From these results it is clear that a new generation of hybrid-atom ion devices, capable of the long coherence times needed for proposed hybrid atom-ion systems [SRD10, DFZ04, SBC11, C00, SML05, Hud09] is in reach. Subsequent work has successfully characterized the role of the electronic excitation in the $\text{Ca}^+ + \text{Rb}$ system [HEH13], including direct observation of the molecular ion reaction product.

6.5 Appendix A: Time-variation of the atom-ion overlap factor

As the Ca MOT exhibits non-uniform particle densities on length scales comparable to the size of laser-cooled ion cloud, it is necessary to carefully consider the

effective density of reactants when evaluating the reaction rate constant. Further, because the chemical reaction leads to loss of ions, the ion cloud size shrinks during the reaction process, resulting in a time-variation of this effective density. This effect can cause various systematic shifts in the measurement of the rate constant if not taken into account. For example, if the ion and atom clouds are nonconcentric, as the ion cloud shrinks the observed reaction rate slows as a result of the reduced reactant density. Thus, to properly measure the reaction rate constant, the time evolution of the effective reactant density is explicitly included via a term that quantifies the spatial overlap of the reactants, defined as $\phi(t) = \int \hat{\rho}_{Ca}(\vec{r})\bar{\rho}_I(\vec{r})d\vec{r}$, where $\hat{\rho}$ denotes a peak normalized density and $\bar{\rho}$ denotes an integral normalized density. With this definition, the evolution of the number of Ba^+ , N , ions is given as:

$$\frac{dN}{dt} = -k\rho\phi(t)N \quad (6.1)$$

where the product of the reaction rate constant, k , to the peak neutral density, ρ , is taken to be the unbiased reaction rate constant Γ_{CEX} .

In principle, $\phi(t)$ can be found numerically from measurements of the cloud widths and relative positions via dual camera fluorescence imaging at various times. However, due to disparate levels of brightness, the MOT and the ions cannot be simultaneously imaged with the current image filtering systems. Therefore, in practice, the relative position of the two clouds and their initial density profiles are measured separately.. With the assumption that the Ca MOT has a roughly spherical gaussian density distribution, while the ion cloud has an ellipsoidal (cigar-shaped) gaussian density distribution, the time evolution of the overlap factor is numerically calculated (in units of Γ_{CEX}^{-1}), as in figure 6.5. Thus, for the determination of Γ_{CEX} for each decay measurement, a numerical function describing the overlap factor is uniquely determined from the images so that the

only physical fitting parameter is Γ_{CEX} . That is, each experimental decay curve is effectively fit to $\frac{dN}{dt} = -\Gamma_{\text{CEX}}\phi(\Gamma_{\text{CEX}}t)N$ with an uniquely determined ϕ . In order to use numerical fitting algorithms, the solution of the differential equation is taken to be $N(t) \sim \exp(-\Gamma_{\text{CEX}}\phi(\Gamma_{\text{CEX}}t))$. This amounts to an assumption that the overlap factor is slowly varying on the timescale of the reaction and for the data reported here leads to systematic error $\leq 30\%$, which is well within the reported experimental error.

6.6 Appendix B: Calculation of Ba⁺ fractional electronic state populations

Because the trapped Ba⁺ ions are laser cooled via a closed three-level electronic system, see figure 6.1(a), it is necessary to account for optical coherence effects to accurately calculate the excited state population fractions realized in the experiment. This is accomplished by solving for the steady-state solution to the quantum Liouville equation for an eight-level optical Bloch Hamiltonian. This calculation is significantly complicated for the MOTION trap due to the presence of a large quadrupole magnetic field necessary for the operation of the Ca MOT as its direction and strength vary in a non-trivial way. This calculation is briefly outlined in this appendix.

Working under the electric dipole approximation in the interaction picture, the eight bare $|\{LS\}, J, M_J\rangle$ states have one of three energies, $E_S = 0, E_P = \delta, E_D = \Delta$, where δ and Δ are the one- and two-photon detunings, respectively. To simplify the geometry of the problem, the quantization axis is defined to be parallel to the direction of the linearly polarized laser used to drive the Ba⁺ $5^2\text{P}_{1/2} \leftarrow 5^2\text{S}$ cooling transition, which is approximately vertical in the labora-

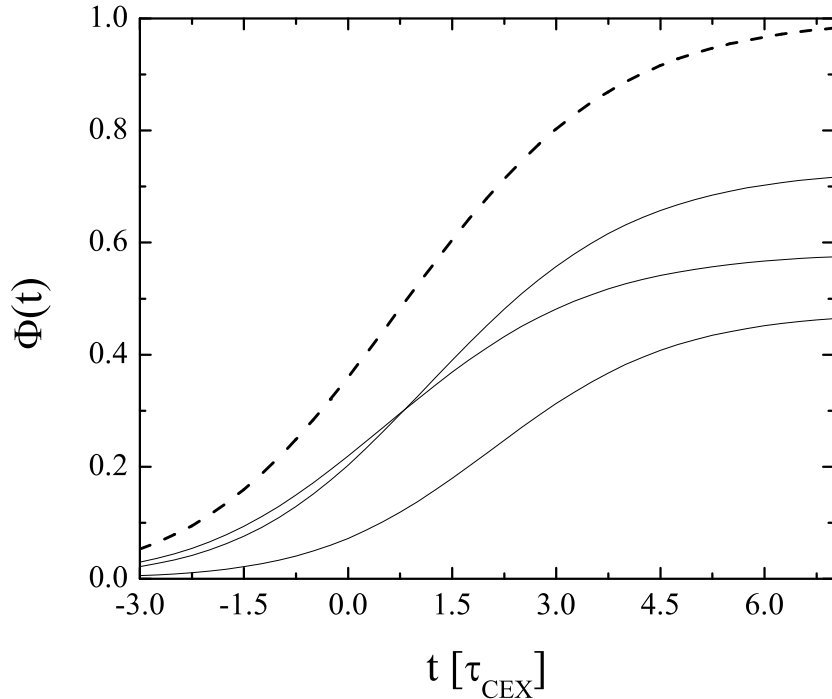


Figure 6.5: The dashed line shows the numerical calculation of the overlap factor as a function of charge exchange lifetimes expired in the case of perfect alignment of relative MOT to ion cloud position, with typical experimental waists and aspect ratio. The other three lines are randomly selected numerical calculations from actual experimental data to show how imperfect alignment changes the curve.

tory frame. The laser used for population repumping on the $5^2\text{P}_{1/2} \leftarrow 5^2\text{D}_{3/2}$ transition is collinear with this cooling laser and is linearly polarized at an angle θ with respect to the z-axis. As a result, the Rabi frequencies for transitions between the different $|\{LS\}J, M_J\rangle$ states of the Ba^+ ion are given as:

$$\Omega_{L',L}(J', M'_J, J, M_J, E_{1,q}) = (-1)^{J'-M'_J} \begin{pmatrix} J' & 1 & J \\ M'_J & q & M_J \end{pmatrix} \langle L', J' | |\vec{d}| | L, J \rangle \mathcal{E}_{1,q} / \hbar \quad (6.2)$$

where the index $L = {}^2\text{S}, {}^2\text{P}_{1/2}, {}^2\text{D}_{3/2}$ and $\mathcal{E}_{1,0} = \mathcal{E}_z$ and $\mathcal{E}_{1,\pm 1} = \pm \frac{1}{\sqrt{2}}(\mathcal{E}_x \mp i\mathcal{E}_y)$ are the spherical irreducible tensor representation of the electric fields of the laser resonant with the $L' \leftarrow L_J$ transition – with the defined geometry, $\mathcal{E}_x = \mathcal{E}_y = 0, \mathcal{E}_z = \sqrt{\frac{2I_{PS}}{\epsilon_0 c}}$ for the cooling laser and is $\mathcal{E}_x = \sqrt{\frac{2I_{PD}}{\epsilon_0 c}} \sin \theta, \mathcal{E}_y = 0, \mathcal{E}_z = \sqrt{\frac{2I_{PD}}{\epsilon_0 c}} \cos \theta$ for the repumping laser, where I_{PL} is the intensity of the laser driving the transition. The angle θ is experimentally chosen to mitigate the effects of coherent population trapping and, in this experiment, is typically $\theta \approx \pi/3$.

Likewise, the effect of the spatially varying magnetic field is calculated by including in the Hamiltonian the diagonal and off-diagonal Zeeman matrix elements:

$$\langle J', M'_J | -\vec{\mu} \cdot \vec{B} | J, M_J \rangle = -\frac{e\hbar}{2m_e} g(J) \left(\frac{J_+ B_{1,-1}}{\sqrt{2}} - \frac{J_- B_{1,1}}{\sqrt{2}} + J_o B_{1,0} \right) \quad (6.3)$$

where $B_{1,0} = B_z$, $B_{1,\pm 1} = \mp \frac{1}{\sqrt{2}}(B_x \pm iB_y)$, and $g(J) = (3J(J+1) + S(S+1) - L(L+1))/(2J(J+1))$. Over the spatial extent of the Ba^+ ion cloud the magnetic field is well approximated as $\vec{B} = \frac{\delta B}{\delta z} \left(\frac{x}{2}\hat{x} + \frac{y}{2}\hat{y} + z\hat{z} \right)$, with $\frac{\delta B}{\delta z} = 0.7 \text{ T/m}$ for the experimental parameters. Off-diagonal Zeeman couplings are ignored between different electronic states, e.g. matrix elements between $\text{P}_{3/2}$ and $\text{P}_{1/2}$ states.

Finally, the effects of spontaneous emission and the resulting decoherence are included via the Lindblad super-operator and result in a relaxation matrix, Γ_r , whose diagonal elements account for the decay and growth of electronic state populations at the respective spontaneous emission rate and whose off-diagonal elements account for the concomitant decay in coherence at half of the spontaneous emission rate.

With all of these terms taken together, the optical Bloch Hamiltonian,

$$i\hbar \frac{d\rho}{dt} = [H(\vec{x}, I_{PS}, I_{PD}, \theta, \delta, \Delta), \rho] + i\hbar\Gamma_r, \quad (6.4)$$

is then solved numerically for given experimental conditions, i.e. a given set of $\{I_{PS}, I_{PD}, \theta, \delta, \Delta\}$, to find the steady state Ba^+ populations at each location in the ion cloud. A spatial average is then performed over these values to give the average electronic state populations of the Ba^+ ions for the experimental conditions. For the conditions studied in this work, this technique gives excellent agreement with measured values of Ba^+ electronic populations, as evidence in figure 6.2(a).

6.7 Appendix C: ab initio calculation

The RMR-RAS-CI method is based on partitioning the occupied and unoccupied molecular orbitals into subsets, which define the construction of the molecular wave function. These symmetry subsets are: core orbitals, which do not participate in the CI procedure; valence orbitals, which are occupied and can have single, double, and triple excitations; and virtual or unoccupied orbitals, which have double excitations. Though the inactive core orbitals do not contribute to correlation effects, they create, a so-called, “self-consistent-field sea” in which the other electrons move. The valence and virtual orbitals are correlated in the

CI expansion. Since the dimension of the CI molecular wave function increases dramatically with the size of the active orbital space, it is necessary to apply restrictive measures.

A non-orthogonal basis set is constructed from numerical Dirac-Fock atomic orbitals as well as relativistic Sturmian functions. A symmetric re-expansion of atomic orbitals from one atomic center to another simplifies the calculation of many-center integrals. At large interatomic separations the molecular wave function has a pure atomic form that appropriately describes the molecular dissociation limit. The $1s^22s^22p^6\dots4d^{10}$ closed shells of barium and $1s^22s^22p^6$ closed shells of calcium atom are included in the core. An R-dependent all-electron core potential is calculated exactly and included in the Hamiltonian. The core-valence basis set is constructed from Dirac-Fock core $5s$ and $5p$ orbitals for *Ba* and $3s$ and $3p$ orbitals for *Ca*. Valence Dirac-Fock orbitals are $6s$, $5d$, and $6p$ for *Ba* and $4s$, $3d$, and $4p$ for *Ca*, while Sturm virtual $7s$, $7p$, $6d$, $8s$ $8p$ and $7d$ orbitals for *Ba* and $5s$, $5p$, $4d$, $6s$, $6p$, and $5d$ orbitals for *Ca* are also included.

CHAPTER 7

Sympathetic vibrational cooling of translationally cold molecules

7.1 Introduction and Motivation

Compared to atoms, molecules have a rich internal structure that offers a host of opportunities for technological and scientific advancement. These include critical insight into quantum chemistry [Smi92, BD01, Kre08], new methods for the manipulation of quantum information [ADD06, SBC11], and improved tests of discrete symmetry violation [KL95, VCG10] and fundamental constant variation [DSS08, CFK09, HLS06]. Harnessing this potential, however, typically requires the preparation of cold samples of molecules in their quantum rovibrational ground state. Unfortunately, the same intricate structure which gives rise to the aforementioned applications severely complicates efforts to produce such samples. Of these complications, energy stored in long-lived vibrational levels is particularly problematic. This is because optical transitions between vibrational levels are not governed by strict selection rules, making laser cooling difficult, and because traditional collisional, or sympathetic, cooling methods are inefficient at quenching molecular vibrational motion [KSF09]. The results detailed in this chapter experimentally demonstrate that collisions with ultracold Ca atoms efficiently quench the vibrational motion of trapped BaCl⁺ molecules at a rate com-

parable to the classical scattering rate. This is over 4 orders of magnitude more efficient than demonstrated in traditional sympathetic cooling schemes [KSF09]. The large cooling rate, a consequence of a strong $-C_4/R^4$ interaction potential due to the high polarizability of Ca, along with the low collision energies involved [Fer86], leads to molecular samples with $\geq 90\%$ vibrational ground state occupancy. This demonstration is allowed by the development a novel thermometry technique that relies on relative photodissociation yields. While a modest decrease in vibrational temperature is observed in these experiments, the large rate allows, with straightforward improvements, the production of molecular samples in the ground vibrational state in less than 100 ms. As sympathetic cooling of molecular rotational motion is far more efficient than vibrational cooling in traditional systems, it is also expected that this method efficiently cools the rotational motion of the molecules. This result should hold for many different combinations of ultracold atoms and molecules, yielding a general technique for cooling a variety of molecules to their absolute quantum ground state and ultimately realizing the long-sought opportunities offered by the internal structure of molecules.

Precision control over the quantum states of atoms has allowed tremendous advancement in both applied and fundamental physics, ranging from ultra-precise clocks [CHK10] and gravity gradiometers [MFF02], to stringent tests on discrete symmetry violations [GSL09] and the production of exotic phases of matter like degenerate Bose and Fermi gases [Lev12]. Extension of these studies to the next simplest such physical system, *i.e.* a diatomic molecule, promises even further advancements. Typically, the starting point for these studies is the production of an ultracold sample, which in the case of atoms, is usually attained via the technique of laser cooling. Applying this technique to molecules, however, is technically challenging, due mainly to the molecular vibrational degree of freedom which has no associated angular momentum. Thus, unlike transitions between

different rotational and electronic levels, transitions between vibrational levels of a molecule are not governed by strict selection rules. As a result, in general, a molecule simply cannot scatter the necessary number of photons needed to enter the ultracold regime before spontaneously decaying to long-lived vibrational levels which are out of resonance with the cooling lasers. While it does appear a subset of molecules are potentially amenable to laser cooling, as has been recently demonstrated for SrF [SBD10] and YO [HYS13], a more general cooling technique is highly desirable. One promising, general method is to use a sample of laser-cooled ultracold atoms to collisionally, *i.e.* sympathetically, cool a co-trapped sample of molecules to ultracold temperatures. Particularly attractive for this technique are charged molecules which, in contrast to neutral molecules, can be trapped over a broad temperature range for extended periods of time in radio-frequency ion traps, allowing ample time for sympathetic cooling to occur.

Sympathetic cooling of charged molecules has been demonstrated with both laser-cooled atomic ions and cryogenic buffer gases [KSF09]. Unfortunately, neither of these methods can produce molecules which are simultaneously ultracold in both their internal and external degrees of freedom. On the one hand, sympathetic cooling with co-trapped, laser-cooled atomic ions quickly cools molecular ions to very low translational temperatures, but due to the long range nature of the Coulomb interaction, the method yields little internal state relaxation of the molecules at low collision energies [OZW06]. To overcome this limitation, techniques of optical pumping [SjS10, SRD10], and state selective photoionization of neutral molecules [TWW10] have been employed in tandem with atomic ion sympathetic cooling to produce translationally cold molecular ions in the lowest few rotational states. Despite their impressive results, these techniques lack generality as they are restricted to certain classes of molecules and require molecule specific lasers. On the other hand, sympathetic cooling with helium buffer gas has

been demonstrated to yield cooling of both the translational and internal states of molecules due to the short-range nature of the ion-neutral collision; however, the method can only be used at temperatures above ~ 300 mK, the point at which the vapor pressure of ^3He becomes negligibly small. Additionally, it is relatively inefficient due to the low polarizability of the helium atoms.

An alternative to these methods is sympathetic cooling with ultracold, laser-cooled atoms which both allows access to sub-mK translational temperatures and is predicted to be very efficient at cooling the internal degrees of freedom as their polarizabilities are over 100 times that of helium atoms. While this scheme uses proven technologies that have existed for decades, it has not previously been implemented, possibly due to the misconception that molecular ions cannot undergo primarily elastic collisions with neutral atoms that are amenable to laser cooling but instead undergo charge exchange chemical reactions leading to energetic neutralized molecules. Previously, it has been shown [Hud09] that, on the contrary, many combinations of molecular ions and neutral laser-cooled atoms (including the particular combination of species used here) can co-exist without undergoing a chemical reaction when colliding. This chapter details the first evidence of internal state cooling of trapped molecular ions due to sympathetic cooling collisions with ultracold atoms co-located in a magneto-optical trap (MOT). While the internal temperatures produced are modest, the method is found to be extremely efficient, with a vibrational quenching rate constant on the order of the classical, or Langevin, atom-ion scattering rate constant. Thus, straightforward improvements (see 8.6) in the apparatus should allow production of molecular samples in the ground vibrational state in less than 100 ms. The following sections detail a novel technique developed to measure relative populations of molecular vibrational levels, briefly describe the apparatus and experimental approach used to implement the sympathetic cooling of BaCl^+ molecules, and

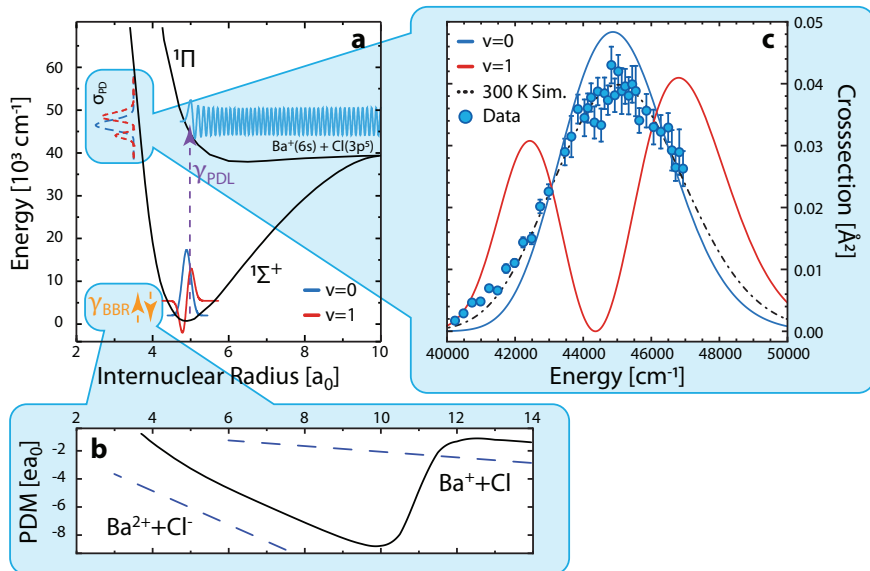


Figure 7.1: Photodissociation Thermometry of BaCl^+ . **a** Potential energy curves for the $X\ ^1\Sigma^+$ and $A\ ^1\Pi$ electronic states and a schematic indicating the photodissociation thermometry method described in the text. The different shapes of the $v = 0$ and $v = 1$ wavefunctions give rise to the different frequency responses of the two levels to the photodissociation laser. **b** The permanent dipole moment (PDM) of BaCl^+ calculated as described in Methods. **c** Improved data (with standard error) obtained for the cross-section of the $A\ ^1\Pi \leftarrow X\ ^1\Sigma^+$ of the photodissociation transition in BaCl^+ using a separate ion trap and time-of-flight system. The dashed line is the thermally averaged cross-section at 300 K. Also shown are the improved calculations of the individual vibrational level contributions of the $v = 0$ and $v = 1$ levels. Although the model described in the methods section incorporates the lowest 4 vibrational levels, here only the $v = 0$ and $v = 1$ levels are shown for clarity.

present data detailing the measured vibrational sympathetic cooling rate.

7.2 Method of Vibrational Level Thermometry

In order to quantify the degree of sympathetic cooling of the molecular internal levels it is necessary to measure the population distribution of rotational and vibrational levels. Typically, this measurement is accomplished with spectroscopic techniques, such as predissociation or multiphoton ionization/dissociation spectroscopy; however, like most molecular ions, the detailed spectroscopic information necessary for these techniques does not yet exist for BaCl⁺. To overcome this challenge, vibrational spectroscopic thermometry is demonstrated utilizing broad-band molecular photodissociation without requiring detailed molecular structure data. This novel and general method is applicable to any molecule that can be directly photodissociated and allows an accurate measurement of the molecular vibrational temperature, as long as the internal state population can be probed on a timescale shorter than or comparable to the vibrational relaxation time. The method exploits the fact that, although the photodissociation cross section is broad, the individual vibrational levels have unique frequency responses for photodissociation, which are given from [CSK11]:

$$\sigma_{vJ}(\nu) = 4\pi^2 \alpha a_0^2 \frac{h\nu}{E_h} \frac{1}{2J+1} \sum_{J'MM'} \frac{|\langle A, EJ'M' | d_z | X, vJM \rangle|^2}{(ea_0/\sqrt{E_h})^2} \quad (7.1)$$

where E_h is the Hartree, a_0 is the Bohr radius, and α is the fine-structure constant. The quantity $\langle A | d_z | X \rangle / (ea_0/\sqrt{E_h})$ is dimensionless and contains both the radial and angular parts of the dipole moment, d . Here, $|X\rangle$ and $|A\rangle$ label the rovibrational wavefunction of the ground ${}^1\Sigma^+$ and first electronic excited ${}^1\Pi$ state, respectively, as shown in figure 7.1a. Because the continuum wavefunctions associated with solutions of the A ${}^1\Pi$ molecular potential are highly oscillatory, the

expectation value of the dipole moment operator can be accurately approximated by considering only the nature of $|A\rangle$ near the classical turning point, R_C . Thus, if the repulsive potential is approximated as linearly dependent on R , with slope $\frac{dV_A}{dR}$, near $R = R_C$, these wavefunctions are well-described by Airy functions and the vibrational photodissociation cross-section is given as:

$$\sigma_{vJ}(\nu) = \frac{4\pi^2\alpha}{e^2} \frac{h\nu}{2J+1} \left(d(R_C) \frac{\phi_v(R_C)}{\sqrt{dV_A/dR}\Big|_{R=R_C}} \right)^2 \quad (7.2)$$

where ϕ_v are the real-valued vibrational wavefunctions. As R_C is linearly related to the photon energy, the shape of the photodissociation cross-section directly reflects the squared probability amplitude of the molecular vibrational wavefunction.

Implementing the photodissociation thermometry technique to be discussed requires knowledge of a photodissociation transition from which an accurate determination of the ϕ_v can be obtained. A BaCl⁺ photodissociation transition is characterized in [CSK11]. However, to implement the thermometry technique it was necessary to better measure the shape of the photodissociation cross-section. To this end, a compact time-of-flight apparatus is developed, described in [SCR12], which has allowed the photodissociation spectrum of BaCl⁺ to be measured with $\sim 10^3$ times improvement in precision over that of ref. CSK11. From this data, shown in figure 7.1(c), slight adjustments to the molecular potentials determined in the earlier measurements have been made, and the contributions of the individual vibrational states to the total photodissociation cross-section can be identified, the lowest two of which (*i.e.* v = 0 and v = 1) are shown as solid lines in figure 7.1(c)

With the individual vibrational level cross sections in hand, the basic idea of the thermometry technique can be understood as follows. Once equilibration has

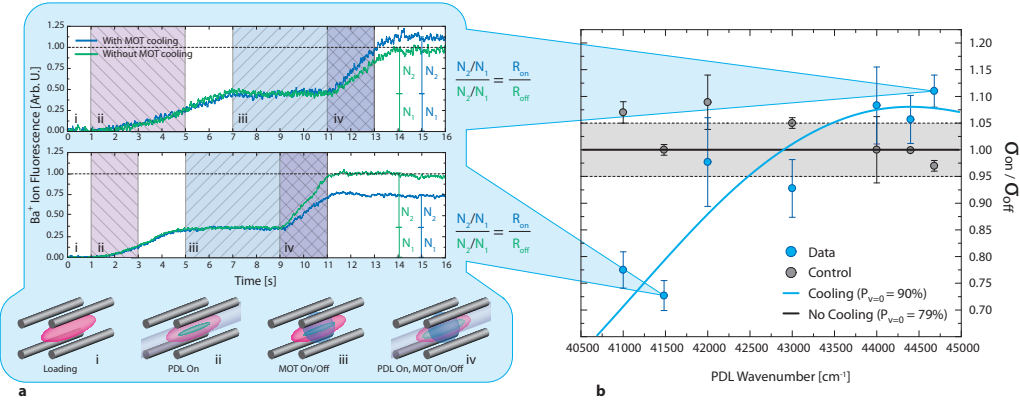


Figure 7.2: Measurement of MOT-induced vibrational quenching of BaCl^+ ions.

a Example traces of the Ba^+ ion fluorescence measured during the experimental sequence. Initially the trap is loaded with a pure BaCl^+ sample (i). The photodissociation laser (PDL) is then turned on to create a mixed sample of BaCl^+ and Ba^+ ions (ii). Once the Ba^+ ions have been laser cooled, the MOT is optionally turned on and the BaCl^+ ions are collisionally cooled by the ultracold Ca atoms (iii). Following that, the BaCl^+ ions are interrogated with the PDL to determine the amount of vibrational relaxation due to the MOT (iv). The ratio of Ba^+ ion number created in each instance of photodissociation is then compared for the two cases when the MOT was on and off. The top and bottom panels are data for a PDL wavenumber of $41,500 \text{ cm}^{-1}$ and $44,675 \text{ cm}^{-1}$, respectively.

b The average of all data points (with standard error) obtained, as described in the Methods, is plotted for various photodissociation wavenumbers. The blue points are cooling data and the grey points are a control analysis which should be consistent with unity (see Methods). The curves are the expected result from a rate equation model of the experimental sequence described in Methods and the agreement with the data shows the BaCl^+ sample has been cooled to a ground state vibrational population of $\sim 90\%$ in the average case.

been established with the 300 K vacuum apparatus, $\approx 79\%$ of the molecules are in the $v = 0$ level, $\approx 15\%$ are in the $v = 1$ level, and the remaining population is essentially all in the $v = 2$ and $v = 3$ levels. While the model introduced later incorporates all of these levels, for illustration purposes it is sufficient to consider only the $v = 0$ and $v = 1$ levels. Because the wavefunction of the $v = 1$ level has a zero crossing (see figure 7.1(b)), the photodissociation cross section contains a node which occurs at $\lambda = 225$ nm ($\nu/c = 44,400$ cm $^{-1}$). A laser tuned to this wavelength will photodissociate molecules in the $v = 0$ level, but will not affect molecules in the $v = 1$ level. Furthermore, as can be inferred by thermally averaging equation 7.2, at the temperatures relevant to this work the rotational distribution does not change the resulting cross sections. As a result, if collisions with the cold Ca atoms quench the vibrational motion of the molecules, it will be signaled by an enhanced photodissociation rate at this wavelength. Conversely, by tuning the photodissociation laser (PDL) closer to one of the maxima of the $v = 1$ level cross section, MOT induced quenching will instead be signaled by suppression of the observed photodissociation rate as molecules are being cooled to the $v = 0$ level, lowering the total cross-section. From the change in photodissociation rate at different photodissociation wavelengths, the change in vibrational temperature can be inferred.

7.3 Experiment

The apparatus used to measure these effects is shown in figure 7.3, and typical data obtained to demonstrate vibrational cooling is plotted in figure 7.2. To begin, BaCl $^+$ molecules created by laser ablation are trapped in a linear quadrupole ion trap (i), which is co-located with a MOT that can be loaded with ultracold Ca atoms. Interestingly, without any cooling, the starting point of the BaCl $^+$

molecules internal and translational temperatures are determined by different mechanisms and are established in the first few seconds after loading the trap. Internally, the BaCl^+ molecules thermalize to 300 K due to blackbody radiation emitted by the room temperature vacuum apparatus, while translationally the temperature is set by the ion dynamics in the trap. To attain the high signal-to-noise ratio measurements necessary to demonstrate vibrational cooling, the system requires the use of an ion cloud composed of approximately $\sim 10^3$ BaCl^+ molecules. At these numbers, the initial translational temperature of the BaCl^+ molecules is primarily set by collisional heating through self-induced micromotion interruption [DeV09] to ~ 1000 K. Therefore, for this experiment, additional translational cooling of the BaCl^+ molecules is implemented by sympathetic cooling with co-trapped laser-cooled Ba^+ ions. These Ba^+ ions are loaded into the trap with unit efficiency by photodissociating a fraction of the BaCl^+ molecules using a pulsed dye laser as discussed in [CSK11] (ii), and once laser-cooled, sympathetically cool the BaCl^+ molecules to millikelvin translational temperatures [OZW06]. These atomic ions also provide an important diagnostic as their fluorescence is used both as a means of determining overlap of the MOTion trap as well as the initial, proportional number of BaCl^+ molecules. Once the BaCl^+ molecules are translationally cold, as indicated by the steady-state value of the Ba^+ ion fluorescence and camera images of the ion cloud, the MOT is turned on (iii) and short range collisions with the highly polarizable, neutral Ca atoms result in internal state cooling. To measure the effect of the cooling, the PDL is then turned on once again (iv), and the increase in fluorescence yields the number of Ba^+ ions produced, thus allowing an inference of the ground state vibrational population of the BaCl^+ molecules. Several systematics can be eliminated (*e.g.* the variable number of BaCl^+ molecules produced in the loading process, possible inaccuracies in the absolute cross section value, and/or the PDL intensity) by

taking the ratio of the final amount of Ba^+ ions produced to the initial amount, $R_{\text{on}} = N_2/N_1$ (see Methods and figure 7.2(a)). This measurement sequence is repeated without turning on the Ca MOT and the same ratio is recorded (denoted R_{off}). It is straightforward to show that in the linear regime the ratio $R_{\text{on}}/R_{\text{off}}$ is equivalent to the ratio of the total cross sections in each case, *i.e.* $\sigma_{\text{on}}/\sigma_{\text{off}}$. This sequence is repeated several times at several PDL wavenumbers and the analyzed data are plotted in figure 7.2(b). These data are compared to a control analysis at each wavelength, which compares measurements where the MOT remained ON or stayed OFF for both points and thus should be consistent with unity (see Methods). From this comparison, it is clear that the deviation of the actual data is the result of MOT-induced vibrational relaxation.

7.4 Results and Conclusion

A simple rate equation model quantifies the cooling efficiency. The model incorporates the continual redistribution of the molecules internal states due to black-body radiation throughout the experiment, as well as MOT-induced vibrational relaxation when the MOT is present (see Methods and Supplementary Information). Because the MOT density and overlap with the ions vary for each of the data points in figure 7.2(b), a best fit line using the rate equation is unsuitable. Rather, using the calculated effective MOT density for each data point, along with the rate equation model, an average vibrational quenching rate constant of $k \approx 1 \times 10^{-9} \text{ cm}^3/\text{s}$ is determined. Using this rate constant with the typical peak MOT density of $\approx 1 \times 10^9 \text{ atoms/cm}^3$ and a typical overlap factor of 0.2, the average expected values of $R_{\text{on}}/R_{\text{off}}$ as predicted from the rate equation model are calculated and shown in figure 7.2(b) as the solid blue curve. From the good agreement of the data with this curve, the rate equations are used to extract the

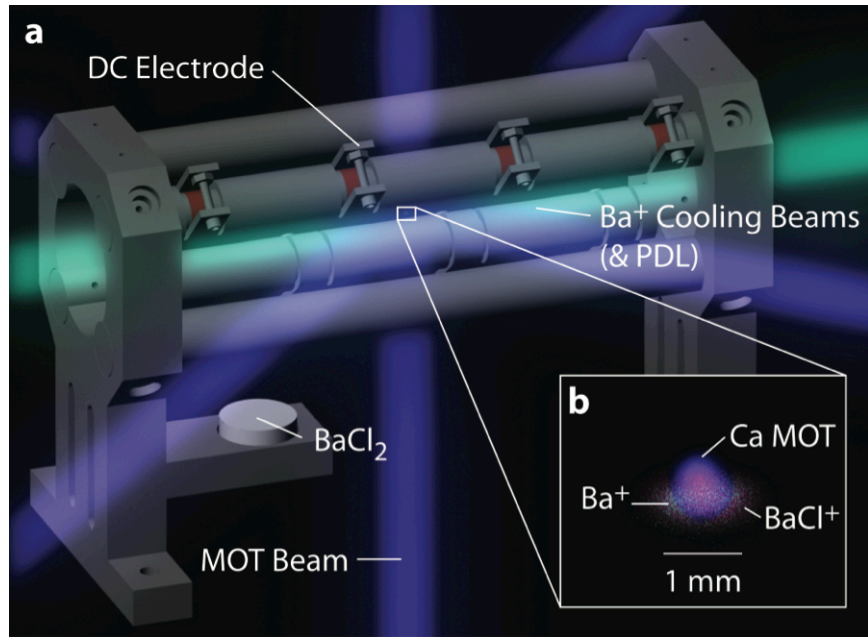


Figure 7.3: Panel (a) shows the hybrid magneto-optical and ion trap (MOTion trap) system used in these experiments. The secular frequencies for the BaCl^+ and Ba^+ ions are 33 and 43 kHz, respectively. BaCl^+ ions are loaded by laser ablation of a solid BaCl_2 target and are then photodissociated into Ba^+ by a pulsed laser beam ($\sim 1 \text{ mJ}$ at a 10 Hz repetition rate) directed down the center axis of the ion trap. The Ba^+ ions are laser cooled, and thus translationally cool the remaining BaCl^+ molecules, by a pair of axial cooling lasers. The intensities of the 493 nm and 650 nm lasers at the ion cloud are $\sim 500 \text{ mW/cm}^2$ and $\sim 100 \text{ mW/cm}^2$, respectively. Spatial overlap between the trapped Ca and the ions is verified by two nearly-orthogonal EMCCD imaging systems. Panel (b) shows an overlaid set of experimentally obtained images of the Ca MOT and laser-cooled Ba^+ cloud. These images have been colorized (the Ca in purple, Ba^+ in green) for clarity. Also included, is a reconstruction of the expected position, taking into account the diminished trap depth due to higher mass, of the BaCl^+ molecular cloud (in red).

vibrational ground state population, which in the case of sympathetic cooling by the Ca MOT is found to be $N_o \geq 90\%$ and set by the competition of sympathetic cooling and blackbody radiation heating from the chamber walls. In contrast, if the MOT had provided no cooling, the data would have been consistent with the solid black line which corresponds to a vibrational ground state population of $\sim 79\%$.

Rigorous quantum scattering calculations of the vibrational quenching rate have never been performed in any similar system. However, the large value of the rate constant, over 10^4 times that observed in traditional sympathetic cooling schemes, is likely due to the strong, long-range $-C_4/R^4$ interaction potential, which occurs between Ca and BaCl⁺. Classically, particles colliding on this potential with energy E and an impact parameter less than the Langevin length, $b_L = \sqrt{C_4/E}$, undergo violent collision trajectories that rapidly spiral inward towards $R = 0$. Quantum mechanically speaking, the system forms a three-body collision complex with reduced mass μ at the Langevin rate, $k_L = \pi\sqrt{2C_4/\mu}$, which facilitates redistribution of the original molecule's vibrational energy between all three particles. Thus, when the collision complex predissociates back into its parent constituents, this energy is carried away by the sympathetic cooling partner, leaving the molecule in a lower vibrational state. The fact that the observed rate constant is nearly the Langevin rate ($k \approx k_L/5$) supports this interpretation [Fer86] and suggests that sympathetic cooling of molecular internal degrees of freedom will be possible with any collision partner that gives rise to long-range interactions conducive to collision complex formation – *e.g.* dipole-dipole and monopole-dipole collisions.

Additionally, no evidence has been observed of any chemical reactions between BaCl⁺ and electronically excited Ca atoms in the MOT, even though they

are energetically allowed. This supports the arguments of [SRK12] and [BJ92], which state that these collisions are suppressed because the long-range atom-ion interaction shifts the atom out of resonance with the atomic cooling laser at large atom-ion separations and thus prevents atoms in their electronically excited state from colliding with the molecular ions. This also provides an important simplification to the originally proposed method [Hud09] as it eliminates the need for an optical dipole trap for the ultracold atoms. Furthermore, it implies that the rate of sympathetic cooling collisions can be safely increased without loss of molecules. Several straightforward experimental modifications, such as modifying the ion trap geometry so that ion cloud is fully contained inside the Ca MOT and replenishing the Ca atom source, are expected to increase the effective Ca MOT density and, as a result the sympathetic cooling collision rate, by ~ 250 times its current value. Such improvements would produce a ground vibrational state population $\geq 99\%$ in less than 100 ms, as well as potentially render the currently employed Ba^+ translational sympathetic cooling unnecessary.

Finally, due to incomplete spectroscopic information for the BaCl^+ molecule, direct measurement of rotational energy quenching is currently not possible. However, as all evidence from sympathetic cooling systems employed to date shows that collisional quenching of the rotational energy proceeds at a much higher rate than vibrational quenching, it is likely that molecules have been cooled rotationally as well; experiments are currently underway to prove this. Ultimately, the minimum attainable rovibrational temperature with this method will be set by the ion radial micromotion, which determines the lowest collision energy with the Ca atoms. This collision energy can be estimated from the amplitude of the micromotion, which is given as a function of electric field as $a_{mm} = \sqrt{2} \frac{eE(\vec{r})}{m\omega\Omega}$, where ω (Ω) are the secular (drive) frequencies [MD68]. The average micromo-

tion kinetic energy ($\frac{1}{2}mv_{mm}^2 = \frac{1}{2}m(a_{mm}\Omega)^2$) over a typical cloud profile in the MOTion apparatus for typical trap parameters (i.e. a radial pseudo-potential of depth ~ 10 eV), is ~ 1 K, while the maximum possible micromotion contribution to a collision (for ions residing at the edge of the cloud) is ~ 10 K. As the BaCl⁺ vibrational splitting corresponds to ~ 500 K, this energy is inconsequential for vibrational cooling. However, the BaCl⁺ rotational splitting is ~ 0.5 K meaning that in the present experiment the lowest few rotational levels could still be populated. Therefore, future experiments aiming to produce samples of pure rovibrational ground state molecules should use smaller samples of molecular ions, so that the cloud size and thus the micromotion are reduced to the point where collision energies are below the molecular rotational splitting. In the present experiment, this regime can likely be reached by working with a sample of order one-tenth the size of the current cloud.

In conclusion, a broadly applicable, general technique has been demonstrated to cool the vibrational motion of polar molecules. A general technique, photodissociation thermometry, has been developed for probing molecular vibrational states, which can be used to determine the vibrational quenching rate constant and ground vibrational state population. This result opens the door for a new route to ultracold molecules and is expected to enable myriad experiments in quantum chemistry [Smi92, BD01, Kre08], precision tests of fundamental physics [LBL11], and quantum information/simulation [ADD06, SBC11].

7.5 Methods

The data acquisition system takes an alternating sequence of data points where the MOT is either on or off during the measurement, and acquires over 100 data points at each PDL wavelength. For each wavelength, the ratio of successive

points (R_{on}/ R_{off}) is computed so as to eliminate unidentified time varying systematics and the results are averaged. For the control analysis, the ratios between successive data points of the same type (*e.g.* $R_{on,1}/ R_{on,2}$, or $R_{off,1}/ R_{off,2}$, *etc.*) are instead computed and the results are averaged. See full methods section for details.

The Ba^+ ion production in the experiment is modelled with a simple rate equation model which includes the lowest 4 vibrational levels of the BaCl^+ molecules, and accounts for population redistribution among the levels throughout the experimental sequence. This redistribution of the levels is due to collisions with the ultracold Ca atoms as well as spontaneous and stimulated emission and absorption of photons by the molecules due to the blackbody radiation field. As knowledge of the spontaneous and stimulated emission and absorption rates requires the dipole moment of the electronic ground state of BaCl^+ , it is calculated directly using a nonrelativistic multiconfigurational second-order perturbation theory (CASPT2) implemented in the MOLCAS software suite [KLM03]. The result is shown in figure 7.1(b).

To eliminate several systematics when comparing the data to this model, *e.g.* the variable number of BaCl^+ ions produced in the loading process, possible inaccuracies in the absolute cross section value and/or the PDL intensity, the fluorescence is used as a measurement of Ba^+ ions created in each instance of photodissociation, and take the ratio of the final amount to the initial amount, $R_{on} = N_2/N_1$ (see figure 7.2(a)). Next, this measurement sequence is repeated without turning on the Ca MOT and record the same ratio, denoted R_{off} . It is straightforward to show that in the linear regime the ratio R_{on}/ R_{off} is equivalent to the ratio of the total cross sections in each case, *i.e.* σ_{on}/σ_{off} . The entire sequence is repeated over 50 times producing a series of data points $R_{on,1}, R_{off,1},$

$R_{on,2}$, $R_{off,2}$, To eliminate monotonic, time varying systematics, the ratios $R_{on,1}/R_{off,1}$, $R_{on,2}/R_{off,2}$, . . . as well as the ratios $R_{on,2}/R_{off,1}$, $R_{on,3}/R_{off,2}$, . . . are computed and averaged. The average of these two results is recorded, and the experiment is repeated at various dissociation wavelengths. These data are plotted as blue circles in figure 7.2b. Also plotted are the black circles, which are the results of a control analysis where the calculation is performed for the ratios $R_{on,1}/R_{on,2}$, $R_{on,3}/R_{on,4}$, . . . as well as $R_{off,1}/R_{off,2}$, $R_{off,3}/R_{off,4}$, . . . , etc. and averaged. As these controls are comparisons of the same data type, they should yield results consistent unity and their variability about it can be used as an indication of the variability in the actual data. Their close agreement with unity shows that the deviation of the true data is due to MOT-induced vibrational relaxation and not a statistical coincidence.

The number of Ba^+ ions created in each instance of photodissociation can be obtained using the following rate equations

$$\begin{aligned}\frac{dN_i}{dt} &= \rho\Phi(k_{i+1,i}N_{i+1} - k_{i,i-1}N_i) - \frac{\sigma_i(\lambda)I}{h\nu}N_i \\ &\quad + \sum_{j>i} A_{ji}N_j - \sum_{j*N_j + \sum_{j\neq i} B_{ij}\rho(\omega)(N_j - N_i)\end{aligned}*$$

$$\frac{dN_{Ba}}{dt} = \sum_i \frac{\sigma_i(\lambda)I}{h\nu}N_i$$

where N_i denotes the number of BaCl^+ molecules in the i^{th} vibrational level (the rotational states have been averaged over) and N_{Ba} is the number of Ba^+ ions. The first term in Eqns. (3) is due to the MOT induced quenching. $k_{i+1,i}$ is the vibrational quenching rate constant for the $i + 1^{th}$ level to the i^{th} level, ρ is the peak density of the MOT, and Φ a factor that quantifies the degree of overlap of the atom and ion clouds. The overlap quantity is defined $\Phi = \int \hat{\rho}_{Ca}(\vec{r})\bar{\rho}_I(\vec{r})d\vec{r}$, where $\hat{\rho}_{Ca}$ is the unit-peak normalized Ca atom density and $\bar{\rho}_I$ is the unit-integral normalized BaCl^+ density, thus $0 < \Phi < 1$. In the liquid phase in which the trap

is operated, it quantifies the effective MOT density experienced by each ion as they move in the trap. The second term results from the photodissociation (σ_i is the wavelength dependent cross section for the i^{th} level, I is the PDL intensity, and ν is the laser frequency). Finally, the last three terms are due to spontaneous emission and BBR induced stimulated emission and absorption written in terms of the spectral energy density, $\rho(\omega)$, and the Einstein A and B coefficients [LF04]. Calculating these coefficients requires knowledge of the dipole moment of the electronic ground state of BaCl^+ , $A_{ij} = \frac{2}{3} \frac{\omega_{ij}^3 \mu_{ij}^2}{\epsilon_0 h c^3}$, where $\mu_{ij} = \langle j | d(R) | i \rangle$ and $|n\rangle$ represents the ro-vibrational wavefunction of the n^{th} ro-vibrational level of the ground electronic state. As this dipole moment function was previously unknown, it is calculated using a nonrelativistic multiconfigurational second-order perturbation theory (CASPT2) implemented in the MOLCAS software suite [KLM03]. The result is shown in figure 7.1(b). With this in hand, the necessary rates are calculated according to ref. LF04, and are ~ 1 Hz. The model incorporates the lowest 4 vibrational levels in the model and ignores terms where $|i - j| > 1$. This model, along with the calculated effective density of the MOT [RSK11] for each data point, allows a determination of the vibrational quenching rate constant, k , as well as the ground state vibrational population, N_0 .

7.5.1 Photodissociative vibrational thermometry: caveats

Central to the technique of photodissociative thermometry is the model used to extract the molecular vibrational temperature. As can be seen in equation 7.3, the model only includes collisions that change the vibrational quantum number by one vibrational quantum. This result, which is predicted by standard Landau-Teller vibrational relaxation theory [Chi74], has been shown to be valid for low vibrational excitation in experiments with supersonic molecular beams, see for

example [BS85]. However, as there is yet no theory for vibrational relaxation of BaCl⁺ by Ca, this point merits further investigation. Nonetheless, even if $|\Delta v| = 2$ collisions did occur at an appreciable rate, the measured relaxation rate can still be interpreted as the realized cooling rate and the central result of this work does not change.

Also neglected in the model of photodissociative thermometry are any effects of collisions involving electronically excited Ca atoms, which could occur because the sympathetic cooling takes place in presence of the laser light used to cool the Ca atoms. Because electronic excitation of the atom represents a large amount of internal energy, there are several processes that are possible if this energy was deposited in the CaBaCl⁺ collision complex, including vibration excitation and/or chemical reaction. However, because the excited Ca 4¹P state has a very different polarizability than the Ca 4¹S state, ~ 157.0 a.u. and ~ 55 a.u., respectively, during the collision the strong monopole field of the ion alters the atomic transition frequency such that the Ca MOT lasers are shifted far from resonance for atom-ion separations of many hundred Bohr radii, a_0 . Thus, though a collision leading to reaction may begin with a Ca atom in an electronically excited state, the short radiative lifetime of the Ca atom (4.5 ns) means that the atom will spontaneously decay back into the ground state before the atom and ion are close enough to react ($< 10a_0$) for the low collision energies encountered in this experiment. Similar effects are observed in 6, where the chemical reaction rate between Ca and Ba⁺ did not measurably vary as a function of Ca excited state fraction. This result is most simply explained by the aforementioned Stark detuning effect, as also discussed by [BJ92],

For example, in the magneto-optical trap used in this work the fraction of the atoms in the excited state has a maximum of ~ 0.2 at large atom-ion separation.

For distances less than $500 a_0$ the cooling lasers are shifted out of resonance, thus the atomic excitation must survive for the time it takes to traverse this distance if an excited state collision is to occur. For ions with collisions energies of 10 K (the highest collision energy likely in this experiment from micromotion far off the RF null) this effect leads to a suppression of excited state collisions by a factor ~ 10 relative to ground state collisions, rendering them unobservable in the current experiment even if they occurred at the Langevin rate. Given that only a small fraction of the ions at the edge of the crystal have 10 K micromotion energy and that this suppression factor grows rapidly, e.g. at 10 mK excited state collisions are suppressed by $\sim 10^6$, excited state collisions should have an undetectable effect. Furthermore, collisions involving electronic excitation of the Ca atom would most likely lead to some chemical reaction, however, no evidence for any chemical reactions between Ca and BaCl⁺ in the MOTion trap have been observed. Therefore, the photodissociation thermometry model does not include any effects of electronic excitation.

CHAPTER 8

Outlook and loose-ends: progress of a direct search for the low-energy ^{229}Th nuclear isomeric transition in a thorium-doped solid with synchrotron radiation

This chapter is for covering the loose-ends and outlook for the work performed for this dissertation over the years. The main project covered in this chapter, a direct search for the thorium-229 ($I^p = 5/2^+ \rightarrow 3/2^+$) nuclear transition, is disjoint from the main subject of this thesis, but there has nonetheless been important work worthy of being written down.

By exposing thorium-doped LiSrAlF_6 crystals to tunable vacuum ultraviolet synchrotron radiation and recording any long-lived fluorescence, a direct search for the nuclear transition is performed.

8.1 Introduction

Since the work of Kroger and Reich almost four decades ago [KW76], it has been thought that the $A = 229$ isotope of thorium possesses the lowest energy nuclear excited state in nature. If true, the electromagnetic transition between the ground nuclear state and this excited nuclear state could enable a host of new technologies

and fundamental physics, including solid-state optical frequency references, next generation optical clocks, robust quantum memories, and sensitive probes of the fundamental constants of nature. The existence of a low-lying state in ^{229}Th , with an estimated natural linewidth, Γ_n in the range 0.1 -10 mHz [TZZ00,RP06], was indirectly established through measurements of γ -ray energies resulting from α -decay of ^{233}U [9]. Subsequent indirect measurements determined the isomeric state ($I^p = 3/2^+$) to be 3.5 eV above the ground state ($I^p = 5/2^+$) [HR94]; however, direct searches for UV emission from this magnetic dipole transition were unsuccessful [TZZ00]. Recently, a new indirect measurement has established that the transition energy is instead 7.6 ± 0.5 eV [BBB07], while another indirect technique suggests that the transition energy is ≤ 7.75 eV and $\Gamma_n = 0.006\text{--}0.009$ mHz [ZEN12]. As indirect measurements cannot control or modulate the measured signal, they are unable to confirm whether or not the observed signal originates from the thorium-229 transition or unknown systematic effects. It is therefore necessary to perform a direct measurement to conclusively measure the energy of the nuclear transition. This chapter details the results of a direct search for the thorium-229 nuclear isomeric transition, where a thorium doped LiSrAlF₆ crystal is illuminated with vacuum ultraviolet (VUV) synchrotron radiation and any resulting long-lived fluorescence is recorded. The preliminary search yields no evidence for the thorium nuclear transition, but due to several unfortunate systematic shortcomings, no new exclusions can yet be made for the transition properties. With planned straightforward improvements, a future experimental run is projected to be capable of ruling out nearly the entire search region of interest.

This chapter explains the experimental design and apparatus, discusses the first search results and analysis. The conclusion of this discussion is a projection for the future sensitivity of the experiment after improvements.

8.2 Experimental Design

The search for evidence of the nuclear transition is by directly observing fluorescence from the thorium-229 doped sample after exposure to a beam of VUV photons. Due to the expected narrow natural linewidth, pneumatic shutters are sufficient to control the timing of the experiment. First, the synchrotron light shutter is opened to directly expose the sample to a flux of VUV photons at a controlled energy. The sample is exposed to the beam for as long as reasonably possible, to allow for more stimulation into the long-lived excited nuclear state. Next, the beam shutter is closed and the shutter in front of the in-vacuum photomultiplier tube (Hamamatsu R7639 PMT) is opened so resulting fluorescence is captured by an in-vacuum imaging system, described in detail later. The resulting photon counting rate are then compared to a model whose inputs are the experimental systematics (light collection efficiencies, beam flux, beam exposure time, and thorium density) and the transition properties (energy and natural linewidth). The number of nucleii in the excited state after being exposed to the synchrotron beam for t_e seconds can be calculated as

$$N_e = \frac{BN_{Th}}{\Gamma + 2B}(1 - \text{Exp}(-(2B + \Gamma)t_e)). \quad (8.1)$$

Where B is the Einstein stimulation coefficient given by

$$B = \frac{4}{6} \frac{\lambda^2}{2\pi} \Phi \frac{\Gamma}{\Gamma_b + \Delta}, \quad (8.2)$$

where N_t is the total number of thorium nucleii addressed by the beam, Φ is the photon count per unit area of the synchrotron beam, λ is the wavelength of the transition, $\Gamma(\Gamma_b)$ is the natural (broadened) linewidth, and Δ is the bandwidth of the beam. Thus, after measuring and accounting for the dopant density of the thorium-229 and the light collection efficiencies, the photon counting rates

measured directly after shuttering the synchrotron beam set constraints on the natural linewidth and energy of the transition.

8.3 Experimental Apparats

8.3.1 $^{229}\text{Th}:\text{LiSrAlF}_6$ crystal

The $^{229}\text{Th}:\text{LiSrAlF}_6$ crystal was grown by AC Materials, using ^{229}Th provided by Oak Ridge National Laboratory. LiSrAlF crystals were found to be VUV transparent with no long-lived background excitation in earlier trips to the ALS with undoped and ^{232}Th doped samples. To measure the density of dopant ^{229}Th , the activity of the sample is measured using a GaAs gamma ray detector. The radiation is measured at three known activity peaks near 85, 193, and 210 keV, and find them to have count rates of 1750, 170, and 141 Hz respectively. Accounting for the known branching ratios in the gamma decay chain, 0.4265, 0.0441, and 0.0297 respectively, the resulting activity is about 114 nCi, or about 52 ng of ^{229}Th . The density in the sample is $\sim 10^{22} \text{ m}^{-3}$, two orders of magnitude lower than expected. This lack of dopant density is the one of the main limitations on the sensitivity of the work so far.

In addition to the gamma ray spectrum, there is a UV radiation background from the radioactivity in the crystal. Shown in figure 8.1 is a spectrum of light coming from the crystal centered at approximately 295 nm with a best fit Gaussian full-width at half-maximum of 75 nm. This spectrum was measured using a visible light photon counting Hamamatsu R1527P PMT, directly mounting the crystal to one of the arms of a McPherson 302 monochromator. This UV light constitutes the primary contribution to the constant background of the measurement.

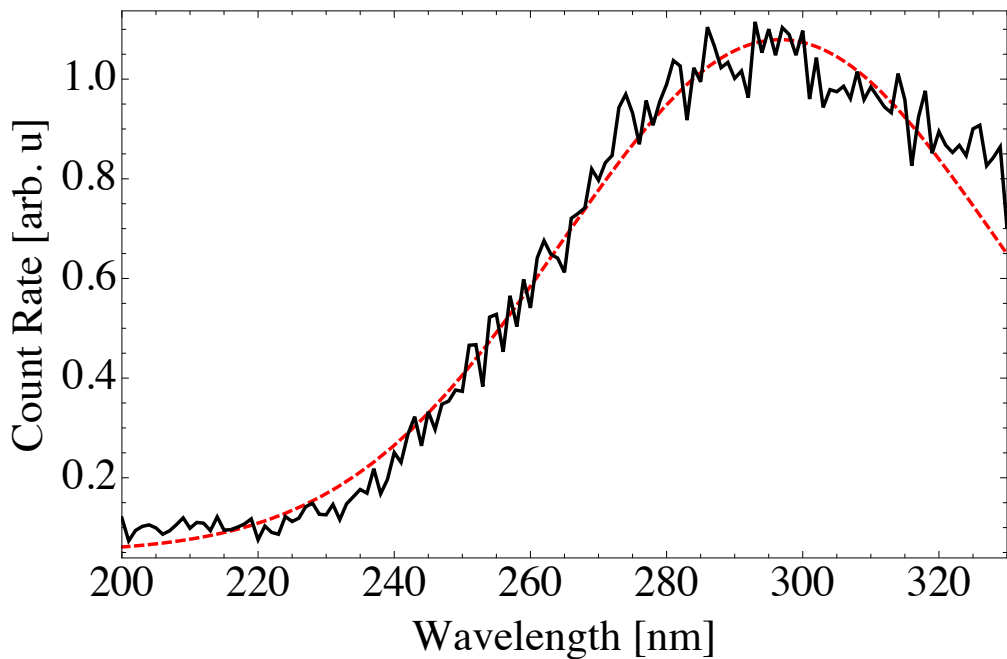


Figure 8.1: Results characterizing the UV radiation background in the thorium-229 doped sample. An emission peak is observed, in solid black, at 295 nm with best-fit, in dashed red, FWHM of 75 nm. In future measurements, VUV bandpass filters will be used to eliminate this background.

8.3.2 Advanced Light Source

The direct search for the thorium-229 ($I^p = 5/2^+ \rightarrow 3/2^+$) nuclear transition uses direct fluorescence excitation via the tunable synchrotron light source at the Advanced Light Source (ALS) beamline 9.0.2 terminal 1 (T1). The photon flux of the beam is characterized with a Opto Diode Corporation (ODC) ODD-SXU-001 VUV damage resistant photodiode, calibrated against a NIST-certified ODC AXUV-100G photodiode. The photon flux is nominally at specification when the synchrotron ring energy is at the typical operational value of 1.9 GeV. However, as shown in Fig 8.2, the flux is low nearly an order of magnitude when the synchrotron is run in the lower energy configuration, 1.5 GeV, which allows for use of photons with energies below 7.5 eV. The lack of flux at the lower photon energies is another of the primary limiting factors for the constraints on the transition at $\lambda > 165$ nm.

8.3.3 Fluorescence detection apparatus

The fluorescence is measured by direct photon counting using a Hamamatsu R7639 PMT and a SRS430 Multi-channel scaler. The thorium doped LiSrAlF₆ crystal is mounted at the end of a lens cage system, with optical axis length of approximately 430 mm from the sample to the PMT. Two lithium fluoride (LiF) lenses, with nominal focal lengths of 75 mm and 250 mm, are used to image the light onto the photocathode. A schematic diagram of the optics mounting flange is shown in figure 8.4. Lithium fluoride lenses are chosen because they have the best available transmission in the VUV. However, since the energy range of interest is near the edge of the LiF transmission band, the index of refraction and transmission varies significantly over the search range of the experiment causing a large chromatic variation in collection efficiency. The measured transmission

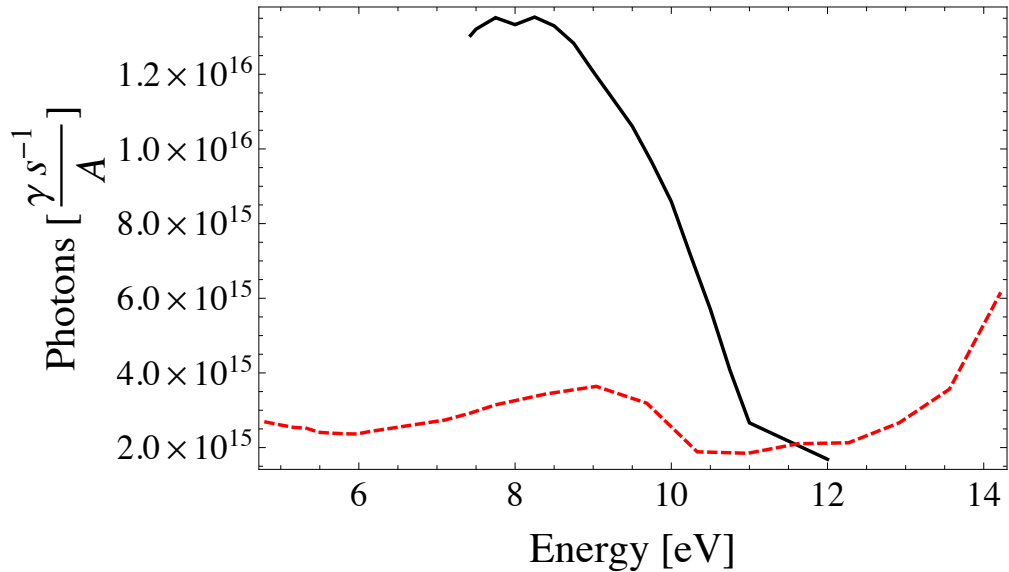


Figure 8.2: Results for the photon flux measurement at beamline 9.0.2 T1 at the Advanced Light Source using a NIST traceable photodiode. In dashed red, the measurement for the 1.5 GeV operation. In solid black, the result for normal operation at 1.9 GeV ring energy. The rate is normalized to the ring current. The drop off at higher energies seen in the black trace is due to the MgF window and Argon gas filter in the beamline. The apparent increase in flux near 14 eV during low energy operation is likely a harmonic leak through.

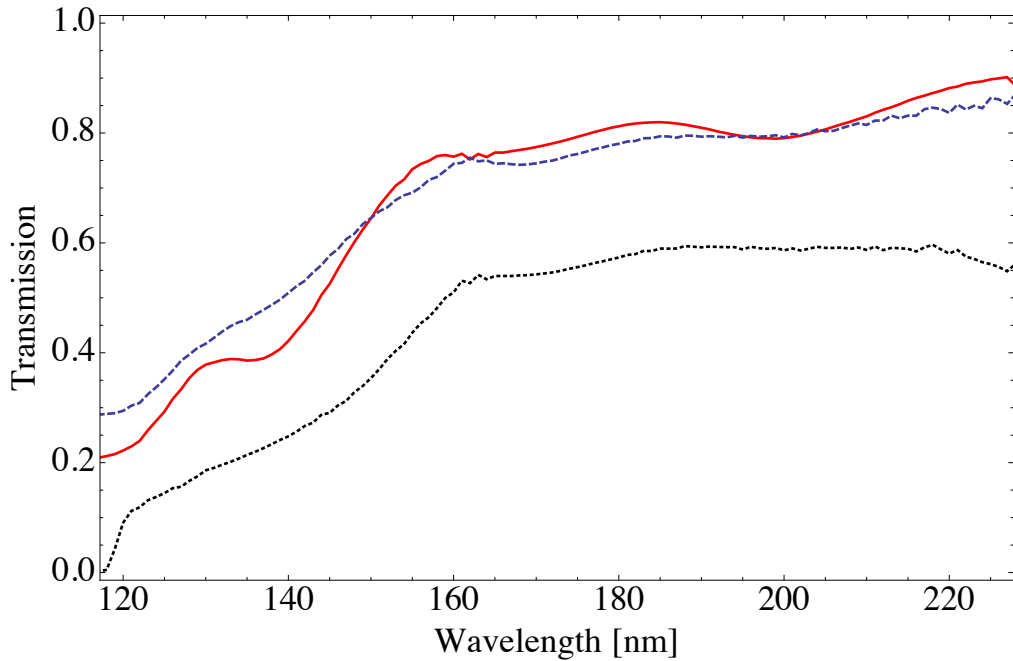


Figure 8.3: Transmission curves measured for the $f = 250\text{mm}$ LiF lens (blue, dashed), the $f = 75\text{mm}$ (red, solid), and the LiSAF crystal itself (black, dotted). The transmission is measured using the McPherson 302 monochromator.

curves for both lenses, and the crystal itself are shown in figure 8.3. The arrangement of the lenses within the imaging system is carefully chosen to optimize the collection efficiency for a particular range of wavelengths.

The apparatus is constructed with two lens configurations, one for 1.9 GeV operation for searching the high energy search region and another for 1.5 GeV operation for the low energy search region. These configurations were chosen by using ZEMAX, a commercial imaging software suite, to optimize the collection efficiency for 159 nm and 190 nm, respectively. For each configuration, the calculation of the effective solid angle as a function of wavelength using both ZEMAX and a simple ray tracing program are in agreement.

To verify the accuracy of the simulation results, a series of calibration measure-

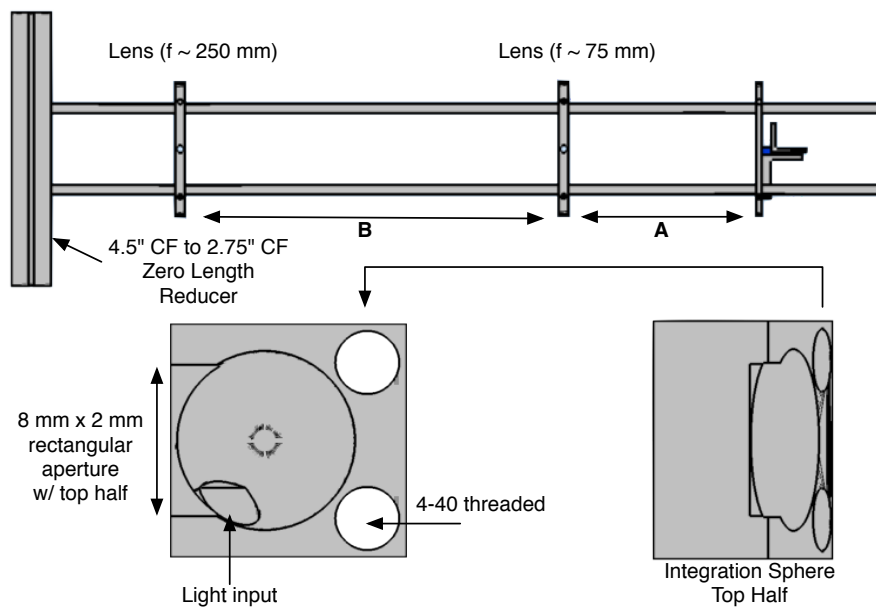


Figure 8.4: A schematic diagram of the optical mounting flange for the thorium experiment. Four 1/8" rods hold adjustable aluminum mounting rings that hold the LiF lenses in place. The 159 nm (190 nm) optimized configuration has A= 59.05 (64.44) mm and B = 225.65 (222.44) mm. Also shown in a drawing of the integration sphere used to measure the collection efficiency.

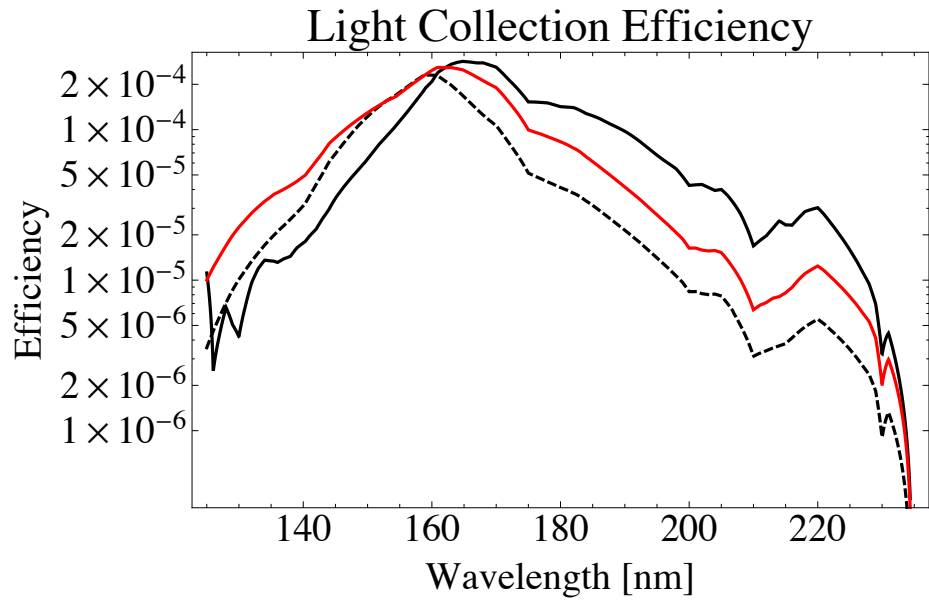


Figure 8.5: Overall light collection efficiency for the LiF lens collection system. The solid black line is a measurement of the collection efficiency performed by shining light from the deuterium lamp source, through the monochromator onto an integration sphere placed at the position the crystal occupies during the actual experiment. The dashed line is the result of a ray tracing model for a one-dimensional source of light at the crystal position. The red line is the result of a ray tracing model for a two-dimensional source of light at the crystal position, to better approximate behavior of the integration sphere.

ments are performed, using a McPherson in-vacuum spectrometer and deuterium lamp as a source of VUV light. The overall light collection efficiency is shown in figure 8.5. The solid black line is a measurement of the collection efficiency performed by shining light from the deuterium lamp source, through a McPherson 302 monochromator with a focusing elbow onto an integration sphere placed at the position the crystal occupies during the actual experiment. The absolute scale of the collection calibration experiment is set by comparing the signal with and without the imaging optics in place. With no optics in place, the solid angle fraction is simply calculated by geometric ray tracing. The dashed line is the result of a ray tracing model for a one-dimensional source of light at the crystal position. The red line is the result of a ray tracing model for a two-dimensional source of light at the crystal position, to better approximate behavior of the integration sphere.

To set an absolute scale for the count rate, one must take the product of the measured/simulated collection efficiency and the quantum efficiency of the R7639 PMT. The PMT is calibrated using the deuterium lamp with the NIST-traced photodiode (figure 8.6)

8.4 Initial Experimental Results

Most of the search data is acquired over the course of several normal 1.9 GeV operation shifts, which allow for longer beam exposure and fluorescence collection times(3000 s and 1500 s, respectively). For the search region to the red of ~ 7.5 eV, there is only data from one special beamtime shift at 1.5 GeV operation, allowing only for much shorter exposure and collection times (840 s and 420 s, respectively). The typical result is shown in figure 8.7. Regardless of the photon energy the crystal is exposed to, there is some short-lived fluorescence at

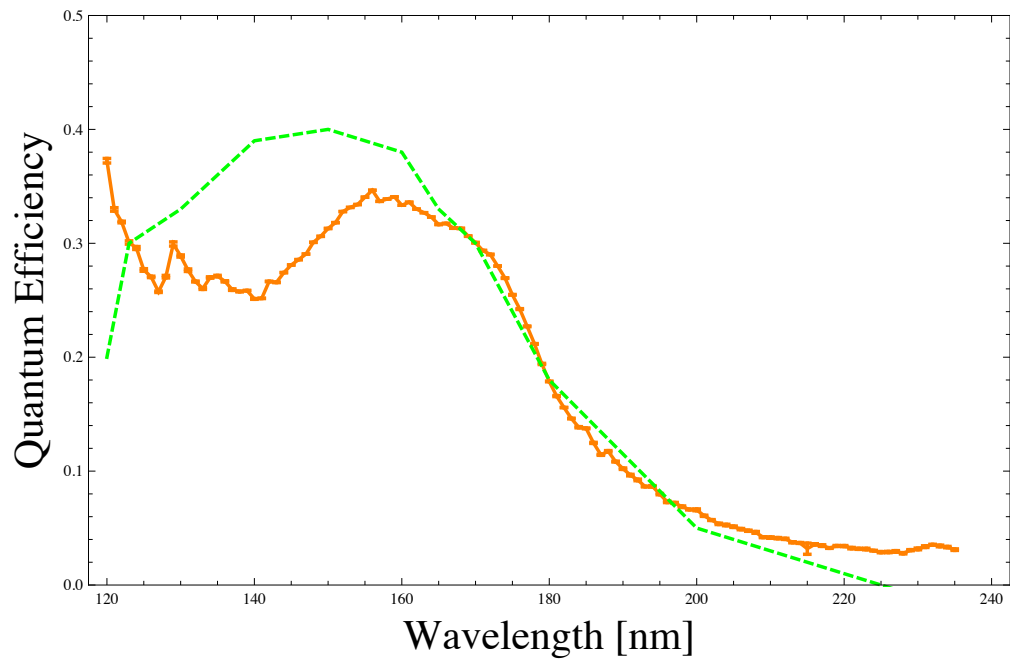


Figure 8.6: Results for the R7639 PMT calibration measurement using the NIST–traceable photodiode. Plotted in dashed green is the manufacturer’s specified typical quantum efficiency. In solid orange, the measured efficiency.

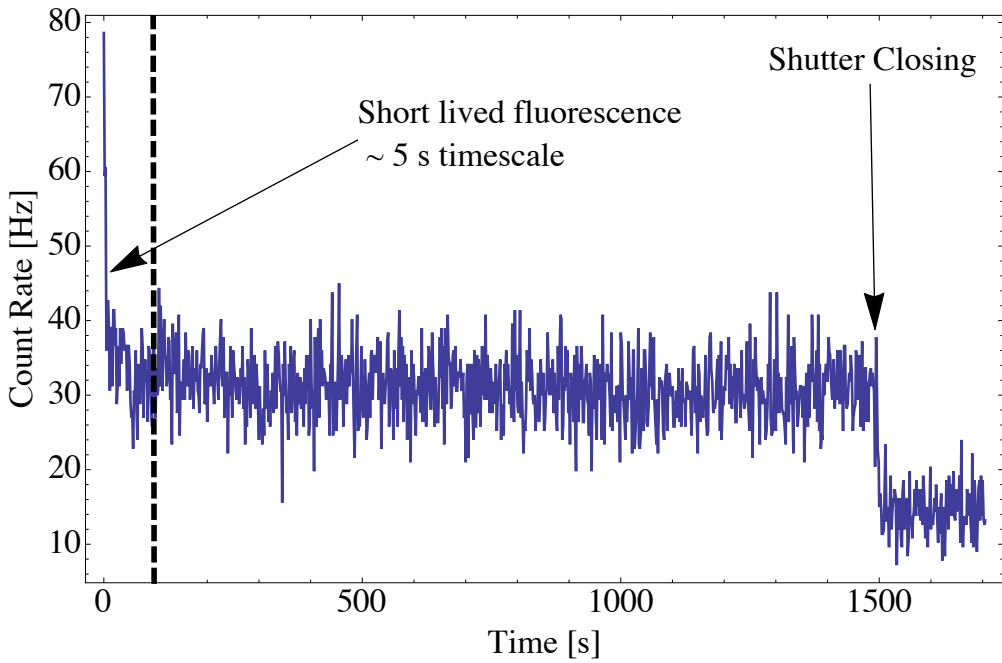


Figure 8.7: Typical measurement result from the first ALS run with the ^{229}Th -doped crystal. All the measurements had some short-lived fluorescence on a characteristic timescale of about 5 seconds. A portion of the measurement time is taken with the PMT shutter closed for a dark count rate.

the early time scale, followed by a roughly 30 Hz overall background, thought to be due to Cherenkov radiation from the crystal's radioactivity. To try to set a limit on longer timescale excitation, the data is statistically analyzed after cutting out the early time ($t_{cut} = 50\text{s}$ marked in figure 8.7). Unfortunately, due to a combination of the background noise and the low overall collection efficiency, no statistically significant limits can be claimed. For example, in a best case scenario of a transition near 160 nm with a natural linewidth of $\frac{\Gamma}{2\pi} = 1\text{mHz}$, the expected initial counting amplitude, by equation 8.1 taking into account the results of effects shown in figures 8.6, 8.5 and 8.3, is only a few Hz (at $t = 0\text{s}$).

8.5 Conclusion and Outlook

The limiting factors in the exclusion regions are limited measurement time, the light collection efficiency, limited flux during 1.5 GeV operations and the UV radiation background. Limited measurement time can be improved by additional time at the light source. The lack of light during 1.5 GeV operation might be improved via changes to mirror positions in beamline 9.0.2. The UV radiation background, which for the current systematic efficiency has a count rate comparable to the current expectation for the signal size, can be eliminated by added VUV bandpass filters to the optical system. To improve the light collection, a head-on, Hamamatsu R6836 PMT with larger effective collection area will be placed in vacuum roughly $\sim 1\text{cm}$ from the crystal, behind only the bandpass filter (E-Source Optics 130-FBB), and a Uniblitz lightproof in-vacuum shutter. With this PMT arrangement the light collection average will be roughly 6%, not including the transmission loss on the crystal face. There will also be no chromatic effects due to not using refractive collection elements. The sum of these improvements should easily lead to more than two orders of magnitude improvement in the sensitivity region.

8.5.1 Monte Carlo exclusion region estimation

To determine overall sensitivity of the improved light collection scheme, a model is used for the expected count rate $\gamma_{signal} = a_0 e^{-\Gamma t}$, where

$$a_0(\Gamma, \lambda) = \Gamma N_e(\Gamma, \lambda) \Omega \eta_{PMT}(\lambda) T_{FBB}(\lambda) T_{xtal}(\lambda). \quad (8.3)$$

N_e is calculated by equation 8.1. Ω is the light collection fraction taken to be least 6% for a 1D line source average. $\eta_{PMT}(\lambda)$ is the quantum efficiency of the PMT. $T_{FBB}(\lambda)$ is the transmission of the VUV bandpass filter, shown as measured in

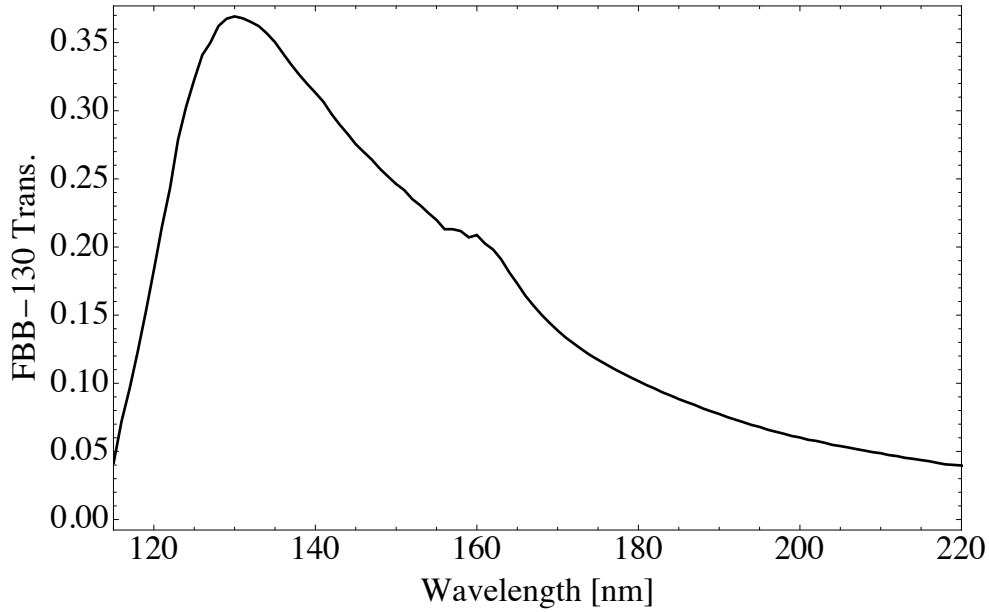


Figure 8.8: Transmission of the Esource Optics broadband VUV bandpass filter is shown as measured with the deuterium lamp source and McPherson spectrometer.

figure 8.5.1. $T_{\text{xtal}}(\lambda)$ is the transmission for passing through a single face of the crystal, taken to be the square root of the transmission measurement, for two faces, shown in figure 8.3.

For each point along the dashed exclusion line in figure 8.5.1, a fake data set produced by generating random integers from a Poisson distribution with mean $\mu = 40\text{Hz} \times 1.667\text{s}$. 1.667s is the counting bin size on the SR430 Multi-Channel Scaler when the experiment is performed at the 3000 s:1500 s duty cycle, so this mean simulates dark noise at a mean rate of 40 Hz. Each Monte Carlo set is then analyzed by first subtracting the mean of the last 5% of the data from the first 95% of the data set. This "zeroed" data set is then fit to a single decaying exponential $a_\tau e^{-t/\tau}$ for an array of lifetimes $\tau = (2\pi 6(1.2)^j \mu\text{Hz})^{-1}$ for $j = 0 \dots 40$. For each lifetime, the fitting algorithm reports a best fit and standard error $(\bar{a}(\tau), \sigma_a(\tau))$ for the only free parameter a_τ . For each fit, a t-statistic is

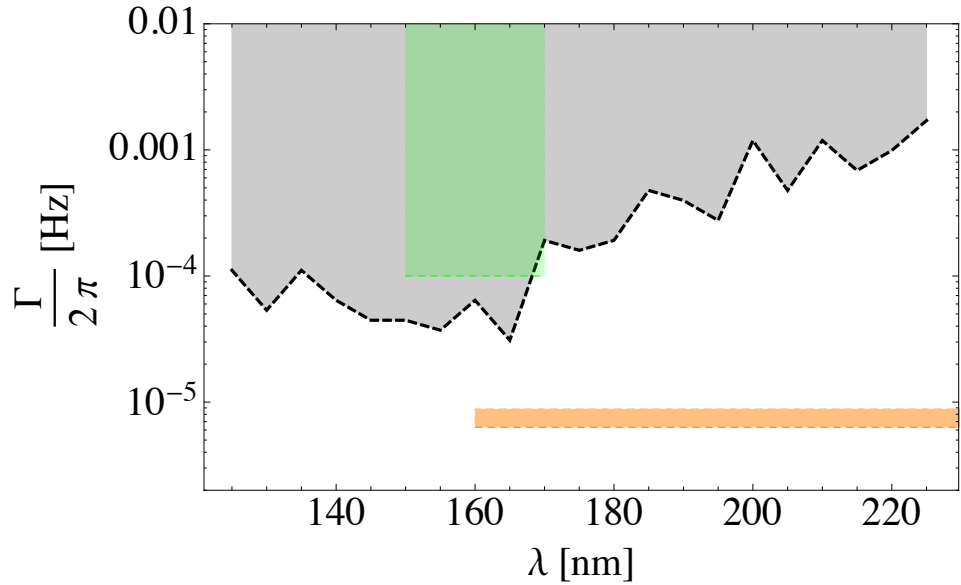


Figure 8.9: Monte Carlo calculation of 95%-confidence exclusion region, in grey, for the ^{229}Th transition properties after planned detection improvements are made. The green region is where the transition is expected to be by indirect measurement in [BBB07]. The orange region is the region where the transition is expected to be after a recent indirect de-excitation measurement [ZEN12]

calculated against the model calculation of equation 8.3 by

$$t = \frac{a_0(\lambda, \tau^{-1}) - \bar{a}(\tau)}{\sqrt{\sigma_a(\tau)^2 + \Delta a_0^2}}, \quad (8.4)$$

where $\Delta a_0 \sim 0.5a_0$ is the total estimated uncertainty in the fluorescence collection model in equation 8.3. The exclusion boundary is then defined by the largest τ such that $t \geq 1.65$. In other words, the mean amplitude of the expected fluorescence must be larger than the fitted amplitude to the Poissonian noise by the 95% confidence quadrature sum error bar. The results of this computation are shown in figure 8.5.1, along with search regions-of-interest from other indirect efforts [BBB07], [ZEN12].

8.6 The future of the MOTion trap - version 2.0

As of Spring 2013, a renovation of the hybrid trap system is underway. Three major improvements are being made to the system. The first improvement is making the ion trap field radius smaller. A smaller field radius facilitates the trapping of smaller ion numbers at higher trap depths, all other parameters held equal. With the smaller field radius, the trap parameters theoretically allow the formation of ion crystals. The second improvement is a higher magnification ($M=8$) imaging system capable of resolving single ions. The enhanced imaging is made possible by a re-entrant flange on the vacuum chamber and a custom objective lens system from Sill Optics. The third addition is a radial ejection time-of-flight (ToF) mass spectrometer for detection of trapped ion chemical reaction products. A schematic of the new vacuum chamber configuration, as well as a picture of the time-of-flight device, is shown in figure 8.10.

8.6.1 Ion trap version 2.0

The new version of the ion trap has a field radius of 6.85 mm, with the same rod diameter as the original trap. The field radius is chosen to meet three goals. First, the trap rods need to allow sufficient optical access to make a dense MOT. Using a variable beam expander (Thorlabs BE02-05-A) to shrink the trap beam waist, it is verified that the smaller beam waist required to not scatter off the ion trap rods does not significantly lower the MOT density. Second, the field radius is chosen such that, at typical trapping voltages, the thermal ion cloud radius, $r_{\text{thermal}} \simeq \sqrt{\frac{qeV_{RF}}{80\omega_s^2}}$, is roughly the same as the MOT radius, to maximize overlap. Finally, the field radius must leave enough space for an angled absorption imaging beam clearance. At $r_0 = 6.85$ mm, there is approximately 2 mm of clearance at the required absorption beam angle.

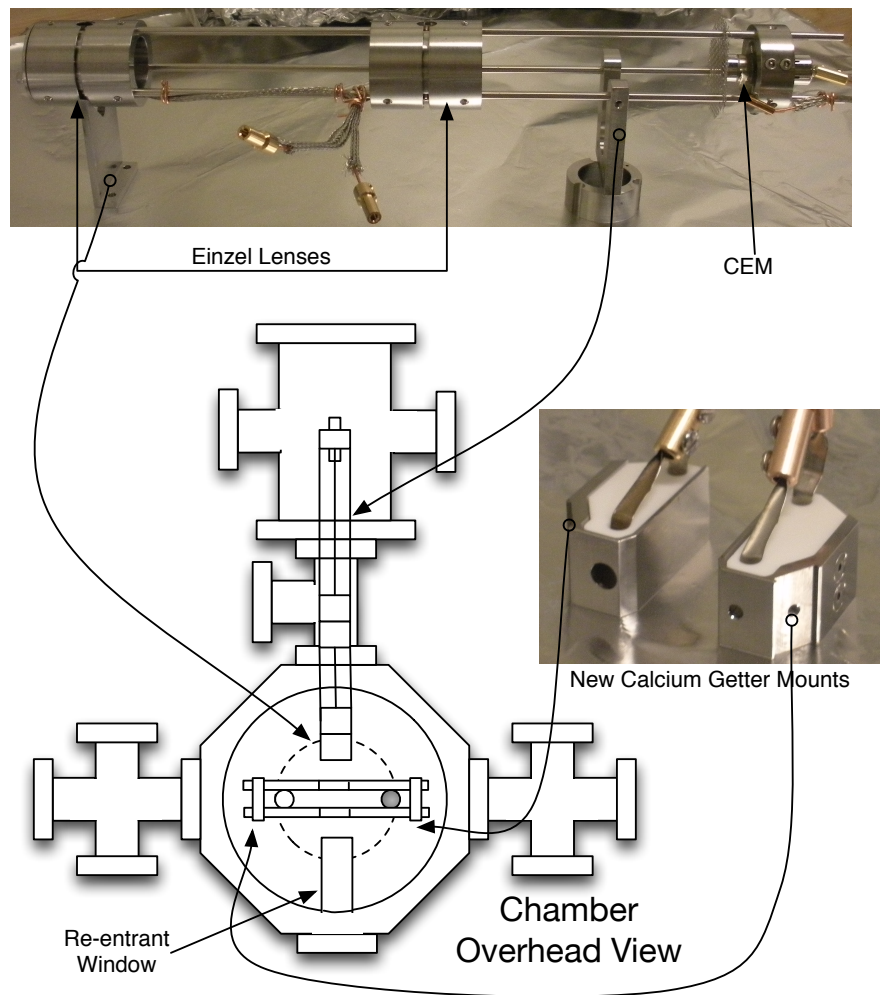


Figure 8.10: Schematic of MOTion trap v2.0. The time-of-flight ion optics are mounted in the former position of the Ca dispensers. New dispenser holders are mounted directly to the ion trap rod holders.

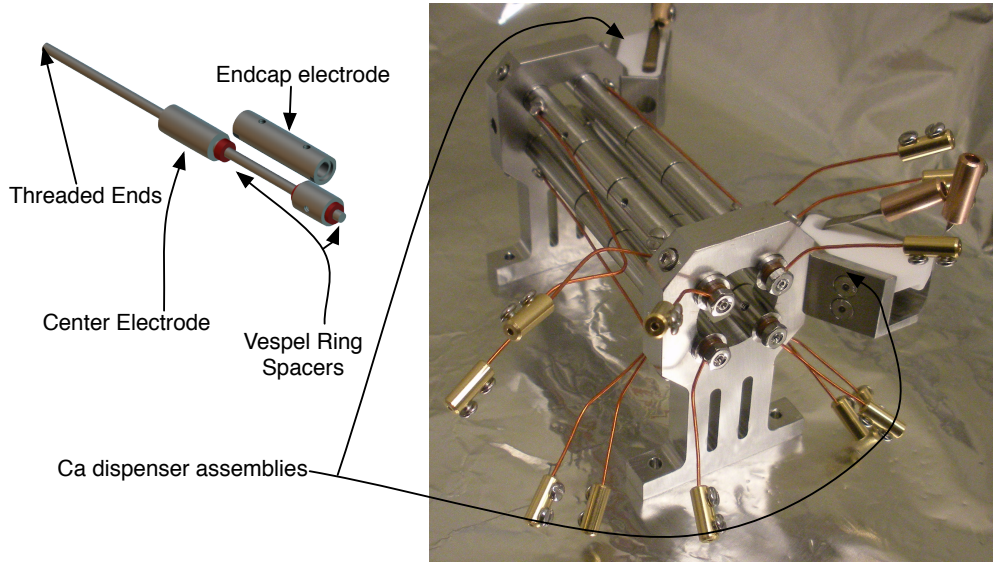


Figure 8.11: Picture of the second iteration ion trap and rendering of the segmented rod design.

The second iteration of the ion trap is a segmented rod model, with twelve total electrodes. The trap is shown fully constructed in figure 8.11, along with a rendering of the segmented rod design. A single piece of stainless steel forms the center electrode, upon which the outer electrodes slide on. Isolation between the different electrodes is provided by Vespel rings. The length of the center trap electrode (0.8 inch) is chosen, by *SIMION* simulation, such that the ion cloud aspect ratio can be tuned through 1:1 using a simple low voltage power supply ($V_{ec} < 30$ V). The segmented design is chosen to improve overall symmetry and has been found, in the simulations of [TRL12], to minimize axial micromotion in large ion clouds.

8.6.2 The radial ejection time-of-flight mass spectrometer

The radial ejection time-of-flight mass spectrometer design is essentially a duplicate of the one built for the BaCl₊ spectroscopy experiment [SCR12], with only minor changes for simplicity of assembly. The dimensions of the ion optics relevant to the performance of the ToF are identical to those in the spectroscopy apparatus, so it is expected that a similar level of resolution will be achieved ($\frac{\Delta m}{m} \sim 50$). This mass resolution is good enough to identify potential molecular ion charge exchange products when revisiting the experiments of chapters 5 and 6.

The time-of-flight distinguishes the ions based on their mass by pushing the ions towards the detector, imparting a roughly fixed amount of kinetic energy. For fixed kinetic energy, lighter ions will arrive at the detector. Detailed in the work of [WMD55] and shown in figure 8.12, a two stage acceleration scheme improves the mass resolution. The first stage consists of a smaller potential drop ($\Delta V \sim 200$ V), by application of a voltage difference between the pairs of rods as shown in figure 8.12. The first stage removes the ions from the trap region while minimizing variation in kinetic energy due to the initial spatial distribution of the ion cloud. The second stage uses a larger potential drop ($\Delta V \sim 1500$ V) over a short distance to accelerate the ejected ions to their final field free flight tube energy.

The ejected ions have an ensemble of velocity components orthogonal to the flight direction. The first Einzel lens, an ion optic that doesn't change the energy of the beam, is three ring electrodes. The outer two ring electrodes are grounded, and the center electrode is held at high voltage. This arrangement of potentials leads to a lensing effect on the off flight-axis velocity components. The spacing and voltage are chosen by simulation in *SIMION*. Some simulated flight

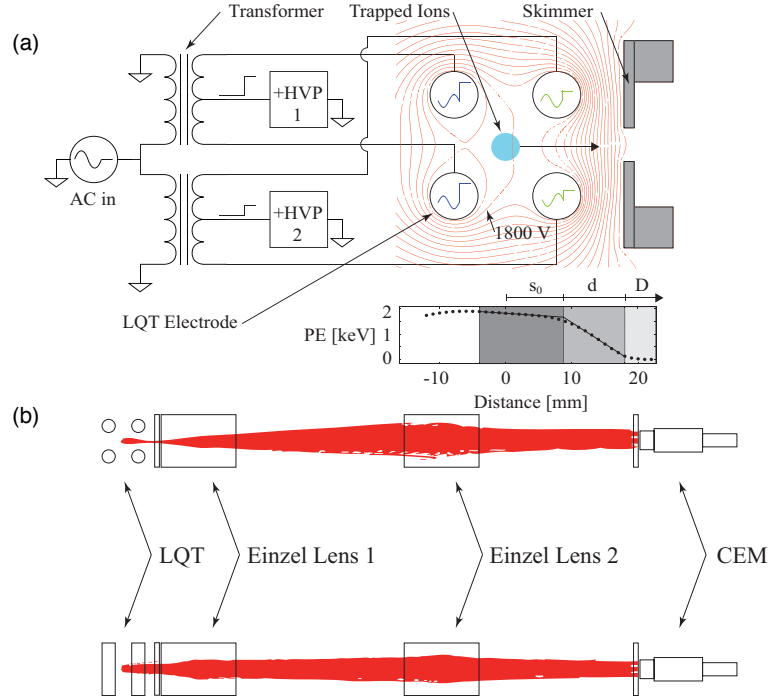


Figure 8.12: Schematic of the time-of-flight device operation. Panel (a) shows the configuration of the high voltage pulsing circuit for the trap rods for two stage acceleration into the flight tube. Panel (b) shows some results of *SIMION* trajectory simulations used to optimizing the collimation and collection of ejected ions.

trajectories are shown in part (b) of figure 8.12.

8.6.3 Outlook

The sum of the improvements to the MOTion trap unlocks the door to colder molecular ions and more precise atom-ion chemistry. The smaller, more symmetric ion trap design (section 8.6.1) will trap smaller ion clouds capable of being imaged with single ion resolution. The smaller, colder ion clouds will allow for even more efficient internal state relaxation. The integrated time-of-flight (section

8.6.2 allows unambiguous identification of atom-ion chemical reaction products and will facilitate accurate photodissociation spectroscopy experiments, such as those using predissociation or multiple photon ionization, for rovibrational state read-out.

REFERENCES

- [ADD06] A André, D DeMille, J M Doyle, M D Lukin, S E Maxwell, P Rabl, R J Schoelkopf, and P Zoller. “A coherent all-electrical interface between polar molecules and mesoscopic superconducting resonators.” *Nature Physics*, **2**(9):636–642, August 2006.
- [AEK12] M Arndt, A Ekers, W V Klitzing, and H Ulbricht. “Focus on modern frontiers of matter wave optics and interferometry.” *New Journal of Physics*, **14**(12):125006, December 2012.
- [All04] O Allard. *Long-range interaction in the calcium dimer studied by molecular spectroscopy*. University of Hannover and Paris XI, 2004.
- [ASP03] O Allard, C Samuelis, A Pashov, H Knöckel, and E Tiemann. “Experimental study of the Ca_2 $^1\text{S}+^1\text{S}$ asymptote.” *Eur. Phys. J. D*, **26**:155, 2003.
- [BBB07] B Beck, J Becker, P Beiersdorfer, G Brown, K Moody, J Wilhelmy, F Porter, C Kilbourne, and R Kelley. “Energy Splitting of the Ground-State Doublet in the Nucleus Th229.” *Phys. Rev. Lett.*, **98**(14):142501, April 2007.
- [BD80] S E Butler and A Dalgarno. “Charge transfer of multiply charged ions with hydrogen and helium Landau-Zener calculations.” *The Astrophysical Journal*, **241**:838, 1980.
- [BD01] N Balakrishnan and A Dalgarno. “Chemistry at ultracold temperatures.” *Chem. Phys. Lett.*, **341**:652–656, 2001.
- [BEM87] T Bergeman, G Erez, and H J Metcalf. “Magnetostatic trapping fields for neutral atoms.” *Phys. Rev. A*, **35**(4):1535, February 1987.
- [BGK91] A S Bell, P Gill, H A Klein, and A P Levick. “Laser cooling of trapped ytterbium ions using a four-level optical-excitation scheme.” *Phys. Rev. A*, 1991.
- [BGM89] N. Beverini, F. Giannanco, E. Maccioni, F. Strumia, and G. Vissani. “Measurement of the calcium $^1\text{P}_1$ - $^1\text{D}_2$ transition rate in a laser-cooled atomic beam.” *Journal of the Optical Society of America B*, **6**(11):2188, November 1989.
- [BJ92] Y B Band and P S Julienne. “Optical-Bloch-equation method for cold-atom collisions: Cs loss from optical traps.” *Phys. Rev. A*, **46**:330, 1992.

- [BMB98] D J Berkeland, J D Miller, J C Bergquist, W M Itano, and D J Wineland. “Minimization of ion micromotion in a Paul trap.” *Journal of Applied Physics*, **83**(10):5025, 1998.
- [BMW93] V Bagnato, L Marcassa, Y Wang, J Weiner, P S Julienne, and Y B Band. “Ultracold photoassociative ionization collisions in a magneto-optical trap: The optical-field-intensity dependence in a radiatively dissipative environment.” *Phys. Rev. A*, **48**:2523, 1993.
- [BN09] I Buluta and F Nori. “Quantum Simulators.” *Science*, **326**(5949):108–111, October 2009.
- [BS85] H Baba and K Sakurai. “Multiple quantum jumps in vibration energy transfer of iodine in the $B\ ^3\Pi_0$ state along a supersonic beam expansion.” *J. Chem. Phys.*, **82**:4977, 1985.
- [BTR06] B Brkić, S Taylor, J Ralph, and N France. “High-fidelity simulations of ion trajectories in miniature ion traps using the boundary-element method.” *Phys. Rev. A*, **73**(1):012326, January 2006.
- [BW99] S C Bennett and C E Wieman. “Measurement of the 6S-7S transition polarizability in atomic cesium and an improved test of the Standard Model.” *Phys. Rev. Lett.*, **82**(12):2484–2487, 1999.
- [BW02] T Baba and I Waki. “Sympathetic cooling rate of gas-phase ions in a radio-frequency-quadrupole ion trap.” *Applied Physics B: Lasers and Optics*, **74**(4-5):375–382, April 2002.
- [C00] R Côté. “From classical mobility to hopping conductivity: Charge hopping in an ultracold gas.” *Phys. Rev. Lett.*, **85**(25):5316–5319, 2000.
- [CFK09] C Chin, V V Flambaum, and M G Kozlov. “Ultracold molecules: new probes on the variation of fundamental constants.” *New Journal of Physics*, **11**(5):055048, May 2009.
- [CGV12] M Cetina, A T Grier, and V Vuletić. “Micromotion-Induced Limit to Atom-Ion Sympathetic Cooling in Paul Traps.” *Phys. Rev. Lett.*, **109**(25):253201, December 2012.
- [Chi74] M S Child. *Molecular collision theory*. Academic Press, New York, 1974.

- [CHK10] C W Chou, D B Hume, J C J Koelemeij, D J Wineland, and T Rosenband. “Frequency comparison of two high-accuracy Al^+ optical clocks.” *Phys. Rev. Lett.*, **104**(7):70802, 2010.
- [Chu98] Steven Chu. “The manipulation of neutral particles.” *Rev. Mod. Phys.*, 1998.
- [CSK11] K Chen, S J Schowalter, S Kotochigova, A Petrov, W G Rellergert, S T Sullivan, and E R Hudson. “Molecular-ion trap-depletion spectroscopy of BaCl^+ .” *Phys. Rev. A*, **83**(3):30501, March 2011.
- [CSR13] K Chen, S T Sullivan, W G Rellergert, and E R Hudson. “Measurement of the Coulomb Logarithm in a Radio-Frequency Paul Trap.” *Phys. Rev. Lett.*, **110**(17):173003, April 2013.
- [Daw95] P H Dawson. *Quadrupole mass spectrometry and its applications*. 1995.
- [Dem64] Y N Demkov. “Charge transfer at small resonance defects.” *Sov. Phys. JETP*, **18**:138, 1964.
- [DeV09] R DeVoe. “Power-Law Distributions for a Trapped Ion Interacting with a Classical Buffer Gas.” *Phys. Rev. Lett.*, **102**(6):063001, February 2009.
- [DFM05] Donald J Douglas, Aaron J Frank, and Dunmin Mao. “Linear ion traps in mass spectrometry.” *Mass spectrometry reviews*, **24**(1):1–29, 2005.
- [DFZ04] A J Daley, P O Fedichev, and P Zoller. “Single-atom cooling by superfluid immersion: A nondestructive method for qubits.” *Phys. Rev. A*, January 2004.
- [Die09] M R Dietrich. *Barium ions for quantum computation*. PhD thesis, 2009.
- [DKW93] R Drozdowski, J Kwela, and M Walkiewicz. “Lifetimes of the $4s4p\ ^3\text{P}_1$ and $4s3d\ ^1\text{D}_2$ states of Ca I.” *Zeitschrift für Physik D*, **324**:321–324, 1993.
- [DMH10] J G Danzl, M J Mark, E Haller, and M Gustavsson. “An ultracold high-density sample of rovibronic ground-state molecules in an optical lattice.” *Nature Physics*, **6**:265, 2010.

- [DSS08] D DeMille, S Sainis, J Sage, T Bergeman, S Kotochigova, and E Tiesinga. “Enhanced Sensitivity to Variation of m_e/m_p in Molecular Spectra.” *Phys. Rev. Lett.*, **100**(4):1–4, January 2008.
- [Dub90] D H E Dubin. “First-order anharmonic correction to the free energy of a Coulomb crystal in periodic boundary conditions.” *Phys. Rev. A*, **42**(8), 1990.
- [EMW95] J Ensher, M Matthews, C Wieman, and E Cornell. “Observation of Bose-Einstein condensation in a dilute atomic vapor.” *Science*, January 1995.
- [FDH85] W Federer, W Dobler, and F Howorka. “Collisional relaxation of vibrationally excited $\text{NO}^+(\nu)$ ions.” *J. Chem. Phys.*, **83**(3):1032–1038, 1985.
- [Fer86] Eldon E Ferguson. “Vibrational quenching of small molecular ions in neutral collisions.” *J. Phys. Chem.*, **4201**(1983):731–738, 1986.
- [FK07] V V Flambaum and M G Kozlov. “Enhanced Sensitivity to the Time Variation of the Fine-Structure Constant and m_p/m_e in Diatomic Molecules.” *Phys. Rev. Lett.*, **99**:150801, 2007.
- [GCO09a] A Grier, M Cetina, F Oručević, and V Vuletić. “Observation of cold collisions between trapped ions and trapped atoms.” *Phys. Rev. Lett.*, January 2009.
- [GCO09b] A T Grier, M Cetina, F Oručević, and V Vuletić. “Observation of Cold Collisions between Trapped Ions and Trapped Atoms.” *Phys. Rev. Lett.*, **102**(22):223201, June 2009.
- [GLJ88] P L Gould, P D Lett, and P S Julienne. “Observation of associative ionization of ultracold laser-trapped sodium atoms.” *Phys. Rev. Lett.*, January 1988.
- [GQS04] M Gottselig, M Quack, J Stohner, and M Willeke. “Mode-selective stereomutation tunneling and parity violation in HOClH^+ and H_2Te_2 isotopomers.” *Int. J. Mass Spec.*, **233**(1-3):373–384, April 2004.
- [Gri04] D J Griffiths. *Introduction to Quantum Mechanics*. Prentice Hall, 2nd edition, 2004.
- [GSL02] K Góral, L Santos, and M Lewenstein. “Quantum Phases of Dipolar Bosons in Optical Lattices.” *Phys. Rev. Lett.*, **88**(17):170406, April 2002.

- [GSL09] W Griffith, M Swallows, T Loftus, M Romalis, B Heckel, and E Fortson. “Improved Limit on the Permanent Electric Dipole Moment of $^{199}\text{Hg}.$ ” *Phys. Rev. Lett.*, **102**:101601, 2009.
- [GWS78] H R Gray, R M Whitley, and C R Stroud. “Coherent trapping of atomic populations.” *Optics letters*, **3**(6):218–20, December 1978.
- [HAB11] Felix Hall, Mireille Aymar, Nadia Boulofa-Maafa, Olivier Dulieu, and Stefan Willitsch. “Light-Assisted Ion-Neutral Reactive Processes in the Cold Regime: Radiative Molecule Formation versus Charge Exchange.” *Phys. Rev. Lett.*, **107**(24):3–7, December 2011.
- [HDL08] P Herskind, A Dantan, M B Langkilde-Lauesen, A Mortensen, J L Sørensen, and M Drewsen. “Loading of large ion Coulomb crystals into a linear Paul trap incorporating an optical cavity.” *Applied Physics B*, **93**(2-3):373–379, September 2008.
- [HEH13] F H J Hall, P Eberle, G Hegi, M Raoult, M Aymar, O Dulieu, and S Willitsch. “Ion-neutral chemistry at ultralow energies: dynamics of reactive collisions between laser-cooled Ca^+ ions and Rb atoms in an ion-atom hybrid trap.” *Molecular Physics*, (August):1–13, April 2013.
- [HLS06] E Hudson, H Lewandowski, B Sawyer, and J Ye. “Cold Molecule Spectroscopy for Constraining the Evolution of the Fine Structure Constant.” *Phys. Rev. Lett.*, **96**(14):143004, April 2006.
- [HR94] R G Helmer and C W Reich. “An excited state of ^{229}Th at 3.5 eV.” *Phys. Rev. C*, **49**(4):1845–1858, 1994.
- [HST02] J Hudson, B Sauer, M Tarbutt, and E Hinds. “Measurement of the Electron Electric Dipole Moment Using YbF Molecules.” *Phys. Rev. Lett.*, **89**(2):023003, June 2002.
- [HTS06] E R Hudson, C Ticknor, B C Sawyer, C A Taatjes, H J Lewandowski, J R Bochinski, J L Bohn, and J Ye. “Production of cold formaldehyde molecules for study and control of chemical reaction dynamics with hydroxyl radicals.” *Phys. Rev. A*, **79**(6):63404, June 2006.
- [Hud09] E R Hudson. “Method for producing ultracold molecular ions.” *Phys. Rev. A*, **79**(3):032716, March 2009.
- [HWS01] C J Hawthorn, K P Weber, and R E Scholten. “Littrow configuration tunable external cavity diode laser with fixed direction output beam.” *Rev. Sci. Instr.*, **72**(12):4477, 2001.

- [HYS13] M T Hummon, M Yeo, B K Stuhl, A L Collopy, Y Xia, and J Ye. “2D Magneto-Optical Trapping of Diatomic Molecules.” *Phys. Rev. Lett.*, **110**(14):143001, April 2013.
- [ICJ09] Z Idziaszek, T Calarco, P S Julienne, and A Simoni. “Quantum theory of ultracold atom-ion collisions.” *Phys. Rev. A*, **79**(1):010702, January 2009.
- [ICZ07] Z Idziaszek, T Calarco, and P Zoller. *Phys. Rev. A*, **76**:33409, 2007.
- [Jav93] J Javanainen. *J. Opt. Soc. Am. B*, **10**:572, 1993.
- [JD99] D.S. Jin and B Demarco. “Onset of Fermi Degeneracy in a Trapped Atomic Gas.” *Science*, **285**(5434):1703–1706, 1999.
- [JSP02] S R Jefferts, J Shirley, T E Parker, T P Heavner, D M Meekhof, C Nelson, F Levi, G Costanzo, A De Marchi, R Drullinger, L Hollberg, W D Lee, and F L Walls. “Accuracy evaluation of NIST-F1.” *Metrologia*, **39**(4):321, 2002.
- [KCC06] D Kielpinski, M Cetina, J a Cox, and F X Kärtner. “Laser cooling of trapped ytterbium ions with an ultraviolet diode laser.” *Optics Letters*, **31**(6):757–9, March 2006.
- [Kin95] J B Kingdon. *Mon. Not. R. Astron. Soc.*, **274**:425, 1995.
- [KKG07] C Kollath, M Köhl, and T Giamarchi. “Scanning tunneling microscopy for ultracold atoms.” *Phys. Rev. A*, **76**:63602, 2007.
- [KL95] M G Kozlov and L Z Labowsky. “Parity violation effects in diatomics.” *J. Phys. B: At. Mol. Opt. Phys.*, **28**:1933–1961, 1995.
- [KLM03] G Karlström, R Lindh, and P Malmqvist. “MOLCAS: a program package for computational chemistry.” *Computational Materials Science*, **28**:222, 2003.
- [Kre08] R V Krems. “Cold controlled chemistry.” *Phys. Chem. Chem. Phys.*, **10**(28):4079–4092, 2008.
- [KRR05] A Kramida, Y Ralchenko, J Reader, and NIST ASD Team. “NIST Atomic Spectra Database.” p. <http://physics.nist.gov/asd>, 2005.
- [KS90] T Kurosu and F Shimizu. “Laser cooling and trapping of calcium and strontium.” *Jpn. J. Appl. Phys.*, 1990.

- [KSF09] R V Krems, W C Stwalley, and B Friedrich, editors. *Cold Molecules: Theory, Experiment, Applications*. CRC Press, Boca Raton, 2009.
- [KT05] S Kotochigova and E Tiesinga. *J. Chem. Phys.*, **123**:174304, 2005.
- [KW76] L A Kroger and Reich C W. “Features of the low-energy level scheme of ^{229}Th as observed in the alpha-decay of ^{233}U .” *Nuclear Physics A*, **259**:29–60, 1976.
- [Lan36] L D Landau. “Kinetic equation for the Coulomb effect.” *Phys. Z. Sowjetunion*, (10):154, 1936.
- [LBL11] A E Leanhardt, J L Bohn, and H Loh. “High-resolution spectroscopy on trapped molecular ions in rotating electric fields: A new approach for measuring the electron electric dipole moment.” *Journal of Molecular Spectroscopy*, **270**(1):1–25, November 2011.
- [Lev12] Fetter A L Stamper-Kurn D Levin, K, editor. *Ultracold Bosonic and Fermionic Gases*. Elsevier, Oxford, 2012.
- [LF04] H Lefebvre-Brion and R W Field. *The Spectra and Dynamics of Diatomic Molecules*. Academic Press, 2004.
- [Lid95] D R Lide, editor. *CRC Handbook of Chemistry*. CRC Press, 74th edition, 1995.
- [LJL10] T D Ladd, F Jelezko, R Laflamme, Y Nakamura, C Monroe, and J L O’Brien. “Quantum computers.” *Nature*, **464**(7285):45–53, April 2010.
- [LLB09] N Lemke, A Ludlow, Z Barber, and T Fortier. “Spin-1/2 optical lattice clock.” *Phys Rev Lett*, January 2009.
- [LMB03] D Leibfried, C Monroe, R Blatt, and D Wineland. “Quantum dynamics of single trapped ions.” *Rev. Mod. Phys.*, **75**(January):281–324, 2003.
- [LNP05] Lippardt, T Nazarova, P Pottie, U Sterr, and J Helmcke. “Calcium optical frequency standard with ultracold atoms: Approaching 10^{-15} relative uncertainty.” *Phys. Rev. A*, January 2005.
- [Lof01] T H Loftus. *Laser Cooling and Trapping of Atomic Ytterbium*. PhD thesis, 2001.
- [LP93] M De Labachelerie and G Passedat. “Mode-hop suppression of Lit-trow grating-tuned lasers.” *Applied Optics*, **32**(3):269–274, 1993.

- [LQZ09] C H Liu, Y Z Qu, Y Zhou, J G Wang, Y Li, and R J Buenker. “Radiative charge transfer in collisions of H^+ with Na at very low energies.” *Phys. Rev. A*, **79**:42706, 2009.
- [LSW92] K Lindquist, M Stephens, and C Wieman. “Experimental and theoretical study of the vapor-cell Zeeman optical trap.” *Phys. Rev. A*, **46**(7):4082–4091, 1992.
- [LVG02] A Luca, D Voulot, and D Gerlich. *WDS Proc. of Contrib. Pap.*, **2**:294, 2002.
- [LZC08] A Ludlow, T Zelevinsky, G Campbell, and S Blatt. “Sr lattice clock at 1×10^{-16} fractional uncertainty by remote optical evaluation with a Ca clock.” *Science*, January 2008.
- [Maj09] F G Major. *Charged Particle Traps II*. Springer, 2009.
- [MBG04] I. Moore, K. Bailey, J. Greene, Z.-T. Lu, P. Müller, T. OConnor, Ch. Geppert, K. Wendt, and L. Young. “Counting Individual Ca41 Atoms with a Magneto-Optical Trap.” *Phys. Rev. Lett.*, **92**(15):153002, April 2004.
- [MCM03] O P Makarov, R Ct, H Michels, and W W Smith. “Radiative charge-transfer lifetime of the excited state of $NaCa^+$.” *Phys. Rev. A*, **67**(4):42705, April 2003.
- [MD68] F G Major and H G Dehmelt. “Exchange-collision technique for the rf spectroscopy of stored ions.” *Phys. Rev.*, **170**:91, 1968.
- [MFF02] J McGuirk, G Foster, J Fixler, M Snadden, and M Kasevich. “Sensitive absolute-gravity gradiometry using atom interferometry.” *Phys. Rev. A*, **65**(3):33608, 2002.
- [MNS11] J J McLoughlin, A H Nizamani, and J D Siversn. “Versatile ytterbium ion trap experiment for operation of scalable ion-trap chips with motional heating and transition-frequency measurements.” *Phys. Rev. A*, pp. 1–9, 2011.
- [MPM05] K L Moore, T P Purdy, K W Murch, S Leslie, S Gupta, and D M Stamper-Kurn. “Collimated, single-pass atom source from a pulsed alkali metal dispenser for laser-cooling experiments.” *Rev. Sci. Instr.*, **76**(2):23106, January 2005.

- [MRM08] R Muhammad, J Ramirez-Serrano, K M F Magalhes, R Paiva, R Shiozaki, J Weiner, and V S Bagnato. “Efficiency in the loading of a sodium magneto-optical trap from alkali metal dispensers.” *Optics Communications*, **281**(19):4926 – 4930, 2008.
- [MTM92] Y Moriwaki, M Tachikawa, Y Maeno, and T Shimizu. “Collision cooling of ions stored in quadrupole radio-frequency trap.” *Jpn. J. Appl. Phys*, 1992.
- [MTR01] M Mérawa, C Tendero, and M Rérat. “Excited states dipole polarizabilities of calcium atom and long-range dispersion coefficients for the low-lying electronic states of Ca₂ and CaMg.” *Chem. Phys. Lett.*, **343**:397, 2001.
- [NGN98] A Nagel, L Graf, A Naumov, E Mariotti, V Biancalana, D Meschede, and R Wynands. “Experimental realization of coherent dark-state magnetometers.” *EPL (Europhysics Letters)*, **44**(1):31, 1998.
- [NHT80] W Neuhauser, M Hohenstatt, P E Toschek, and H Dehmelt. “Localized visible Ba⁺ mono-ion oscillator.” *Phys. Rev. A*, (3), 1980.
- [Nic81] R W Nicholls. “Franck-Condon factor formulae for astrophysical and other molecules.” *The Astrophysical Journal Supplement Series*, 1981.
- [NOM08] K Ni, S Ospelkaus, and MHG De Miranda. “A high phase-space-density gas of polar molecules.” *Science*, **322**:231, 2008.
- [NVH11] J H V Nguyen, C R Viteri, E G Hohenstein, C D Sherrill, K R Brown, and B Odom. “Challenges of laser-cooling molecular ions.” *New Journal of Physics*, **13**(6):063023, June 2011.
- [OBF99] C W Oates, F Bondu, R W Fox, and L Hollberg. “A diode-laser optical frequency standard based on laser-cooled Ca atoms: Sub-kilohertz spectroscopy by optical shelving detection.” *Eur. Phys. J. D*, **460**:449–460, 1999.
- [OL77] J J Olivero and R L Longbothum. “Empirical fits to the Voigt line width: a brief review.” *J. Quant. Spectrosc. Radiat. Transfer*, **17**:233–236, 1977.
- [OYM07] S Olmschenk, K Younge, D Moehring, D Matsukevich, P Maunz, and C Monroe. “Manipulation and detection of a trapped Yb⁺ hyperfine qubit.” *Phys. Rev. A*, **76**(5):052314, November 2007.

- [OZW06] A Ostendorf, C Zhang, M Wilson, D Offenberg, B Roth, and S Schiller. “Sympathetic Cooling of Complex Molecular Ions to Millikelvin Temperatures.” *Phys. Rev. Lett.*, **97**(24):1–4, December 2006.
- [PCS04] M Pichler, H Chen, and W Stwalley. “Photoassociation spectroscopy of ultracold Cs below the 6P limit.” *J. Chem. Phys.*, January 2004.
- [PD06] S G Porsev and A Derevianko. “High-accuracy calculations of dipole, quadrupole, and octupole electric dynamic polarizabilities and van der Waals coefficients C_6 , C_8 , and C_{10} for alkaline-earth dimers.” *Journal of Experimental and Theoretical Physics*, **102**(2):195–205, February 2006.
- [PS53] W Paul and H Steinwedel. “Ein neues Massenspektrometer ohne Magnetfeld.” *Zeitschrift für Naturforschung*, **8**:448–450, 1953.
- [RBO98] C. Raab, J. Bolle, H. Oberst, J. Eschner, F. Schmidt-Kaler, and R. Blatt. “Diode laser spectrometer at 493 nm for single trapped Ba + ions.” *Applied Physics B: Lasers and Optics*, **67**(6):683–688, December 1998.
- [RGM10] V S Reddy, S Ghanta, and S Mahapatra. “First principles quantum dynamical investigation provides evidence for the role of polycyclic aromatic hydrocarbon radical cations in interstellar physics.” *Phys. Rev. Lett.*, **104**:111102, 2010.
- [RHS08] T Rosenband, D Hume, P Schmidt, C W Chou, A Brusch, L Lorini, W H Oskay, R E Drullinger, T M Fortier, J E Stalnaker, S A Diddams, W C Swann, N R Newbury, W M Itano, D J Wineland, J C Bergquist, and T Et al. “Frequency ratio of Al⁺ and Hg⁺ single-ion optical clocks; metrology at the 17th decimal place.” *Science*, **319**(5871):1808–12, March 2008.
- [Ros04] M D Rosa. “Laser-cooling molecules.” *Eur. Phys. J. D*, **31**(2):395–402, November 2004.
- [RPC87] E L Raab, M Prentiss, Alex Cable, S Chu, and D E Pritchard. “Trapping of Neutral Sodium Atoms with Radiation Pressure.” *Phys. Rev. Lett.*, **59**(23):2631–2634, 1987.
- [RP06] E Ruchowska, W Pociennik, J ylicz, H Mach, J Kvasil, a. Alggora, N Amzal, T Bäck, M Borge, R Boutami, P Butler, J Cederkäll, B Cederwall, B Fogelberg, L Fraile, H Fynbo, E Hagebø, P Hoff, H Gausemel, A Jungclaus, R Kaczarowski, a. Kerek,

- W Kurcewicz, K Lagergren, E Nacher, B Rubio, A Syntfeld, O Tengblad, A Wasilewski, and L Weissman. “Nuclear structure of Th²²⁹.” *Phys. Rev. C*, **73**(4):1–17, April 2006.
- [RSK11] W G Rellergert, S T Sullivan, S Kotochigova, A Petrov, K Chen, S J Schowalter, and E R Hudson. “Measurement of a large chemical reaction rate between ultracold closed-shell ⁴⁰Ca atoms and open-shell ¹⁷⁴Yb⁺ ions held in a hybrid atom-ion trap.” *Phys. Rev. Lett.*, **107**(24):243201, December 2011.
- [RWG91] S Rolston, C Westbrook, and P Gould. “Laser modification of ultracold collisions: Experiment.” *Phys. Rev. Lett.*, January 1991.
- [RWN01] U Rapol, A Wasan, and V Natarajan. “Loading of a Rb magneto-optic trap from a getter source.” *Phys. Rev. A*, **80**(1):13409, January 2001.
- [RZS12] L Ratschbacher, C Zipkes, C Sias, and M Köhl. “Controlling chemical reactions of a single particle.” *Nature Physics*, **8**:649, July 2012.
- [SBC11] D I Schuster, L S Bishop, I L Chuang, D DeMille, and R J Schoelkopf. “Cavity QED in a molecular ion trap.” *Phys. Rev. A*, January 2011.
- [SBD10] E S Shuman, J F Barry, and D Demille. “Laser cooling of a diatomic molecule.” *Nature*, **467**(7317):820–3, October 2010.
- [SCR12] S J Schowalter, K Chen, W G Rellergert, S T Sullivan, and E R Hudson. “An integrated ion trap and time-of-flight mass spectrometer for chemical and photo- reaction dynamics studies.” *The Rev. Sci. Instr.*, **83**(4):43103, April 2012.
- [SCT07] M H Shah, H A Camp, and M L Trachy. “Model-independent measurement of the excited fraction in a magneto-optical trap.” *Phys. Rev. A*, **75**:53418, 2007.
- [SHD10] S Schmid, A Härtter, and J Denschlag. “Dynamics of a Cold Trapped Ion in a Bose-Einstein Condensate.” *Phys. Rev. Lett.*, **105**:133202, 2010.
- [SIM07] SIMION. *SIMION Collision Model HS1*, 2007.
- [SjS10] P F Staananum, Højbjørre, P S Skyt, A K Hansen, and M Drewsen. “Rotational laser cooling of vibrationally and translationally cold molecular ions.” *Nat Phys*, **6**(4):271–274, 2010.

- [Smi92] D Smith. “The ion chemistry of interstellar clouds.” *Chemical Reviews*, **92**:1473, 1992.
- [SML05] W W. Smith, O P. Makarov, and J Lin. “Cold ionneutral collisions in a hybrid trap.” *Journal of Modern Optics*, **52**(16):2253–2260, November 2005.
- [SRD10] T Schneider, B Roth, H Duncker, I Ernsting, and S Schiller. “All-optical preparation of molecular ions in the rovibrational ground state.” *Nat Phys*, **6**(4):275–278, 2010.
- [SRK11] S T Sullivan, W G Rellergert, S Kotochigova, K Chen, S J Schowalter, and E R Hudson. “Trapping molecular ions formed via photo-associative ionization of ultracold atoms.” *Phys. Chem. Chem. Phys.*, **13**(42):18859, January 2011.
- [SRK12] S T Sullivan, W G Rellergert, S Kotochigova, and E R Hudson. “Role of Electronic Excitations in Ground-State-Forbidden Inelastic Collisions Between Ultracold Atoms and Ions.” *Phys. Rev. Lett.*, **109**(22):223002, November 2012.
- [SSL03] L Santos, G V Shlyapnikov, and M Lewenstein. “Roton-Maxon Spectrum and Stability of Trapped Dipolar Bose-Einstein Condensates.” *Phys. Rev. Lett.*, **90**(25):250403, June 2003.
- [Ste05] S Stenholm. *Foundations of Laser Spectroscopy*. Dover books on physics. Dover Publications, 2005.
- [SZ96] P C Stancil and B Zygelman. “Radiative charge transfer in collisions of Li with H⁺.” *The Astrophysical Journal*, **472**:102, 1996.
- [TJT88] M Tichy, G Javahery, N D Twiddy, and E E Ferguson. “Vibrational quenching of HCl⁺(v=1) and DCl⁺(v=1) by Ar and Kr.” *Chem. Phys. Lett.*, **144**(2):131–135, February 1988.
- [TRG97] P. Taylor, M. Roberts, S. Gateva-Kostova, R. Clarke, G. Barwood, W. Rowley, and P. Gill. “Investigation of the ^{2}S_{-1/2}-^{2}D_{-5/2} clock transition in a single ytterbium ion.” *Phys. Rev. A*, **56**(4):2699–2704, October 1997.
- [TRL12] D A Tabor, V Rajagopal, Y Lin, and B Odom. “Suitability of linear quadrupole ion traps for large Coulomb crystals.” *Applied Physics B*, **107**(4):1097–1104, May 2012.

- [TWW10] X Tong, A H Winney, and S Willitsch. “Sympathetic Cooling of Molecular Ions in Selected Rotational and Vibrational States Produced by Threshold Photoionization.” *Phys. Rev. Lett.*, **105**:143001, 2010.
- [TZZ00] E V Tkalya, A N Zherikhin, and V I Zhudov. “Decay of the low-energy nuclear isomer $^{229}\text{Th}^m(3/2^+, 3.5 \pm 1.0 \text{ eV})$ in solids (dielectrics and metals): A new scheme of experimental research.” *Physical Review C*, **61**:1–6, 2000.
- [Van05] J Vanier. “Atomic clocks based on coherent population trapping: a review.” *Applied Physics B*, **81**(4):421–442, July 2005.
- [VCG10] A C Vutha, W C Campbell, Y V Gurevich, N R Hutzler, M Parsons, D Patterson, E Petrik, B Spaun, J M Doyle, G Gabrielse, and D DeMille. “Search for the electric dipole moment of the electron with thorium monoxide.” *J. Phys. B: At. Mol. Opt. Phys.*, **43**(7):74007, 2010.
- [WB08] S Willitsch and M T Bell. “Chemical applications of laser-and sympathetically-cooled ions in ion traps.” *Phys. Chem. Chem. Phys.*, **10**:7200, 2008.
- [WBZ99] J Weiner, V S Bagnato, S Zilio, and P S Julienne. “Experiments and theory in cold and ultracold collisions.” *Rev. Mod. Phys.*, **71**:1, 1999.
- [WFG95] C Wieman, G Flowers, and S Gilbert. “Inexpensive Laser Cooling and Trapping Experiment For Undergraduate Laboratories.” *Am. J. Phys.*, **63**(4):317–330, January 1995.
- [WMD55] W C Wiley, I H McLaren, V H Dibeler, D F Eggers, M Wolff, W E Stephens, and S S Friedland. “Timeofflight mass spectrometer with improved resolution.” *Rev. Sci. Instr.*, **26**(12), 1955.
- [WMG89] T Walker, C Monroe, A Gallagher, and C Wieman. “Collisional losses from a light-force atom trap.” *Phys. Rev. Lett.*, January 1989.
- [Woo07] J Woodall. “The UMIST database for astrochemistry 2006.” *Astronomy and Astrophysics*, **466**:1197, 2007.
- [WSD95] C D Wallace, V Sanchez-Villicana, T P Dinneen, and P L Gould. “Suppression of Trap Loss Collisions at Low Temperature.” *Phys. Rev. Lett.*, **74**(7):1087–1090, February 1995.

- [Ye04] C Ye. *Tunable External Cavity Diode Lasers*. World Scientific Publishing Company Incorporated, 2004.
- [YM00] N Yu and L Maleki. “Lifetime measurements of the $4f^{14}5d$ metastable states in single ytterbium ions.” *Phys. Rev. A*, **61**(July 1999):12–15, 2000.
- [ZD88] B Zygelman and A Dalgarno. “Radiative quenching of He (2^1S) induced by collisions with ground-state helium atoms.” *Phys. Rev. A*, **38**:1877, 1988.
- [ZD07] P Zhang and A Dalgarno. “Static dipole polarizability of ytterbium.” *J. Phys. Chem. A*, **111**:12471–12476, 2007.
- [ZDC09] Peng Zhang, Alex Dalgarno, and Robin Côté. “Scattering of Yb and Yb^+ .” *Phys. Rev. A*, **80**:30703, 2009.
- [ZDK89] B Zygelman, A Dalgarno, M Kimura, and N F Lane. “Radiative and nonradiative charge transfer in $\text{He}^+ + \text{H}$ collisions at low energy.” *Phys. Rev. A*, **40**(5):2340–2345, 1989.
- [ZEN12] X Zhao, M de Escobar, Y Natali, R Rundberg, E M Bond, A Moody, and D J Vieira. “Observation of the Deexcitation of the ^{229}Th Nuclear Isomer.” *Phys. Rev. Lett.*, **109**(16):160801, October 2012.
- [ZPR10] C Zipkes, S Palzer, L Ratschbacher, C Sias, and M Köhl. “Cold heteronuclear atom-ion collisions.” *Phys. Rev. Lett.*, **105**:133201, May 2010.
- [ZPS10] C Zipkes, S Palzer, C Sias, and M Köhl. “A trapped single ion inside a BoseEinstein condensate.” *Nature*, **464**(7287), February 2010.
- [ZS04] L B Zhao and P C Stancil. “Radiative charge transfer in collisions of O with He^+ .” *The Astrophysical Journal*, **615**:1063, 2004.